申报	系列：教师系列 教学科研并重型
	专业：农业机械化工程
	职称：副教授

业绩成果材料

（申报人的业绩成果材料包括论文、科研项目、获奖以及其他成果等）

单　位（二级单位）　工程学院

姓　名　　赵润茂

材料核对人:　　单位盖章:

核对时间:

华南农业大学制

目　录（模板）

2.科研平台

五、其他业绩

1.指导学生学科竞赛

2.个人荣誉

3.社会服务

【佐证材料切记与目录页所列页码对应，不要用图片格式的材料进行打印。】

一、教学研究业绩

教育部学位与研究生教育发展中心

学位中心函〔2024〕8号

关于反馈2023年度主题案例立项结果的函

华南农业大学:

2023年12月，教育部学位与研究生教育发展中心面向全国研究生培养单位开展主题案例征集工作，扎根中国大地，聚焦时代热点，汇聚各方力量，开发具有时代性、引领性、学理性、创新性的高质量案例。经过“单位审核推荐”“专家分组评议”“案例专家委审核”三级评议审核及结果公示，你校共有3项选题入围，其中“大国智造”主题2项，“区域协调发展”主题1项，详细清单附后。

项目将于2024年7月开展中期交流，10月启动结项验收，具体安排另行通知。请组织并支持各首席专家团队推动项目实施，产出高质量案例成果。

感谢对中国专业学位案例建设事业的支持!

附件：2023年度主题案例立项结果清单

教育部学位与研究生教育发展中心

2024年3月25日

附件

2023年度主题案例立项结果清单

（按主题方向及首席专家姓氏笔画排序）

单位名称：华南农业大学

序号	项目编号	首席专家	主题方向	选题名称
1	ZT-231056410	胡炼	大国智造	智能农机实现无人化智慧农场的探索与实践——以广东万绿智慧无人农场为例
2	ZT-231056407	谭成全	大国智造	高产母猪精准营养与智慧养殖
3	ZT-231056408	陈灿	区域协调发展	农业集群品牌价值共创研究——以“万绿河源”为例

结项证书

CERTIFICATE OF COMPLETION

项目类别：　中国专业学位案例中心 2023 年度主题案例

项目编号：　ZT-231056410

项目名称：　智能农机实现无人化智慧农场的探索与实践——以广东万绿智慧无人农场为例

首席专家：　胡炼

团队成员：　何杰,汪沛,黄培奎,赵润茂,高锐涛

本项目经审核准予结项，特发此证。

教育部学位与研究生教育发展中心

2025 年 08 月

华南农业大学文件

华南农教〔2025〕57号

关于公布华南农业大学2025年度校级本科教学质量与教学改革工程项目立项名单的通知

各学院、部处、各单位:

根据《关于开展2025年度校级本科教学质量与教学改革工程项目申报工作的通知》精神,经项目负责人申请、所在单位推荐、本科生院审核、学校组织专家评审和公示(无异议)等程序,决定立项“善境伦理学与风景园林专业实践教学深度融合的探索与实践”等127个项目为2025年度校级本科教学改革项目,立项“筑基·焕新·赋能:食品质量与安全专业‘新工科’建设暨工程教育认证提质创新工程”等52个项目为2025年度校级本科质量工程项目。具体名单见附件。

请各项目负责人按照项目建设任务及要求,及时开展各项改

革工作; 各单位要切实履行项目建设主体责任，加强对项目建设的督促、指导，以确保项目建设任务高质量完成。

特此通知。

附件：1. 2025 年度校级本科教学改革项目立项名单

2. 2025 年度校级本科质量工程项目立项名单

华南农业大学

2025 年 10 月 14 日

（联系人：孙齐胜；电　话：85288020）

公开方式：主动公开

华南农业大学党政办公室　　2025 年 10 月 15 日印发

23	JG2025023	聚焦机器视觉课程改革—基于产教融合、科教融汇的卓越应用型人才培养路径探索	重点	电子工程学院（人工智能学院）	杨意	刘金龙，马稚昱，刘勇，牟英辉
24	JG2025024	AI赋能学生论文写作的教学改革与实践——基于学生认知视角	重点	经济管理学院	石敏	贺梅英、谭莹
25	JG2025025	英国文学史课程的AI知识图谱构建及数智化教学实践研究	重点	外国语学院	李良博	吕靖、张丁元、侯金萍、袁庆锋
26	JG2025026	AI赋能《数学分析》一流课程建设的改革与实践研究	重点	数学与信息学院、软件学院	金玲玉	金玲玉、房少梅、杨德贵、雷春林、危苏婷
27	JG2025027	AI背景下面向农经专业本科生的《大数据 分析与挖掘》课程体系建设与教学模式优化	重点	经济管理学院	文乐	李琴、陈有华、谭莹、伍敬文
28	JG2025028	基于大模型辅助的软件体系结构课程生成式编程教学改革与实践	重点	数学与信息学院、软件学院	林毅申	林毅申、曹维、周运华、梁早清
29	JG2025029	《种子加工与贮藏学》“理论-实践-实习”三位一体教学的探索和实践	重点	农学院	张亚锋	徐振江、邓婧、江院、张慧
30	JG2025030	中华优秀传统文化融入高校思政课程的路径研究——聚焦《马克思主义基本原理》课程	重点	马克思主义学院	禹规娥	何艳玲、王竹波、蒋正峰、谢翾
31	JG2025031	新时代应用型人才培养模式创新改革与实践研究——以环境工程专业为例	重点	资源环境学院	陈烁娜	方秋中、卫泽斌、黄柱坚、钟媛卿
32	JG2025032	产教融合视域下《家具定制技术》课程“三融四阶五维”教学模式创新与实践	重点	材料与能源学院	郭琼	宋杰、欧荣贤、涂登云，徐宁
33	JG2025033	面向AI赋能的《机械设计基础》“1+1+1+N”混合式教学方法	重点	工程学院	王慰祖	夏红梅、甄文斌、卢家欢、程碧懿
34	JG2025034	“科研-竞赛-创新”协同融合培养智慧农业拔尖人才探索与实践	重点	工程学院	何杰	何杰，汪沛，胡炼，高锐涛，赵润茂
35	JG2025035	基于RAMP原则的“学科——安全”化学实验双线融合教育体系构建与实践	重点	基础实验与实践训练中心	林碧敏	郑明轩，肖勇，刘维，刘小波
36	JG2025036	基于人工智能与虚拟仿真融合的《分子生物学》智慧课程体系建设与教学模式改革	重点	食品学院	叶志伟	赵雷、黎攀、邹苑
37	JG2025037	产科教融合视角下茶学专业课程体系优化与实践——以《茶树栽培学》为例	重点	园艺学院	郑鹏	孙彬妹、曹藩荣、刘少群、晏嫦妤
38	JG2025038	生成式AI驱动农林院校“新文科”教学模式创新 —《应急管理概论》智慧课程的建设实践	重点	公共管理学院	游艳玲	刘志明、赵国洪、马启彬、张建桃
39	JG2025039	面向实践能力提升的新文科（管理学类）AI课堂：数据分析可视化的“教-学-练-评”闭环体系构建	重点	数学与信息学院、软件学院	古万荣	唐德玉，余平祥，韦婷婷，毛宜军
40	JG2025040	基于“课程思政+产教融合”双驱动的茶叶审评与检验实习课程创新实践	重点	园艺学院	孟慧	谭新东、孙彬妹、张凌云、周仁杰
41	JG2025041	基于智能网络的生物化学全英课程改革与实践	重点	生命科学学院	洪梅	朱国辉、母培强、张智胜
42	JG2025042	植物病理学课程思政教育的创新与实践	自筹	植物保护学院	司徒俊键	孔广辉；习平根；李敏慧；姜子德
43	JG2025043	三全育人视域下的《病媒生物》思政教学探索与实践	自筹	植物保护学院	王德森	王磊、黄嘉

华南农业大学教育教学研究和改革项目

申 报 书

项目类别 2025年度教育教学改革项目重点项目

项目名称 “科研-竞赛-创新”协同融合培养智慧农业拔尖人才探索与实践

项目负责人 何 杰

职 称 副教授

手机号码 [redacted]

所在单位 工程学院（公章）

申报日期 2025.6.15

华南农业大学 本科生院 制

二〇二五年 五月

一、项目及项目负责人、项目组简况

<table>
<tr><td rowspan="3">项目简况</td><td>项目名称</td><td colspan="5">“科研-竞赛-创新”协同融合培养智慧农业拔尖人才探索与实践</td></tr>
<tr><td>项目类别</td><td colspan="5">■1.重点项目　　□2.自筹项目</td></tr>
<tr><td>起止年月</td><td colspan="5">2026 年 1 月-2027 年 12 月</td></tr>
<tr><td rowspan="15">项目申请人</td><td>姓名</td><td>何杰</td><td>性别</td><td>男</td><td>出生年月</td><td>1985.08.28</td></tr>
<tr><td>专业技术职务/行政职务</td><td colspan="2">副教授/无</td><td colspan="2">最终学位/授予国家</td><td>博士/中国</td></tr>
<tr><td rowspan="2">所在单位及联系方式</td><td>单位名称</td><td colspan="2">工程学院</td><td>手机号码</td><td></td></tr>
<tr><td>电子邮箱</td><td colspan="4">hooget@scau.edu.cn</td></tr>
<tr><td rowspan="10">主要教学工作简历</td><td>时间</td><td>课程名称</td><td>授课对象</td><td>学时</td><td>所在单位</td></tr>
<tr><td>2023-2025</td><td>电路与模拟电子技术</td><td>2022-2023 车辆工程 本科</td><td>128</td><td>工程学院</td></tr>
<tr><td>2024-2025</td><td>数字电子技术</td><td>2022-2023 车辆工程 本科</td><td>64</td><td>工程学院</td></tr>
<tr><td>2018-2023</td><td>自动控制理论实验</td><td>2015-2021 自动化、电气工程及其自动化本科</td><td>16</td><td>工程学院</td></tr>
<tr><td>2018-2023</td><td>PLC 实验</td><td>2015-2021 自动化、电气工程及其自动化本科</td><td>16</td><td>工程学院</td></tr>
<tr><td>2018-2023</td><td>传感器与检测实验</td><td>2015-2022 自动化、电气工程及其自动化、机器人工程本科</td><td>16</td><td>工程学院</td></tr>
<tr><td>2018-2023</td><td>计算机控制技术实验</td><td>2015-2021 自动化、电气工程及其自动化本科</td><td>16</td><td>工程学院</td></tr>
<tr><td>2019-2023</td><td>智能农机装备</td><td>2019-2022 工程研究生</td><td>8</td><td>工程学院</td></tr>
<tr><td>2025</td><td>智慧农业</td><td>2024 工程研究生</td><td>16</td><td>工程学院</td></tr>
<tr><td>主要教学</td><td>时间</td><td colspan="2">项目名称</td><td colspan="2">获奖情况</td></tr>
</table>

<table>
<tr><td rowspan="4"></td><td rowspan="4">改革和科学研究工作简历</td><td>2022</td><td colspan="3">科教融合的智慧农业创新人才培养模式探索与实践</td><td colspan="3"></td></tr>
<tr><td>2020</td><td colspan="3">《农业机器人》教学模式与创新实践</td><td colspan="3"></td></tr>
<tr><td></td><td colspan="3"></td><td colspan="3"></td></tr>
<tr><td colspan="7"></td></tr>
<tr><td rowspan="8">项目组</td><td rowspan="2">总人数</td><td colspan="3">职称</td><td colspan="3">学位</td><td></td></tr>
<tr><td>高级</td><td>中级</td><td>初级</td><td>博士后</td><td>博士</td><td>硕士</td><td>参加单位数</td></tr>
<tr><td>6</td><td>6</td><td>0</td><td>0</td><td>1</td><td>1</td><td>2</td><td>1</td></tr>
<tr><td rowspan="6">主要成员（不含申请者）</td><td>姓名</td><td>性别</td><td>出生年月</td><td>职称</td><td>工作单位</td><td>分工</td><td>签名[2]</td></tr>
<tr><td>汪沛</td><td>女</td><td></td><td>副教授</td><td>工程学院</td><td>教学研究</td><td></td></tr>
<tr><td>胡炼</td><td>男</td><td></td><td>研究员</td><td>工程学院</td><td>教学研究</td><td></td></tr>
<tr><td>高锐涛</td><td>男</td><td></td><td>教授</td><td>工程学院</td><td>教学研究</td><td></td></tr>
<tr><td>黄培奎</td><td>男</td><td></td><td>高级工程师</td><td>工程学院</td><td>教学研究</td><td></td></tr>
<tr><td>赵润茂</td><td>男</td><td></td><td>副教授</td><td>工程学院</td><td>教学研究</td><td></td></tr>
</table>

[2]此页须成员手写签字后扫描成 PDF 电子版。

華南農業大學

本科教学成果奖

获奖证书

获奖成果：“一库两基地”产科教汇融平台赋能智能农机类拔尖人才培养模式的探索与实践

获 奖 者：胡　炼、何　杰、赵润茂、汪　沛、罗锡文、许细薇、王红军

获奖等级：一等奖

证书编号：JXCG24015

2025年9月9日

二、科研项目

31001204-2109

国家自然科学基金

资助项目准予结题通知

赵润茂　同志：

您承担的国家自然科学基金项目：(融合视觉伺服感知及执行定位容差的非结构环境下茶叶嫩梢采摘机理)，批准号：(52105284)按有关规定已审核完毕，准予结题。

与本项目资助有关的后续成果，请您继续及时报送。

祝您在研究工作中取得更好的成绩！

国家自然科学基金委员会

工程与材料科学部

2025年3月27日

子课题编号：2024YFD200010052

国家重点研发计划
子课题任务合同书

子课题名称：	水稻“四良融合”与单产提升应用模式示范
所属课题：	粮油作物“四良融合”与单产提升应用模式构建及示范
所属项目：	粮油作物大面积单产提升智能装备创制与智慧系统集成应用
课题承担单位：	北大荒信息有限公司（盖章）
子课题承担单位：	华南农业大学（盖章）
子课题负责人：	赵润茂
执行期限：	2024 年 12 月　至　2027 年 11 月

2024 年 12 月

子课题基本信息表

<table>
<tr><td colspan="2">子课题名称</td><td colspan="6">水稻“四良融合”与单产提升应用模式示范</td></tr>
<tr><td colspan="2"></td><td colspan="6">2024YFD200010052</td></tr>
<tr><td colspan="2"></td><td colspan="6">粮油作物“四良融合”与单产提升应用模式构建及示范</td></tr>
<tr><td colspan="2">所属项目</td><td colspan="6">粮油作物大面积单产提升智能装备创制与智慧系统集成应用</td></tr>
<tr><td colspan="2">经费预算</td><td colspan="6">总需求 50 万元，其中中央财政专项资金需求 50 万元</td></tr>
<tr><td colspan="2" rowspan="2">子课题周期节点</td><td>起始时间</td><td>2024 年 12 月</td><td>结束时间</td><td colspan="2">2027 年 11 月</td></tr>
<tr><td>实施周期</td><td>共 36 个月</td><td>预计中期时间点</td><td colspan="2">2026 年 05 月</td></tr>
<tr><td rowspan="7">子课题承担单位</td><td>单位名称</td><td colspan="2">华南农业大学</td><td>单位法定代表人姓名</td><td colspan="2">薛红卫</td></tr>
<tr><td>单位性质</td><td colspan="2">大专院校</td><td>组织机构代码</td><td colspan="2">12440000455416563
4</td></tr>
<tr><td></td><td colspan="2">广东省</td><td>地市（市、自治州）</td><td colspan="2">广州市</td></tr>
<tr><td>通信地址</td><td colspan="2">华南农业大学农业工程楼 307</td><td>邮政编码</td><td colspan="2">510642</td></tr>
<tr><td>单位开户名称</td><td colspan="4">华南农业大学</td></tr>
<tr><td>开户银行（全称）</td><td colspan="2">中国工商银行广州五山支行</td><td>汇入地点</td><td colspan="2"></td></tr>
<tr><td>银行账号</td><td colspan="2">3602002609000310520</td><td>银行机构代码</td><td colspan="2"></td></tr>
<tr><td rowspan="6">子课题负责人</td><td>姓 名</td><td>赵润茂</td><td>性 别</td><td>☑男☐女</td><td>出生日期</td><td>90.12.18</td></tr>
<tr><td>证件类型</td><td>身份证</td><td>证件号码</td><td colspan="3">[redacted]</td></tr>
<tr><td>所在单位</td><td colspan="5">华南农业大学工程学院</td></tr>
<tr><td>最高学位</td><td colspan="5">☑博士 ☐硕士 ☐学士 ☐其他</td></tr>
<tr><td>职 称</td><td colspan="3">☐正高级 ☑副高级 ☐中级 ☐初级 ☐其他</td><td>职务</td><td>无</td></tr>
<tr><td>电子邮箱</td><td colspan="2">rmzhao@scau.edu.cn</td><td>移动电话</td><td colspan="2">1[redacted]</td></tr>
<tr><td></td><td></td><td colspan="5">高级职称 0 人，中级职称 0 人，初级职称 0 人，其他 4 人；</td></tr>
<tr><td></td><td></td><td colspan="5">— —</td></tr>
</table>

八、合同书签订各方签章

课题承担单位（盖章）：

课题负责人（签字）：

年　月　日

子课题承担单位（盖章）：

子课题负责人（签字）：

年　月　日

合同编号：

技术服务合同

项目名称：指导研发水稻收获机自动作业系统

委 托 方：重庆市农业科学院（盖章）

受 托 方：华南农业大学（盖章）

签订时间：2024 年 7 月 29 日

签订地点：广东广州

有效期限：2024 年 8 月-2024 年 12 月

技术服务合同

委托方（甲方）：重庆市农业科学院（盖章）

单　位　地　址：重庆市九龙坡区白市驿镇农科大道

法 定 代 表 人：苟小红

项 目 联 系 人：杜　斌

联　系　方　式：

通　讯　地　址：重庆市九龙坡区白市驿镇农科大道

电　　话：

传　　真：

电 子 邮 箱：

受托方（乙方）：华南农业大学 （盖章）

单　位　地　址：广东省广州市天河区五山路 483 号

法 定 代 表 人：薛红卫

项 目 联 系 人：赵润茂

联　系　方　式：

通　讯　地　址：华南农业大学农业工程楼

电　　话：

传　　真：

电 子 邮 箱：rmzhao@scau. edu. cn

出工作事项和技术支撑需求，甲方应指定专人负责接待、联络并及时反馈信息；

2. 甲方对乙方所提工作事项应予以积极支持，尽量满足其需求，并做好相关项目的人员组织及计划安排工作；

3. 双方对合作的项目和内容，都具有保密义务，对涉及合作项目和领域的技术、文档、数据及相关信息等内容双方进一步商量签订具体保密措施。

第四条：甲方向乙方支付技术服务报酬及支付方式为：

1. 技术服务费总额为：99000（大写：玖万玖仟元整）

2. 技术服务费由甲方一次（一次或分期）支付乙方。

具体支付方式和时间如下：2024 年 12 月 31 日前完成支付。

乙方开户银行名称、地址和帐号为：

开户银行：中国工商银行广州五山支行

地址：广州市天河区五山路 483 号

帐号：3602 0026 0900 0310 520

第五条：本合同技术服务经费由乙方按照《华南农业大学横向科技项目及经费管理办法》执行，甲方不得妨碍乙方正常工作。

第六条：本合同的变更必须由双方协商一致，并以书面形式确定。

第七条：双方确定以下列标准和方式对乙方的技术服务工作成果进行验收：

1. 技术服务工作成果的验收标准：①收获机能够实现路径自动跟踪、割台自动升降、自动卸粮，全程自动作业；②自动导航直线

甲　方：重庆市农业科学院

（盖章）

法定代表人／委托代理人：　　（签名）

2024 年 9 月 30 日

乙　方：华南农业大学

（盖章）

法定代表人／委托代理人：　　（签名）

年　　月　　日

印花税票粘贴处：

子课题编号：2025YFD230040401　　**密　　级：公开**

国家重点研发计划
子课题任务书

子 课 题 名 称：	标准一致耕深自保持技术开发及水田旋耕起浆装备创制
子课题承担单位：	华南农业大学
子课题负责人：	汪沛
课 题 名 称：	面向东北水田（水稻）的边缘智能技术开发及精准作业装备创制
课题承担单位：	华南农业大学
项 目 名 称：	东北地区规模化粮食作物智慧农场构建技术
项目牵头单位：	潍柴雷沃智慧农业科技股份有限公司
执行期限：	2025 年 12 月至 2028 年 11 月

中华人民共和国科学技术部制

课题基本信息表

<table>
<tr><td>子课题名称</td><td colspan="5">标准一致耕深自保持技术开发及水田旋耕起浆装备创制</td></tr>
<tr><td>子课题编号</td><td colspan="5">2025YFD230040401</td></tr>
<tr><td>课题名称</td><td colspan="5">面向东北水田（水稻）的边缘智能技术开发及精准作业装备创制</td></tr>
<tr><td>课题编号</td><td colspan="5">2025YFD2300404</td></tr>
<tr><td>密级</td><td colspan="2">■公开 □秘密 □机密</td><td>单位总数</td><td colspan="2">1</td></tr>
<tr><td>课题类型</td><td colspan="5">□基础前沿 □重大共性关键技术 ■应用示范研究 □其他</td></tr>
<tr><td>课题活动类型</td><td colspan="5">□基础前沿 ■应用研究 □试验发展</td></tr>
<tr><td>课题研究
所属学科</td><td colspan="5">自然科学相关工程与技术
农业工程</td></tr>
<tr><td>课题成果应用的主要国民经济行业</td><td colspan="5">农、林、牧、渔业
农业
谷物种植
稻谷种植</td></tr>
<tr><td>课题的社会
经济目标</td><td colspan="5">农林牧渔业发展
农林牧渔业发展一般问题</td></tr>
<tr><td>经费预算</td><td colspan="5">总需求 70.00 万元，其中中央财政专项资金需求 70.00 万元</td></tr>
<tr><td rowspan="2">课题周期节点</td><td>起始时间</td><td>2025 年 12 月</td><td>结束时间</td><td colspan="2">2028 年 11 月</td></tr>
<tr><td>实施周期</td><td>共 36 个月</td><td>预计中期时间点</td><td colspan="2">2027 年 6 月</td></tr>
<tr><td rowspan="8">子课题
承担
单位</td><td>单位名称</td><td colspan="2">华南农业大学</td><td>单位法定代表人姓名</td><td>薛红卫</td></tr>
<tr><td>单位性质</td><td colspan="2">大专院校</td><td>组织机构代码</td><td>124400004554165634</td></tr>
<tr><td>单位主管部门</td><td colspan="2">广东省教育厅</td><td>隶属关系</td><td>地方</td></tr>
<tr><td>单位所属地区</td><td colspan="2">广东省</td><td>地市（市、自治州、盟）</td><td>广州市 天河区</td></tr>
<tr><td>通信地址</td><td colspan="2">广东省广州市天河区五山路 483 号</td><td>邮政编码</td><td>510642</td></tr>
<tr><td>单位开户名称</td><td colspan="4">华南农业大学</td></tr>
<tr><td>开户银行（全称）</td><td colspan="2">中国工商银行股份有限公司广州五山支行</td><td>汇入地点</td><td>广东省 广州 市</td></tr>
<tr><td>银行账号</td><td colspan="2">3602002609000310520</td><td>银行机构代码</td><td>102581000546</td></tr>
</table>

<table>
<tr><td rowspan="6">子课题负责人</td><td>姓 名</td><td>汪沛</td><td>性 别</td><td>□男■女</td><td>出生日期</td><td>- -</td></tr>
<tr><td>证件类型</td><td>身份证</td><td>证件号码</td><td colspan="3"></td></tr>
<tr><td>所在单位</td><td colspan="5">华南农业大学</td></tr>
<tr><td>最高学位</td><td colspan="5">■博士 □硕士 □学士 □其他</td></tr>
<tr><td>职 称</td><td colspan="3">□正高级 ■副高级 □中级 □初级 □其他</td><td>职务</td><td>副主任</td></tr>
<tr><td>电子邮箱</td><td colspan="2">wangpei@scau.edu.cn</td><td>移动电话</td><td colspan="2"></td></tr>
<tr><td rowspan="3">课题联系人</td><td>姓 名</td><td>赵润茂</td><td>电子邮箱</td><td colspan="3">rmzhao@scau.edu.cn</td></tr>
<tr><td>固定电话</td><td>020-</td><td>移动电话</td><td colspan="3"></td></tr>
<tr><td>证件类型</td><td>身份证</td><td>证件号码</td><td colspan="3"></td></tr>
<tr><td rowspan="3">课题财务负责人</td><td>姓 名</td><td>肖斐</td><td>电子邮箱</td><td colspan="3">37115980@qq.com</td></tr>
<tr><td>固定电话</td><td>020-</td><td>移动电话</td><td colspan="3"></td></tr>
<tr><td>证件类型</td><td>身份证</td><td>证件号码</td><td colspan="3"></td></tr>
<tr><td rowspan="2">课题参加人数</td><td rowspan="2">34 人。其中：</td><td colspan="5">高级职称 5 人，中级职称 0 人，初级职称 1 人，其他 24 人；</td></tr>
<tr><td colspan="5">博士学位 5 人，硕士学位 0 人，学士学位 6 人，其他 2 人。</td></tr>
<tr><td>子课题简介(限 500 字以内)</td><td colspan="6">以东北水稻生产全流程处方决策为基础，以“实时感知-边缘决策-精准执行”为核心技术主线，开展标准一致耕深自保持技术研究，集成创制耕深自保持智能旋耕起浆机，重点突破旋耕起浆深度实时感知与抗扰精准控制，解决传统规模作业模式粗放的难题。</td></tr>
</table>

九、子课题参加人员基本情况表

填表说明： 1.专业技术职称：A、正高级　B、副高级　C、中级　D、初级　E、其他；
2.投入本课题的全时工作时间（人月）是指在课题实施期间该人总共为课题工作的满月度工作量；累计是指课题组所有人员投入人月之和；
3.课题固定研究人员需填写人员明细；
4.是否有工资性收入：Y、是　N、否；
5.人员分类代码：B、课题负责人　C、项目/课题骨干　D、其他研究人员；
6.工作单位：填写单位全称，其中高校要具体填写到所在院系。

序号	姓名	性别	出生日期	证件类型	证件号码	专业技术职称	职务	最高学位	专业	投入本课题的全时工作时间（人月）	人员分类代码	在课题中分担的任务	是否有工资性收入	工作单位
1	汪沛	女	- -	身份证		B	无	博士	农业电气化与自动化	18	B	课题方案实施	Y	华南农业大学
2	赵润茂	男	- -	身份证		B	无	博士	农业机械化	18	C	耕深运动模型建立	Y	华南农业大学
3	陈禹琦	男	- -	身份证		E	无	学生	农业工程	18	C	耕深实时估计算法与系统优化改进	N	华南农业大学
4	孙正	男	- -	身份证		E	无	硕士	农业工程	18	C	旋耕起浆耕深感知	N	华南农业大学
5	吕家驹	男	- -	身份证		E	无	学士	控制工程	18	C	旋耕起浆耕深感知	N	华南农业大学
6	邓小兵	男	- -	身份证		E	无	学士	农业工程	18	C	旋耕起浆耕深控制	N	华南农业大学
7	陈高隆	男	- -	身份证		D	无	博士	农业工程	18	C	自抗扰控制算法与系统优化改进	Y	华南农业大学

合同编号：

技术服务合同

项目名称：广东省益信无人化智慧农场建设技术服务

委 托 方：广东省益信农业科技有限公司

（甲 方）

受 托 方：华南农业大学

（乙 方）

有效期限：2025 年 1 月 1 日－2026 年 12 月 31 日

技术服务（委托）合同书

甲方：广东省益信农业科技有限公司

住　所　地：肇庆封开县江口街道封州二路178号二楼

法定代表人：余益耀

项目联系人：温超然

联系方式：[illegible]

通讯地址：封开县江口街道封州二路178号二楼

电　　话：_____ 传　　真：_____

电子信箱：_____

乙方：华南农业大学

住　所　地：广州市天河区五山路483号

法定代表人：薛红卫

项目联系人：何杰

联系方式：华南农业大学农业工程楼307

通讯地址：广州市天河区五山路483号

电　　话：[illegible] 传　　真：[illegible]

电子信箱：hooget@scau.edu.cn

甲方委托乙方就广东省益信无人化智慧农场建设技术服务项目进行专项技术服务，并支付相应的技术服务报酬。各方经过平等协商，在真实、充分地表达各自意愿的基础上，根据《中华人民共和国民法典》的规定，达成如下协议，并由各方共同恪守。

第一条：甲方委托乙方进行技术服务的内容如下：

1. 技术服务的目标：乙方协助甲方建设水稻无人化智慧农场，实现耕种管收无人化作业以及远程管控，无人农机与属地化的智慧农业平台互联。

2. 乙方技术服务的内容：（1）协助制定无人农场建设规划；（2）协

第四条：甲方向乙方支付技术服务费用及支付方式为：

1．技术服务费总额：30 万元（含税）（大写：人民币叁拾万元整）。

2．技术服务费由甲方 一次 支付乙方。

具体支付方式和时间如下：

（1）乙方开户银行名称、地址和账号为：

开户银行：中国工商银行广东省分行广州市五山支行

地　　址：广州市天河区五山路 483 号

账　　号：3602002609000310520

（2）支付时间：签订合同十五日内。

（3）甲方付款前，乙方应提供合法有效的等额发票，否则甲方有权拒付。

（4）经费的支出和使用按照《华南农业大学横向科技项目及经费管理办法》执行。

第五条：各方确定因履行本合同应遵守的保密义务如下：

甲方：

1.保密内容（包括技术信息和经营信息）:乙方提供的注明要求保密的技术资料和培训资料。

2．涉密人员范围：参加项目及培训的人员；

3．保密期限：项目合同签订之日起五年内；

4．泄密责任：承担因泄密造成的损失。

乙方：

1.保密内容（包括技术信息和经营信息）：甲方提供的技术资料以及在实施项目的过程中接触到的所有甲方未公开的信息；

2．涉密人员范围: 参加项目开发的人员以及与前述人员有密切接触有可能接触到保密信息的人员；

3．保密期限：项目合同签订之日起五年内；

第十一条：违约责任

乙方迟延履行本合同第二条第 3 款的“技术服务进度”中确定的各个阶段的工作的，每个阶段每延误一天，按照技术服务费用总额的千分之五向甲方支付违约金，各个阶段均有迟延的，前述违约金累计计算。

第十二条：各方因履行本合同而发生的争议，应协商、调解解决。协商、调解不成的，确定按以下第 1 种方式处理：

1．提交 肇庆 仲裁委员会仲裁；

2．依法向人民法院起诉。

第十三条：各方确定：本合同及相关附件中所涉及的有关名词和技术术语，其定义和解释如下：

1．无

第十四条：本合同一式 四 份，具有同等法律效力。

第十五条：本合同经各方签字盖章后生效。

（以下无正文）

甲方：广东省益信农业科技有限公司 （盖章）

法定代表人／委托代理人： （签名）

2025 年 1 月 20 日

乙方：华南农业大学 （盖章）

法定代表人／委托代理人： （签名）

2025 年 1 月 23 日

技术服务合同

项目名称：2025 年水稻智慧化生产技术指导及试验示范项目

委 托 方：广西壮族自治区农业机械化服务中心

（甲方）

受 托 方：华南农业大学

（乙方）

委托方（甲方）：广西壮族自治区农业机械化服务中心

住所地：南宁市青秀区思贤路 59 号

法定代表人：李凤云

项目联系人：黄严

联系方式：

通讯地址：南宁市青秀区思贤路 59 号

电子邮箱：kejtgb@njfwzx.gxzf.gov.cn

受托方（乙方）：华南农业大学

住所地：广东省广州市天河区五山路 483 号

法定代表人：薛红卫

项目联系人：汪沛

联系方式：

通讯地址：广州市天河区华南农业大学农业工程楼 307

电子邮箱：wangpei@scau.edu.cn

乙方应在合同期限届满前20个工作日（即12月4日前）出具技术服务成果，并提交甲方评估验收。

3.技术服务次数：乙方提供的技术服务次数根据甲方需求而定，但每年现场服务次数不少于3次。

4.技术服务质量要求：应甲方需求及时解决水稻智慧化生产技术过程中出现的农业智能装备相关技术难题，并总结出一套切实可行的可复制、可推广的广西水稻智慧化生产技术规范。

5.技术服务期限要求：在约定技术服务进度期限内完成约定的技术服务内容。

第三条：为保证技术服务工作顺利进行，甲乙双方应提供下列工作条件和协作事项：

1.甲方提供技术资料及工作条件：

（1）制定水稻智慧农场项目建设实施方案；

（2）配合乙方在港北区水稻智慧农场开展相关技术试验示范的落实、检查和指导等工作。

2.乙方提供技术资料及工作条件：

广西水稻智慧化生产技术总结、技术规范等相应支撑材料。

3.双方确定，服务过程中产生的技术服务成果，其知识产权归甲方所有。

第四条：甲方向乙方支付技术服务工作经费、支付方式为：

1.服务费总额为：壹拾伍万元整(¥150，000 元)。该费

以下无正文，仅签字盖章页。

甲方：广西壮族自治区农业机械化服务中心（盖章）

法定代表人/委托代理人：（签名）

2025年9月8日

乙方：（盖章）

法定代表人/委托代理人：（签名）

2025年9月8日

合同编号：

技术服务合同

项目名称：“龙岩供销农场”数智化建设

委 托 方：龙岩市供销合作社联合社（甲方）
福建供销百农汇科技有限公司（丙方）

受 托 方：华南农业大学(乙方)

签订时间：2025 年 7 月 18 日

签订地点：福建龙岩

有效期限：2025 年 8 月—2027 年 7 月

中华人民共和国科学技术部印制

项目联系人：黄培奎

联系方式

通讯地址：华南农业大学农业工程楼307

电　　话：　　传真：

电子信箱：pkhuang@scau.edu.cn

为进一步深化广龙对口合作，促进龙岩大米提质、降本、增效，提升大米品牌，更好地进入广州市场，本合同甲方委托乙方就“龙岩供销农场”数智化建设项目进行的专项技术服务，并支付相应的技术服务报酬。双方经过平等协商，在真实、充分地表达各自意愿的基础上，根据《中华人民共和国民法典》的规定，达成如下协议，并由双方共同恪守。

第一条：甲方委托乙方进行技术服务的内容如下：

1．技术服务的目标：乙方为甲方提供技术支持，协助甲方开展供销农场数字化、智能化改造，协助甲方打造供销农场数字化2.0版、智能化3.0版，协助甲方争创农业农村部智慧农业（水稻生产）引领区。

2．技术服务的内容：①提供“空、天、地”数字化农田技术支持，指导帮助甲方建立数字化农田；②提供“无人农场”无人机生长监测、病虫害自动识别及决策建议和无人机水稻制种授粉等技术支持，指导帮助甲方在长汀、新罗2个县建立“龙岩供销农场智慧农业服务中心”，其他县如有需要，乙方应提供技术服务支持。③提供数字化农田、无人机生长监测等配套软件系统给甲方使用，并培训系统与智能装备专业操作人员2~3名。④提供龙岩市水稻智慧农场建设相关技术的咨询与服务。

3．技术服务的方式：①线上线下会议；②乙方派出专业研发人员或研究生前往甲方指定地点进行测绘、系统应用指导。

第二条：乙方应按下列要求完成技术服务工作：

1．技术服务地点：龙岩市

2．技术服务期限：2025 年 8 月—2027 年 7 月

3．技术服务进度：乙方在收到甲方技术服务费 1 个月内，派出人员至甲方指定地点进行实地考察；乙方在收到甲方技术服务费 3 个月内完成系统配置，交付甲方使用并培训甲方专业技术人员。

第三条：为保证乙方有效进行技术服务工作，甲方应当向乙方提供下列工作条件和协作事项：

1．甲、乙双方应加强信息沟通与交流，乙方应主动向甲方提出工作事项和技术支撑需求，甲方应指定专人负责接待、联络并及时反馈信息；

2．甲方对乙方所提工作事项应予以积极支持，尽量满足其需求，并做好相关项目的人员组织及计划安排工作；

3．甲方负责智慧系统所需要的硬件（不限于电脑、智慧硬件等）、云服务器及日常管理人员的配备，乙方负责技术支持与指导。

4．双方对合作的项目和内容，都具有保密义务，对涉及合作项目和领域的技术、文档、数据及相关信息等内容双方进一步商量签订具体保密措施。

第四条：技术服务报酬及支付方式为：

1．技术服务费总额为：300000（大写：叁拾万元整）

2．技术服务费由甲方委托丙方分三次支付给乙方。

具体支付方式和时间如下：签约完成 10 个工作日内支付 10 万元（大写：拾万元整）；2025 年 12 月底完成系统搭建后支付 15 万元（大写：拾伍万元整）； 2027 年 7 月底完成系统验收后支付 5 万元（大写：伍万元整）。（见附件工作进度安排表）

委托方（甲方）：

龙岩市供销合作社联合社 （盖章）

法定代表人／委托代理人： （签名）

年 月 日

福建供销百农汇科技有限公司（丙方） （盖章）

法定代表人／委托代理人： （签名）

年 月 日

受托方（乙方）：华南农业大学 （盖章）

法定代表人／委托代理人： （签名）

年 月 日

合同编号：

服务合同

项目名称：建设会昌县小密乡水稻智慧农场

委 托 方：会昌县小密硒谷农业发展有限公司
（甲 方）

受 托 方：华南农业大学
（乙 方）

委托方（甲方）：会昌县小密硒谷农业发展有限公司

住　所　地：　会昌县小密乡杉背美食城

法定代表人：　王冬华

项目联系人：刘荣生

联系方式　：[illegible]

通讯地址：会昌县小密乡富密街 70 号

电　　话：[illegible]

受托方（乙方）：华南农业大学

住　所　地：广州市天河区五山路 483 号

法定代表人：　薛红卫

项目联系人：　汪沛

联系方式　：广州市天河区五山路 483 号华南农业大学

通讯地址：广州市天河区五山路 483 号

电　　话：[illegible]　　传真：020－38676975

电子信箱：hooget@scau.edu.cn

甲方委托乙方就“建设会昌县小密乡水稻智慧农场项目”进行专项服务，并支付相应的服务报酬。双方经过平等协商，在真实、充分地表达各自意愿的基础上，根据《中华人民共和国民法典》的规定，达成如下协议，并由双方共同恪守。

第一条：甲方委托乙方进行服务的内容如下：

1. 服务团队：指定华南农业大学罗锡文院士团队负责实施。

第四条：甲方向乙方支付服务费用及支付方式为：

1.服务费总额为：￥200.000（人民币贰拾万元整）。

2.服务费由甲方分期支付乙方。

具体支付方式和时间如下：

（1）签订合同后，乙方开具合同款70%的增值税专用发票提供甲方，经甲方审核无误后七个工作日内支付给乙方，即140.000元（人民币壹拾肆万元整）；

（2）项目完成全部服务内容，并通过验收后，乙方开具合同款30%的增值税专用发票提供甲方，经甲方审核无误后七个工作日内支付给乙方，即60.000元（人民币陆万元整）。

（3）经费支出和使用按照《华南农业大学横向科技项目及经费管理办法》执行。

乙方开户银行名称、地址和账号为：

开户银行：中国工商银行广东省分行广州市五山支行

地　　址：广州市天河区五山路483号

帐　　号：3602002609000310520

第五条：本合同的变更必须由双方协商一致，并以书面形式确定。

第六条：双方确定以下列标准和方式对乙方的服务工作成果进行验收：

1.乙方完成服务工作的形式：　按甲方要求提供。

2.服务工作成果的验收标准：方案合理可靠，完成全部服务内容。

3.服务工作成果的验收方法：完成服务内容后，由甲方按照按项目合同第一条约定服务内容进行验收。

4.验收的时间和地点：2025年12月30日之前，由双方协商确定。

甲方：　　（盖章）

法定代表人／委托代理人：　刘荣生　　（签名）

2024 年 3 月 16 日

乙方：　　（盖章）

法定代表人／委托代理人：　　（签名）

年　　月　　日

三、论文、著作等

SCAULIB202626228

检索证明

根据委托人提供的论文材料，委托人华南农业大学工程学院 赵润茂(学科类型:自然科学)6篇论文收录情况如下表。

序号	论文名称	发表刊物及发表的年月卷期/页码等	作者排名	论文等级	作者文中单位	收录情况	影响因子	中科院大类分区	引用
1	A Variable-Threshold Segmentation Method for Rice Row Detection Considering Robot Travelling Prior Information	AGRICULTURE-BASEL 出版年：2025 出版日期：FEB 卷期：15 4 页码：- 文献号：413 文献类型：Article	通讯作者	A类	南方农业机械与装备关键技术教育部重点实验室，华南农业大学	SCI	IF2-year=3.6 IF5-year=3.8 （2024）	农林科学 2区 Top 期刊：否 OA 期刊：是 （2025）	SCI 核心合集 总引：2
2	Design and experiment of a new double needle type piezoelectric jetting dispenser	SMART MATERIALS AND STRUCTURES 出版年：2023 出版日期：MAR 1 卷期：32 3 页码：- 文献号：035022 文献类型：Article	第一作者	B类	浙江理工大机械与自动控制学院	SCI	IF2-year=3.7 IF5-year=3.8 （2023）	材料科学 3区 Top 期刊：否 OA 期刊：否 （2023）	SCI 核心合集 总引：8
3	IMVTS: A Detection Model for Multi-Varieties of Famous Tea Sprouts Based on Deep Learning	HORTICULTURAE 出版年：2023 出版日期：JUL 卷期：9 7 页码：- 文献号：819	第一作者	B类	浙江理工大学机械工程学院	SCI	IF2-year=3.1 IF5-year=3.1 （2023）	农林科学 3区 Top 期刊：否 OA 期刊：是 （2023）	SCI 核心合集 总引：10

		文献类型：Article							
4	Method and Experiments for Acquiring High Spatial Resolution Images of Abnormal Rice Canopy by Autonomous Unmanned Aerial Vehicle Field Inspection	AGRONOMY-BASEL 出版年：2023 出版日期：NOV 卷期：13 11 页码：- 文献号：2731 文献类型：Article	通讯作者	A 类	岭南现代农业科学与技术广东省实验室	SCI	IF2-year=3.3 IF5-year=3.7 （2023）	农林科学 2 区 Top 期刊：否 OA 期刊：是 （2023）	SCI 核心合集 总引：2
5	Method for estimating vertical kinematic states of working implements based on laser receivers and accelerometers	BIOSYSTEMS ENGINEERING 出版年：2021 出版日期：MAR 卷期：203 页码：9-21 文献类型：Article	第一作者	A 类	华南农业大学工程学院	SCI	IF2-year=5.002 IF5-year=5.321 （2021）	农林科学 2 区 Top 期刊：是 OA 期刊：否 （2021）	SCI 核心合集 总引：5
6	Rapid development methodology of agricultural robot navigation system working in GNSS-denied environment	ADVANCES IN MANUFACTURING 出版年：2023 出版日期：DEC 卷期：11 4 页码：601-617 文献类型：Article	第一作者	A 类	浙江理工大学机械工程学院	SCI	IF2-year=4.2 IF5-year=4.6 （2023）	工程技术 2 区 Top 期刊：否 OA 期刊：否 （2023）	SCI 核心合集 总引：8

说明：论文等级和中科院大类分区按《华南农业大学学术论文评价方案（试行）》划分。

报告免责声明:如未盖章,报告无效

检索员：尹银怀

华南农业大学图书馆

暨南大学
文献收录证明

检索课题：华南农业大学赵润茂发表的文献在 EI 数据库中的收录情况。

检索工具及年限：

EI (Engineering Village2)　　1969-2026 年

检索结果：根据委托方提供的文献目录，经上述数据库及年限范围内检索，共计 4 篇论文被 EI 收录，结果如下：

序号	文献信息	作者顺序	文献类型
1.	Research on Lightweight Image Segmentation Model for Grain Tank of an Unmanned Grain Cart in Rice Harvesting Zhao, Runmao (Guangdong Laboratory for Lingnan Modern Agriculture, South China Agricultural University, Guangzhou; 510642, China); Huang, Jiatao; Man, Zhongxian; Luo, Xiwen; Hu, Lian; He, Jie; Wang, Pei; Huang, Peikui Source: Nongye Jixie Xuebao/Transactions of the Chinese Society for Agricultural Machinery, v 56, n 6, p 196-204, June 2025 Language: Chinese Database: Compendex Accession number:20252618671155 Document type:Journal article (JA)	第一作者	Journal article (JA)
2.	Error Compensation Improved MPC Track-laying Weeding Machine Path Tracking Control Method Zhao, Runmao (College of Engineering, South China Agricultural University, Guangzhou; 510642, China); Ding, Shuaiqi; He, Jie; Man, Zhongxian; He, Zihao; Ruan, Qingqiang; Hu, Lian; Wei, Zhenghui Source: Nongye Jixie Xuebao/Transactions of the Chinese Society for	第一作者	Journal article (JA)

	Agricultural Machinery, v 56, n 9, p 326-334 and 354, September 2025 Language: Chinese Database: Compendex Accession number:20253919240577 Document type:Journal article (JA)		
3.	Describing Height and Outline of Tea Canopy in Natural Field with 3D Sensing Zhao, Runmao (School of Mechanical Engineering, Zhejiang Sci-Tech University, Hangzhou; 310018, China); Fan, Guoshuai; Chen, Jianneng; Wu, Chuanyu; Du, Xiaoqiang; Huan, Xiaolong Source: Nongye Jixie Xuebao/Transactions of the Chinese Society for Agricultural Machinery, v 54, n 12, p 234-241, December 2023 Language: Chinese Database: Compendex Accession number:20240615499222 Document type:Journal article (JA)	第一作者	Journal article (JA)
4.	Structural Design and Test of Supported Paddy-field Leveling Machine Chen, Gaolong (College of Engineering, South China Agricultural University, Guangzhou; 510642, China); Hu, Lian; Wang, Pei; Zhao, Runmao; Feng, Dawen; Tian, Li; Huang, Zhicheng; Chen, Yuqi; Wang, Jingting Source: Nongye Jixie Xuebao/Transactions of the Chinese Society for Agricultural Machinery, v 56, n 2, p 252-260 and 274, February 2025 Language: Chinese Database: Compendex Accession number:20251018008994 Document type:Journal article (JA)	通讯作者	Journal article (JA)

声明：本证明的文献信息由委托人提供，检索结果已由委托人核实确认无误。如果由于委托人提供信息不实而造成任何后果，本查新站概不负责。

检索员：

教育部科技查新工作站(Z15)

暨南大学图书馆学科服务与咨询部

2026 年 3 月 13 日

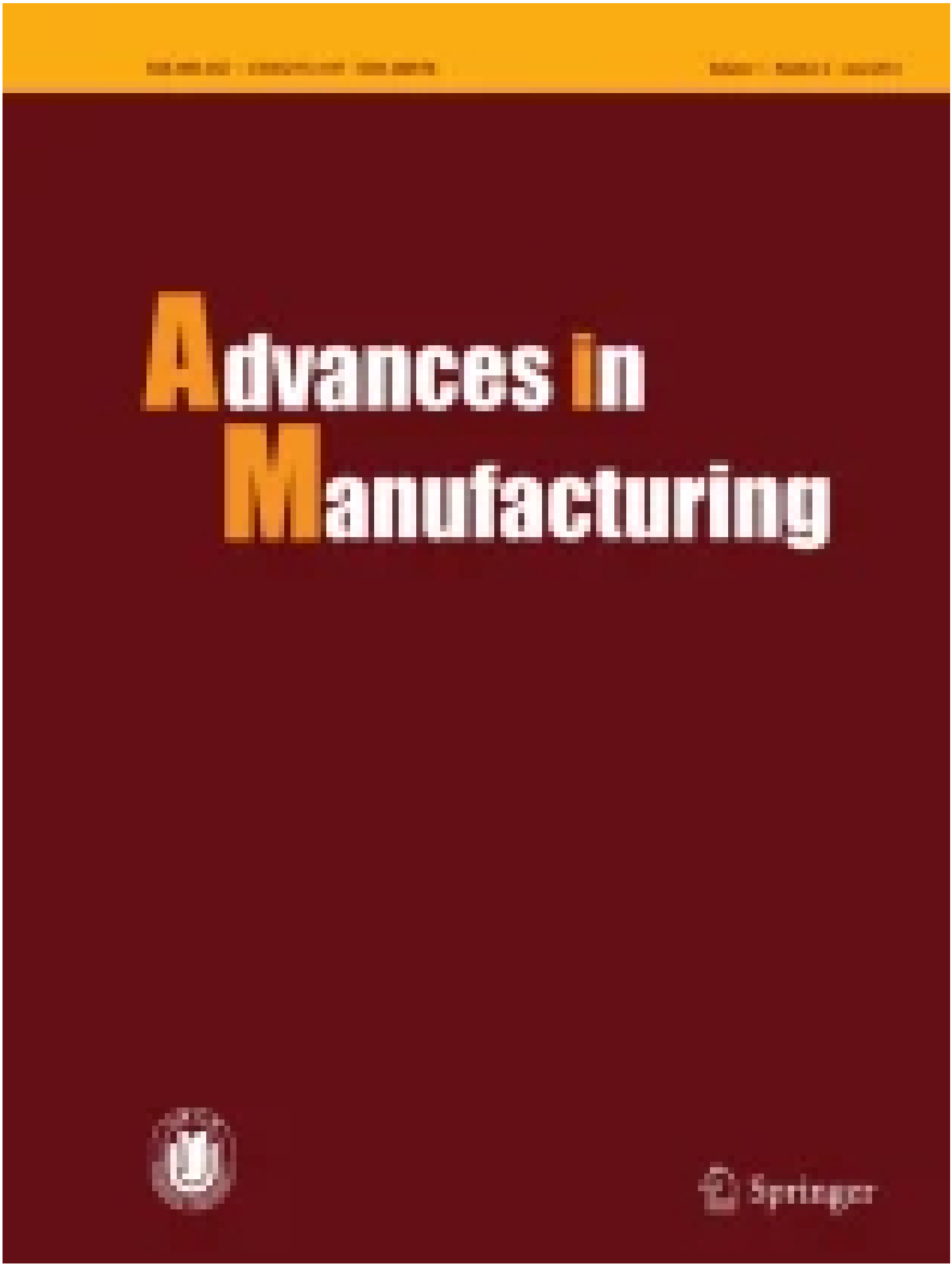
Advances in
Manufacturing
Springer

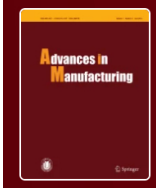

Advances in Manufacturing

Publishing model
Hybrid

Volume 11, Issue 4

December 2023

10 articles in this issue

Adv. Manuf. (2023) 11:601–617
https://doi.org/10.1007/s40436-023-00438-0

Rapid development methodology of agricultural robot navigation system working in GNSS-denied environment

Run-Mao Zhao[1,2] · Zheng Zhu[1] · Jian-Neng Chen[1,2] · Tao-Jie Yu[1] · Jun-Jie Ma[1] · Guo-Shuai Fan[1] · Min Wu[1,3] · Pei-Chen Huang[4]

Received: 31 July 2022 / Revised: 25 September 2022 / Accepted: 19 February 2023 / Published online: 18 May 2023

Abstract Robotic autonomous operating systems in global n40avigation satellite system (GNSS)-denied agricultural environments (green houses, feeding farms, and under canopy) have recently become a research hotspot. 3D light detection and ranging (LiDAR) locates the robot depending on environment and has become a popular perception sensor to navigate agricultural robots. A rapid development methodology of a 3D LiDAR-based navigation system for agricultural robots is proposed in this study, which includes: (i) individual plant clustering and its location estimation method (improved Euclidean clustering algorithm); (ii) robot path planning and tracking control method (Lyapunov direct method); (iii) construction of a robot-LiDAR-plant unified virtual simulation environment (combination use of Gazebo and SolidWorks); and (vi) evaluating the accuracy of the navigation system (triple evaluation: virtual simulation test, physical simulation test, and field test). Applying the proposed methodology, a navigation system for a grape field operation robot has been developed. The virtual simulation test, physical simulation test with GNSS as ground truth, and field test with path tracer showed that the robot could travel along the planned path quickly and smoothly. The maximum and mean absolute errors of path tracking are 2.72 cm, 1.02 cm; 3.12 cm, 1.31 cm, respectively, which meet the accuracy requirements of field operations, establishing the effectiveness of the proposed methodology. The proposed methodology has good scalability and can be implemented in a wide variety of field robot, which is promising to shorten the development cycle of agricultural robot navigation system working in GNSS-denied environment.

Keywords Agricultural robot · Global navigation satellite system (GNSS)-denied environment · Navigation system · 3D light detection and ranging (LiDAR) · Rapid developing · Methodology

1 Introduction

The automatic navigation of agricultural machinery is one of the key supporting technologies for smart agriculture. After nearly two decades of development, the global navigation satellite system (GNSS) has matured and is widely used in many mechanized field crop production links [1–4]. In comparison, agricultural robots that operate autonomously in a GNSS-denied environment are not yet popular. One reason is that the blocked satellite signal makes it difficult for robots to apply the mature, low-cost GNSS technology. Therefore, in a GNSS-denied environment, the positioning and navigation methods of agricultural robots have become a research hotspot in recent years. Chen et al. [5] used an RGB camera in the cucumber greenhouse and proposed a prediction-point Hough transform algorithm to extract the navigation path of the picking robot. However, the disadvantage of machine vision is that the image quality is easily affected by light and the positioning accuracy is unstable [6].

✉ Jian-Neng Chen
jiannengchen@zstu.edu.cn

1 School of Mechanical Engineering, Zhejiang Sci-Tech University, Hangzhou 310018, People's Republic of China

2 Key Laboratory of Transplanting Equipment and Technology of Zhejiang, Province, Hangzhou 310018, People's Republic of China

3 School of Transportation, Zhejiang Industry Polytechnic College, Shaoxing 312000, Zhejiang, People's Republic of China

4 College of Automation, Zhongkai University of Agriculture and Engineering, Guangzhou 510225, People's Republic of China

Papadimitriou et al. [7] and Zhu [8] developed ultra-wide band-based (UWB-based) and odometer-based navigation systems, respectively, used for robotic autonomous operation in unknown indoor and outdoor environments. However, using UWB and wheel speed sensors alone results in low positioning accuracy and cannot meet the needs of precise operation. Multi-sensor fusion technology [9] is generally required to improve accuracy, which will require multi-coordinate system registration, making engineering implementation difficult and costly. Using the principle of time of flight (ToF), 2D light detection and ranging (LiDAR) can obtain the two-dimensional coordinates of the surrounding environment of the carrier, but because of the sparse point cloud data and the lack of environmental information, it is more used in plant protection [10, 11] and harvesting [12, 13] tools to assist perception of target operations.

3D LiDAR has a larger field of view and can provide richer environmental perception information and is widely used in local path planning of car automatic driving systems [14, 15]. However, due to hardware cost constraints in the field of agricultural engineering, 3D LiDAR was initially used in situations where the requirement for real-time data operation was not high, such as geometric parameter acquisition [16], phenotyping [17], and reverse reconstruction of agricultural plants [18]. For example, Cheraïet et al. [19] proposed a Bayesian point cloud classification algorithm to segment the canopy of the vine point cloud scanned by 3D LiDAR, estimate the height and width of the canopy, and realize variable spraying in orchards. Chen et al. [20] used drones to carry 3D LiDAR to measure the canopy area and diameter of each fruit tree, and they analyzed the impact of different spatial resolutions on the detection and extraction results of single tree canopy. As the cost continues to drop, scholars have begun to pay attention to and adopt 3D LiDAR for the development of agricultural robot navigation systems. Jones et al. [21] developed a heavy-duty platform capable of performing tree line tracking and navigation as well as autonomous transportation under the canopy of kiwifruit pergolas, but the test window period was limited due to the test site and crop growth season, and the development cycle was lengthy. Jiang et al. [22], aiming to solve the problem of robot positioning and navigation in the greenhouse environment, integrated the 3D LiDAR-perceived environmental point cloud, odometer, and inertial measurement unit (IMU) information and used the simultaneous localization and mapping (SLAM) algorithm to ensure that the robot realized the three-dimensional reconstruction of the greenhouse environment. To study the effect of traveling velocity on the navigation accuracy, the above two studies need to repeatedly adjust the algorithm parameters and carry out field tests, so the development efficiency is low. Liu [23], to address the poor reusability of robot software and weak environmental adaptability, designed a robot equipped with the robot operating system (ROS) system and combined MATLAB and Gazebo to build a virtual environment to carry out simulation tests, which improved the efficiency of algorithm development, but Gazebo's built-in mapping tools limited modeling capabilities and could not restore the unique details and characteristics of real scenes. Therefore, the adaptability of the developed algorithms to specific application scenarios needs to be verified. To summarize, there are still issues in the research of LiDAR navigation systems for agricultural robots in a GNSS-denied environment. Firstly, during multiple experiments, LiDAR perception information and robot motion state data cannot be reproduced, and the experimental results cannot be repeated, which brings a lot of inconvenience to the parameter tuning of the algorithm. In addition, the absolute coordinates of the robot and environmental objects cannot be known because of the lack of satellite signals. Therefore, the evaluation of navigation accuracy lacks a true value basis, and the methods and indicators for the evaluation of navigation accuracy are not uniform.

In summary, this study proposes a development process for the development of robot navigation systems in an agricultural GNSS-denied environment, for example, in green houses, on farms, or under the canopy. The structure of the study is as follows. The first part reviews the perception methods of agricultural robot navigation and positioning and puts forward the problems existing in the development of 3D LiDAR navigation systems in a star-free environment. The second part introduces the materials required for the development of the 3D LiDAR-based robot navigation system and the development process of the navigation system innovatively proposed in this study. In the third part, tests have been carried out in virtual simulated environments, physical simulated environments, and field environments which verify the effectiveness and accuracy of the navigation system developed with the proposed process. The fourth part summarizes the main contributions of this study.

2 Materials and methods

2.1 Materials

The SCOUT MINI four-wheel differential steering mobile chassis (627 mm × 549 mm × 248 mm) used in the study is shown in Fig. 1. The display terminal is fixed to the chassis through a ball bracket. 3D LiDAR (hereinafter referred to as LiDAR) (RoboSense, RS-Helios) is used to sense the working environment and perform robot positioning and navigation. The robot's attitude change induced by the field unevenness will affect the positioning accuracy of the robot. The AHRS (attitude and heading reference system, XSENS, Mti-300) is fixedly connected to the LiDAR, and

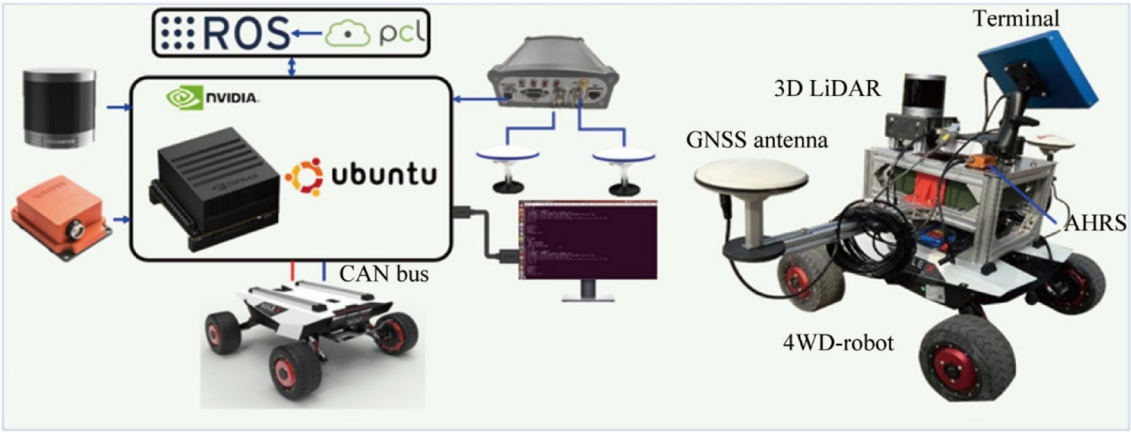

Fig. 1 Robot overall structure

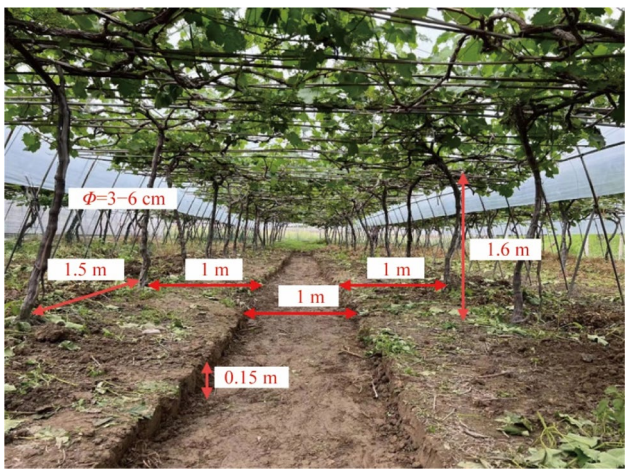

Fig. 2 Research object and environment (grassed grape fields)

the three-dimensional attitude of the LiDAR point cloud is measured and corrected in real time. The NVIDIA Jetson AGX Xavier edge computing platform, deployed with Linux (melodic), is used as the sensor data processing and decision control center. The dual-antenna GNSS (unicorecomm UM482) is installed laterally on the vehicle body (with a baseline distance of 1 m) to provide the true value for the accuracy verification of the LiDAR navigation system. The connection method and installation position of each piece of hardware of the robot are shown in Fig. 1. In the Linux (melodic) environment, the mixed programming of Python and C++ is used for algorithm development and hardware networking communication.

The working scene is located in the grape planting base of Moore Manor, Qiantang District, Hangzhou City, Zhejiang Province (120.45°E, 30.31°N), as shown in Fig. 2. There are brackets installed around and on the top of the field. The grape stems are slender and have different shapes, and the cultivation row and plant spacing are large, so it is not suitable for GNSS or 2D LiDAR for positioning. Therefore, the research will use 3D LiDAR as the perception sensor of the robot and demonstrate the development process of the robot navigation system for grape field operation.

2.2 Methods

2.2.1 Frame of reference transformation

As shown in Fig. 3, the coordinate systems involved in the robot's navigation system are: the odom of the global coordinate system with the origin of the robot's initial position; the base_link of the robot coordinate system with the geometric center of the robot chassis as the origin; LiDAR sensor coordinate system rslidar_link; the GNSS coordinate system GNSS_link with the right antenna as the origin and the AHRS sensor coordinate system imu_link. The TF tree provided by ROS can be used to maintain all the transformation relationships among the robot and the mounted sensors. We established a communication node for each sensor, and manually measured the installation distances (mechanical dimensions) of the sensors relative to the navigation point (geometric center of the robot chassis). As a result, the TF calculated transformation between any two coordinate systems, and all the coordinate systems were projected to the navigation points automatically. The TF tree is shown in Fig. 4.

2.2.2 LiDAR point clouds pre-processing

The horizontal field of view of RS-Helios is 360°, with the horizontal resolution of 0.2° and the maximum scanning distance of 150 m. The beam is 32; the vertical field of view is from –55° to 15°; and the frequency is 576 000 points per second. In the process of environmental

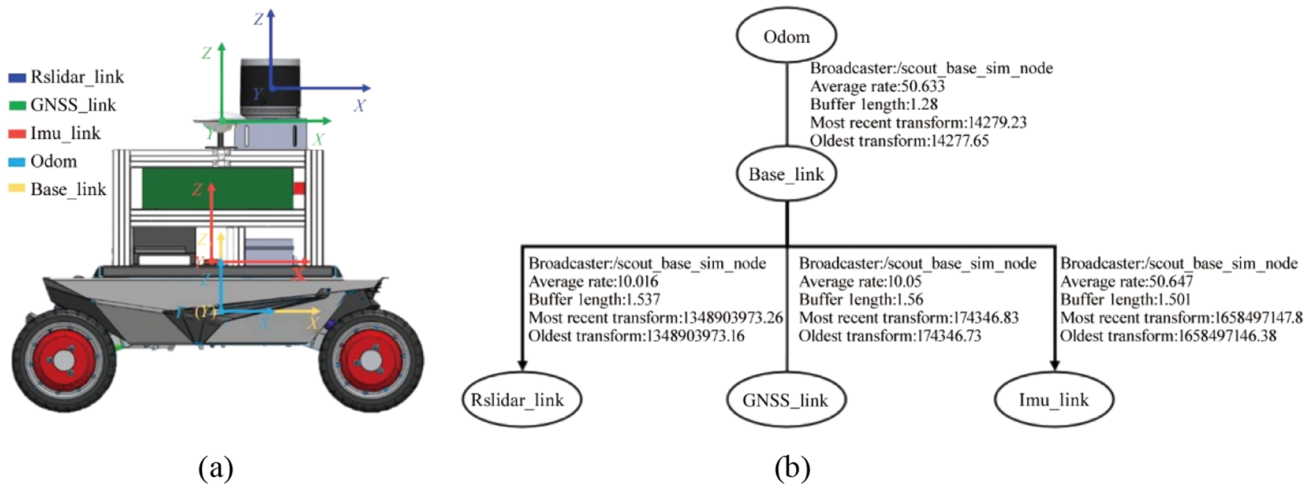

Fig. 3 Coordinate systems and transformations involved in robots **a** robot's coordinate system, **b** robot's tf_tree

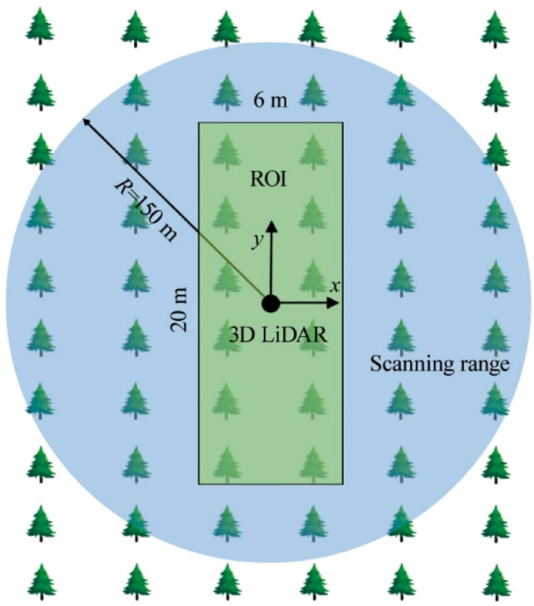

Fig. 4 Range of interest

perception, a large number of point clouds unrelated to the target plant, such as weeds, the ground, and surrounding buildings, will be scanned, which will increase the computational burden and affect the segmentation of the target point clouds. Therefore, real-time data preprocessing is required without changing the characteristics of the point clouds.

(i) ROI and VoxelGrid filter

Taking the installation position of the 3D LiDAR as the origin, and the heading of the mobile robot as the *y*-axis, a Cartesian coordinate system is established (as shown in Fig. 4). According to the field environment, range of interest (ROI) areas of 6 m, 20 m, and 2 m were set on the *x*-axis, *y*-axis, and *z*-axis, respectively. The point that clouds in the ROI area is down-sampled by voxel filtering, and the size of the voxel unit is 0.1 m × 0.1 m × 0.1 m. The centroid coordinate of each cube is estimated to represent all point clouds within the cube. This method can effectively reduce the amount of point cloud data and speed up data processing on the premise of avoiding the loss of point cloud features.

(ii) Ground point clouds segmentation

The Ray Ground Filter is used to segment the ground point clouds, with the specific method as follows. Firstly, according to the horizontal angular resolution of LiDAR, the point clouds are divided into $360 \div 0.2 = 1\,800$ longitudinal sections, and the points in each longitudinal section are sorted by distance. Secondly, set the slope threshold (local_max_slope, unit: degree) of two adjacent points on the same scan line and the slope threshold of the entire ground (general_max_slope, unit: degree) and obtain the height threshold based on these two slope thresholds and the radius of the current point (to the horizontal distance of LiDAR). Thirdly, if the height value of the current point is within the range of the ground plus or minus height threshold, it is determined as a ground point and deleted.

(iii) Outlier removal

Affected by interfering factors such as system measurement noise and environmental characteristics, there are some outliers in the 3D LiDAR point clouds, which are far from the target point clouds in terms of data features and should be filtered out. Radius filter-

ing was used to remove outlier point clouds around the backbone. The radius filtering method runs fast, and the points left by sequential iterations must be of highest density. It is extremely suitable for scenarios with large amounts of point cloud data and high real-time requirements.

2.2.3 *Plant individual segmentation and position estimation*

Preprocessed point clouds are segmented by Euclidean clustering to obtain individual plants. As shown in Fig. 5a, for vertically growing grape stems, the centroid of the grape stem section can be used as the location of the single plant. If the point clouds of the segmented plant are used to estimate the position of the individual for the vertical lower part and the upper sloping grape plant shown in Fig. 5b, the centroid will be shifted, resulting in a deviation between the extracted navigation path and the ideal furrow centerline. To solve this problem, a method for estimating the position of grape stems suitable for various growth attitudes is designed, and the specific process is as follows.

(i) Create a corresponding K-dimension tree (KD-tree) according to the point cloud data to be segmented. KD-tree is a high-dimensional indexed tree data structure, which is often used for K-neighbor search of large-scale high-dimensional data to speed up the Euclidean clustering and reduce the required time.

(ii) Set the distance threshold d, randomly select an initial point P_{start} in the point cloud to be segmented, create a point-clouds set R_{start}, and add P_{start} to R_{start}. According to KD-tree, the point clouds to be segmented are searched for the point set $Q_{\text{start}} = \{P_1, P_2, \cdots, P_n\}$ within the range of the initial point P_{start} distance threshold D_{tree}, and it is added to R_{start} and marked point P_{start}. Then extract the unlabeled point P from R_{start}, and search for the point set $Q_{\text{start+1}}=\{P_1, P_2, \cdots, P_n\}$ in the point clouds to be segmented within the range of the distance threshold of the point P according to the KD-tree, add it to R_{start}, mark the point P. Continue to extract the unmarked point P_i from R_{start} and repeat the previous steps until no new points are added to R_{start}. At this time, R_{start} is used as a target for segmentation completion.

(iii) Extract another unlabelled point from the point clouds to be segmented as the initial point $P_{2\text{start}}$, repeat the preceding steps until all of the points in the three-dimensional point clouds to be segmented are marked, complete the Euclidean clustering of the point cloud data, and realize the plant's individual segmentation.

(iv) Calculate the maximum coordinates ($x_{\max}$, $x_{\min}$, $y_{\max}$, $y_{\min}$) of the ith grape stem point clouds set along the x and y axes after the data clustering of the kth frame. According to Eqs. (1)–(4), the widths x_{ki} and y_{ki} in the x-axis and y-axis directions of the grape stem are obtained. And according to Eqs. (5) and (6), the average values $\hat{x}_k$, $\hat{y}_k$, in the x-axis direction and the y-axis direction of the grape stem in all ROI areas of the point cloud data of the kth frame are obtained and set as the threshold of the centroid of the grape stem.

(v) As shown in Fig. 5c, determine whether the distance between the x-axis direction and the y-axis direction of the ith grape stem in the kth frame of point clouds data is greater than the threshold. If it is greater than the threshold, the point clouds with the maximum value in the z-axis direction are truncated. Repeat the process (iv) until the centroid of the grape stem meets the threshold requirement.

(vi) Project the centroid of the grape stem to a two-dimensional plane to obtain the final position coordinates of the stem (O_X, O_Y, O), record the position coordinates O_{ki} of all the grape stems under the kth frame, and realize the target position estimation, as shown in Fig. 5c.

$$x_{j_i} = \frac{x\max_i + x\min_i}{2}, \tag{1}$$

$$y_{j_i} = \frac{y\max_i + y\min_i}{2}, \tag{2}$$

$$x_{ki} = x\max - x\min, \tag{3}$$

$$y_{ki} = y\max - y\min, \tag{4}$$

$$\hat{x}_k = \frac{x_{k1} + x_{k2} + \cdots + x_{ki}}{i}, \tag{5}$$

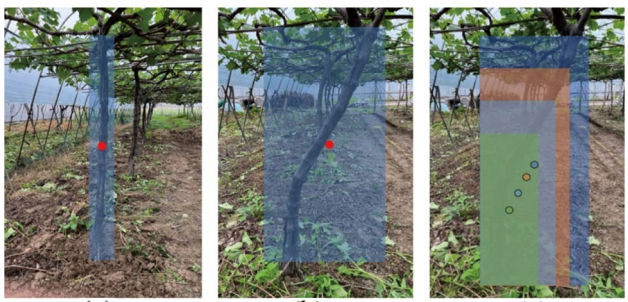

Fig. 5 Estimation of individual position of grape plants **a** general grape stem position estimation, **b** curved grape stem position estimation, **c** improved grape stem position estimation

$$\hat{y}_k = \frac{y_{k1} + y_{k2} + \cdots + y_{ki}}{i}. \tag{6}$$

2.2.4 Navigation path planning

The least square method (LSM) was used to fit all the stem centers of individual grape estimated in Sect. 2.2.3 and generate plant rows. LSM, with small error and fast speed, is more in line with practical application requirements. In addition, in order to avoid the yaw of the robot because of misidentification of plant rows during driving, the LSM for fitting plant rows was improved, and the flow is shown in Fig. 6.

(i) After the straight line is initially fitted by the least squares method, the slope the slope k_l of the left tree-line L_l and the slope k_r of the right tree-line L_r are estimated, respectively. If the value of k_l and k_r are not between –tan 75° and tan 75°, it is believed that the estimation is effective.

(ii) Calculate the distance from each coordinate point to the fitted line and delete the coordinate points in descending order of length. After each deletion, return to perform a least squares fitting.

(iii) Calculate the slope of the newly fitted straight line, then repeat steps (i) and (ii) until a straight line $y = kx + b$ that meets the target condition is fitted.

$$L_l : y = k_l x + b_l, \tag{7}$$

$$L_r : y = k_r x + b_r, \tag{8}$$

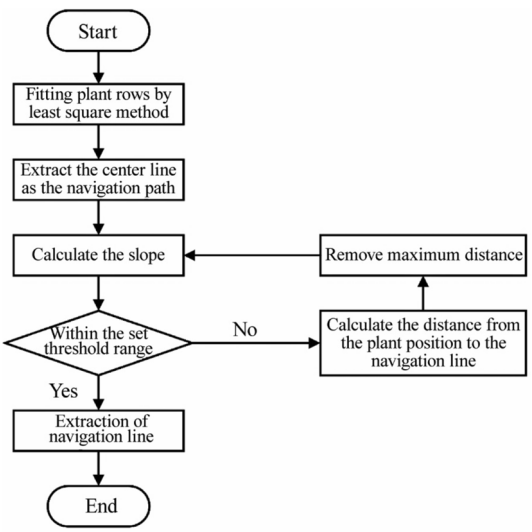

Fig. 6 Improved least squares fitting plant row flow chart

$$L_{\text{finally}} : y = \frac{(k_l + k_r) + (b_l + b_r)}{2}, \tag{9}$$

where b_l and b_r are the intercept of the L_l and L_r, respectively. According to Eq. (9), calculate the midpoint set of L_l and L_r, that is, the reference navigation line L_{finally} is estimated.

2.3 Path following control

In the global coordinate system *OXY*, set a point on the navigation line as the preview point *P* of the robot, as shown in Fig. 7. The blue line is the fitted plant row, the red line being the desired path, *O*' the robot's navigation control point, *P* the target point on the robot's navigation path, and (e_x, e_y), e_θ are the position deviation and heading deviation between the robot control point *O*' and the target point *P*, respectively. The pose vector of the robot in the global coordinate system is $\boldsymbol{p}_c = \begin{bmatrix} x_c & y_c & \theta_c \end{bmatrix}^T$, and the motion vector is $\boldsymbol{q}_c = \begin{bmatrix} v_c & \omega_c \end{bmatrix}^T$; the pose vector of the reference robot in the global coordinate system is $\boldsymbol{p}_r = \begin{bmatrix} x_r & y_r & \theta_r \end{bmatrix}^T$, and the motion vector is $\boldsymbol{q}_r = \begin{bmatrix} v_r & \omega_r \end{bmatrix}^T$.

From the principle of kinematics, the following relationship can be defined

$$\begin{cases} \dot{\boldsymbol{p}}_c = \begin{bmatrix} \dot{x}_c \\ \dot{y}_c \\ \dot{\theta}_c \end{bmatrix} = \begin{bmatrix} \cos\theta_c & 0 \\ \sin\theta_c & 0 \\ 0 & 1 \end{bmatrix} \boldsymbol{q}_c, \\ \dot{\boldsymbol{p}}_r = \begin{bmatrix} \dot{x}_r \\ \dot{y}_r \\ \dot{\theta}_r \end{bmatrix} = \begin{bmatrix} \cos\theta_r & 0 \\ \sin\theta_r & 0 \\ 0 & 1 \end{bmatrix} \boldsymbol{q}_r. \end{cases} \tag{10}$$

In the global coordinate system, the error of the robot's actual pose relative to the reference pose is

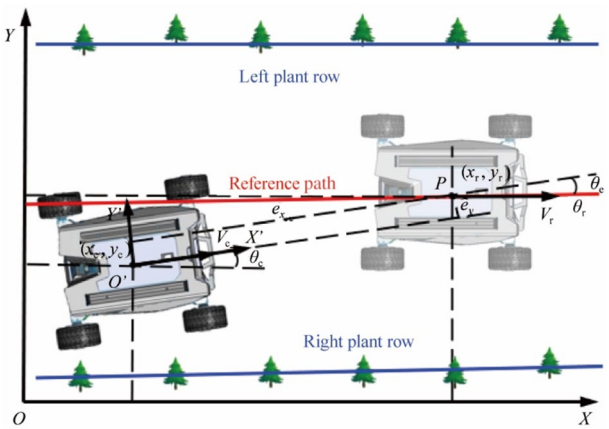

Fig. 7 Robot trajectory tracking model

$$\boldsymbol{p}_{\mathrm{E}} = \boldsymbol{p}_{\mathrm{r}} - \boldsymbol{p}_{\mathrm{c}} = \left[x_{\mathrm{r}} - x_{\mathrm{c}} \;\; y_{\mathrm{r}} - y_{\mathrm{c}} \;\; \theta_{\mathrm{r}} - \theta_{\mathrm{c}} \right]^{\mathrm{T}}. \tag{11}$$

From the transformation relationship of the robot pose, the expression of the robot pose error in the local coordinate system can be obtained as follows

$$\dot{\boldsymbol{p}}_{\mathrm{e}} = \begin{bmatrix} x_{\mathrm{e}} \\ y_{\mathrm{e}} \\ \theta_{\mathrm{e}} \end{bmatrix} = \begin{bmatrix} \cos\theta_{\mathrm{c}} & \sin\theta_{\mathrm{c}} & 0 \\ -\sin\theta_{\mathrm{c}} & \cos\theta_{\mathrm{c}} & 0 \\ 0 & 0 & 1 \end{bmatrix} \boldsymbol{p}_{\mathrm{E}} = \boldsymbol{R}_{\mathrm{e}} \boldsymbol{p}_{\mathrm{E}}. \tag{12}$$

In the formula, $\boldsymbol{R}_{\mathrm{e}}$ is the transformation matrix. Taking the derivation of Eq. (12), and combining Eq. (10), we can obtain

$$\dot{\theta}_{\mathrm{e}} = \dot{\theta}_{\mathrm{r}} - \dot{\theta}_{\mathrm{c}} = \omega_{\mathrm{r}} - \omega_{\mathrm{c}}. \tag{13}$$

The differential equation of the robot pose error after finishing is

$$\begin{aligned} \dot{x}_{\mathrm{e}} &= \left(\dot{x}_{\mathrm{r}} - \dot{x}_{\mathrm{c}}\right)\cos\theta_{\mathrm{c}} - \dot{\theta}_{\mathrm{c}}\left(x_{\mathrm{r}} - x_{\mathrm{c}}\right)\sin\theta_{\mathrm{c}} + \left(\dot{y}_{\mathrm{r}} - \dot{y}_{\mathrm{c}}\right) \\ &\quad \sin\theta_{\mathrm{c}} + \dot{\theta}_{\mathrm{c}}\left(y_{\mathrm{r}} - y_{\mathrm{c}}\right)\cos\theta_{\mathrm{c}} \\ &= v_{\mathrm{r}}\cos\left(\theta_{\mathrm{r}} - \theta_{\mathrm{c}}\right) - v_{\mathrm{c}} + \omega_{\mathrm{c}}\left(\left(y_{\mathrm{r}} - y_{\mathrm{c}}\right)\cos\theta_{\mathrm{c}} - \left(x_{\mathrm{r}} - x_{\mathrm{c}}\right)\sin\theta_{\mathrm{c}}\right) \\ &= \omega_{\mathrm{c}} y_{\mathrm{e}} - v_{\mathrm{c}} + v_{\mathrm{r}}\cos\theta_{\mathrm{e}}, \end{aligned} \tag{14}$$

$$\begin{aligned} \dot{y}_{\mathrm{e}} &= -\left(\dot{x}_{\mathrm{r}} - \dot{x}_{\mathrm{c}}\right)\sin\theta_{\mathrm{c}} - \dot{\theta}_{\mathrm{c}}\left(x_{\mathrm{r}} - x_{\mathrm{c}}\right)\cos\theta_{\mathrm{c}} + \left(\dot{y}_{\mathrm{r}} - \dot{y}_{\mathrm{c}}\right) \\ &\quad \cos\theta_{\mathrm{c}} - \dot{\theta}_{\mathrm{c}}\left(y_{\mathrm{r}} - y_{\mathrm{c}}\right)\sin\theta_{\mathrm{c}} \\ &= v_{\mathrm{r}}\sin\left(\theta_{\mathrm{r}} - \theta_{\mathrm{c}}\right) - \omega_{\mathrm{c}}\left(\left(x_{\mathrm{r}} - x_{\mathrm{c}}\right)\cos\theta_{\mathrm{c}} + \left(y_{\mathrm{r}} - y_{\mathrm{c}}\right)\sin\theta_{\mathrm{c}}\right) \\ &= -\omega_{\mathrm{c}} x_{\mathrm{e}} + v_{\mathrm{r}}\sin\theta_{\mathrm{e}}, \end{aligned} \tag{15}$$

$$\dot{\boldsymbol{p}}_{\mathrm{e}} = \begin{bmatrix} \dot{x}_{\mathrm{e}} \\ \dot{y}_{\mathrm{e}} \\ \dot{\theta}_{\mathrm{e}} \end{bmatrix} = \begin{bmatrix} \omega_{\mathrm{c}} y_{\mathrm{e}} - v_{\mathrm{c}} + v_{\mathrm{r}}\cos\theta_{\mathrm{e}} \\ -\omega_{\mathrm{c}} x_{\mathrm{e}} + v_{\mathrm{r}}\sin\theta_{\mathrm{e}} \\ \omega_{\mathrm{r}} - \omega_{\mathrm{c}} \end{bmatrix}. \tag{16}$$

Through the transformation of Eqs. (10)–(15), the tracking control problem of the robot is transformed into the stabilization problem of the error system (see Eq. (16)).

Make the control parameters k_1, k_2, and k_3 all greater than zero and bounded, and design the control law as

$$\boldsymbol{U} = \begin{bmatrix} v \\ \omega \end{bmatrix} = \begin{bmatrix} v_{\mathrm{r}}\cos\theta_{\mathrm{e}} + k_2 x_{\mathrm{e}} \\ \omega_{\mathrm{r}} + k_1 v_{\mathrm{r}} y_{\mathrm{e}} + k_3 \sin\theta_{\mathrm{e}} \end{bmatrix}. \tag{17}$$

Construct the Lyapunov function as

$$V = \frac{k_1}{2}\left(x_{\mathrm{e}}^{\,2} + y_{\mathrm{e}}^{\,2}\right) + 2\left(\sin\frac{\theta_{\mathrm{e}}}{2}\right)^2. \tag{18}$$

Derivate Eq. (18) and substitute Eq. (17) into

Table 1 URDF parameter configuration of LiDAR perception model

Characteristic parameters	Numerical value
Line number	32
Dead zone/m	0.2
Ranging ability/m	0.2 – 150
Horizontal field/(°)	360
Horizontal angular resolution/(°)	0.2
Vertical field/(°)	15 – 55
Vertical angular resolution/(°)	1.5
Frame rate/Hz	10

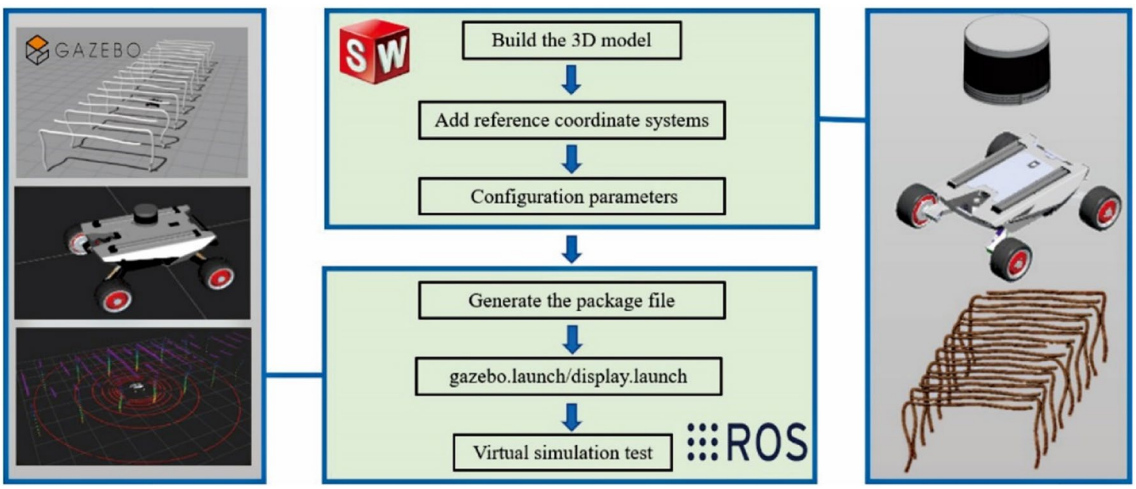

Fig. 8 Virtual simulation environment construction flow chart

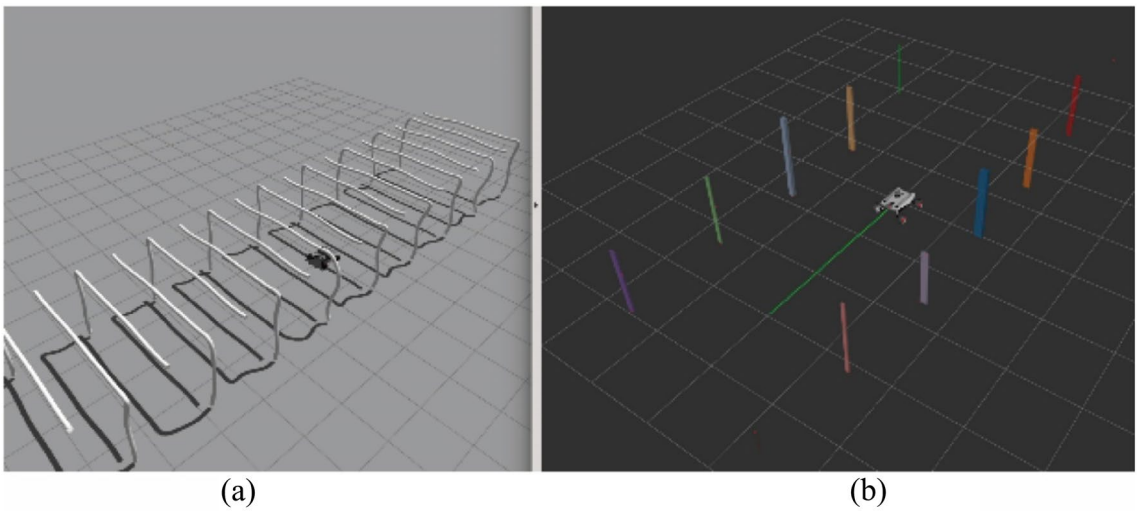

Fig. 9 Simulated motion of the robot in the simulated grape trellis **a** robot motion state in Gazebo, **b** robot motion state in RVIZ

$$\begin{aligned}\dot{V} &= k_1\left(x_e\dot{x}_e + y_e\dot{y}_e\right) + 2\sin\frac{\theta_e}{2}\cos\frac{\theta_e}{2}\dot{\theta}_e e \\ &= k_1\left(x_e v_r\cos\theta_e - x_e\left(v_r\cos\theta_e + k_2 x_e\right) + y_e v_r\sin\theta_e\right) \\ &\quad + \left(\omega_r - \left(\omega_r + k_1 v_r y_e + k_3\sin\theta_e\right)\right)\sin\theta_e \\ &= -k_1 k_2 {x_e}^2 - k_3\sin^2\theta_e \leqslant 0\end{aligned} \tag{19}$$

$\forall p_e \neq 0, V > 0, \dot{V} < 0$; therefore, the control law Eq. (17) makes the control system converge to the equilibrium point $p_e = 0$ asymptotically; that is, the robot can track the upper reference trajectory.

2.4 Robot-LiDAR-plant multi-domain unified virtual simulation environment

In order to verify the effect and reliability of the designed robot navigation system, the research adjusts the information processing and automatic control algorithm parameters, builds a unified virtual simulation environment of robot-LiDAR-plant in ROS, simulates the real scene of the robot running in the grape field, and conducts the simulation test. The unified robot description format (URDF) is a language format for describing robots under the XML syntax framework. Using URDF tags, simple multibody dynamics virtual simulation models and environments can be created. For complex structures, such as grape fields and robots, directly describing the URDF command line

Fig. 10 Robot navigation path and path true value data and error **a** navigation simulation test scenario, **b** GNSS measurement simulates the true value of plant coordinates

is difficult. Therefore, first use Solidworks to design a 3D model, and then export the URDF file of the model through the sw_urdf_exporter plug-in. After modeling, simulate and debug the created multi-body model in Gazebo while visualizing sensor and robot state information in RVIZ. The modeling process is as follows

(i) Mobile chassis virtual simulation model
Build a physical model of the robot in SolidWorks, set the reference axis at the center of the body and four wheels, and establish a coordinate system. Then define the body coordinate system base_link as the parent object; the coordinate systems right_front_wheel, right_back_wheel, left_front_wheel, and left_back_wheel of the four wheels as child objects; and set the joint type of the wheel to continuous.
(ii) Test virtual simulation environment
Build a virtual simulation environment in Gazebo according to the actual test scene, set the reference axis on the ground and the center of the plant, and establish the coordinate system. Set the ground as the parent object, set the plant as the child object, select the reference coordinate system of the plant, and set the joint type to be fixed to complete the construction of the virtual simulation environment.
(iii) 3D LiDAR perception model
Call the LiDAR_Simulator URDF file and configure the URDF description parameters of LiDAR according to Table 1.

The three-dimensional modeling of the robot, 3D LiDAR, and the test environment is completed, the relative positional relationship between the coordinate systems is defined according to the actual installation position, and the construction of the virtual simulation environment is completed, as shown in Fig. 8.

2.5 Test

2.5.1 Virtual simulation test

The field test is carried out in the virtual simulation environment built in Sect. 2.4 to improve the success rate and optimize the robot perception and automatic control algorithm parameters, as shown in Fig. 9a. According to the 3D point cloud processing method proposed in Sect. 2.2, the hybrid parameter adjustment of perception and navigation algorithms is carried out as follows

(i) Different thresholds of ground slope, Euclidean clustering point cloud quantity threshold, and plant stem cross-section threshold were selected for virtual simulation tests, and the point cloud processing results of each parameter were compared.
(ii) The row spacing of grape plants is about 3 m, and the plant spacing is about 1 m. The degree of bending of the stems is different from each other, and they are basically enclosed in a cylinder with a diameter of 15 cm. Therefore, the 3D simulation scenario was constructed referring to the experiment field as similarly as possible, including reconstructing the cultivation pattern and attitudes of grape stems. And on this basis, center estimations of the grape stems before and after using improved Euclidean clustering algorithm were compared via simulation.

Fig. 11 Test site grape fields **a** robots conduct field test, **b** the yellow sand grains record the movement path of the robot during navigation

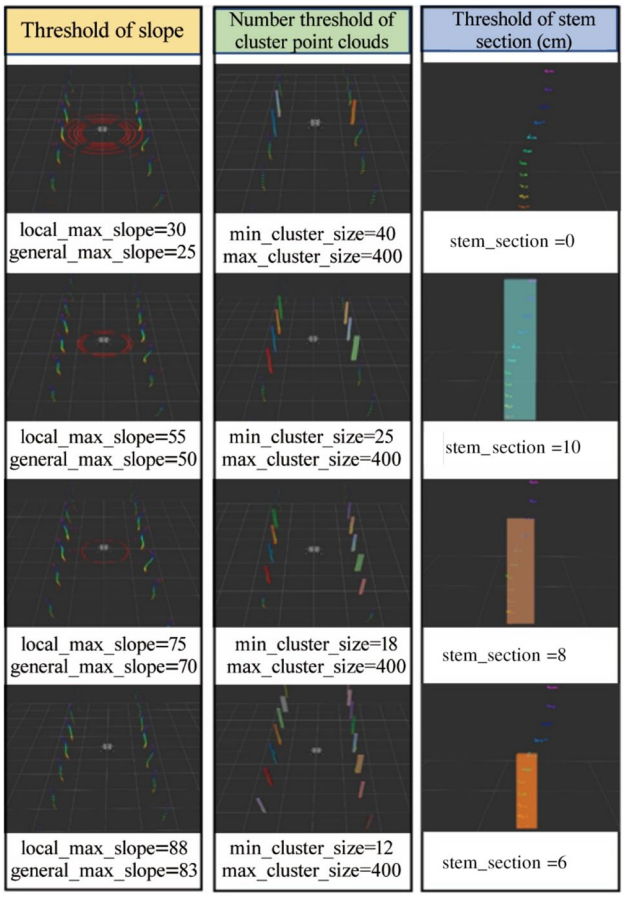

Fig. 12 Mixed parameters

(iii) Fit the navigation path, calculate the robot linear velocity and angular velocity according to the navigation control law designed in Section 2.3, control the robot movement, and visualize it in RVIZ (green straight line), as shown in Fig. 9b.

2.5.2 Path tracking physical simulation test

A path tracking physical simulation test was carried out at Zhejiang Sci-Tech University in order to verify the accuracy of the designed navigation system, as shown in Fig. 10. First, 16 plastic circular tubes with diameters of 40–60 mm and heights of 1 m were placed on the ground in two rows with a row spacing of (3 ± 0.1) m to simulate plant rows. The RTK-GNSS antenna was used to measure the absolute coordinate value of each circular tube in the east-north-up (ENU) coordinate system. A least-square fit was used to simulate plant rows, and the centerline of the 2 straight lines was calculated as the true path value. Second, the initial position deviations of the robot were set to be (0 ± 0.1) m and (0.5 ± 0.1) m, respectively, and the travel speeds were 0.3 m/s, 0.5 m/s, and 0.7 m/s, respectively. A straight line tracking test was carried out to record the real motion path points of the robot. Third, the distance from the robot path point to the center line as the position deviation of the simulated test was calculated, and the online time, max absolute error (MaxErr) and mean absolute error (MeanErr) of each group of tests were analyzed.

2.5.3 Field test

To verify the feasibility of the designed navigation system development process and that the navigation system can effectively estimate and automatically navigate plant point clouds information in a GNSS-denied environment. Field navigation tests were conducted in grape fields (see Fig. 11a), and the results of LiDAR point cloud processing in the virtual simulation environment and the real environment were compared.

Firstly, an hourglass with yellow sand particles was installed on the front of the vehicle to record the real path of the robot, as shown in Fig. 11b. Secondly, the navigation test was carried out at 0.3 m/s, 0.5 m/s and 0.7 m/s, respectively. After each test was completed, the vertical distance from the grape stem to the navigation track was measured by ruler, and the test results were recorded. The test was repeated five times in total. Thirdly, the difference between the navigation path line and the center line of the grape plant row was defined as the error amount; the influence of the European clustering algorithm was compared before and after the improvement on the autonomous navigation of the robot; and the MaxErr and MeanErr were calculated. Finally, after comparing the results of the field test and the physical simulation test, the navigation accuracy of the robot is evaluated, and the practical application effect of the navigation system developed according to the proposed methodology in the GNSS-denied environment is analyzed.

3 Results and discussion

3.1 Virtual simulation test

3.1.1 Navigation system parameter optimization

As shown in Fig. 12, the yellow box represents the effect of ground point cloud segmentation under different local_max_slope and general_max_slope parameters. If the selected two slope thresholds are too small, the ground point clouds will not be completely segmented. In contrast, some target point clouds will also be regarded as ground point clouds. When local_max_slope = 88 and general_max_slope = 83, the ground point-clouds and the plant point-clouds are completely separated. The green box is the clustering effect of plants under different cluster_size. Use the BoundingBoxArray plug-in in RVIZ to select each piece of point cloud that has been classified. If the threshold of the number of point clouds

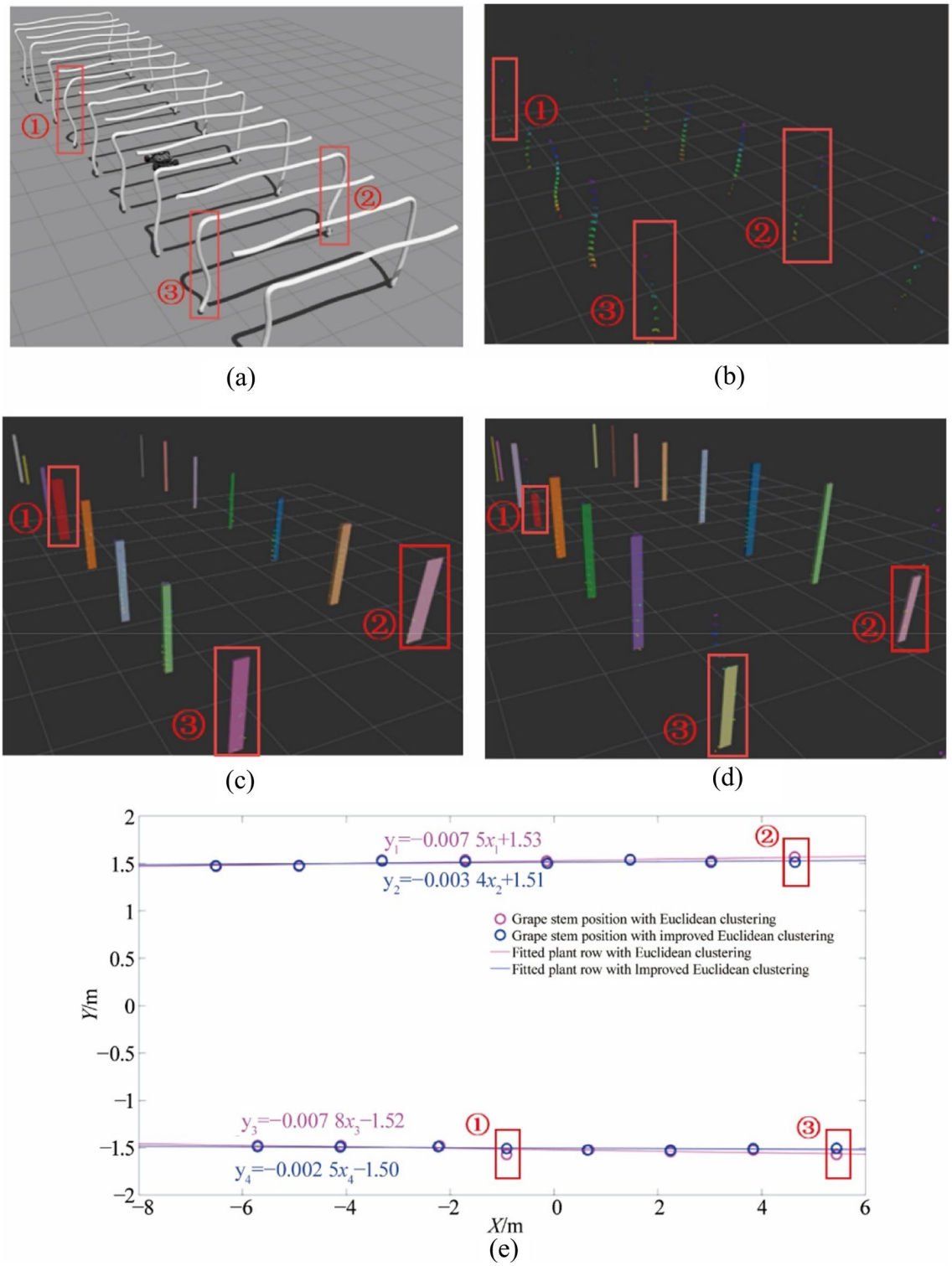

Fig. 13 Clustering results before and after the improvement of Euclidean clustering **a** construction of virtual scenario of grape field, **b** point clouds acquired from virtual grape stems, **c** clustering results of original Euclidean clustering algorithm, **d** clustering results of improved Euclidean clustering algorithm, **e** estimation results of grape stems position before and after Euclidean clustering improvement

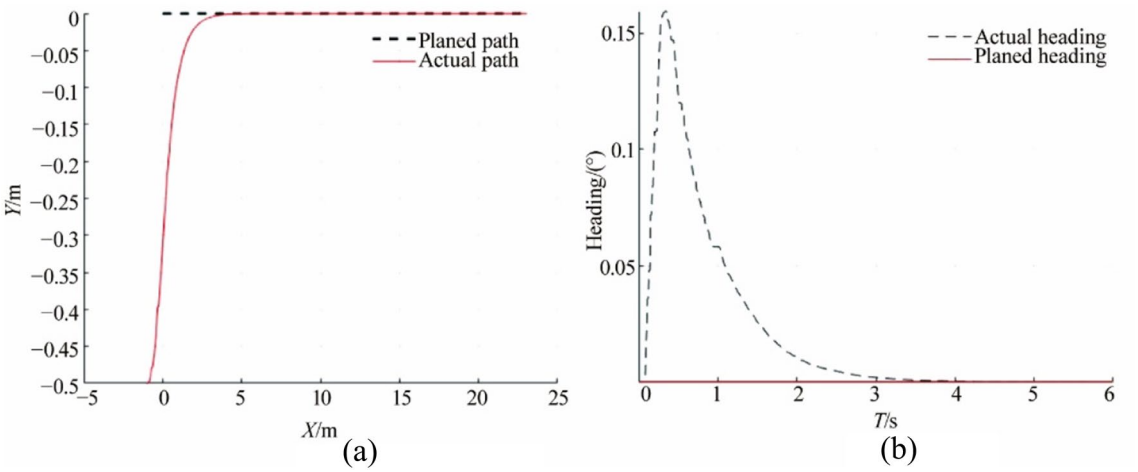

Fig. 14 Navigation controller virtual simulation navigation results **a** robot path tracking, **b** robot heading tracking

Table 2 Accuracy results of 3D LiDAR physical simulation navigation test

Number	Velocity/(m·s^{-1})	Initial deviation/m	Heading to the planed path time/s	Max absolute error/cm	Mean absolute error/cm
1	0.3	0 ± 0.1	3.75	2.72	1.02
2	0.5	0 ± 0.1	2.42	3.08	1.64
3	0.7	0 ± 0.1	1.34	4.95	2.06
4	0.3	0.5 ± 0.1	6.35	2.83	1.36
5	0.5	0.5 ± 0.1	4.53	3.46	1.68
6	0.7	0.5 ± 0.1	3.96	5.15	2.27

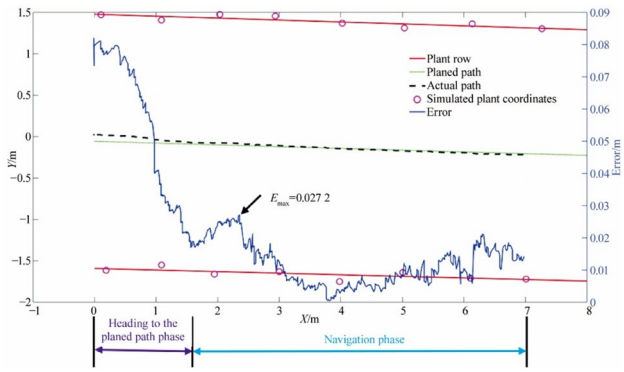

Fig. 15 Results of the simulated navigation test

is set too small, some noise points will also be regarded as clustered point clouds and be incorrectly selected by the box. In contrast, some grape stems are missed due to distance, occlusion, etc., when min_cluster_size = 12 and max_cluster_size = 400, achieving the ideal clustering effect. The blue box is the effect of the BoundingBox-Array box selection under the stem_section of different plants. According to the measured value of grape stem diameter of 3–6 cm, found that if the threshold value of stem_section is seted too small, the centroid may be missed due to too few point clouds of grape stem; On the contrary, the centroid will have a large offset, Therefore, when stem_section = 8 cm, obtain a more accurate estimate of the stem centroid position.

3.1.2 *Improved euclidean clustering for grape stem position estimation*

Figure 13a shows the constructed virtual simulation scenario in Gazebo, and Fig. 13b shows the point cloud acquired from the constructed virtual grape stems. The applied results of original and improved Euclidean clustering algorithm on grape stems are shown in Figs. 13c and d, respectively. Among them, the red boxes numbered ①, ② and ③ in the Fig. 13 are grape stems with obvious curvature, which illustrates that the sizes of the bounding boxes of grape stems with obvious curvature are bigger than those with small curvature. Before the improvement, the maximum width of the bounding box was 15 cm; after the improvement, the maximum width was 8 cm. The estimated center coordinates of the bounding boxes clustered

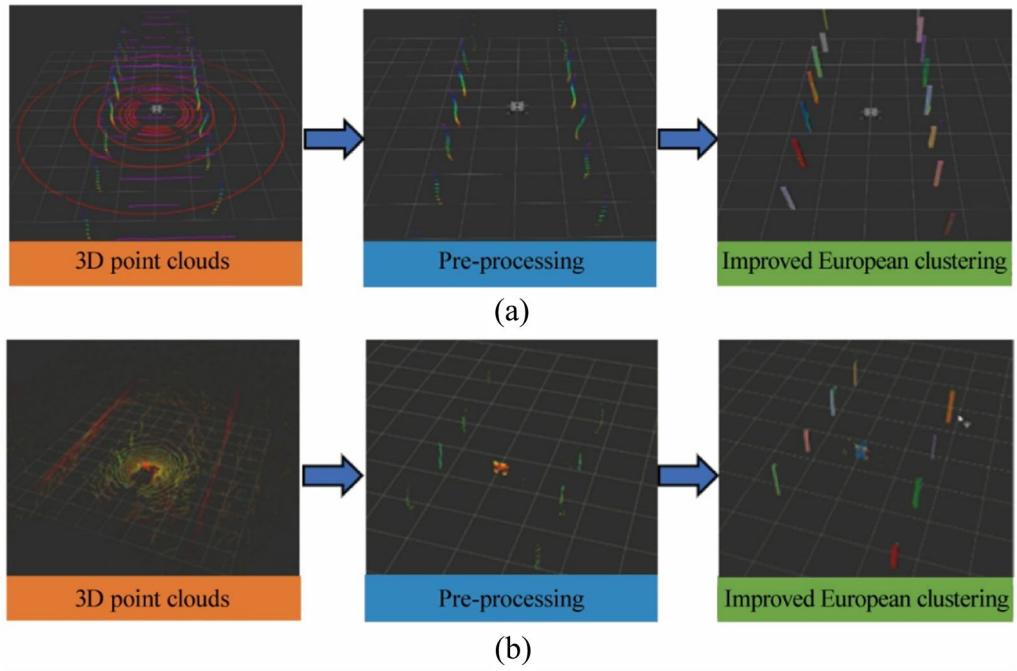

Fig. 16 Grape field point clouds processing flow, **a** virtual simulation environment, **b** field environment

Table 3 Accuracy results of 3D LiDAR field navigation test

	European clustering			Improved European clustering		
Number	1	2	3	4	5	6
Velocity/(m·s^{-1})	0.3	0.5	0.7	0.3	0.5	0.7
Max absolute error/cm	4.95	6.32	7.85	3.12	4.21	5.07
Mean absolute error/cm	2.07	3.15	3.64	1.31	1.98	2.52

by two methods are shown in Fig. 13e. Figure 13e shows that the improved Euclidean clustering can finally improve the estimation accuracy of plant rows.

3.1.3 Path following control simulation

Set the linear velocity and angular velocity of the reference robot as $v_r = 0.3$ m/s, $\omega_r = 0°$/s; the initial pose error is $\underline{e}(0) = [-1.5\,\text{m}, -0.5\,\text{m}, 15°]^T$, $k_1 = 4, k_2 = 2.2, k_3 = 2.5$. Start the virtual simulation, the navigation results recorded by RVIZ are shown in Fig. 14.

The results show that the control law under this parameter, under the condition that the initial deviation is 0.5 m, the heading angle changes within 0–0.5 s, indicating that the robot is in the process of going online. Beginning at 0.5 s, the heading angle gradually converges, completes the line at about 3 s and starts to track the target straight line. Therefore, the designed path following control law is effective.

3.2 Physical simulation test

The linear navigation of the robot is divided into the online phase and the linear tracking phase. After the robot goes online smoothly, the navigation error is calculated, and the initial deviation, Online time, MaxErr and MeanErr of the robot path and the true value are recorded for each test. Test results are shown in Table 2. The results show that, under the same initial deviation, with the increase in velocity, MaxErr and MeanErr also increase; navigation accuracy is reduced; and the online process is accelerated. Therefore, in practical applications, under the premise of meeting the requirements, reducing the traveling velocity as much as possible can improve the navigation accuracy. When travelling velocity is constant, online time, MaxErr and MeanErr all increase as the Initial deviation increases. Therefore, in practical applications, the initial deviation should be minimized to improve the navigation effect. The best navigation effect is in the first group of trials, with a MaxErr of 2.72 cm and a MeanErr of 1.02 cm, as shown in Fig. 15. The planned path

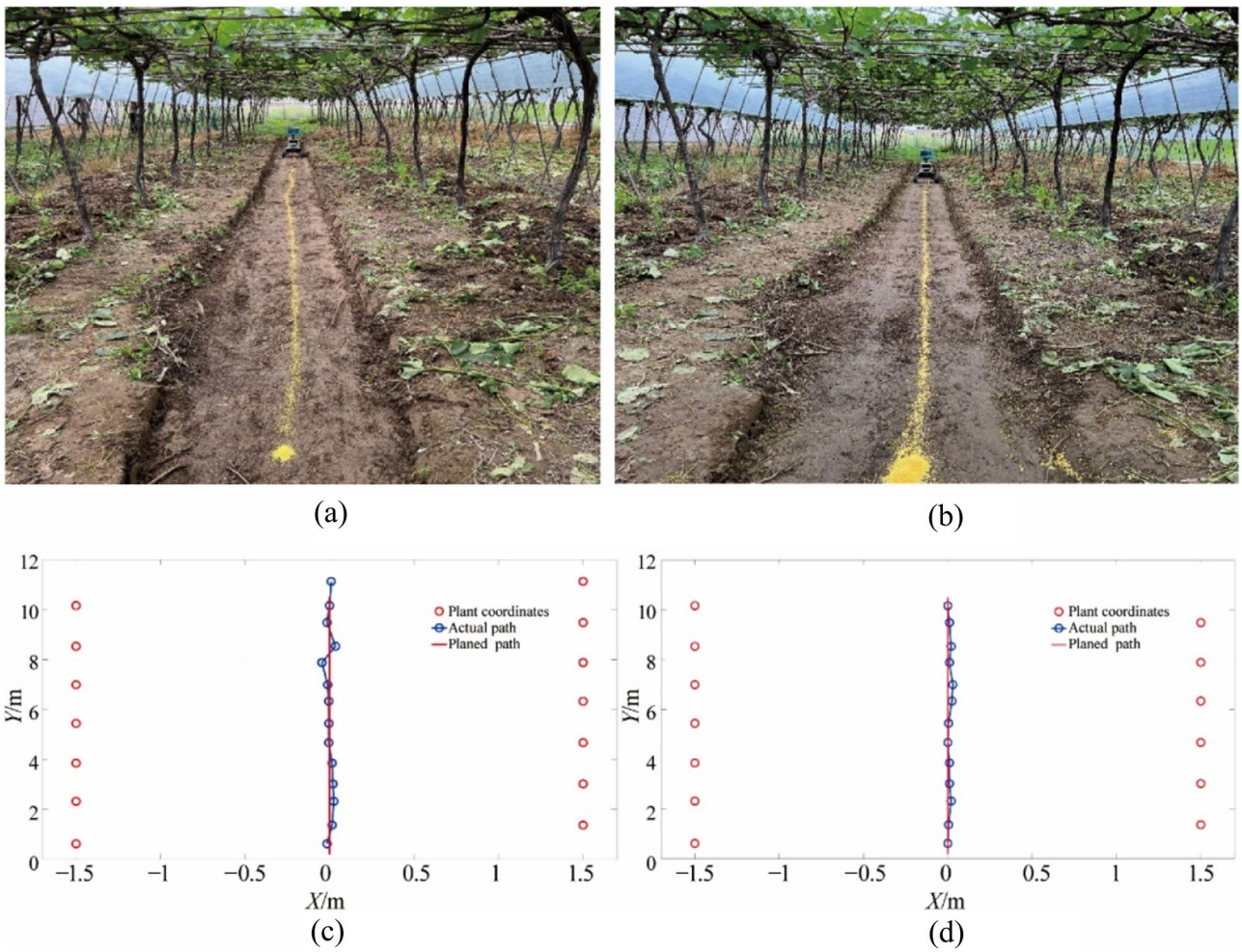

Fig. 17 Field test robot navigation path (yellow sand) **a** navigation path of the robot field test before the improvement of Euclidean clustering, **b** navigation path of robot field test after improvement of European clustering, **c** navigation results of robotic field test before European clustering improvements, **d** navigation results of the robot field test after the European clustering were improved

is basically ideally tracked. The possible causes of errors include measurement errors between sensors and GNSS, calibration errors between LiDAR coordinate systems and GNSS coordinate systems, LiDAR installation errors, and numerical calculation errors.

3.3 Field test

Figures 16a and b show the LiDAR point cloud processing effects in the virtual simulation environment and field test, respectively. The 3D LiDAR scans the environmental point clouds. After preprocessing and improving the Euclidean clustering, the effect of the point clouds is consistent with the processing results of the point clouds in the virtual simulation environment. Therefore, the results show that the system parameters optimized in the virtual simulation environment are also suitable for the field test environment.

In the field experiment, the robot trajectory was tracked by the yellow sand running out from a hourglass. After then, the vertical distance from each grape stem to the recorded navigation trajectory was measured to locate the waypoints on the navigation trajectory corresponding to each real grape stem. Tests were carried out at different initial velocities, and the comparative test results are shown in Table 3. In the field test, it shows the same characteristic as the physical simulation test in Sect. 3.2. With the increase of velocity, MaxErr, and MeanErr will also increase. In the comparative test of European and improved European clustering, when the velocities are 0.3 m/s, 0.5 m/s and 0.7 m/s, respectively, the effect of improved European clustering is better than that of European clustering. The accuracy results are best when velocity is 0.3 m/s; MaxErr is 3.12

cm; and MeanErr is 1.31 cm. As shown in Figs. 17a and b, the navigation path of the robot field test after the improvement of the European clustering is smaller than the navigation path of the robot field test before the improvement of the European clustering, which is smoother and closer to the planned path. In Fig. 17c, at $y = 8$ m, the Actual path has the largest error of 4.95 cm, and at $y = 9$ m, there is a large deviation in the opposite direction. The grape stems on both sides were significantly bent, which caused the planned path to deviate from the ideal centerline, and the tracking error was the largest. In Fig. 17d, the curve of the actual path is very smooth, and the maximum error is only 3.12 cm. Most of the curves are close to the planned path, and a few are slightly to the right.

The field test results show that the navigation system designed by the methodology proposed in this study can realize the effective estimation of plant information and the automatic navigation of the robot in a star-free environment.

4 Conclusions

Aiming at the problems existing in the development of agricultural robot navigation systems in a GNSS-denied environment, such as long development cycles and unrepeatable field test data, a 3D LiDAR-based navigation system development methodology is proposed. It specifically includes: (i) point cloud data preprocessing methods, (ii) individual plant segmentation and position estimation method, (iii) plant row fitting and path planning, (iv) non-linear path following control law, (v) construction of a robot-LiDAR-plant multi-domain unified virtual simulation environment in ROS/Gazebo, (vi) carrying out virtual simulation test, physical simulation test and field test to verify the effectiveness of the proposed methodology. The physical simulation test results show that when the travelling velocity of the robot is 0.3 m/s and the initial deviation is 0 ± 0.1, the MaxErr and MeanErr are 2.72 cm and 1.02 cm, respectively. The field test results show that, the point cloud processing and automatic control algorithm parameters in the virtual simulation environment are also applicable to the field, and consistent navigation results are obtained. When the travelling velocity of the robot is 0.3 m/s, the MaxErr and MeanErr are 3.12 cm and 1.31 cm, respectively. Above all, the proposed method provides a good solution on improving the development technique for agricultural robot navigation systems that operate in GNSS-denied environments. This study has good scalability and its methodology can be implemented in a wide variety of field robot, which is promising to shorten the development cycle of agricultural robots. Future study will focus on the reconstruction of complicated field scenario in virtual simulation environment and in which the obstacle avoidance algorithm of agricultural robots will be studied.

Acknowledgements This research is funded by the Agricultural Equipment Department of Jiangsu University (Grant No. NZXB20210106), the National Natural Science Foundation of China (Grant No. 52105284), the Leading Goose Program of Zhejiang Province (Grant No. 2022C02052), the China Agriculture Research System of MOF and MARA and Basic, and the Applied Basic Research Project of Guangzhou Basic Research Program in 2022 (Grant No. 202201011691). We also thank the anonymous reviewers for their critical comments and suggestions for improving the manuscript.

References

1. Li SC, Zhang M, Ji YH et al (2021) Agricultural machinery GNSS/IMU-integrated navigation based on fuzzy adaptive finite impulse response Kalman filtering algorithm. Comput Electron Agr 191:106524. https://doi.org/10.1016/J.COMPAG.2021.106524
2. Zhao CH, Yang ZY, Cheng XR et al (2022) SINS/GNSS integrated navigation system based on maximum versoria filter. Chin J Aeronaut 35(8):168–178
3. Li ZK, Liu Z, Zhao L (2021) Improved robust Kalman filter for state model errors in GNSS-PPP/MEMS-IMU double state integrated navigation. Adv Space Res 67(10):3156–3168
4. Tang YN, Jiang JG, Liu JH et al (2022) A GRU and AKF-based hybrid algorithm for improving INS/GNSS navigation accuracy during GNSS outage. Remote Sen-Basel 14(3):752. https://doi.org/10.3390/RS14030752
5. Chen JQ, Qiang H, Wu JH et al (2021) Navigation path extraction for greenhouse cucumber-picking robots using the prediction-point Hough transform. Comput Electron Agr 180:105911. https://doi.org/10.1016/j.compag.2020.105911
6. Malavazi F, Guyonneau R, Fasquel JB et al (2018) LiDAR-only based navigation algorithm for an autonomous agricultural robot. Comput Electron Agr 154:71–79
7. Papadimitriou A, Mansouri SS, Nikolakopoulos G (2022) Range-aided ego-centric collaborative pose estimation for multiple robots. Expert Syst Appl 202:117052. https://doi.org/10.1016/J.ESWA.2022.117052
8. Zhu DJ (2021) Research on localization algorithm of patrol robot based on fusion of vision and wheel encoder. Dissertation, University of Science and Technology of China
9. Long ZH, Xiang Y, Lei XM et al (2022) Integrated indoor positioning system of greenhouse robot based on UWB/IMU/ODOM/LIDAR. Sensors 22(13):4819. https://doi.org/10.3390/s22134819
10. Wężyk P, Hawryło P, Szostak M et al (2019) Using LiDAR point clouds in determination of the scots pine stands spatial structure meaning in the conservation of lichen communities in "Bory Tucholskie" national park. Archives of Photogrammetry, Cartography and Remote Sensing 31:85–103
11. Zhang MN, Lv XL, Qiu W et al (2017) Calculation method of leaf area density based on three-dimensional laser point cloud. Trans Chin Soc Agricultural Mach 48(11):172–178
12. Shendryk Y, Sofonia J, Garrard R et al (2020) Fine-scale prediction of biomass and leaf nitrogen content in sugarcane using UAV LiDAR and multispectral imaging. Int J Appl Earth Obs 92:102177. https://doi.org/10.1016/j.jag.2020.102177
13. Blanquart JE, Sirignano E, Lenaerts B et al (2020) Online crop height and density estimation in grain fields using LiDAR. Biosys Eng 198:1–14
14. Karimi HR, Liang B, Basin M et al (2021) EKF-DRNN autopilot for VLCC heading hybrid control. T I Meas Control 43(13):2983–2999

15. Dai XH, Ke CX, Quan Q et al (2021) RFlySim: automatic test platform for UAV autopilot systems with FPGA-based hardware-in-the-loop simulations. Aerosp Sci Technol 114:106727. https://doi.org/10.1016/J.AST.2021.106727
16. Carvalho EA, Magalhães RR, Santos FL (2016) Geometric modeling of a coffee plant for displacements prediction. Comput Electron Agr 123:57–63
17. Zhang XB, Zhu YH, Su YL et al (2021) Quantitative extraction and analysis of pear fruit spot phenotypes based on image recognition. Comput Electron Agr 190:106474. https://doi.org/10.1016/J.COMPAG.2021.106474
18. Jiang SF, Wang KQ, Zhou ZY (2021) Experimental study on the complementary inverse reconstruction of tree growth state data by radar detection and 3D raster scan. Ferroelectrics 578(1):51–65
19. Cheraïet A, Naud O, Carra M et al (2020) An algorithm to automate the filtering and classifying of 2D LiDAR data for site-specific estimations of canopy height and width in vineyards. Biosys Eng 200:450–465
20. Chen RQ, Li CC, Yang GJ et al (2020) Extraction of crown information from individual fruit tree by UAV LiDAR. Trans Chin Soc Agricultural Eng 36(22):50–59
21. Jones MH, Bell J, Dredge D et al (2019) Design and testing of a heavy-duty platform for autonomous navigation in kiwifruit orchards. Biosys Eng 187:129–146
22. Jiang SK, Wang SL, Yi ZY et al (2022) Autonomous navigation system of greenhouse mobile robot based on 3D Lidar and 2D Lidar SLAM. Front Plant Sci 13:815218. https://doi.org/10.3389/FPLS.2022.815218
23. Liu SQ (2022) Research on autonomous mapping and navigation technology of tracked robot in unknown environment based on ROS. Dissertation, Shandong University

Run-Mao Zhao is currently a lecturer of School of Mechanical Engineering, Zhejiang Sci-Tech University, P.R. China. He received Ph.D. from South China Agricultural University, P.R. China. His research interest is agricultural robot.

Zheng Zhu is currently a Master degree candidate of Mechanical Engineering at Zhejiang Sci-Tech University, P.R. China. His research interest is autonomous navigation system for agricultural robot.

Jian-Neng Chen is currently a professor of School of Mechanical Engineering, Zhejiang Sci-Tech University, P.R. China. His research interests include analysis and synthesis of mechanism, agricultural equipment and robot.

Tao-Jie Yu is currently a Master degree candidate of Mechanical Engineering at Zhejiang Sci-Tech University, P.R. China. His research interests include 2D and 3D machine vison in agriculture.

Jun-Jie Ma is an undergraduate student at Zhejiang Sci-Tech University. His research interest is agricultural robot.

Guo-Shuai Fan is currently a Master degree candidate of Mechanicalm Engineering at Zhejiang Sci-Tech University, P.R. China. His research interests are agricultural environment sensing and modelling.

Min Wu is currently a Ph.D. candidate of Mechanical Engineering at Zhejiang Sci-Tech University, P.R. China. His research interests include intelligent agricultural equipment and control technology.

Pei-Chen Huang is currently a lecturer of College of Automation at Zhongkai University of Agriculture and Engineering, P.R. China. His research interests include agricultural robot visual navigation, motion control, deep learning, etc.


Biosystems
ENGINEERING
63

Biosystems Engineering

Supports open access

10.1 CiteScore | 5.3 Impact Factor

Volume 203

Pages 1-124 (March 2021)

Previous vol/issue | Next vol/issue

Download full issue

Actions for selected articles

Select all / Deselect all

Download PDFs

Export citations

Show all article previews

Contents

Research Paper

Available online at www.sciencedirect.com

ScienceDirect

journal homepage: www.elsevier.com/locate/issn/15375110

Research Paper

Method for estimating vertical kinematic states of working implements based on laser receivers and accelerometers

Runmao Zhao [a,b], Lian Hu [a,c,*], Xiwen Luo [a,c], Wenyu Zhang [a], Gaolong Chen [a], Hao Huang [a], Sangyu Lai [a], Hailong Liu [a]

[a] College of Engineering, South China Agricultural University, Wushan Road 483, 510642, Guangzhou, China
[b] Faculty of Mechanical Engineering and Automation, Zhejiang Sci-Tech University, Second Avenue, 310018, Hangzhou, China
[c] Guangdong Laboratory for Lingnan Modern Agriculture, Wushan Road 483, 510642, Guangzhou, China

ARTICLE INFO

Article history:
Received 20 January 2020
Received in revised form
15 December 2020
Accepted 30 December 2020

Keywords:
Working implement
Kinematic states
Estimation
Laser receiver
Accelerometer

To overcome the limitations of existing methods in acquiring the vertical kinematic states of implements subject to vulnerable signal or operating surroundings, the Kalman filter was used to fuse a laser receiver's rough height indicated by photocell set and its acceleration to obtain the vertical displacement and velocity of the implement. This is called the Kalman filter based method for fusing laser receiver and accelerometer (KFLA). By using the linear motion transducer as a comparative metric, laboratory experiments of accuracy evaluation were conducted within the motion range of −77 to +77 and −11 to +11 mm, respectively. The maximum absolute errors of the displacement estimated by the KFLA were 14.6 mm and 5.7 mm, respectively; and the root mean square errors were 5.6 mm and 1.9 mm, respectively. Meanwhile, the velocity estimated by the KFLA showed similar but smoother variations than the displacement difference. Vertical height estimation result of the implement of a field-travelling levelling machine showed that the KFLA curve passed through the bars represented by the rough height and corresponding deviation with a higher frequency of 50 Hz. Above all, the KFLA could calculate the height of the implement when the motion was beyond the sensing range of the receiver, which showed the stable acquisition of sensing signal enables KFLA to be competent for measurement tasks operating in complex terrain. Overall, the KFLA is a promising method to estimate the kinematic states of the implements in indoor/outdoor environments, dryland, and paddy fields.

1. Introduction

Because of the poor levelling of farmlands, agricultural machinery needs a height adjustment mechanism to compensate for the operational impact of an uneven surface and obtain a uniform working height that facilitates the standardised implementation of subsequent processes. The height adjustment mechanisms are of passive and active types. Passive mechanisms have a simple form and are easy

* *Corresponding author*. College of Engineering, South China Agricultural University, Wushan Road 483, 510642, Guangzhou, China.
E-mail address: lianhu@scau.edu.cn (L. Hu).

https://doi.org/10.1016/j.biosystemseng.2020.12.015
1537-5110/

Nomenclature

Symbol	Meaning of symbol [unit]
T_0	Sample interval [s]
S_k	Actual vertical displacement of the receiver [mm]; subscript k denotes the sampling order
a_k	Actual vertical acceleration of the receiver [mm s^{-2}]
z_k	Height level indicated by the enabled photocell unit(s) [mm]
e_k	Error between the observation and actual vertical displacement of the laser receiver [mm]
$\mathbf{X}_k$	Two-dimensional state vector
u_k	Manoeuvring acceleration [mm s^{-2}]
w_k	Non-manoeuvring acceleration [mm s^{-2}]
$\boldsymbol{A}$	State transition matrix
$\boldsymbol{B}$	Input matrix
$\boldsymbol{H}$	Observation matrix
$\widehat{\mathbf{x}}_{k-1}(-)$	Prior estimation of the system state
$\widehat{\mathbf{x}}_{k-1}(+)$	Posteriori estimation of the system state
$\mathbf{P}_k(-)$	Prior covariance of the error of $\widehat{\mathbf{x}}_k(-)$
$\mathbf{P}_k(+)$	Posteriori covariance of the error of $\widehat{\mathbf{x}}_k(-)$
$\mathbf{Q}$	Process noise covariance matrix
Q_H	Variance of the displacement process
Q_v	Variance of the velocity process
R	Observation noise covariance
K_k	Kalman gain
$\boldsymbol{I}$	Unit vector
$Y(k)$	Low-pass output [mm s^{-2}]
$X(k)$	Sampling value of the accelerometer [mm s^{-2}]
α	Low-pass filter coefficient
$D(a)$	Variance of the pre-processed acceleration signal

to implement. Generally, by adjusting the pretension length of the linear spring, the contouring motion of the machine relative to the field can be achieved within a certain range. Passive mechanisms are mostly used for agricultural traction implements, such as the seeding device of a single precision seeder. However, for integrally suspended working implements with large inertia and operating scenarios with large fluctuations in the terrain, the passive adjustment solution cannot meet the requirements of highly accurate control of the implement. With the continuous advancement and development of precise agricultural concepts and applications, the acquisition and active control technology of the farm implement height continue to attract the attention of researchers. Nielsen et al. (2017) combined ultrasonic and linear displacement sensors to monitor the depth of the disk coulter and developed a corresponding depth active control system (Nielsen et al., 2018). Cui et al. (2019) used a smoothing filter and a limiting filter to integrate the data from three ultrasonic sensors installed under the boom of a sprayer to dynamically measure the height of the nozzles relative to the canopy. Similarly, ultrasonic sensors have also been successfully used to sense the canopy height of wild blueberries, providing a height reference for automatic height adjustment of harvester headers (Chang et al., 2017). Wang et al. (2019) used a near-infrared distance sensor installed in front of the wheels to detect the terrain in front of an agricultural vehicle to estimate the attitude of the chassis, thereby achieving rapid control of the attitude of the vehicle platform. The above sensors are widely used to obtain machine height information (relative to the field surface or canopy) in dry farmlands, but their application is limited in Asian paddy fields, which are the main rice production areas.

Tang et al. (2018) proposed a paddy field surface (mud-water mixture) extraction algorithm based on two-dimensional (2D) LiDAR information. This method can calculate the height of the work implement relative to the ideally horizontal water surface, but the operation is best performed within 10.5–24 h after rotary cultivation to minimise the time variations in the measurements. To support precision agriculture, GNSS (global navigation satellite system) equipment can be used for tracking the spatial positioning of the vehicle in the earth-fixed coordinate system for autonomous robot navigation (Gonzalez-de-Soto et al., 2016) and continuous recording of the three-dimensional soil parameters. Fountas et al. (2013) designed a rapid resistance measurement system using a GPS receiver, comparing the effects of five different tillage methods on soil compaction at different depths. Similar studies were also conducted by Sudduth et al. (2008) and Andrade-Sanchez et al. (2008). Although the GNSS equipment can be used in paddy fields and dryland, and provide up to centimetre-level accuracy working in RTK (real-time kinematic) mode, GNSS signals are easily blocked by obstacles and appear to have differential lockout or multipath effects. Therefore, auxiliary sensors are required for information fusion estimations (Rovira-Más et al., 2015), resulting in higher overall costs.

The laser levelling technologies, including dry land levellers (İrsel & Altinbalik, 2018), paddy field levellers (Hu et al., 2019), and levellers for construction machinery (Leica, 2019), use a laser receiver installed on the scraper to sense the position of the laser beam emitted by the laser transmitter to obtain the height difference between the scraper and the laser scanning plane. The hardware of the height measurement system adopted by the laser leveller is composed of a laser receiver and laser transmitter, which has lower cost and stronger anti-interference ability than the GNSS equipment, providing an accuracy of 3–10 mm among products. Moreover, the laser height sensing system (LHSS) can be used both indoors and outdoors; thus, it is a promising approach to measure the height of a working implement despite its shortcomings. First, the laser receiver outputs digitally encoded signals according to the enabled state of the internal photocell set. It has high precision, but the resolution is low and limited by the physical size of the photocell unit. In addition, the range of the LHSS depends on the overall length of the photocell set. When used in off-road conditions, especially in paddy fields with uneven bottom layers (Zhao et al., 2019), the motion of the tractor motion fluctuates greatly (Hu

et al., 2019), and even exceeds the effective measurement range, causing measurement failures. Moreover, the data acquisition frequency of the LHSS is determined by the rotary speed of the laser head, which is usually only 10 Hz, causing undersampling of the height measurements, especially for implements with high moving speeds.

The objective of this work is to propose an improved sensing system and corresponding signal processing algorithm on the basis of the current LHSS, which can not only estimate the elevation of working implements in real time with higher precision, reliability, and update frequency but also estimate the vertical velocity that is absent in the original LHSS. Furthermore, it is expected that the proposed system has a wider range of application scenarios, such as concrete levellers used indoors and agricultural implements in dryland as well as paddy fields.

2. Material and methods

2.1. The laser receiver

The laser receiver's photosensitive area consists of 36 pieces of 2CR93 silicon photocells with a size of 20 mm × 5 mm. The effective length of a single chip is 20 mm. The silicon photocells are divided into four columns with nine pieces in each column. The four columns of the photocells are arranged symmetrically, and every two adjacent columns are perpendicular to each other so that the laser beam can be detected at any incident angle. For each column, the photocells are connected in a 2-2-1-2-2 manner with 2-mm space in between (Fig. 1(a)). The receiver uses five (denoted by PA0–PA4) independent processing circuits to perform photoelectric conversion, amplification filtering, pulse shaping, and comparison stretching on the signal, and then transmits it to the STM32F103RBT6 processor's general-purpose input/output (GPIO) (Ke and Luo, 2014). The processor distinguishes the photocell(s) enabled by the laser beam according to the logic value(s) of PA0–PA4 of the GPIO. In Fig. 1(b), the red horizontal dotted line represents the laser beam, and the vertical line perpendicular to it represents the beam diameter. The position value of the middle photocell (PA2) is set at 0; by considering the size and arrangement of the photocell units, the receiver can sense and output nine height levels: when the laser beam irradiates at any position in PA4, it indicates that the current height difference between the receiver and laser reference plane is level 77; when the laser beam irradiates at any position in PA3, it indicates that the current height level is 33; when the laser beam irradiates at any position in PA2, it indicates that the current height level is 0; when the laser beam irradiates in both PA4 and PA3, it indicates that the current height level is 55; when the laser beam irradiates in both PA3 and PA2, it indicates that the current height level is 11. For the photocell units below PA2, the height levels are still symmetric but have negative values.

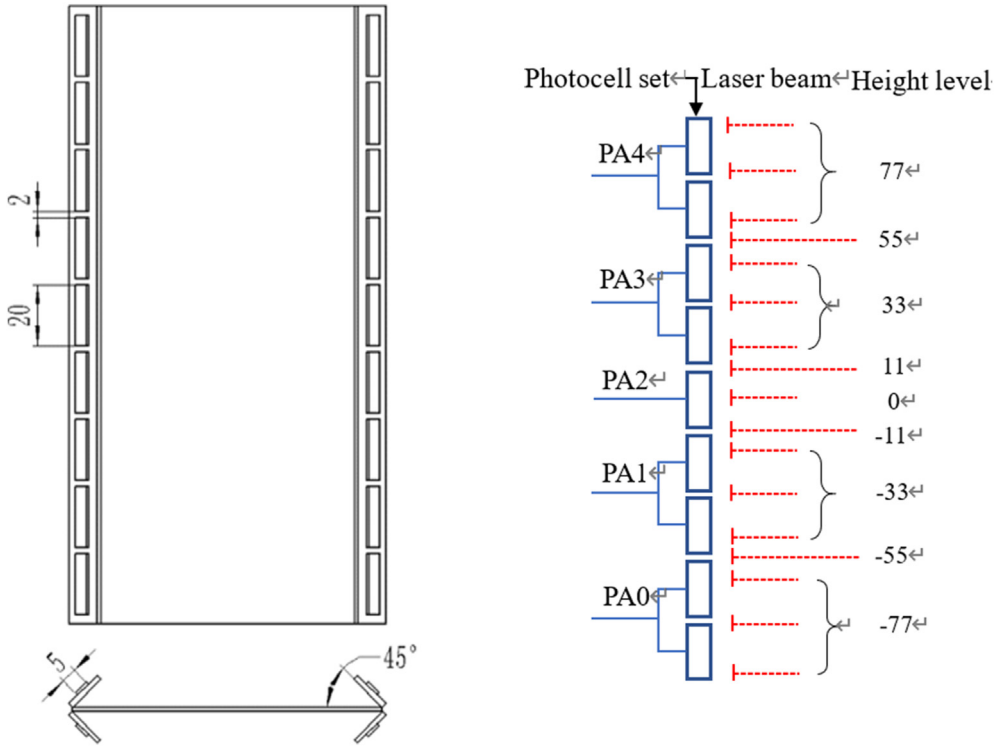

Fig. 1 – Working principle of the laser receiver (unit in the figure: mm). (a) Size and arrangement of photocell unit. (b) Relationship between height level value and irradiation position.

2.2. *Kalman information fusion algorithm based on the laser receiver and accelerometer (KFLA)*

The photocell set indicates the actual laser beam position information, but the observation variance is large and the update frequency is low. Accelerometers can provide high-frequency height estimation, but digital integration tends to cause error accumulation. Therefore, by fusing the external laser source data with good long-term accuracy and inertial sensor data with good short-term accuracy, an optimal overall estimate of the receiver's motion position can be acquired. Here, the Kalman filter is used to fuse the height level and the acceleration information to estimate the kinematic states of the laser receiver, to improve the measurement accuracy and signal update frequency.

The vertical motion of the receiver can be described using the following equation:

$$S_{k+1} = S_k + \dot{S}_k T_0 + 0.5 a_k T_0^2 \tag{1a}$$

$$\dot{S}_{k+1} = \dot{S}_k + a_k T_0 \tag{1b}$$

where T_0 is the sample interval, s; S_k is the actual vertical displacement of the receiver, mm; subscript k denotes the sampling order; a_k is the actual vertical acceleration of the receiver, mm s^{-2}; the dot indicates differentiation with respect to sample interval.

The height level at sample time k indicated by the enabled photocell units is given by z_k, which is composed of the actual vertical displacement and observation error:

$$z_k = S_k + e_k \tag{2}$$

where e_k is the error between the observation and actual vertical displacement of the laser receiver, mm.

The displacement and velocity of the laser receiver serve as the two-dimensional (2D) state vector, x_k, in the receiver's kinematic state space:

$$\mathbf{x_k} = \begin{bmatrix} S_k \\ \dot{S}_k \end{bmatrix} \tag{3}$$

When an accelerometer is used to measure the acceleration, a_k in Eq. (1) is composed of manoeuvring acceleration u_k and non-manoeuvring acceleration w_k:

$$a_k = u_k + w_k \tag{4}$$

Using Eqs. (1)–(4), the recursive equation for the kinematic states of the laser receiver can be expressed as follows:

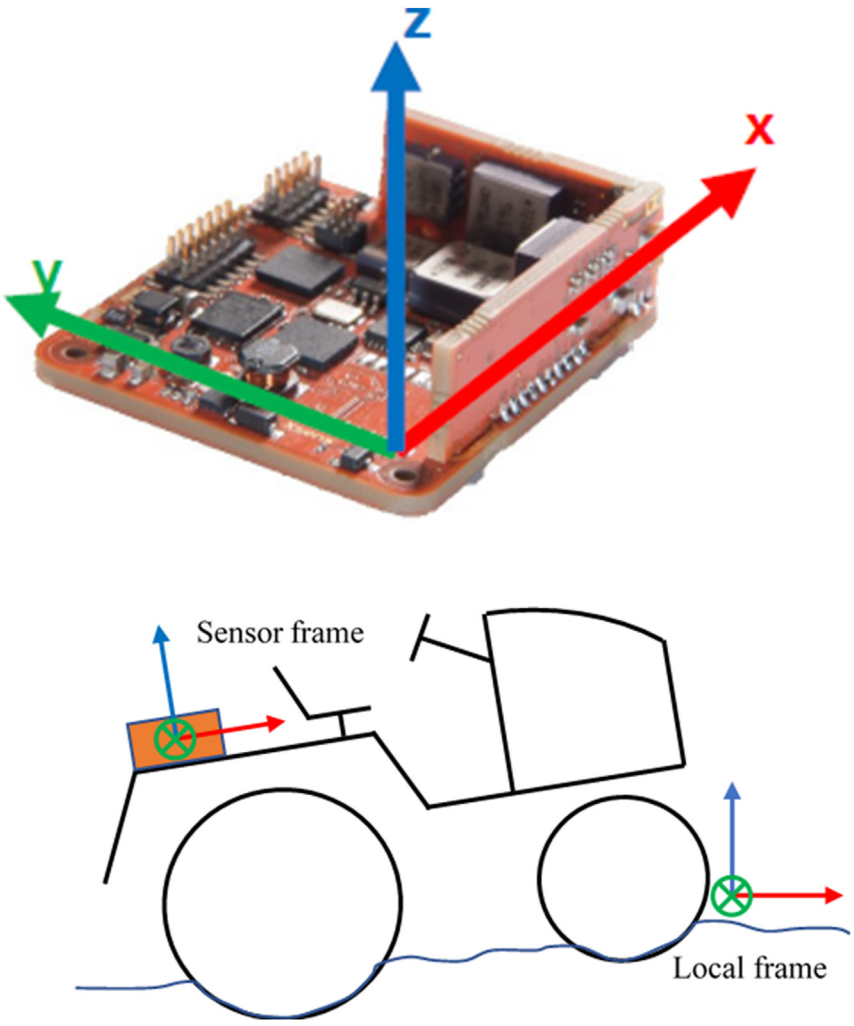

Fig. 2 – Coordinate system illustration. (a) AHRS (sensor) coordinates. (b) Presentation of the two coordinates.

$$\mathbf{x_k} = \mathbf{A}\mathbf{x}_{k-1} + \mathbf{B}u_{k-1} + \mathbf{B}w_{k-1} \tag{5a}$$

where $\mathbf{A} = \begin{bmatrix} 1 & T_0 \\ 0 & 1 \end{bmatrix}$ is the state transition matrix; $\mathbf{B} = \begin{bmatrix} 0.5T_0^2 \\ T_0 \end{bmatrix}$ is the input matrix.

The observation equation for the kinematic states of the laser receiver is

$$z_k = \mathbf{H}x_k + e_k \tag{5b}$$

where $\mathbf{H} = [1 \;\; 0]$ is the observation matrix.

The process of the Kalman filter fusing the receiver acceleration and the height level perceived by the photocell set can be summarised as follows:

1) Prior estimation of the system state at step k:

$$\widehat{\mathbf{x}}_k(-) = \mathbf{A}\widehat{\mathbf{x}}_{k-1}(+) + \mathbf{B}u_{k-1} \tag{6a}$$

where $\widehat{\mathbf{x}}_k(-)$ is the current state value recursed from the state vector at step k−1, which is the state prediction (a prior estimate); $\widehat{\mathbf{x}}_{k-1}(+)$ is the optimal estimate of the receiver's kinematic state (a posteriori estimate).

2) The prior covariance of the error of $\widehat{\mathbf{x}}_k(-)$:

$$\mathbf{P}_k(-) = \mathbf{A}\mathbf{P}_{k-1}(+)\mathbf{A}^{\mathrm{T}} + \mathbf{Q} \tag{6b}$$

where $\mathbf{Q} = \begin{bmatrix} Q_H & 0 \\ 0 & Q_v \end{bmatrix}$ is the process noise covariance; Q_H is the variance of the displacement process; Q_v is the variance of the velocity process.

3) Kalman gain K_k at step k:

$$K_k = P_k(-)H^{\mathrm{T}}[HP_k(-)H^{\mathrm{T}} + R]^{-1} \tag{6c}$$

4) Posterior estimation of the kinematic states at step k:

$$\widehat{x}_k(+) = \widehat{x}_k(-) + K_k[z_k - H\widehat{x}_k(-)] \tag{6d}$$

Table 1 – Simulation results of traversal filter coefficient.

α	0.01	0.02–0.03	0.04–0.05	0.06–0.07	0.08–0.10	0.11–0.12
Std.	0.0053	0.0052	0.0051	0.0050	0.0049	0.0048
α	0.13–0.15	0.16–0.17	0.18–0.20	0.21–0.23	0.24–0.26	0.27–0.30
Std.	0.0047	0.0046	0.0045	0.0044	0.0043	0.0042
α	0.31–0.35	0.36–0.41	0.42–0.58	0.59–0.64	0.65–0.69	0.70–0.73
Std.	0.0041	0.0040	0.0039	0.0040	0.0041	0.0042
α	0.74–0.76	0.77–0.79	0.80–0.82	0.83–0.84	0.85–0.87	0.88–0.89
Std.	0.0043	0.0044	0.0045	0.0046	0.0047	0.0048
α	0.90–0.92	0.93–0.94	0.95–0.96	0.97–0.98	0.99	
Std.	0.0049	0.0050	0.0051	0.0052	0.0053	

Note: In order to simplify the form, the Std. value in the table was only listed with two significant digits. The actual simulation result was a double-precision floating-point number with 13 significant digits.

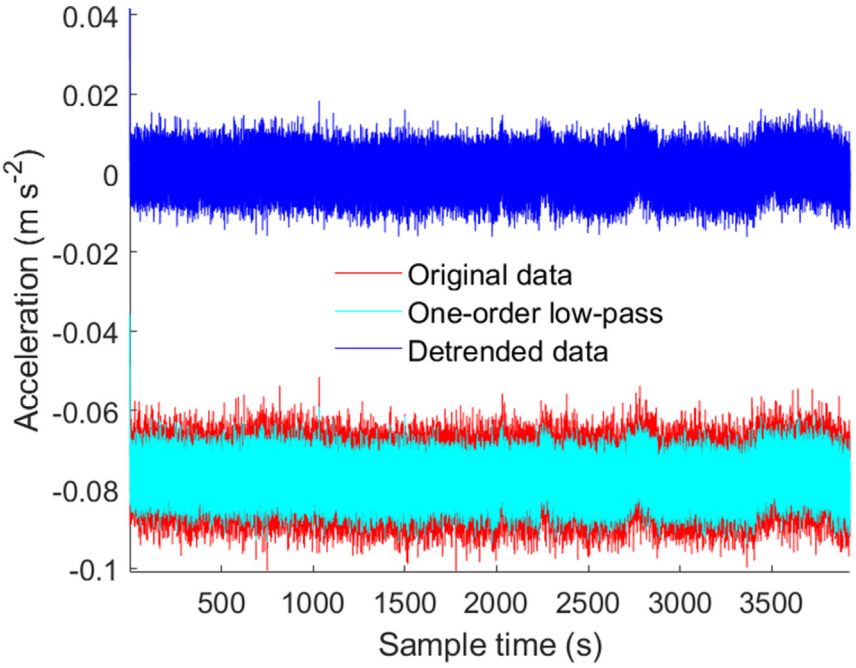

Fig. 3 – Acceleration signal pre-processing.

5) Posterior estimation of the covariance of the error at step k:

$$P_k(+) = [I - K_k H]P_k(-) \tag{6e}$$

where $I = \begin{bmatrix} 1 \\ 1 \end{bmatrix}$ is the unit vector.

2.3. Measurement of laser receiver acceleration

2.3.1. Measuring sensor

The MTi-300-2A5G4 attitude and heading reference system (AHRS) produced by Xsens Technologies B.V. was used to obtain the vertical acceleration of the laser receiver. It integrates a high-performance three-axis accelerometer, three-axis vibration suppression gyroscope, three-axis magnetometer, and high-end hardware such as a pressure sensor (Fig. 2(a)). The AHRS is configured to output the z-axis free acceleration (the acceleration in the Global coordinate system, in East North Up, from which the local gravity is deducted). It is the free acceleration that represents the vertical acceleration of the receiver, and the free acceleration based on the global frame is not affected by the attitude movement of the vehicle (Fig. 2(b)).

2.3.2. Acceleration data preprocessing

The initial free acceleration output of the AHRS includes noise and zero offset. Acceleration noise was processed by first-order low-pass filtering. The filtering equation is presented in Eq. (7).

$$Y(k) = (1-\alpha)Y(k-1) + \alpha X(k) \tag{7}$$

where $Y(k)$ is the low-pass filter output at current step k, m s^{-2}; $X(k)$ is the accelerometer sample value, m s^{-2}; α is the low-pass filter coefficient.

In order to select the optimal filter coefficient α, the static free acceleration signal with a length of 60 min was collected. Taking the signal sample standard deviation (Std.) as the metric of selection, in Matlab 2016b, the traversal calculation

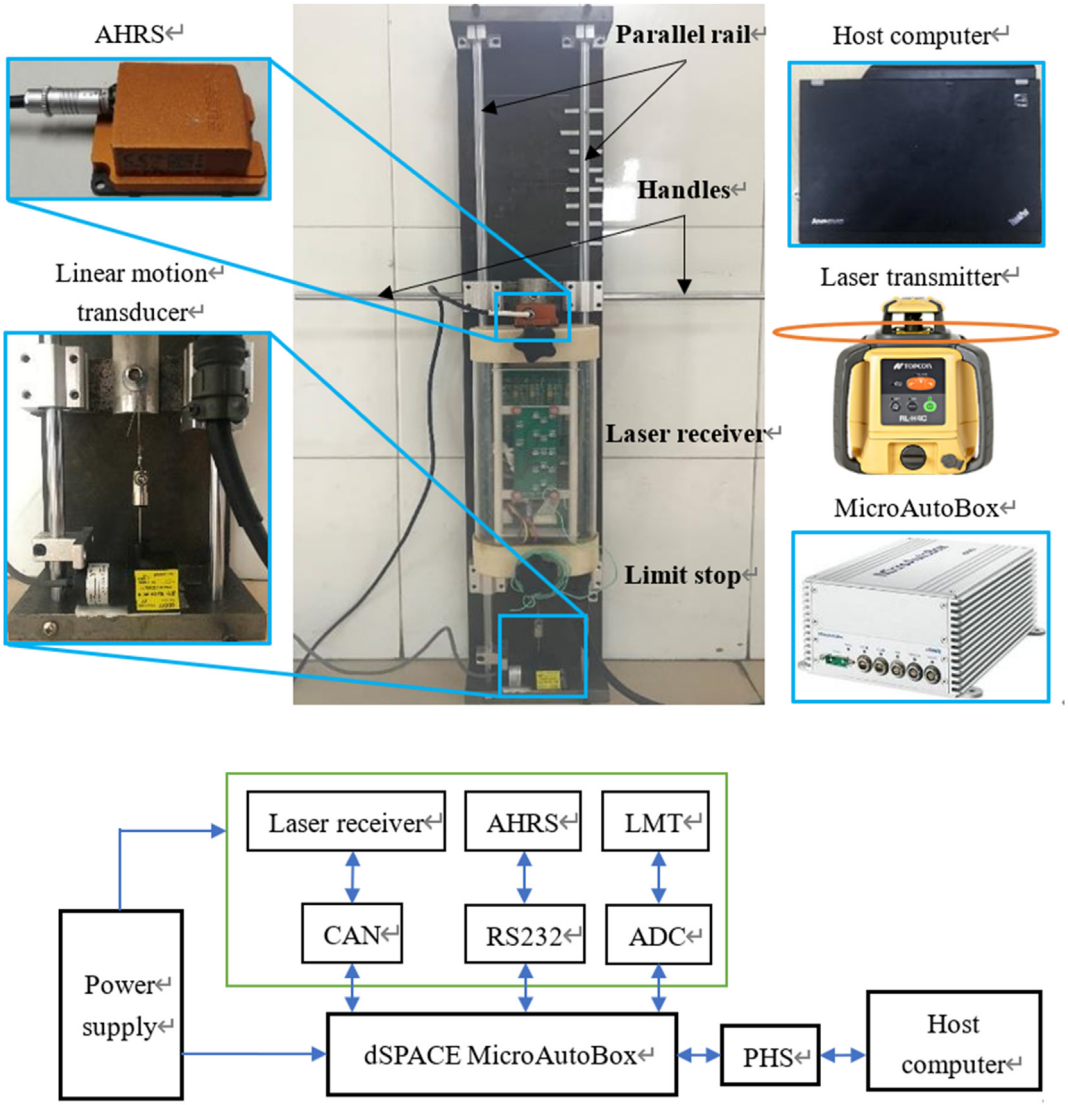

Fig. 4 – Laboratory experiment materials. (a) Parallel rail platform. (b) Hardware connection.

of α was performed within the interval [0.01, 0.99] in increments of 0.01. The results are presented in Table 1.

Table 1 shows that as the value of α increases, Std. of the signal decreases first and then increases. When $\alpha = 0.50$, the acceleration Std. reaches the minimum, decreasing from 0.00531998 to 0.00390391. We set $\alpha = 0.50$ to perform a first-order low-pass filtering on the original sampled signal. The filtered data had a constant zero bias of 0.075. The trend term was extracted and removed using the least square method. The acceleration preprocessing result is shown in Fig. 3.

2.3.3. *Covariance matrix determination*

The values of the process noise covariance matrix **Q** and the observation noise covariance matrix *R* have important effects on the KF filtering results. It is the ratio between **Q** and *R*, not their individual values, that determines the performance of the KF (Akhlaghi et al., 2017). Based on the estimation of the variance $D(a)$ of the pre-processed acceleration signal in Fig. 3 and the nature of the variance calculation, we obtained $Q_H = (0.5T_0^2)^2 D(a)$, $Q_v = T_0^2 D(a)$. The value of $R = 5$ was obtained by a trial-and-error search after **Q** was determined.

2.4. *Algorithm accuracy evaluation and validation*

2.4.1. *Laboratory experimental method*

In order to validate the KFLA and evaluate its precision, a parallel rail platform (Fig. 4(a)) was set up to conduct experiments in Key Laboratory of Key Technology for South Agricultural Machine and Equipment, Ministry of Education, South China Agricultural University. The TOPCON RL-H4C

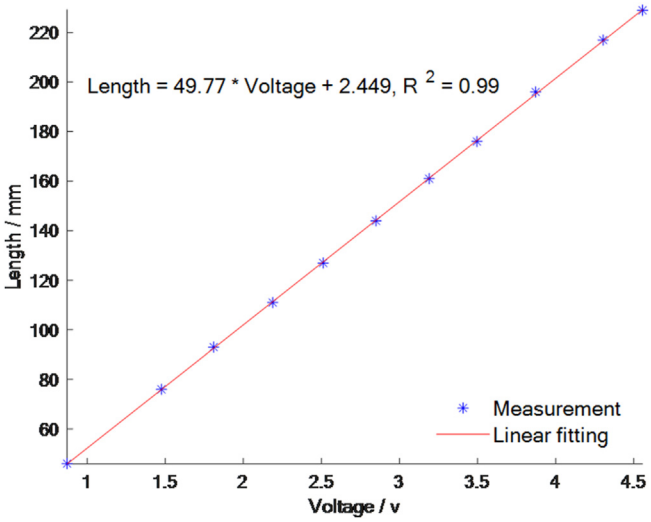

Fig. 5 – Calibration of the linear motion transducer (LMT).

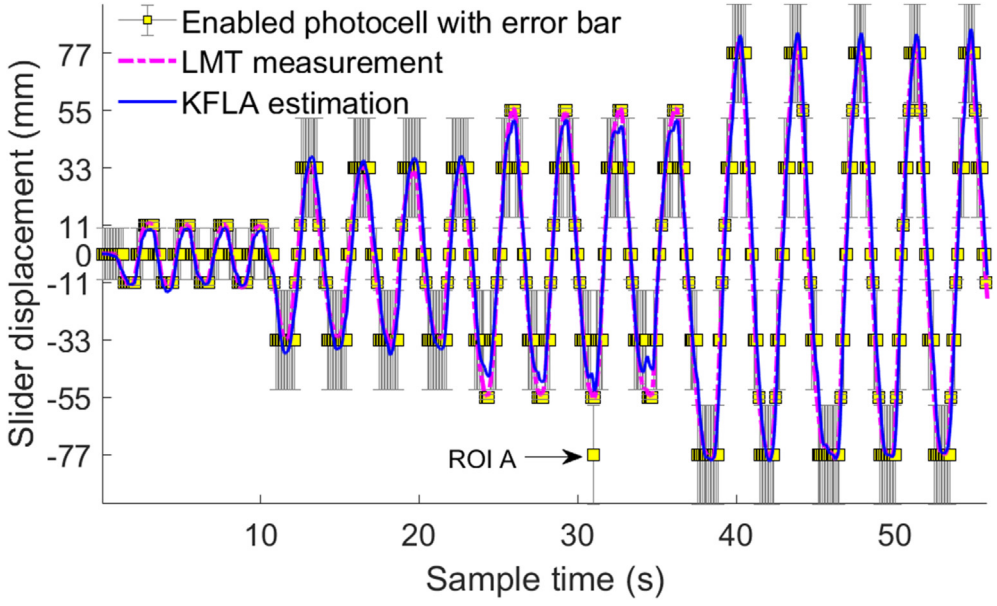

Fig. 6 – Laboratory results of displacement estimation (range of motion: -77 – 77 mm).

laser transmitter (Topcon Corporation, Japan (www.topcon.co.jp)) was selected to provide the laser-scanning plane. The effective range of the laser transmitter is 800 m. The laser head can be self-levelled within ±5° and rotates at a speed of 600 rpm; i.e., the data update frequency of the laser receiver is 10 Hz. A linear motion transducer (LMT) (WXXY MILLAY, WXXY15M-400-R, 0–300 mm, linearity 0.05%) was used to measure the real-time height of the laser receiver, whose readings was regard as the actual displacement of the receiver movement. We calibrated the LMT with a ruler (1 mm) and the voltage-displacement relationship can be expressed as Length = 49.77 × Voltage + 2.449 (Fig. 5). The MicroAutoBox II ds1401/1513/1514 produced by dSPACE was used as the sensor data processing and computing platform. The MicroAutoBox communicates with the host computer (Lenovo X220, CORE i5, 8G) via peripheral high-speed bus (PHS), and the development environment is Matlab 2016b. The laser receiver and the AHRS communicate with MicroAutoBox via CAN bus and RS-232, respectively. The signal type of the LMT is analogue voltage, which can be sampled by the analogue-to-digital converter (ADC) of the MicroAutoBox. GWINSTEK DC regulated power supply (SPD-3606, 0–36 V, 0–6 A, ≤3mARMS) was used to power both the MicroAutoBox and the auxiliary equipment. The hardware connection mode is illustrated in Fig. 4(b).

The laser transmitter was set at a distance of 5 m in front of the laser receiver. We then turned on the laser transmitter and waited for the laser head to self-level and start rotating. Then, we aligned the PA2 to the laser-scanning plane; thus, the initial state vector value is expressed as follows:

$$x_0 = \begin{bmatrix} S_0 \\ \dot{S}_0 \end{bmatrix} = \begin{bmatrix} 0 \\ 0 \end{bmatrix} \tag{8}$$

We manually pushed and pulled the handle to make the laser receiver alternately accelerate and decelerate on the

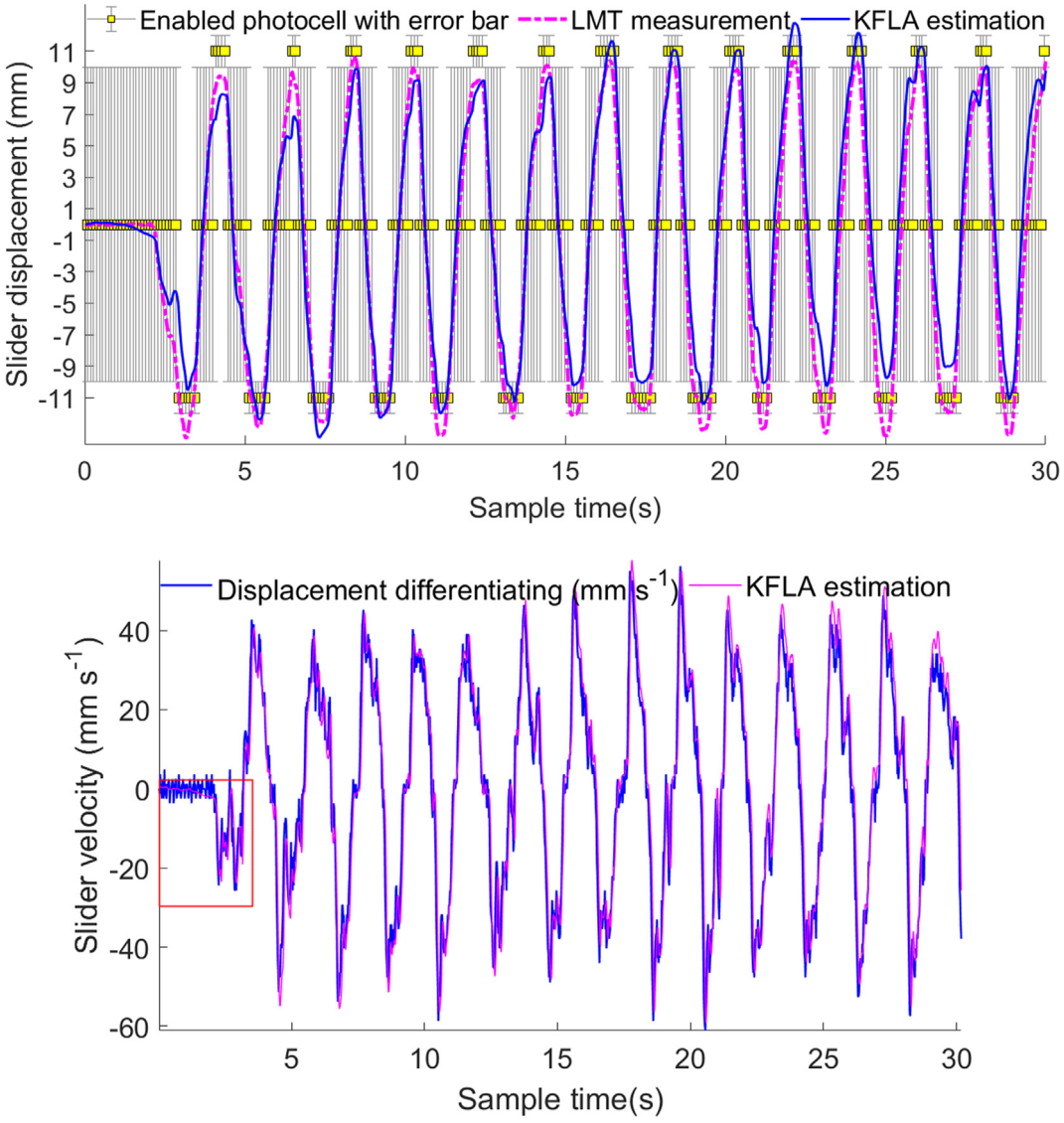

Fig. 7 – Laboratory results of motion estimation (range of motion: -11 – 11 mm). (a) Result of displacement estimation. (b) Result of velocity estimation.

guide rail. dSPACE synchronously read (50 Hz) the height level message transmitted by the receiver to the CAN bus, the AHRS z-axis free acceleration, and the LMT voltage. At the same time, MicroAutoBox fused the sensors online and output the KFLA estimations of the laser receiver's kinematic states. During the experiment, we prevented the slider from colliding with the limit stop to avoid introducing external acceleration caused by the collision into the state calculation.

2.4.2. *Field trial method*

In order to examine the performance of the KFLA in dynamic scenarios, the system described in Section 2 was installed on a paddy field laser levelling machine powered by a Kubota rice transplanter: the laser receiver was installed on the upper part of the lifting mast, and the AHRS was installed on the lower part of the lifting mast (Fig. 8). The experiment was conducted in Zengcheng Teaching and Research Base, South China Agricultural University. The size of the selected field was 100 m × 30 m (Fig. 9(a)). The soil of the field was compacted and covered with weeds. A small part of the field is muddy due to incomplete drying. There were several wheel ruts distributed along the longitudinal direction and two artificially excavated drainage ditches with a width of 30 cm and a depth of 20 cm in the transverse direction (Fig. 9(b)).

The experimental steps can be listed as follows: 1) Set up and turn on the laser transmitter, lift the scraper about 30 cm off the ground, and fix the height to prevent the scraper from being damaged during the travel; 2) adjust the lifting mast so

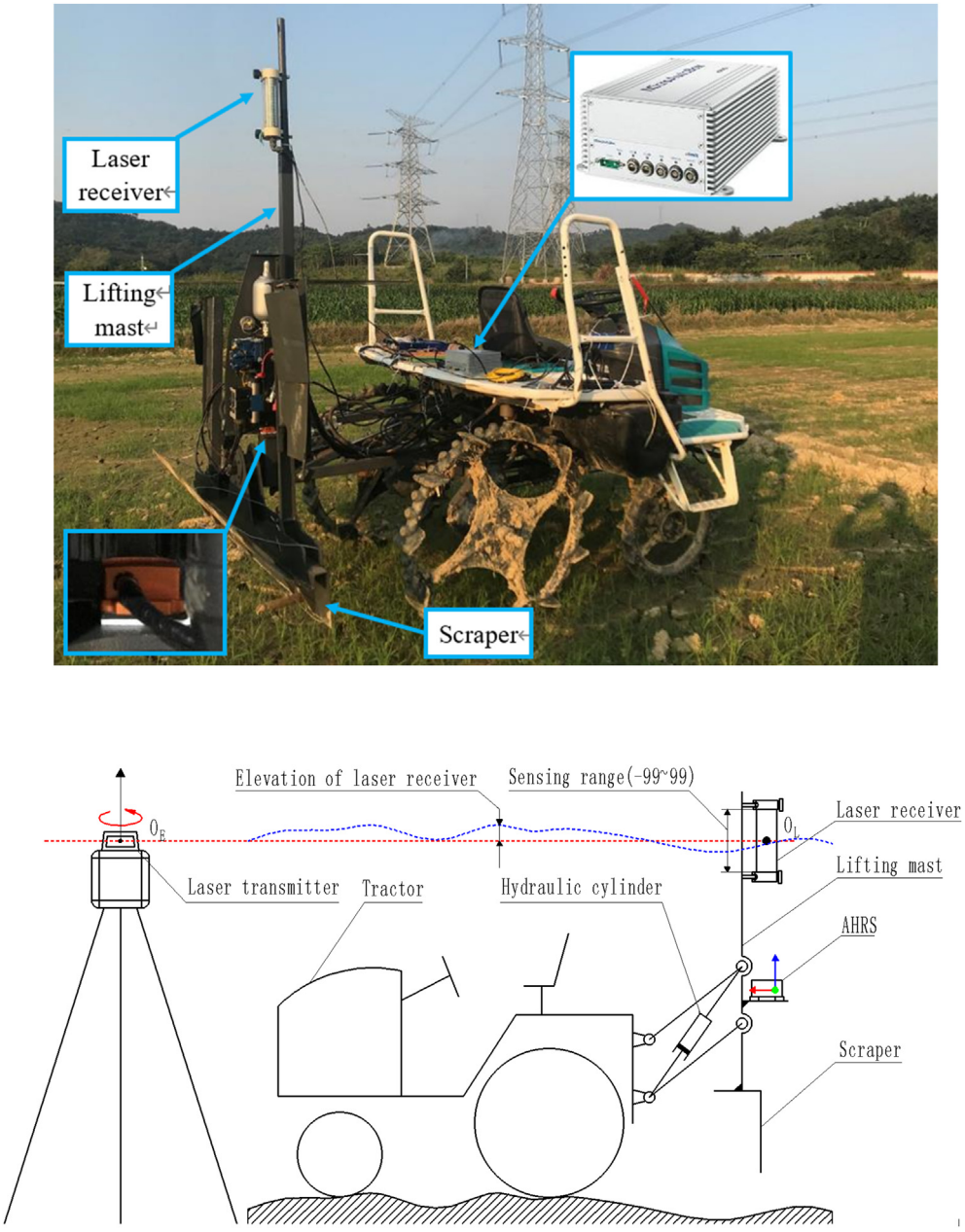

Fig. 8 – Principle of field experiment. (a) Experiment platform: levelling machine. (b) Levelling machine equipped with KFLA system.

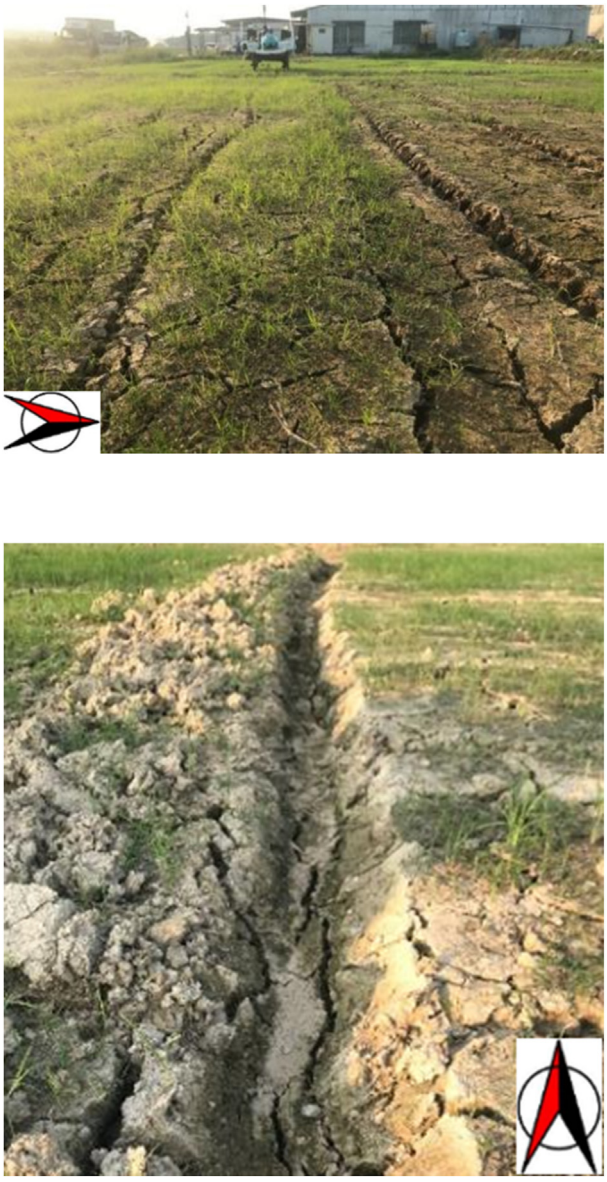

Fig. 9 – Field condition for experiment. (a) Overall condition. (b) Drainage ditch.

that the PA2 photocell can be aligned to the laser beam emitted from the laser transmitter; 3) drive the leveller machine in the field at a working speed of 1 m s^{-1}. The MicroAutoBox records the KFLA estimation (vertical distance between point O_L and O_E in Fig. 8(b)) as well as the height level indicated by the laser receiver.

3. Results and discussion

3.1. *Accuracy of the KFLA methodology*

After the experiment was completed, the KFLA results were compared with the actual displacement measured by the LMT (Fig. 6). Figure 6 shows that the actual displacement of the receiver acquired by the LMT passes through the bars represented by the height level and corresponding deviation, indicating that the photocell set is effective in displacement measurements but has insufficient precision. The KFLA could track the actual displacement curve of the receiver measured by the LMT, and four kinematic states were recursively acquired between every two height levels indicated by the photocell set, thus increasing the height measurement frequency from 10 Hz to 50 Hz. The MAE of the receiver displacement estimated by the KFLA was 14.6 mm, and the RMSE was 5.6 mm. The accuracy was higher than the height level indicated by the photocell set. The ROI A (Range of Interest, ROI) showed that when the laser beam moved from PA2

to PA3, although the height level jumped from −55 to −77, the KFLA could continuously and precisely track the motion of the laser receiver.

In the practical application of the implement height measurement, more attention is paid to the sensing accuracy near the target value. Therefore, another experiment was conducted to push-and-pull the handles between ±11 mm to drive the receiver back and forth for verifying the accuracy of the KFLA's estimation. The results are displayed in Fig. 7(a). The MAE value was 5.7 mm, and RMSE was 1.9 mm. According to the design of the state variables, the KFLA output also includes the receiver's velocity; thus, the first-order difference of the displacement value measured by the LMT was used as a reference to compare the receiver's motion speed. The KFLA output and displacement difference curves are shown in magenta and blue, respectively, in Fig. 7(b). The KFLA estimation of the receiver velocity well tracks the variations of the reference curve. The enlarged view in Fig. 7(b) shows that the process of the KFLA estimation is smoother.

Velocity information of working implement is indispensable to many kinds of control laws, like to proportional–integral–difference (PID) or fuzzy control. The KFLA can provide an optimal estimation of the receiver's velocity, thereby expanding the selectivity of the related control algorithms. In the process of validation, the error was analyzed based on the metric provided by the LMT measurements. However, due to the objective existence of non-linearity, installation error, and calibration error, there are a few differences between the measurements and actual values. Particularly, when the displacement difference was taken as a reference for the actual velocity of the receiver, the system error and measurement noise were amplified, which made the displacement difference no longer suitable as a reference for the quantitative analysis of velocity. Therefore, only a quali-

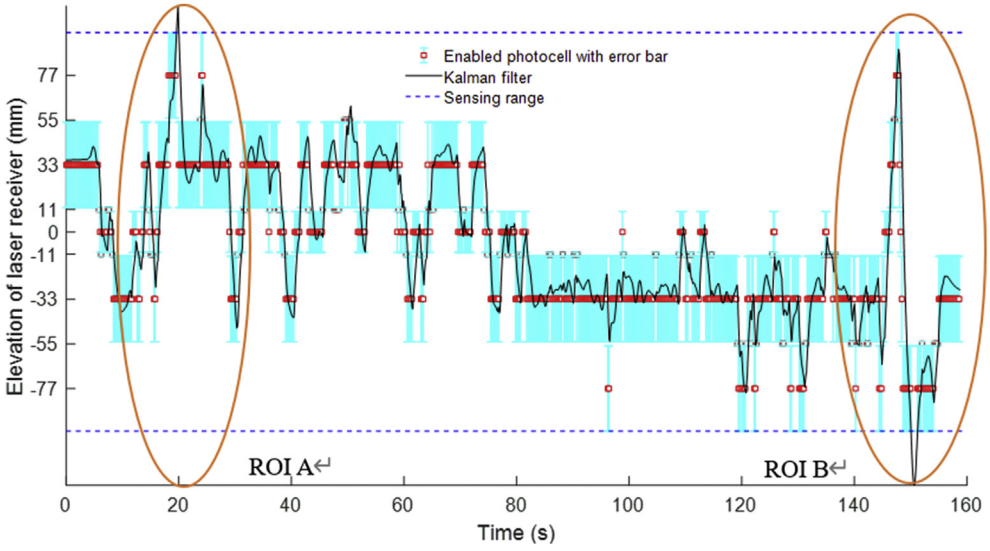

Fig. 10 – Field experiment result of elevation estimation.

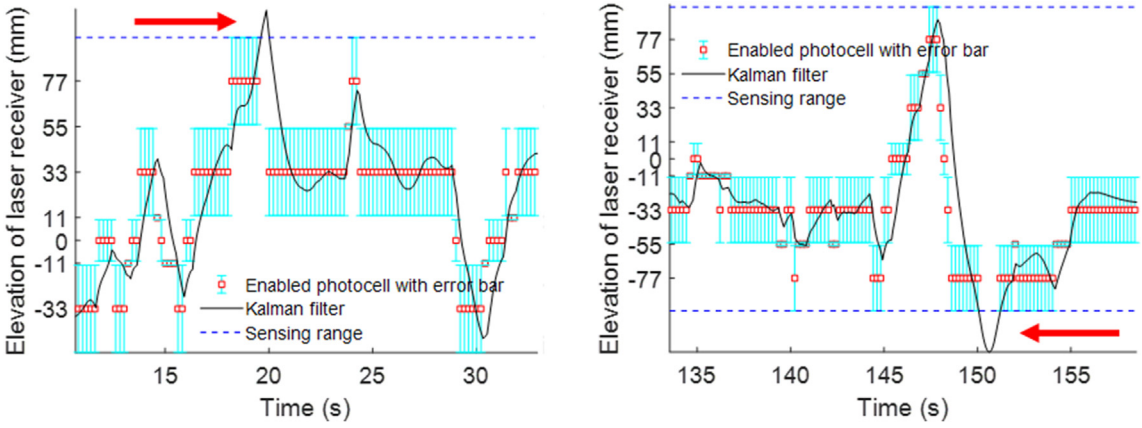

Fig. 11 – Enlarged view of ROI A and ROI B. (a) ROI A. (b) ROI B.

tative analysis of the velocity estimation process was performed. Thus, a more advanced velocity measuring technique or device should be applied to assess the precision and accuracy of the velocity estimated by the KFLA in follow-up studies.

3.2. *Field validation and performance of the KFLA methodology*

The comparative analysis results are displayed in Fig. 10. Figure 10 shows that in the process of the levelling machine's contouring motion on the field surface, the photocell set discretely indicates the level of the scraper height, while the KFLA is able to estimate the kinematic states of the scraper continuously. While the levelling machine was travelling across the ditch shown in Fig. 9(b), the front wheels fell into the ditch first. At the same time, the machine's pitch angle suddenly turned into negative, and the scraper rose to a certain height. Similarly, while the rear wheels were entering the ditch, the pitch angle of the vehicle became positive, causing the scraper to descend suddenly. Figure 11(a,(b) are partially enlarged views of ROI A and ROI B in Fig. 10, respectively. While the vehicle was travelling through the ditch, the mast height abruptly exceeded the receiver's effective sensing range. The KFLA used the equation of state to recursively calculate the real-time height of the scraper when the mast moved beyond the sensing range of the laser receiver and no observation data were acquired, which would provide reliable sensing information for the continuous control of the implement.

4. Conclusions

In this study, a Kalman Filter based method (KFLA) was proposed to fuse the laser receiver's height level indicated by the photocell set and the receiver's acceleration to obtain a real-time estimation of the 2D state vector composed of implement's displacement and velocity.

Laboratory results of accuracy evaluation regarding to displacement estimation showed that, for motion within ±77 mm, the MAE was 14.6 mm and RMSE was 5.6 mm; for motion within ±11 mm, the MAE was 5.7 mm and RMSE was 1.9 mm. Meanwhile, results of velocity estimation were tally with the reference curve but smoother. Field trial performed to validate the KFLA performance under dynamic condition showed that the KFLA was able to estimate the vertical kinematic states even if the scraper motioned out of the laser receiver's sensing range.

Overall, options for control laws on implement position can be increased as the proposed KFLA not only improves measurement precision of laser receiver up to sub-centimetre level but also achieves the optimal estimation of velocity. Additionally, compared with other non-contact distance sensors such as GNSS, LiDAR, Ultrasonic, the KFLA has the advantages of static zero position (measurement reference), robust signal, and low cost. It can be used both indoor and outdoor, in dry land or complex paddy field, which has great potential for application in agricultural and constructional engineering.

Declaration of competing interest

The authors declare that they have no known competing financial interests or personal relationships that could have appeared to influence the work reported in this paper.

Acknowledgements

This research is funded by the National Key Research and Development Program of China (No. 2016YFD0700301); the Key Research and Development Program of Guangdong Province of China (No. 2019B020224001); and supported by the Graduate Student Domestic Study Program from South China Agricultural University, China (No. CX2019N008). We also thank the anonymous reviewers for their critical comments and suggestions for improving the manuscript.

REFERENCES

Akhlaghi, S., Zhou, N., & Huang, Z. (2017). *Adaptive adjustment of noise covariance in Kalman filter for dynamic state estimation.* Chicago, IL, USA: IEEE Power & Energy Society General Meeting.

Andrade-Sanchez, P., Upadhyaya, S. K., Plouffe, C., & Poutre, B. (2008). Development and field evaluation of a field-ready soil compaction profile sensor for real-time applications. *Applied Engineering in Agriculture, 24*(6), 743–750.

Chang, Y. K., Zaman, Q. U., Rehman, T. U., Farooque, A. A., Esau, T., & Jameel, M. W. (2017). A real-time ultrasonic system to measure wild blueberry plant height during harvesting. *Biosystems Engineering, 157*, 35–44.

Cui, L. F., Xue, X. Y., Ding, S. M., & Le, F. X. (2019). Development of a DSP-based electronic control system for the active spray boom suspension. *Computers and Electronics in Agriculture, 166*, 105024.

Fountas, S., Paraforos, D., Cavalaris, C., Karamoutis, C., Gemtos, T. A., Abu-Khalaf, N., & Tagarakis, A. (2013). A five-point penetrometer with GPS for measuring soil compaction variability. *Computers and Electronics in Agriculture, 96*, 109–116.

Gonzalez-de-Soto, M., Emmi, L., Perez-Ruiz, M., Aguera, J., & Gonzalez-de-Santos, P. (2016). Autonomous systems for precise spraying - evaluation of a robotised patch sprayer. *Biosystems Engineering, 146*, 165–182.

Hu, L., Xu, Y., He, J., Du, P., Zhao, R., & Luo, X. (2019a). Design and test of tractor-attached laser-controlled rotary scraper land leveller for paddy fields. *Journal of Irrigation and Drainage Engineering*. https://doi.org/10.1061/(ASCE)IR.1943-4774.0001448. Manuscript accepted for publication.

Hu, L., Yang, W., He, J., Zhou, H., Zhang, Z., Luo, X., Zhao, R., Tang, L., & Du, P. (2019b). Roll angle estimation using low cost MEMS sensors for paddy field machine. *Computers and Electronics in Agriculture, 158*, 183–188.

İrsel, G., & Altinbalik, M. T. (2018). Adaptation of tilt adjustment and tracking force automation system on a laser-controlled land leveling machine. *Computers and Electronics in Agriculture, 150*, 374–386.

Ke, X., & Luo, X. (2014). Optimization design of laser receiver amplification circuit of laser leveler for paddy field. *Nongye Gongcheng Xuebao/Transactions of the Chinese Society of Agricultural Engineering, 30*(14), 1–7.

Leica. (2019). Rugby 320 SG & 410/420 DG. Retrieved from https://abtech.cc/wp-content/uploads/2018/03/Leica_Rugby_320_410_420_BRO.pdf.

Nielsen, S. K., Munkholm, L. J., Lamandé, M., Nørremark, M., Edwards, G. T. C., & Green, O. (2018). Seed drill depth control system for precision seeding. *Computers and Electronics in Agriculture, 144*, 174–180.

Nielsen, S. K., Munkholm, L. J., Lamandé, M., Nørremark, M., Skou-Nielsen, N., Edwards, G. T. C., & Green, O. (2017). Seed drill instrumentation for spatial coulter depth measurements. *Computers and Electronics in Agriculture, 141*, 207–214.

Rovira-Más, F., Chatterjee, I., & Sáiz-Rubio, V. (2015). The role of GNSS in the navigation strategies of cost-effective agricultural robots. *Computers and Electronics in Agriculture, 112*, 172–183.

Sudduth, K. A., Chung, S., Andrade-Sanchez, P., & Upadhyaya, S. K. (2008). Field comparison of two prototype soil strength profile sensors. *Computers and Electronics in Agriculture, 61*(1), 20–31.

Tang, L., Hu, L., Zang, Y., Luo, X., Zhou, H., Zhao, R., & He, J. (2018). Method and experiment for height measurement of scraper with water surface as benchmark in paddy field. *Computers and Electronics in Agriculture, 152*, 198–205.

Wang, Z., Yang, J., Liu, P., Long, X., Li, H., & Wei, W. (2019). Development of an agricultural vehicle levelling system based on rapid active levelling. *Biosystems Engineering, 186*, 337–348.

Zhao, R., Hu, L., Luo, X., Zhou, H., Du, P., Tang, L., He, J., & Mao, T. (2019). A novel approach for describing and classifying the unevenness of the bottom layer of paddy fields. *Computers and Electronics in Agriculture, 162*, 552–560.

IOP Publishing

Smart Materials and Structures

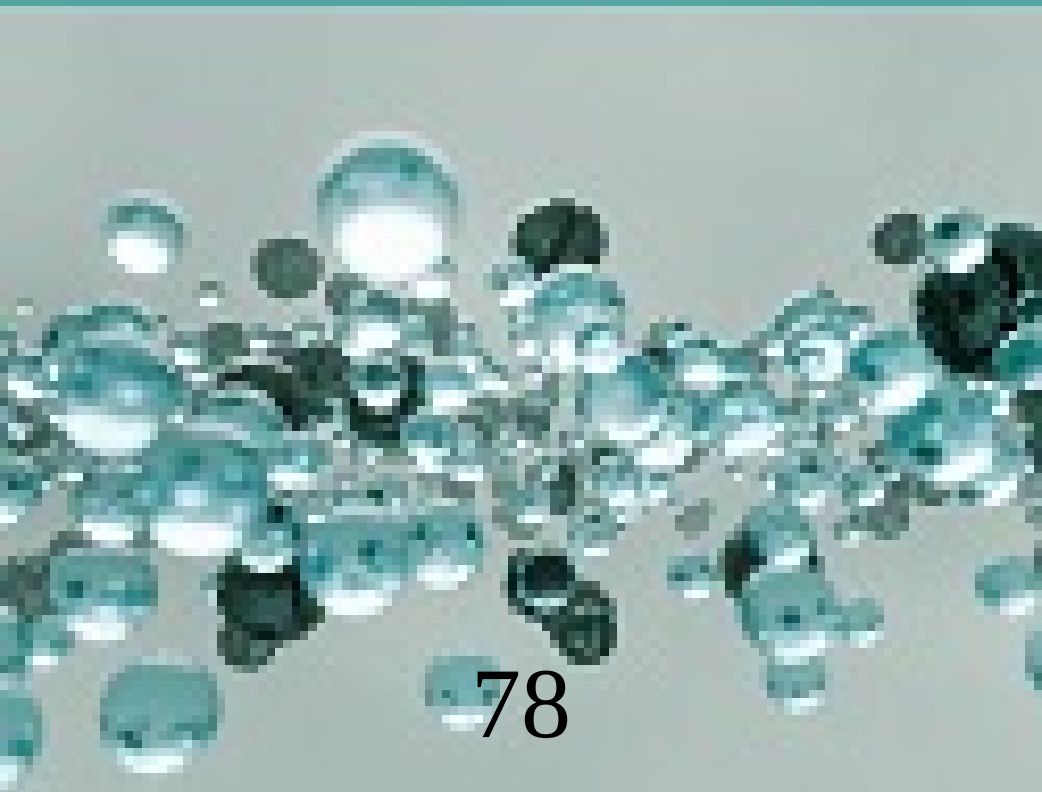

Table of contents for issue 3, volume 32, Smart Materials and Structures

Volume 32
Number 3, March 2023

← Previous issue Next issue →

Buy this issue in print

Open all abstracts

Letter

Pressure sensing of Ga_2O_3 thin film 03LT01
Zeng Liu, Shaohui Zhang, Maolin Zhang, Junpeng Fang, Ling Du, Jian Zhang, Chang Xu, Yufeng Guo and Weihua Tang
View article PDF Open abstract

Special Issue Articles

Damage identification of thin plate-like structures combining improved singular spectrum analysis and multiscale cross-sample entropy (SSA-MCSEn) 034001
Jiacheng Wang, Guangtao Lu, Huijun Song, Tao Wang and Dan Yang
View article PDF Open abstract

ResNet-integrated very early bolt looseness monitoring based on intrinsic feature extraction of percussion sounds 034002
Rui Yuan, Yong Lv, Shijie Xu, Li Li, Qingchao Kong and Gangbing Song
View article PDF Open abstract

OPEN ACCESS
Laboratory evaluation of climbing helmets: assessment of linear acceleration 034003
Mark Begonia, Bethany Rowson, Blake Sicilo and John Eric Goff
View article PDF Open abstract

Vibration acoustic modulation for bolt looseness monitoring based on frequency-swept excitation and bispectrum 034004
Nan Zhao, Huo Linsheng and Gangbing Song
View article PDF Open abstract

OPEN ACCESS
An audio-tactile interface based on dielectric elastomer actuators 034005
Sebastian Gratz-Kelly, Timi Krüger, Gianluca Rizzello, Stefan Seelecke and Giacomo Moretti
View article PDF Open abstract

OPEN ACCESS
3D printed negative stiffness meta-structures with superior energy absorption and super-elastic shape-recovery features 034006
M Hosseinabadi, E Etemadi, A Serjouei and M Bodaghi
View article PDF Open abstract

OPEN ACCESS
Insulated rail joint (IRJ) contact characterisation-an ultrasonic reflectometry approach for a cross-material interface 034007
Lu Zhou, Yun-Ke Luo and Roger Lewis
View article PDF Open abstract

Modeling and analysis of frequency-variable 2–2 cement-based piezoelectric transducers 034008
Chengming Lan, Lijie Wen, Jianjun Wang, Weijie Li and Lihua Tang
View article PDF Open abstract

Papers

A 3D re-entrant structural metamaterial with negative Poisson's ratio reinforced by adding arrow structures 035001
Jie Wang, Zongze Wu, Rui Xiao, Changyu Tang and Yangguang Xu
View article PDF Open abstract

Force and stability mechanism analysis of two types of nonlinear mono-stable and multi-stable piezoelectric energy harvesters using cantilever structure and magnetic interaction 035003
Shualing Sun, Yonggang Leng, Sunghoon Hur, Fei Sun, Xiaoyu Chen, Hyun-Cheol Song and Chong-Yun Kang
View article PDF Open abstract

Acoustic insulation characteristics improvement of a thick CNT-reinforced doubly-curved shell by using GPLRC and MEE composite layers 035004
M Ghasabi and R Talebitooti
View article PDF Open abstract

Piezoelectric performance of lead-free PDMS/CNT/$BaTiO_3$ piezocomposites with imperfect interphases and CNT agglomerations 035005
Francisco J Cañamero, Federico C Buroni, Ferri M H Aliabadi and Luis Rodríguez-Tembleque
View article PDF Open abstract

OPEN ACCESS
Manufacturing thin ionic polymer metal composite for sensing at the microscale 035006
Paul Motreuil Ragot, Andres Hunt, Leandro Nicolas Sacco, Pasqualina Maria Sarro and Massimo Mastrangeli
View article PDF Open abstract

Magnetorheological fluids subjected to non-uniform magnetic fields: experimental characterization 035007
Michal Kubík, Janusz Goldasz, Ondřej Macháček, Zbyněk Strecker and Bogdan Sapiński
View article PDF Open abstract

OPEN ACCESS
Novel polyhedral mechanical metamaterial exhibiting negative Poisson's ratio 035008
A Sorrentino and D Castagnetti
View article PDF Open abstract

A bistable energy harvester with low base-acceleration and high root mean square output for train bogies: theoretical modeling and experimental validation 035009
Dilong Tu, Yuan Zhang, Lei Zhu, Yong Qin, Yanping Du, Mengzhou Liu and Ao Ding
View article PDF Open abstract

Research on a percussion-based bolt looseness identification method based on phase feature and convolutional neural network 035010
Pengtao Liu, Xiaopeng Wang, Tianning Chen, Yongquan Wang, Feiran Mao and Wenhang Liu
View article PDF Open abstract

OPEN ACCESS
Design and experimental characterization of a bypass magnetorheological damper featuring variable stiffness and damping 035011
Moustafa Abdalaziz, Hossein Vatandoost, Ramin Sedaghati and Subhash Rakheja
View article PDF Open abstract

Linear flexible capacitive sensor with double helix structure based on multi-needle water-bath electrospinning technology 035012
Xiao Han, Mengjing Fan, Xinyan Yue, Xiaoman Zhao, Yongkun Liu, Jianhan Hong and Leigen Liu
View article PDF Open abstract

Research on fatigue crack quantitative monitoring based on eddy current sensor with an interactive induction coil layout 035013
Xianghong Fan, Yuting He and Tao Chen
View article PDF Open abstract

Multiple Tendon-inspired Sensors for Hand Motion Detection 035014
Jiyong Min, Taehun Choi and Youngsu Cha
View article PDF Open abstract

Using binary-stiffness beams within mechanical neural-network metamaterials to learn 035015
Jonathan B Hopkins, Ryan H Lee and Pietro Sainaghi
View article PDF Open abstract

OPEN ACCESS
A global-local damage localization and quantification approach in composite structures using ultrasonic guided waves and active infrared thermography 035016
Kaleeswaran Balasubramaniam, Shrinandu Sikdar, Dominika Ziaja, Michał Jurek, Rohan Soman and Paweł Malinowski
View article PDF Open abstract

A U-shaped and alternately driven ultrasonic motor using three bending coupled modes 035017
Dongmei Xu, Wenzhong Yang, Xuhui Zhang, Simiao Yu and Tenglin Liang
View article PDF Open abstract

Robustness analysis of magnetorheological elastomer-based vibration isolation system with optimal fuzzy controller 035018
Jie Fu, Jing Liu, Junjie Lai, Can Zhong, Zhenyu Dai and Miao Yu
View article PDF Open abstract

OPEN ACCESS
Numerical and experimental investigation of the energy harvesting performance of electromechanically coupled piezoelectric prestressed beams subjected to nonlinear vibrations 035019
I G C Kardatzalis, N A Chrysochoidis, D Varelis and D A Saravanos
View article PDF Open abstract

Resonant printing flexible piezoresistive pressure sensor with spherical microstructures 035020
Zhiheng Yu, Guohong Hu, Jian Chen, Fengli Huang, Yun Zhao and Jijun Feng
View article PDF Open abstract

3D printed multilayer dielectric elastomer actuators 035021
Sen Su, Tian He and Hui Yang
View article PDF Open abstract

Design and experiment of a new double needle type piezoelectric jetting dispenser 035022
Guimiao Zhao, Siyuan Lv, Gang Chen, Jianneng Chen, Qicheng Wang, Min Wu and Junjie Zheng
View article PDF Open abstract

Analysis modeling and experiment of bionic winding soft actuator inspired by plant tendrils 035023
Jian Li, Zhibo Luan, Yangwei Wang, Meizhen Huang, Jie Yan and Yuhan Wang
View article PDF Open abstract

Displacement sensing with quasi-zero stiffness structure and flexoelectricity 035024
Haoyu Gu, Hui Ji, Shuwen Zhang, Chongqu Zhai and Mingliang Xu
View article PDF Open abstract

Structural health dynamic monitoring for gear transmission based on guided waves 035025
Yuan Chai, Xihua Wang, Qingyu Lu and Yulin Ding
Ashok Kumar Kargaralur, Shubham Kadam, Hemantha Kumar and M Arun
View article PDF Open abstract

OPEN ACCESS
Development and prototyping of SMA-metamaterial biaxial composite actuators 035027
Luke Mizzi, Seyedeh Farzaneh Hoseini, Marco Formigheri and Andrea Spaggiari
View article PDF Open abstract

OPEN ACCESS
Model-based investigations of ferroelectric energy harvesting with regard to an improvement of life span and operability 035028
Andreas Warkentin, Lennart Behlen and Andreas Ricoeur
View article PDF Open abstract

Active signal-generating spacer-fabric-type continuous touch/pressure sensor 035029
Kazuki Tonomura, Annie Yu and Yuya Ishii
View article PDF Open abstract

A thermo-viscoelastic constitutive model addressing the cyclic shape memory effect for thermo-induced shape memory polymers 035030
Jian Li, Zhihong Liang, Junjie Liu, Chao Yu, Xuelian Zhang and Qianhua Kan
View article PDF Open abstract

Study on new magnetorheological chemical polishing process for GaN crystals: polishing solution composition, process parameters, and roughness prediction model 035031
Jinzhong Wu, Burhan Afzal, Zhilong Huang, Maoju Yang and Shuaishuai Sun
View article PDF Open abstract

Preparation and processing performance of high steady-state magnetorheological finishing fluid 035032
Zhuoshan Shen, Jisheng Pan, Jianwen Zhang and Qiusheng Yan
View article PDF Open abstract

On the characterization of the compressive response of shape memory alloys using bending 035033
Yadollah Mohammad Hashemi, Mahmoud Kadkhodaei, Emanuele Sgambitterra and Carmine Maletta
View article PDF Open abstract

Low-power vibrothermography detection technique for surface cracks on composite sucker rod 035034
Pengqian Liu, Changhang Xu, Yubin Zhang, Yi Qin, Yinsheng Xu, Jing Xie and Gangbing Song
View article PDF Open abstract

Measurements for static shape control optimization of silicon mirror using nonlinear piezoceramic actuators 035035
Sumit, S R Kane, Tapas Ganguli and Rahul Shukla
View article PDF Open abstract

PEDOT/CNT/Bi_2Te_3 coated porous thermoelectric yarns for textile based wearable thermoelectric generator 035036
Ding Ding, Qian Wu, Yinan Gao, Jinmei Wang, Yinan Chen and Qian Li
View article PDF Open abstract

Lignin precipitation-driven fabrication of gradient porous hydrogel actuator with temperature response 035037
Ying Chen, Feipei Kuang, Xiaochen Shen, Xiaowei Lv, Yushu Wang, Weihan Yin, Tongqing Zou, Ben Wang, Yupeng Liu and Quli Fan
View article PDF Open abstract

Damage monitoring of the planting balcony in vertical greenery buildings using the EMI method 035038
Ying Li, Mingkang Wei and Xiaobin Hu
View article PDF Open abstract

Probabilistic seismic assessment of innovative concrete bridge piers with Engineered Cementitious Composites (ECC) by different types of shape memory alloys (SMAs) bars 035039
Amirmozafar Bensharis, Farzad Hatami and Meisbah Saybani
View article PDF Open abstract

OPEN ACCESS
Design and analysis of a d15 mode piezoelectric energy generator using friction-induced vibration 035040
Yu Xiao, Sviatoslav Karnaoukh and Nan Wu
View article PDF Open abstract

Investigation on recovery stress and stability of hot-drawn $Ni_{47}Ti_{44}Nb_9$ SMA 035041
Shengshan Pan, Dong Yan, Xue Zhang, Cunyu Zou, Yuanmeng Chen, Huaxing Hu, Sile Chen and Bassem Andraws
View article PDF Open abstract

Effect of a V-shaped groove on the performance of a circular-cylinder energy harvester 035042
Thannit Sritham and Chawalit Kitichaikarn
View article PDF Open abstract

Design and experiment of a new double needle type piezoelectric jetting dispenser

IOP Publishing Smart Materials and Structures
Smart Mater. Struct. **32** (2023) 035022 (11pp) https://doi.org/10.1088/1361-665X/acb745

Design and experiment of a new double needle type piezoelectric jetting dispenser

Runmao Zhao[1,2], Siyuan Lv[1], Gang Chen[1], Jianneng Chen[1,2,*], Qicheng Wang[1], Min Wu[3] and Junjie Zheng[1]

[1] School of Mechanical Engineering and Automation, Zhejiang Sci-Tech University, Hangzhou 310018, People's Republic of China
[2] Key Laboratory of Transplanting Equipment and Technology of Zhejiang Province, Hangzhou 310018, People's Republic of China
[3] School of Transportation, Zhejiang Industry Polytechnic College, Shaoxing 312000, People's Republic of China

E-mail: jiannengchen@zstu.edu.cn

Received 30 August 2022, revised 18 November 2022
Accepted for publication 30 January 2023
Published 9 February 2023

Abstract

To improve the performance of piezoelectric (PZT) jetting dispensers in the electronic packaging industry and address the problems of oversized, easily fatigued elastic hinges and low repetition accuracy of conventional PZT jetting dispensers with a compliant mechanism-based lever, a new double needle PZT jetting dispenser prototype was developed. The advantage of the proposed structure over compliant mechanism-based lever was demonstrated by dynamics analysis. Firstly, the design stroke of the needle and the modal state of the dispenser body were analyzed using ANSYS. Secondly, the theoretical model of adhesive injection was established, the fluid pressure change process inside the nozzle during the working cycle of the jetting dispenser was simulated using Fluent, and the effects of the supply pressure and needle stroke on the injection speed of the droplet were investigated. Finally, a test bench was built to conduct the experiment, and the results showed that the supply pressure and the driving signal duty cycle between 20% and 80% were positively correlated with the size of droplet diameter, whereas the driving signal frequency was negatively correlated with the droplet diameter, thereby validating the proposed adhesive injection model. Under the experimental conditions, the highest operating frequency of the designed PZT jetting dispenser was 400 Hz, which is close to the high-frequency level of existing studies, and the minimum droplet diameter obtained was 0.36 mm, which is 0.1–0.2 mm less than that of the existing PZT jetting dispenser with a compliant mechanism drive, meeting the industry requirements for the working performance of a PZT jetting dispenser.

Keywords: piezoelectric stack, jetting dispenser, double needle, physical design, performance analysis

(Some figures may appear in colour only in the online journal)

* Author to whom any correspondence should be addressed.

1. Introduction

The jetting dispenser [1, 2] is a device used for the precise quantitative distribution of adhesives. It can inject the adhesive onto any specified position on the workpiece according to the required diameter or volume to realize the bonding between structural parts. It is widely used in electronics packaging [3], LED manufacturing [4], medicine [5], and other industries. The main driving methods of the jetting dispenser include piezoelectric (PZT) stack drive [6, 7], pneumatic drive [8], and electromagnetic drive [9]. The PZT stack drive is the most common among the three because of its large output force, high-frequency response, and linear controllability. However, limited by the packaging size, the PZT stack has a small stroke and cannot meet the minimum displacement required for the movement of the jetting dispenser. Therefore, mechanisms need to be designed to transmit and amplify the PZT stack's actuation. At present, most of the transmission is realized using an elastic-compliant mechanism. Wang *et al* [10] designed a jetting dispenser that used a triangular structure to amplify displacement, injecting droplets as small as 1.07 mm. Jeon *et al* [11] used elastic linear levers to amplify displacement. Hu *et al* [12] designed a bridge-type compliant structure with a linear lever for transmission, reaching an operating frequency of up to 250 Hz. Moreover, other compliant mechanisms exist, such as rhombus [13] and nested rhombus [14]. The compliant mechanisms used in these studies use the deformation of elastic materials to realize the transmission of motion from the PZT stack to the needle. This structure requires the needle to be fixed and connected with the compliant mechanism to achieve a reset. In this way, as the needle rotates around the rotating pair of the transmission mechanism, component forces in both axial and radial directions will be generated, as shown in figure 1(a). Axial force effectively drives the needle to achieve adhesive jetting, whereas radial force accelerates the friction between the needle and the sealing assembly, reducing the life of oil sealings. For this reason, Deng *et al* [15] designed a pin joint to coordinate radial motion. However, the elastic rotating pair of the compliant mechanism was easily fatigued, which would affect the repeatability of elastic deformation, and even lead to the failure of the jetting operation, such as jet-flow [16] and satellite drops [17, 18].

This study focuses on developing a new type of transmission mechanism for the jetting dispenser to avoid the problems mentioned above. It improves the transmission of the driving force and the amplification of displacement. Its advantages include easy replacement of seals and adjustable displacement of the needle. The remainder of this paper is organized as follows. Section 2 presents the calibration of the stroke and vibration effects of the designed jetting dispenser via theoretical analysis and ANSYS simulations. Section 3 discusses a fluid dynamics model of adhesive injection in the nozzle as well as a Fluent simulation of the adhesive injection process. The factors that introduce additional cost or difficulty in the experimental testing of adhesive injection are also discussed. Section 4 describes the fabrication of a prototype jetting dispenser and the development of a test platform. The experimental analysis tested the influence of the electrical control parameters such as the supply pressure, driving signal frequency, and driving signal duty cycle on the diameter of the adhesive droplets and verified the working performance of the designed double needle jetting dispenser.

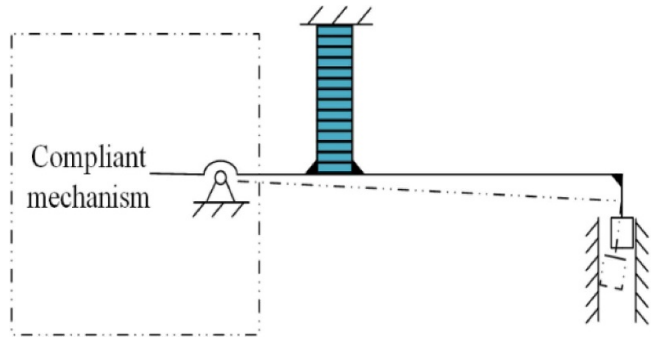

(a) compliant mechanism-based transmission lever

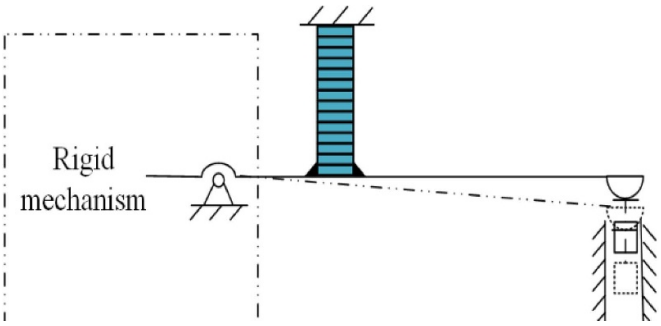

(b) rigid mechanism-based transmission lever

Figure 1. Schematic diagram of two transmission structures.

2. Structure design and working principle of jetting dispenser

2.1. Dynamic performance comparison of two transmission structures

The PZT stack is simplified as a spring system, and the load (needle and spring) is simplified as a spring damping system, as shown in figure 2. The dynamic models of the needle based on rigid mechanism-based transmission lever and compliant mechanism-based transmission lever are established respectively, and their dynamic characteristics are compared.

Dynamic equation with PZT stack as research object is built as equation (1):

$$m_{pt}\ddot{x}_{pt} + k_{pt}x_{pt} = F_{pt} - F_1, \tag{1}$$

where, m_{pt} is the mass of the PZT, kg; k_{pt} is the stiffness of the PZT, N m^{-1}; x_{pt} is the displacement of the PZT, m; F_{pt} is the output force of the PZT, N; F_1 is the force of the PZT on transmission lever, N.

Dynamic equation with load (needle and spring) as research object is built as equation (2):

$$m_s\ddot{x}_s + \mu\dot{x}_s + k_s x_s = F_2, \tag{2}$$

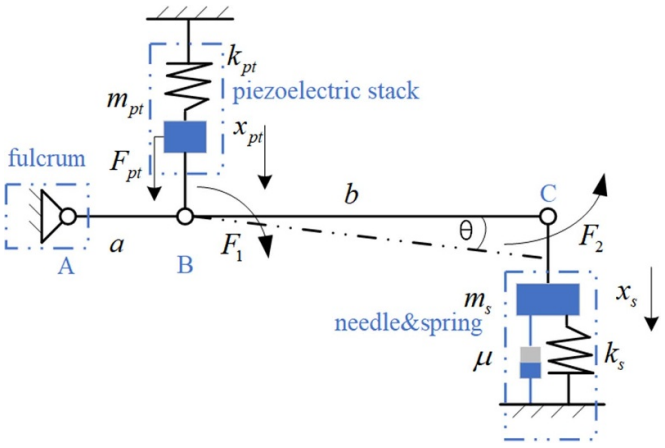

Figure 2. Dynamics model of piezoelectric jetting dispenser.

where, m_s is the mass of the load, kg; x_s is the displacement of the load, m; k_s is the stiffness of the load, N m^{-1}; μ is the damp of the load; F_2 is the preload force of the spring on transmission lever, N.

The torque equilibrium equation is built for the transmission lever as equation (3):

$$F_1 \cdot a - F_2 \cdot (a+b) = 0, \tag{3}$$

where, a is the length of AB, m; b is the length of BC, m.

According to lever principle, equation (4):

$$\frac{x_{pt}}{x_s} = \frac{\dot{x}_{pt}}{\dot{x}_s} = \frac{a}{a+b}. \tag{4}$$

According to the output force of the PZT, equation (5):

$$F_{pt} = k_{pt}(d_{33} \cdot n \cdot u - x_{pt}), \tag{5}$$

where, d_{33} is the strain coefficient, (N m^{-1}); n is the number of PZT patch; u is working voltage, V.

F_1 can be solved according to equations (1) and (5):

$$F_1 = k_{pt}d_{33}nu - m_{pt}\ddot{x}_{pt} - k_{pt}x_{pt}. \tag{6}$$

Case I: rigid mechanism-based transmission lever

F_2 can be solved according to equations (2) and (4). Substitute F_1 and F_2 into equation (3):

$$m_{pt}\ddot{x}_{pt} + 2k_{pt}x_{pt} + \frac{a+b}{a}(m_s\ddot{x}_2 + \mu\dot{x}_2 + k_s x_2) = k_{pt}d_{33}nu. \tag{7}$$

Laplace transformation of equation (7):

$$(m_{pt}s^2 + 2k_{pt})X_1(s) + \frac{a+b}{a}(m_s s^2 + \mu s + k_s) \times X_2(s) = k_{pt}d_{33}nU(s). \tag{8}$$

Laplace transformation of equation (4):

$$X_1(s) = \frac{a+b}{a}X_2(s), \tag{9}$$

where, s is the operator of complex domain.

Substitute equation (9) into equation (8):

$$G_1(s) = \frac{X_2(s)}{U(s)} = \frac{b_0}{a_2 s^2 + a_1 s + a_0}, \tag{10}$$

where, $b_0 = k_{pt}d_{33}n$, $a_0 = \frac{2ak_{pt}}{a+b} + \frac{(a+b)k_s}{a}$, $a_1 = \frac{a+b}{a}\mu$, $a_2 = \frac{a}{a+b}m_{pt} + \frac{a+b}{a}m_s$.

Case II: compliant mechanism-based transmission lever.

The dynamic equation is built for the transmission lever as equation (11):

$$I\ddot{\theta} - F_1 a + F_2(a+b) = 0, \tag{11}$$

where, I is the moment of inertia of elastic material, m^4; $\ddot{\theta} = \frac{\ddot{x}_1}{a}$, is angular acceleration.

Substitute F_1 and F_2 into equation (11):

$$\left(m_{pt} + \frac{I^2}{a}\right)\ddot{x}_{pt} + 2k_{pt}x_{pt} + \frac{b}{a}(m_s\ddot{x}_2 + \mu\dot{x}_2 + k_s x_2) = k_{pt}d_{33}nu. \tag{12}$$

Laplace transformation of equation (12):

$$G_2(s) = \frac{X_2(s)}{U(s)} = \frac{b_0}{a_2 s^2 + a_1 s + a_0}, \tag{13}$$

where, $b_0 = k_{pt}d_{33}n$, $a_0 = \frac{2ak_{pt}}{a+b} + \frac{(a+b)k_s}{a}$, $a_1 = \frac{a+b}{a}\mu$, $a_2 = \frac{a}{a+b}m_{pt} + \frac{a+b}{a}m_s + \frac{I}{a(a+b)}$.

For the systems described by equations (10) and (13), the undamped natural frequency is $\omega_n = \sqrt{\frac{a_0}{a_2}}$, $\omega_{n1} > \omega_{n2}$. Therefore, under the same structural parameters, the rigid mechanism-based transmission lever has better high-frequency characteristic.

2.2. Physical design of jetting dispenser

Figure 3 shows a three-dimensional (3D) structural diagram, and table 1 lists the structural parameters of the designed PZT jetting dispenser. The parts of the device include dispenser body, PZT, preload screw, PZT upper cap, transmission lever (needle I), needle II, return spring, adjusting bolt, and nozzle assembly (nozzle, nozzle nut, and oil sealing). The two ends of the PZT are fixed with the ball head to prevent the PZT from bearing tangential force when used. The PZT upper cap was designed to fix and preload PZT. The two ball heads of the PZT are in contact with the spherical surfaces on the PZT upper cap and the transmission lever, respectively. The compression spring is fixed and connected to the needle II to realize the movement reset of the needle II, and the preload length of the spring can be changed by adjusting the bolt. The nozzle is fastened between the nozzle nut and the nozzle body, and its stroke relative to the nozzle can be changed by adjusting the nozzle nut.

During long-term use, the nozzle and the oil sealing are vulnerable to wear and failure. To facilitate replacement, the nozzle assembly is designed to be detachable and fixed to the dispenser body by screws. There is a gap between the nozzle body and the dispenser body. The heat released from the PZT is isolated from the adhesive, in case the property change of

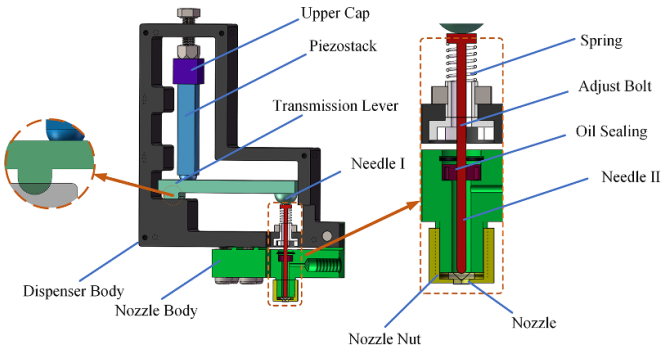

Figure 3. 3D design structure diagram of double needle jetting dispenser.

Table 1. Structural parameters of main parts of jetting dispenser.

Component	Parameter	Value
Piezoelectric stack	Width × length × height	7 × 7 × 36 mm
	Maximum displacement	38 μm
	Stiffness	49 N μm^{-1}
	Capacitance	7.2 μF
	Output force	1960 N
	Displacement from hinge to piezoelectric stack	4 mm
Lever	Displacement from hinge to needle	45.5 mm
	Thickness	5 mm
	Width	10 mm
Needle	Length	38.75 mm
	Diameter	1.5 mm
Nozzle	Diameter	0.2 mm
	Length	0.55 mm

the adhesive would affect the injection performance. Furthermore, it prevents the adhesive from leaking into the valve and causing pollution.

2.3. Working principle of jetting dispenser

Before the jetting dispenser works, preload the PZT stack with the preload screw according to equation (14):

$$T = 0.2Fd, \tag{14}$$

where, T is the required preload torque, N m^{-1}; F is the required preload force, N; d is the screw diameter, m.

In Phase I, initially, the PZT is not energized. Subsequently, under the action of adhesive supply pressure, the adhesive begins to enter the nozzle cavity, as shown in figure 4(a). In Phase II, PZT stretches after power-on, then drives the transmission lever to move the needle downward. In the nozzle, the adhesive is hit by the needle and gets kinetic energy to inject, as shown in figure 4(b). Under the driving signal, the PZT continuously elongates and recovers and drives the needle to move up and down to reach the continuous injection of adhesive.

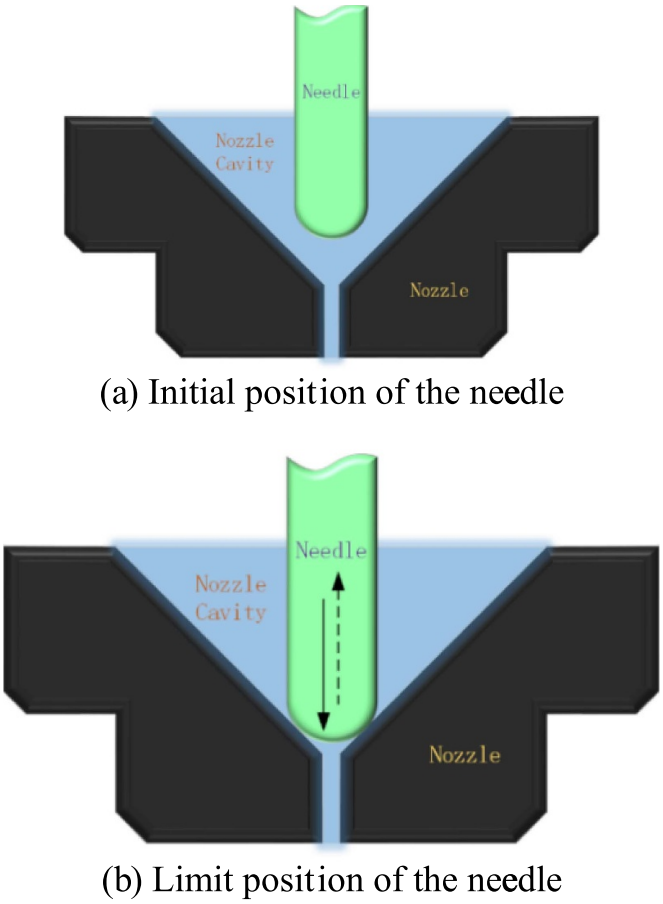

Figure 4. Working process of jetting dispenser.

2.4. Simulation analysis of transmission lever

The primary condition for the completion of work of the jetting dispenser is the reasonable displacement of the needle. If the needle displacement is too small, the injection kinetic energy of the adhesive in the nozzle cavity will be insufficient, and the droplet will be prone to sticking to the nozzle, which affects the dispensing quality. If the needle displacement is too large, the upper limit of the working frequency of the dispensing valve and the minimum volume of the adhesive drop will be limited. Therefore, the designed stroke is approximately 0.2–0.4 mm [19, 20]. To evaluate the influence of the preload on the output displacement of the PZT, first, we need to determine the structural parameters of the transmission lever. Next, analyze the high-frequency motion performance of the needle. And lastly, carry out kinematics simulation calculation in ANSYS. We need to import the needle and transmission mechanism models and the PZT and MEMS Body modules for the simulation. They can couple the structural and electric fields in the PZT material, which allows us to analyze the output displacement of the needle after preloading the PZT. The simulation model of the transmission link and needle is shown in figure 5(a), and the simulation material parameters are listed in table 2.

Simulation parameters are set according to table 2. The rotary pair is set between the lever and the body, and the ball

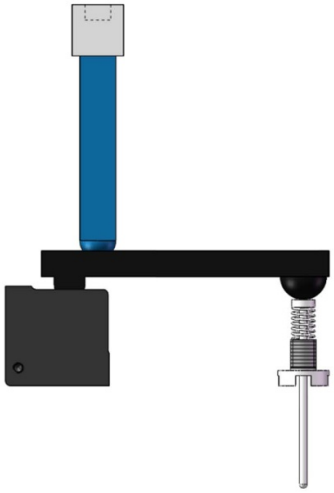

(a) Simulation model of transmission lever and needle

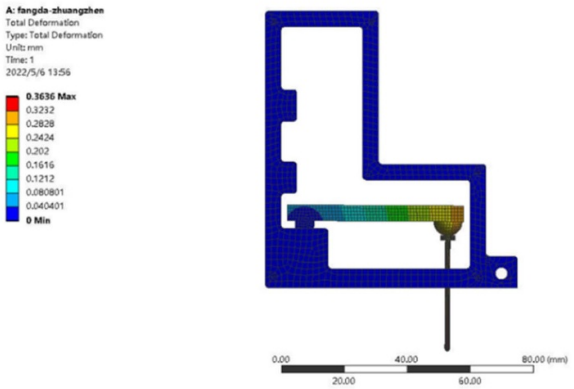

(b) Simulation results of transmission mechanism

Figure 5. Statics analysis of lever transmission mechanism.

head on the right side of the lever is in fixed contact with the needle. The drive displacement of 38 μm is input at the contact point between the PZT and the lever, and the output displacement of the striker is calculated to be 360 μm by simulation, as shown in figure 5(b). The leverage ratio is about 9.51. In the simulation process, the loading voltage of the PZT stack was gradually increased from 30 to 150 V, with an interval of 10 V. The output displacement of the needle is shown in figure 6. It can be seen that with the increase of the loading voltage, the output displacement of the needle increases from 84.6 to 386.2 μm. The results show that the output displacement of the PZT is directly related to the loading voltage. Therefore, when the magnification ratio of the transmission mechanism is 8–10 times, the designed needle stroke of 200–400 μm can be achieved. Using the current design mechanism, the loading voltage needs to be greater than 70 V, and the output displacement of the needle can reach 200 μm, which meets the basic displacement requirements of the adhesive injection. However, a larger loading voltage is likely to cause heat concentration of the PZT stack, which seriously impacts its lifespan. Therefore, the voltage of approximately 70–120 V is generally appropriate.

Table 2. Materials and physical properties of main simulation components of the injection valve.

Material	Parameter	Value	Components
Carbide	Density	7800 kg m^{-3}	Needle
	Poisson ratio	0.25	
	Young's modulus	5.7×10^{11} Pa	
	Bulk modulus	3.8×10^{11} Pa	
	Shear modulus	2.28×10^{10} Pa	
Steel	Density	7850 kg m^{-1}	Lever cap
	Poisson ratio	0.3	
	Young's modulus	2.0×10^{11} Pa	
	Bulk modulus	1.67×10^{11} Pa	
	Shear modulus	7.69×10^{10} Pa	
Ceramic (Coremorrow, DJF73601)	Density	3900 kg m^{-3}	Piezoelectric stack
	Poisson ratio	0.36	
	Young's modulus	5.5×10^{11} Pa	
	Bulk modulus	6.54×10^{11} Pa	
	Shear modulus	2.02×10^{11} Pa	

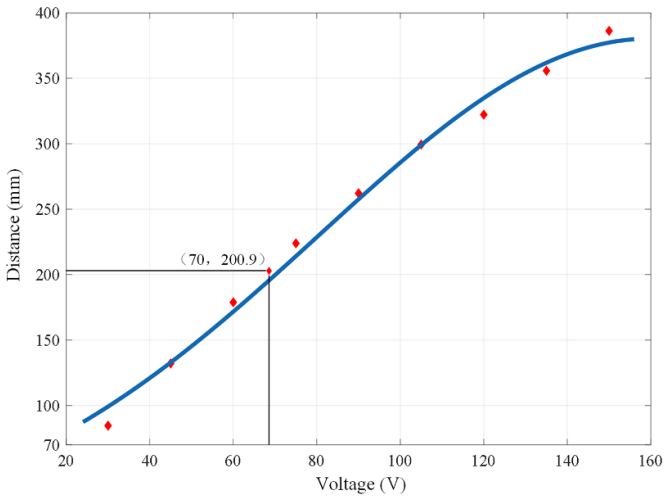

Figure 6. Output displacement of the needle under different loading voltages.

To avoid the structural resonance of the jetting dispenser under high-frequency working conditions, ANSYS is used to conduct a modal analysis of the structure. The side of the casing and the preload screw are set as fixed constraints, the transmission mechanism and the casing form a pair of rotating pairs, and the friction coefficient is set at 0.1. The first six modal mode shapes and resonance frequencies are obtained, as shown in figure 7.

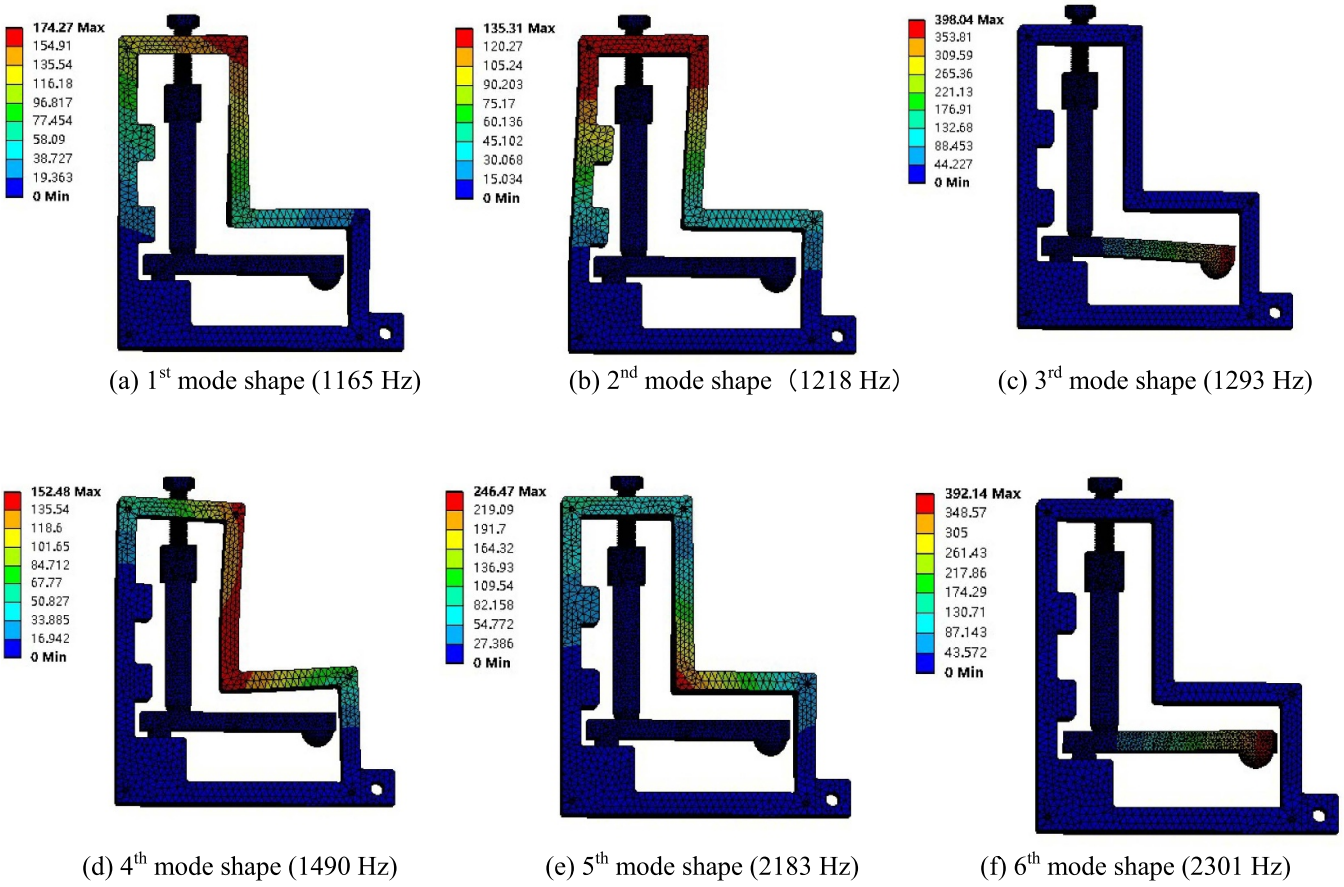

(a) 1st mode shape (1165 Hz) (b) 2nd mode shape (1218 Hz) (c) 3rd mode shape (1293 Hz)

(d) 4th mode shape (1490 Hz) (e) 5th mode shape (2183 Hz) (f) 6th mode shape (2301 Hz)

Figure 7. Modal analysis results of jetting dispenser structure.

3. Fluid dynamics analysis of injection process

3.1. Inject theoretical model

As shown in figure 8, if we take the circular with the inner radius of the nozzle as r, the length as d_y, and the thickness as d_z, then the coordinate system is established according to the distribution of adhesive in the nozzle cavity when the jetting dispenser is working.

According to Newton's second law, the force on the adhesive in the nozzle is:

$$2\pi r dr \cdot P - 2\pi r dr\left(P + \frac{\partial P}{\partial Z}dz\right) - 2\pi\left(r + dr\right)dz \left(\tau + \frac{\partial \tau}{\partial r}dr\right) + 2\pi r dz \cdot \tau + 2\pi r dr dz \cdot \rho g = 2\pi r dr dz \cdot \rho \cdot a \tag{15}$$

where ρ is the density of the circular adhesive (kg m^{-3}); a is the adhesive acceleration that is generated by the combined effect of gravity g, the transverse shear force τ on the circular ring, the pressure P on the upper surface of the ring and the pressure $P + \frac{\partial_p}{\partial_z}$ on the lower surface.

Suppose $\frac{d_w}{d_t}$ is used instead of the acceleration a, where w is the instantaneous velocity of the circular adhesive (the nozzle area is fixed and only varies in Z direction) equation (15) can be converted to the following form:

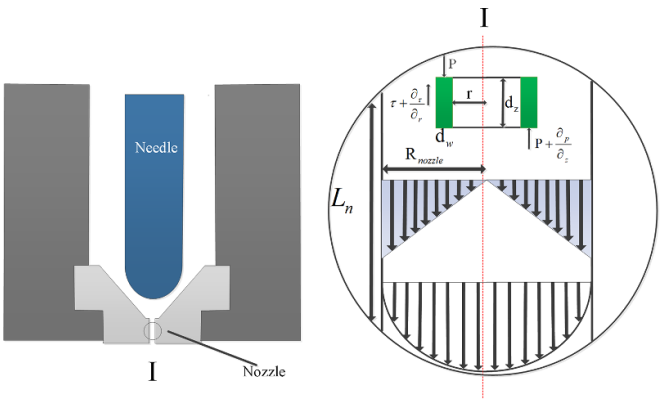

Figure 8. Needle-nozzle hydrodynamic model.

$$-\frac{\partial P}{\partial Z} - \frac{1}{r}\cdot\frac{\partial}{\partial r}\left(\tau \cdot r\right) = \rho\frac{dw}{dt}, 0 \leqslant r \leqslant R_n. \tag{16}$$

The Bernoulli equation for viscous fluids yields the mechanical energy lost due to friction, where a unit length of adhesive flow is a constant value of C, i.e:

$$\frac{dP}{dZ} = \frac{\Delta P}{L_n} = \frac{P_{\text{input}} - P_{\text{output}}}{L_n} = C, \tag{17}$$

where P_{input} is the pressure of the inner surface of the nozzle, Pa; P_{output} is the pressure of the outer surface of the nozzle,

which is the standard atmospheric pressure value, Pa; ΔP is the pressure difference between the inner and outer surface of the nozzle (Pa); and L_n is the length of the nozzle (mm).

The relationship between shear stress τ and adhesive viscosity is obtained from the rheological model of the fluid, given by

$$\tau = -\mu\left(-\frac{\partial w}{\partial r}\right)^n, \tag{18}$$

here n is the flow index and μ is the kinetic viscosity of the adhesive, Pa s.

When the adhesive is in the nozzle for constant flow, the change in velocity $\frac{d_w}{d_t} = 0$. By substituting equations (17) and (18) into equation (16), we obtain:

$$\frac{\Delta P}{L_n} - \mu\,\frac{1}{r}\,\frac{\partial}{\partial r}\left(r\left(-\frac{\partial w}{\partial r}\right)^n\right) = 0\,, \tag{19}$$

where under the no-slip boundary conditions,$w = 0$ for $r = R_n$; $\tau_0 = 0$ for $r = 0$. Substituting the boundary conditions into equation (19) yields the distribution of the adhesive flow velocity along the r direction as follows:

$$\mu(r) = \frac{n}{n+1}\left(\frac{\Delta p}{2\mu L_p}\right)^{\frac{1}{n}}\left(R_p^{1+\frac{1}{n}} - r^{1+\frac{1}{n}}\right). \tag{20}$$

The volume flow rate Q_n and the flow rate are related as

$$Q_n = \int_0^{Rn} 2\pi r w\,(r)\mathrm{d}r \tag{21}$$

From equation (21) we can obtain the average flow rate $\overline{v(r)}$ of the adhesive in the nozzle and the volume V_{output} of the outflowing adhesive as

$$\overline{v(r)} = \frac{Q_n}{\pi R_n^2} = \frac{\Delta P}{8\mu L_n} R_n^2 (n=1)\,, \tag{22}$$

$$V_{\text{output}} = \int_0^{t_{on}} Q_n\,\mathrm{d}t = \frac{\pi}{8}\,\frac{\Delta P}{\mu L_n} R_n^4 t_{on}\;(n=1)\,, \tag{23}$$

where t_{on} is the time to energize the piezoelectric stack (s).

3.2. Numerical simulation of jet process

It can be seen from equation (23) that the speed and volume of the droplet are related to the pressure difference between the two ends of the nozzle, the diameter of the nozzle, the viscosity of the adhesive, the stroke of the needle and other factors. To further understand the injection process of the droplet when the jetting dispenser is working, Fluent was used to simulate the working process of the jetting dispenser. Since the whole model is a revolving body, the model is simplified to a two-dimensional plane problem during simulation. Due to the small size of the nozzle, its mesh is denser than other parts. The results are shown in figure 9, and the specific simulation parameters are shown in table 3.

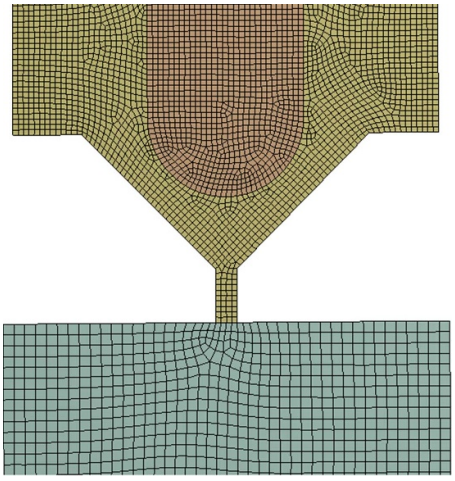

Figure 9. Meshing diagram of the needle-nozzle model.

Table 3. Fluid simulation parameters.

Parameter	Value
Dynamic viscosity	1.412 Pa s
Density of fluid	1.262 g cm^{-3}
Surface tension	63.3 mN m^{-1}
Nozzle length	0.5 mm
Feed pressure	0.1–0.9 MPa
Nozzle diameter	0.2 mm
Needle displacement	0.1–0.7 mm
Needle velocity	0.33 m s^{-1}

The stroke of the needle was set to 0.4 mm. It hit the nozzle at a speed of 0.3 m s^{-1}. The pressure change process in the nozzle cavity is shown in figure 10. Figure 11 shows the pressure curve in the nozzle cavity during the injection process of the jetting dispense.

Figures 10 and 11 show the process when the needle squeezes the adhesive downward from the highest position until it is injected. When the needle is just starting to move downward, it is far from the nozzle, and the adhesive flows upward along the outside of the striker and the inside of the adhesive cavity under the extrusion of the needle. At this time, the pressure of the adhesive near the nozzle is mainly the supply pressure. When the needle moves down to a small gap from the nozzle, due to the viscous force and surface tension of the adhesive itself, it is difficult to pass through the small gap and flow upward along the outside of the needle, resulting in the continuous increase of the adhesive pressure near the nozzle. At the same time, since part of the pressure is converted into kinetic energy of the adhesive and the distance between the needle and the nozzle is getting narrower, the pressure at the nozzle shows a steady increase. When the needle hits the nozzle downward, the needle and the nozzle are in a state of complete fit and the channel was cut off for the adhesive to enter the nozzle, and the pressure in the adhesive cavity suddenly decreases. Due to the uniform distribution of injection velocity, the injected adhesive gradually forms a

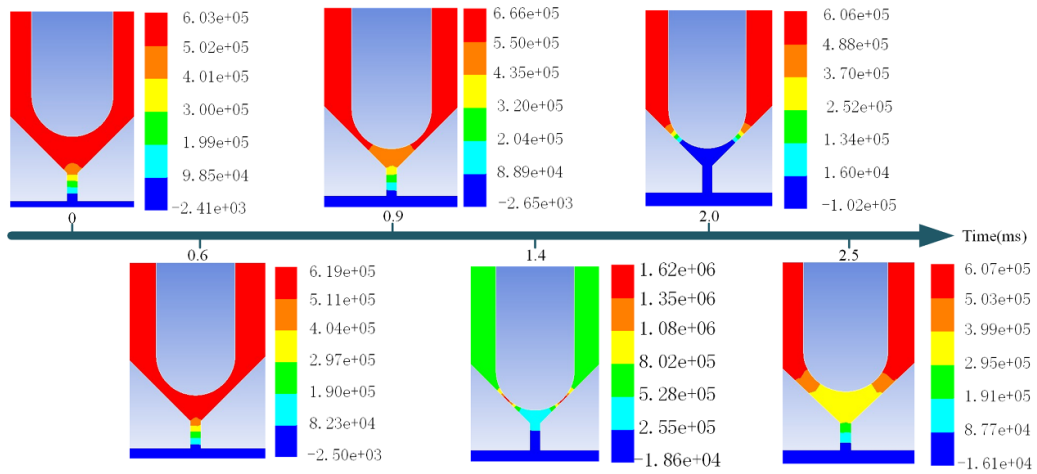

Figure 10. Cloud map of pressure distribution in the nozzle cavity during a working cycle of the jetting dispenser.

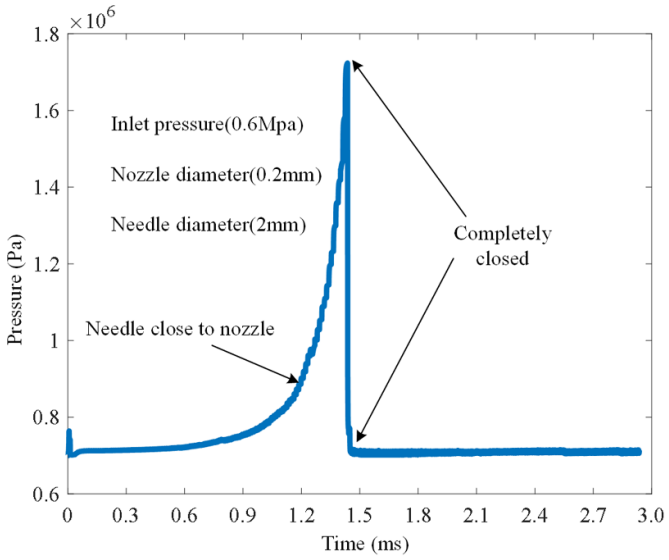

Figure 11. Pressure curve in the nozzle cavity.

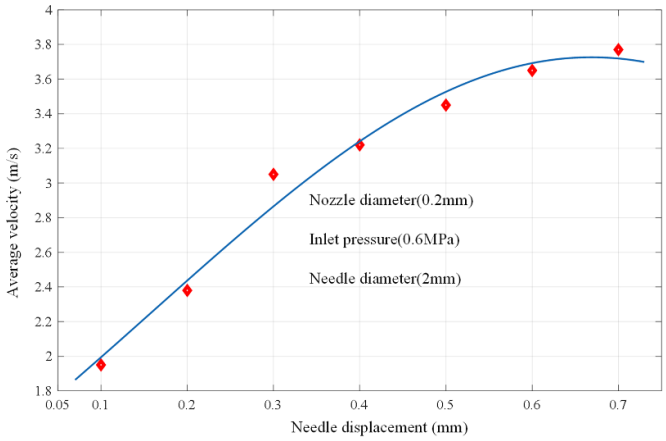

Figure 12. Effect of needle stroke on droplet injection velocity.

spherical shape at the lower end, and under the action of surface tension, the tail of the jet is broken, and the jet that leaves the jetting dispenser reaches the bottom plate to form a complete adhesive droplet.

3.3. Analysis of factors affecting droplet velocity

3.3.1. Influence of the stroke of the needle on the speed of the droplet. The simulation results are shown in figure 12 for a needle stroke range of approximately 0.1–0.7 mm. The simulation analysis is carried out at 0.1 mm intervals while keeping other simulation parameters unchanged. It can be seen from figure 11 that with the increase of the stroke of the needle, the flow rate of the adhesive in the nozzle also increases. This is because the stroke size of the needle determines the amount of adhesive that is fed into the nozzle cavity. The larger the stroke, the larger the amount of adhesive feed, which creates more pressure in the nozzle cavity. According to equation (9), when ΔP increases, the velocity of the droplet injection increases. However, when the stroke is greater than 0.5 mm, the flow rate of the adhesive does not increase significantly. This is due to the fact that when the needle is far away from the nozzle, the extrusion of the needle has little effect on the pressure near the nozzle, and an excessively large stroke will limit the maximum operating frequency of the jetting dispenser. Therefore, according to the needs of different injecting quantities, the stroke of the needle of 0.2–0.4 mm is generally selected.

3.3.2. Influence of supply pressure on the injection speed of droplet. The supply pressure is the main source of power in the initial state of the adhesive, and is the main factor affecting ΔP in equation (9). The numerical simulation results of the droplet injection velocity in the nozzle flow channel are shown in figure 13, given that other simulation parameters remain unchanged and only the supply pressure is varied. As can be seen from figure 13, the velocity of the adhesive in the nozzle flow channel is positively correlated with the supply pressure. Based on the simulation results, it is inferred that increasing the supply pressure can better complete the injection of high viscosity and high flow rate adhesive, which is consistent

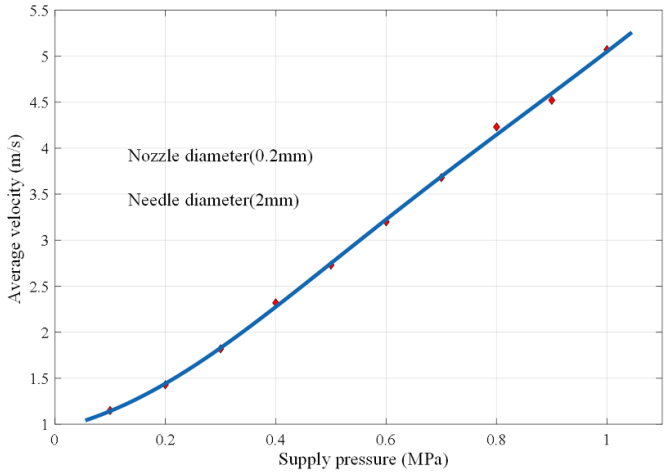

Figure 13. Effect of different supply pressures on the droplet injection speed.

with the analysis of equation (9); that is, increasing ΔP can effectively improve the injection speed of glue droplets, but too large of an injection speed will form satellite droplets and scattering points.

4. Experiment

4.1. Materials and methods

To test the working performance of the designed jetting dispenser prototype and verify the correctness of the theoretical model in section 3.1, the jetting dispenser system shown in figure 14 was built. The system is mainly composed of the PZT jetting dispenser prototype, PZT stack (HPV-C type, BOSHI precision measurement, and control), air pump (EWS 24–680 W, Eluan), signal generator (UTG-2000B, UNI-TREND technology), moving guide rail and adhesive droplet collecting plate. To facilitate the adhesive's cleaning and adjustable viscosity range, a mixture of glycerin and alcohol with a mixing ratio of 1:2 was prepared as the experimental object, and the prototype used a nozzle with a diameter of 200 μm and a needle with a diameter of 2 mm. The minimum diameter of the droplet is the main indicator of the performance of the prototype. The experiment mainly analyzes the influence of the driving signal duty cycle, supply pressure, and operating frequency on the quality of the droplet.

4.2. Influence of different driving signal duty ratios on the droplet diameter

To analyze the influence of the duty ratio of the driving signal on the diameter of the droplet, between 20% and 80%, at 10% intervals, a pulse signal with a frequency of 100 Hz (the supply pressure is 0.6 MPa) was applied to the jetting dispenser. The diameter change of the sprayed adhesive drop is shown in figure 15. It can be seen that when the duty cycle increases from 20% to 80%, the diameter of the droplet increases from 0.96 to 1.81 mm, indicating that the signal duty cycle is positively correlated with the droplet diameter. Essentially, the

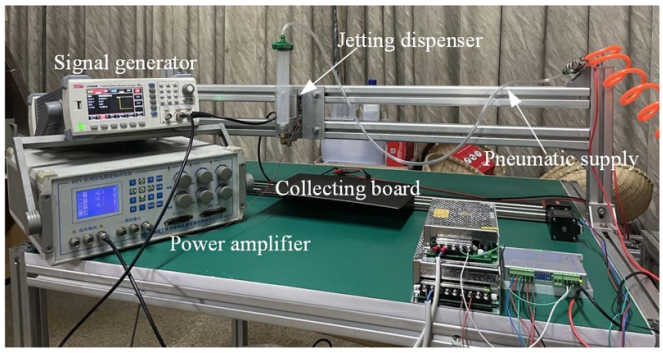

Figure 14. Jetting dispenser experiment platform.

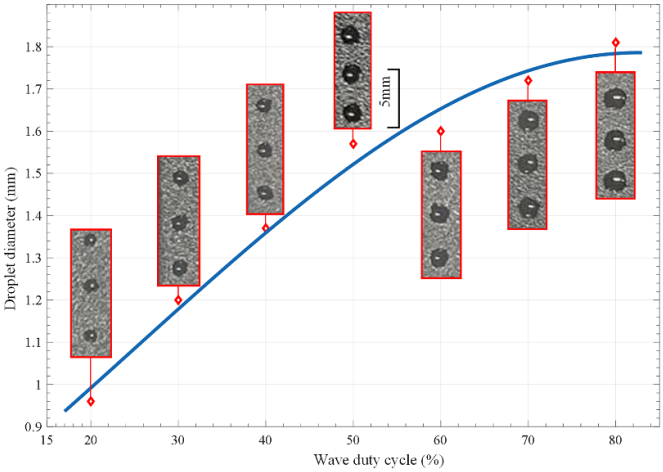

Figure 15. Effect of signal duty cycle on droplet diameter.

duty cycle determines the magnitude of the value of t_{on} in equation (23) and experimentally verifies the correctness of the results. When the duty cycle is less than 20% because the force of the needle to hit the nozzle is small or even resets without hitting the nozzle, the injected droplet cannot overcome its own adhesion, and the phenomenon of sticking occurs. When the duty cycle is greater than 80%, due to the large force of the needle hitting the nozzle at this time, the droplet obtains large kinetic energy, and the droplet appears scattered. Therefore, when the jetting dispenser is working, it is appropriate to select a duty cycle of between 20% and 80%.

4.3. Influence of different supply pressure on the droplet diameter

The supply pressure changes the value of ΔP in equation (23) and affects the size of the droplet. To verify the effect of the glue supply pressure on the droplet diameter, the jetting dispenser is connected to a drive signal with a frequency of 100 Hz and a duty cycle of 50%. The adhesive supply pressures used were 0.2, 0.3, 0.4, 0.5, 0.6, 0.7, and 0.8 MPa. The diameter change of the injected droplets obtained by changing the supply pressure is shown in figure 16. When the supply pressure increases from 0.2 to 0.8 MPa, the diameter of the injected droplets gradually increases from 0.81 to 2.06 mm, indicating that the larger supply pressure extrusion produces

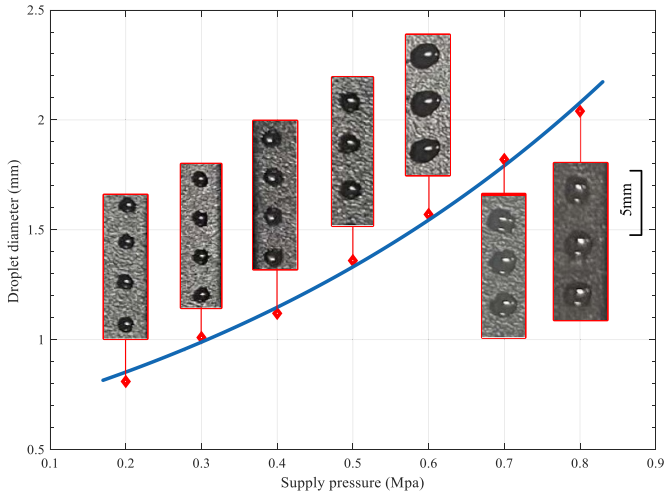

Figure 16. Effect of different supply pressures on droplet diameter.

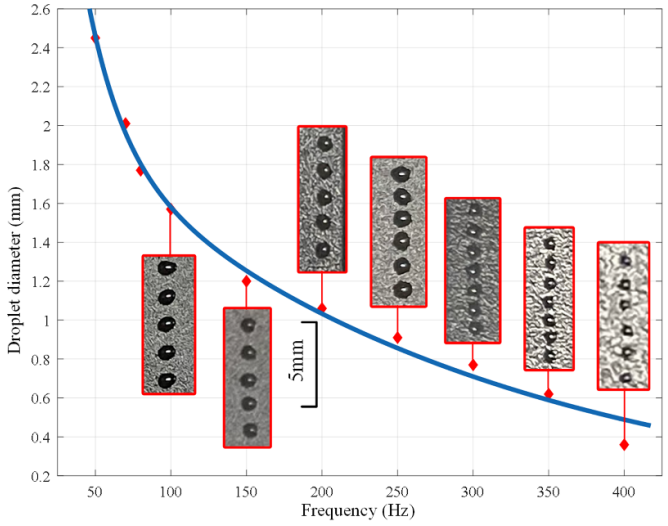

Figure 17. Effect of different operating frequencies on droplet diameter.

faster droplet injection speed. The size of the droplet can be changed by changing the supply pressure, but excessive supply pressure will aggravate the wear of the oil sealing, and the nozzle body is prone to leakage and other phenomena.

4.4. Influence of different signal frequencies on the droplet diameter

The driving frequency of the jetting dispenser is the most important performance parameter of the product and determines the value of t_{on} in equation (23). To test the high frequency performance of the jetting dispenser, the supply pressure was set to 0.6 MPa, the duty cycle of the drive signal to 50%, and the frequencies to be used are 50, 70, 80, 100, 150, 200, 250, 300, 350, 400 Hz, respectively. Figure 17 shows the change of the diameter of the droplet at different frequencies. It can be seen from figure 17 that as the driving frequency increases, the diameter of the droplet gradually decreases from 2.45 to 0.36 mm with the increase of the operating frequency. In contrast, due to the increase of the signal pulse frequency, the adhesive is not fully gathered into the adhesive cavity when the needle is lifted a single time, and is squeezed and injected by the needle, so the diameter also decreases. Owing to the limitation of the physical properties of PZT stack, the theoretical displacement cannot be achieved at high frequencies, and the stroke of the needle is reduced, which will also lead to a reduction in the diameter of the droplet.

5. Conclusion

In this study, a new prototype of double needle PZT injection valve with rigid transmission lever is developed. Its structural advantage, key parameters and injection process are analyzed and verified through numerical modeling, simulation and experiments. The transmission design of the jetting dispenser avoids the compliant mechanism that is often used in the literature and has some shortcomings. In terms of function, it has the advantages of easy replacement of wearing parts and mechanical adjustment of the size of the droplet. First, the coupled dynamic simulation results of the PZT stack and rigid body parts in ANSYS show that the maximum stroke of the needle is 386 μm (150 V), and the first-order resonance frequency of the device is 1186 Hz, which meets the requirements of the working conditions. Second, the fluid dynamics model of the adhesive near the needle-nozzle was established by analytical method, the numerical model was verified by Fluent simulation, and the process of pressure change at the nozzle when the jetting dispenser was working was discussed. Both the needle stroke and the supply pressure are positively related to the adhesive droplet injection speed. Finally, the trial production prototype was tested, and the results showed that: the supply pressure is positively correlated with the diameter of the droplet; the duty ratio of the drive signal should be between 20% and 80%, which is positively correlated with the diameter of the droplet. The frequency of the drive signal is negatively correlated with the diameter of the droplet, and under the experimental conditions, the highest operating frequency of the designed PZT jetting dispenser is 400 Hz, which reaches the high-frequency level of existing studies. The minimum droplet diameter obtained is 0.36 mm, which is approximately 0.1–0.2 mm smaller than the existing PZT jetting dispenser with a compliant mechanism, meeting the industry requirements for the performance of the PZT jetting dispenser. In addition to the driving and air pressure, the structure of the needle and the nozzle also affected the jetting process and shape of the adhesive droplet. Therefore, the development of a multi-domain unified model of the jetting dispenser and the combined influence of multiple factors on the jetting performance will be studied in the future.

Data availability statement

All data that support the findings of this study are included within the article (and any supplementary files).

Acknowledgments

This research is funded by the National Natural Science Foundation of China (Grant No. 52105284), and supported by Zhejiang Sci-Tech University (20022307-Y). We also thank the anonymous reviewers for their critical comments and suggestions for improving the manuscript.

ORCID iD

Runmao Zhao https://orcid.org/0000-0002-9859-2424

References

[1] Shan X, Li H-X, Si H and Chen Y 2018 Integrated sensing-/model-based online estimation of jet dispensing *IEEE Trans. Compon. Packag. Manuf. Technol.* **8** 300–9

[2] Trimzi M A, Ham Y B, An B C, Choi Y M, Park J H and Yun S N 2020 Development of a piezo-driven liquid jet dispenser with hinge-lever amplification mechanism *Micromachines* **11** 117

[3] Kim K, Lee Y-C, Chang H, Lee R-F and Wu H-W 2019 Jetting dispenser height effect on the accuracy of test strip for blood glucose *J. Med. Biol. Eng.* **39** 109–16

[4] Chu Y, Chen C, Tsou C and 2015 A silicon-based LED packaging substrate with an island structure for phosphor encapsulation shaping *IEEE Trans. Compon. Packag. Manuf. Technol.* **5** 155–62

[5] Li J, Zhang X, Liu L and Han L 2013 interfacial characteristics and dynamic process of Au- and Cu-wire bonding and overhang bonding in microelectronics packaging *J. Microelectromech. Syst.* **22** 560–8

[6] Lu S, Jiang H, Li M, Liu J, Gu S, Jiao X and Liu X 2015 Nozzle and needle during high viscosity adhesive jetting based on piezoelectric jet dispensing *Smart Mater. Struct.* **24** 105023

[7] Lu S, Chai B, Liu Y, Liu J, Jiang H, Gu S and Liu J 2016 The experimental study on the influence factors in adhesive dispensing dot diameter of impact jetting valve *IEEE Trans. Compon. Packag. Manuf. Technol.* **6** 326–30

[8] Nguon B and Jouaneh M 2004 Design and characterization of a precision fluid dispensing valve *Int. J. Adv. Manuf. Technol.* **24** 251–60

[9] Zhou C *et al* 2016 The principle and physical models of novel jetting dispenser with giant magnetostrictive and a magnifier *Sci. Rep.* **5** 1–13

[10] Wang L, Du X, Li Y, Luo Z, Zheng G and Sun D 2013 Simulation and experiment study on adhesive ejection behavior in jetting dispenser *J. Adhes. Sci. Technol.* **28** 53–64

[11] Jeon J, Hong S-M, Choi M and Choi S-B 2014 Design and performance evaluation of a new jetting dispenser system using two piezostack actuators *Smart Mater. Struct.* **24** 15020

[12] Hu J F, Liang L and Zhao Y C 2019 Design and performance analysis of a piezoelectric microspray dispensing system based on a flexure mechanism *Opt. Precis. Eng.* **27** 1990–2001

[13] Lu S, Zhang J, Liu Y, Zheng H, Ren C and liu W 2019 Droplet formation study of a liquid micro-dispenser driven by a piezoelectric actuator *Smart Mater. Struct.* **28** 055003

[14] Ueda J, Secord T W and Asada H H 2010 Large effective-strain piezoelectric actuators using nested cellular architecture with exponential strain amplification mechanisms *IEEE/ASME Trans. Mechatronics* **15** 770–82

[15] Deng G, Cui W, Zhou C and Li J 2018 A piezoelectric jetting dispenser with a pin joint *Optik* **175** 163–71

[16] Yang Y, Gu S, Lv Q, Liu J, Yang Z, Li C and Tian H 2019 Influence of needle impact velocity on the jetting effect of a piezoelectric needle-collision jetting dispenser *AIP Adv.* **9** 045302

[17] Huang X, Lin X, Jin H, Lin S, Bu Z, He G, Sun D and Wang L 2019 Effect of enhanced squeezing needle structure on the jetting performance of a piezostack-driven dispenser *Micromachines* **10** 850

[18] Sohn J W, Jeon J, Choi M and Choi S-B 2018 Critical operating factors of a jetting dispenser driven by piezostack actuators: statistical analysis of experimental results *J. Adhes. Sci. Technol.* **32** 359–74

[19] Nguyen Q H and Choi S B 2009 Performance evaluation of a high-speed jetting dispenser actuated by a ring-type piezostack *Proc. Inst. Mech. Eng.* C **223** 1401–13

[20] Guan Z, Zou Y, Zhang M, Lv J, Shen H, Yang P, Zhang H, Zhu Z and James Yang C 2014 A highly parallel microfluidic droplet method enabling single-molecule counting for digital enzyme detection *Biomicrofluidics* **8** 014110


horticulturae
IMPACT FACTOR 3.1
CITESCORE 2.4
New Wine Grape Varieties Cross-Bred from Monastrell Authorized in Murcia, Spain
Volume 9 · Issue 7 | July 2023
MDPI
mdpi.com/journal/horticulturae
ISSN 2311-7524

horticulturae

3.0 Impact Factor | 5.1 CiteScore | 17 days Time to First Decisi

Horticulturae, Volume 9, Issue 7

2023 July - 120 articles

Cover Story: This paper describes the white genotype, 'Calblanque', and the red genotypes, 'Calnegre', 'Gebas', and 'Myrtia', the first wine grape varieties registered by the IMIDA as commercial varieties after the winemaking quality of their grapes in the warm area of Murcia (Spain) was confirmed. The red genotypes were selected for their phenolic quality—superior to that of the parentals—and the white variety 'Calblanque' was selected for its good balance of acidity and aromatic profile. From a sensorial point of view, the new varieties of wines have higher scores than their parentals do. The attributes of these new varieties could mean they are better adapted to the effects of climate change, which impact the grape and wine quality in warm areas and the development of a sustainable viticulture. View this paper

Issues are regarded as officially published after their release is announced to the table of contents alert mailing list.

You may sign up for email alerts to receive table of contents of newly released issues.

PDF is the official format for papers published in both, html and pdf forms. To view the papers in pdf format, click on the "PDF Full-text" link, and use the free Adobe Reader to open them.

Number of Papers 120

Articles (10)

Search | 1 Selected | Select all | Export | Most cited

Review — 22 Citations | 7,060 Views | 14 Pages

Plant Production with Microalgal Biostimulants

Domenico Prisa and Damiano Spagnuolo

Horticulturae **2023**, *9*(7), 829; https://doi.org/10.3390/horticulturae9070829 - 20 July 2023

In order to ensure food security worldwide in the face of current climate changes, a higher quality and quantity of crops are necessary to sustain the growing human population. By developing a sustainable circular economy and biorefinery approaches,... Show more

Full Article →

Feature Paper | Article — 15 Citations | 4,557 Views | 16 Pages

Egyptian *Opuntia ficus-indica* (OFI) Residues: Recovery and Characterization of Fresh Mucilage from Cladodes

Ahmed Elshewy, Federica Blando, Hammam Bahlol, Ahmed El-Desouky, Palmira De Bellis and Ibrahim Khalifa

Horticulturae **2023**, *9*(7), 736; https://doi.org/10.3390/horticulturae9070736 - 23 June 2023

The utilization of biopolymers gained recent attention worldwide due to their effective role in producing eco-friendly and economical products. Mucilage from *Opuntia ficus-indica* (OFI, and other succulent plants) has the capacity to absorb huge amoun... Show more

Full Article →

Article — 13 Citations | 3,806 Views | 16 Pages

Influence of Spraying Some Biostimulants on Yield, Fruit Quality, Oil Fruit Content and Nutritional Status of Olive (*Olea europaea* L.) under Salinity

Adel M. Al-Saif, Muhammad Moaaz Ali, Ahmed B. S. Ben Hifaa and Walid F. A. Mosa

Horticulturae **2023**, *9*(7), 825; https://doi.org/10.3390/horticulturae9070825 - 19 July 2023

Salinity currently affects more than 20% of agricultural land and is expected to pose potential challenges to land degradation and agricultural production in the future. It is a leading global abiotic stress that affects general plants and cultivated... Show more

Full Article →

Article — 9 Citations | 5,095 Views | 15 Pages

Comparison of the Growth, Physio-Biochemical Characteristics, and Quality Indices in Soilless-Grown Strawberries under Greenhouse and Open-Field Conditions

Jalil Rahim Doust, Mohammad Javad Nazarideljou, Mousa Arshad and Antonio Ferrante

Horticulturae **2023**, *9*(7), 774; https://doi.org/10.3390/horticulturae9070774 - 6 July 2023

Soilless cultivation represents a promising method for the future of the horticulture industry as it offers advantages such as improved quality control over the growth environment and mitigation of uncertainties related to soil, water, and nutrient a... Show more

Full Article →

Article — 9 Citations | 2,419 Views | 15 Pages

IMVTS: A Detection Model for Multi-Varieties of Famous Tea Sprouts Based on Deep Learning

Runmao Zhao, Cong Liao, Taojie Yu, Jianneng Chen, Yatao Li, Guichao Lin, Xiaolong Huan and Zhiming Wang

Horticulturae **2023**, *9*(7), 819; https://doi.org/10.3390/horticulturae9070819 - 17 July 2023

The recognition of fresh tea leaf sprouts is one of the difficulties in the realization of the automated picking of fresh tea leaves. At present, the research on the detection of fresh tea leaf sprouts is based on a single variety of tea leaves for a... Show more

Full Article →

Article — 8 Citations | 3,177 Views | 14 Pages

The Effects of Calcium and Sulfur Fertilizers Accompanied by Different Side Elements on the Growth and Cd Uptake of *Spinacia oleracea* Grown in Cd-Contaminated Alkaline Soil

Yanmei Li, Xiangnan Xu, Linna Suo, Yanxin Sun, Na Sun, Jing Liu, Shunjiang Li, Guoyuan Zou and Shangqiang Liao

Horticulturae **2023**, *9*(7), 835; https://doi.org/10.3390/horticulturae9070835 - 21 July 2023

The detoxification of crops grown in Cadmium (Cd)-contaminated acid soil has been widely studied, but for contaminated alkaline soil, there is still inadequate research or information. In order to investigate the effects of calcium and sulfur fertili... Show more

Full Article →

Review — 7 Citations | 4,769 Views | 20 Pages

Advancements in Lily Viruses Management: Challenges and Solutions in Elimination and Detection

Huiling Gong, Leonce Dusengemungu, Peng Lv and Clement Igiraneza

Horticulturae **2023**, *9*(7), 790; https://doi.org/10.3390/horticulturae9070790 - 11 July 2023

Lilies are important crops that are commonly used as cut flowers (*Lilium* spp.) and edible bulb crops (*Lilium davidii* var. *unicolor*). However, virus infections can significantly impact the quantity and quality of lily production. Various methods have... Show more

Full Article →

Article — 6 Citations | 3,123 Views | 11 Pages

The Relationship between Different Fruit Load Treatments and Fruit Quality in Peaches

Xiaojun Wang, Mingliang Yu, Shaolei Guo, Ruijuan Ma and Binbin Zhang

Horticulturae **2023**, *9*(7), 817; https://doi.org/10.3390/horticulturae9070817 - 16 July 2023

The effects of different fruit load treatments during peach growth and development on the internal and external quality of peach fruit were studied. At 47 days after full bloom, the plant materials were divided into four treatments: about 100%, 75%,... Show more

Full Article →

Article — 2 Citations | 2,007 Views | 12 Pages

A Systematic Profiling of the Volatile Compounds in 53 *Cerasus humilis* Genotypes Using Headspace Solid-Phase Microextraction and Gas Chromatography-Mass Spectrometry

Lingjuan Zhang, Xuanxuan Han, Shuai Zhang, Junjie Du, Jiancheng Zhang, Yu Gary Gao, Pengfei Wang and Xiaopeng Mu

Horticulturae **2023**, *9*(7), 806; https://doi.org/10.3390/horticulturae9070806 - 14 July 2023

The fruits of *Cerasus humilis* have a unique and pleasant aroma. In this study, the volatile compounds of ripe fruits of 53 *C. humilis* genotypes were extracted via headspace solid-phase microextraction (HS-SPME) and identified via gas chromatography c... Show more

Full Article →

Correction — 969 Views | 1 Page

Correction: Torguet et al. Evaluation of Fungicides and Application Strategies for the Management of the Red Leaf Blotch Disease of Almond. *Horticulturae* 2022, *8*, 501

Laura Torguet, Lourdes Zazurca, Guillem Martínez, Gemma Pons-Solé, Jordi Luque and Xavier Miarnau

Horticulturae **2023**, *9*(7), 810; https://doi.org/10.3390/horticulturae9070810 - 14 July 2023

The authors wish to add the following statement to the Acknowledgments section of article [...]

Full Article →

horticulturae

IMPACT FACTOR 3.0

CITESCORE 5.1

Article

IMVTS: A Detection Model for Multi-Varieties of Famous Tea Sprouts Based on Deep Learning

Runmao Zhao, Cong Liao, Taojie Yu, Jianneng Chen, Yatao Li, Guichao Lin, Xiaolong Huan and Zhiming Wang

Special Issue

Application of Smart Technology and Equipment in Horticulture

Edited by

Dr. Chenglin Wang and Dr. Lufeng Luo

MDPI

https://doi.org/10.3390/horticulturae9070819

horticulturae

MDPI

Article

IMVTS: A Detection Model for Multi-Varieties of Famous Tea Sprouts Based on Deep Learning

Runmao Zhao [1,2,3], Cong Liao [1], Taojie Yu [1], Jianneng Chen [1,2,3], Yatao Li [2,3,4], Guichao Lin [5], Xiaolong Huan [1,2,3] and Zhiming Wang [6,*]

[1] School of Mechanical Engineering, Zhejiang Sci-Tech University, Hangzhou 310018, China; rmzhao@zstu.edu.cn (R.Z.); 13517960753@163.com (C.L.); 202130605347@mails.zstu.edu.cn (T.Y.); jiannengchen@zstu.edu.cn (J.C.); huanxl@zstu.edu.cn (X.H.)
[2] Key Laboratory of Transplanting Equipment and Technology of Zhejiang Province, Hangzhou 310018, China; ytli@zstu.edu.cn
[3] Key Laboratory of Agricultural Equipment for Hilly and Mountainous Areas in Southeastern China (Co-Construction by Ministry and Province), Ministry of Agriculture and Rural Affairs, Hangzhou 310018, China
[4] School of Textile Engineering, Zhejiang Sci-Tech University, Hangzhou 310018, China
[5] College of Mechanical and Electrical Engineering, Zhongkai University of Agriculture and Engineering, Guangzhou 510225, China; guichaolin@zhku.edu.cn
[6] Jinhua Polytechnic Zhejiang Key Laboratory of Crop Harvesting Equipment Technology, Jinhua 321017, China
* Correspondence: jhcwzm@163.com

Abstract: The recognition of fresh tea leaf sprouts is one of the difficulties in the realization of the automated picking of fresh tea leaves. At present, the research on the detection of fresh tea leaf sprouts is based on a single variety of tea leaves for a specific period or specific place, which has no advantage for the spread, promotion, and application of the methods. To address this problem, an identification of multiple varieties of tea sprouts (IMVTS) model was proposed. First, images of three different varieties of tea (ZhongCha108 (ZC108), ZhongHuangYiHao (ZH), ZiJuan (ZJ)) were obtained, and the multiple varieties of tea (MVT) dataset for training and validating models was created. In addition, the detection effects of adding a convolutional block attention module (CBAM) or efficient channel attention (ECA) module to YOLO v7 were compared. In the detection of the MVT dataset, YOLO v7+ECA and YOLO v7+CBAM showed a higher mean average precision (mAP) than YOLO v7, with 98.82% and 98.80%, respectively. Notably, the IMVTS model had the highest AP for ZC108, ZH, and ZJ compared with the two other models, with 99.87%, 96.97%, and 99.64%, respectively. Therefore, the IMVTS model was proposed on the basic framework of the ECA and YOLO v7. To further illustrate the superiority of the model, this study also conducted a comparison test between the IMVTS model and the mainstream target detection models (YOLO v3, YOLO v5, FASTER-RCNN, and SSD) and the IMVTS model on the VOC dataset, and it is clear from the test results that the mAP of the IMVTS model is ahead of the remaining models. Concisely, the detection accuracy of the IMVTS model can meet the engineering requirements for the automatic harvesting of autumn fresh famous tea leaves, which provides a basis for the future design of detection networks for other varieties of autumn tea sprouts.

Keywords: fresh tea leaf sprouts; multiple varieties detecting; IMVTS; YOLO v7; ECA

Citation: Zhao, R.; Liao, C.; Yu, T.; Chen, J.; Li, Y.; Lin, G.; Huan, X.; Wang, Z. IMVTS: A Detection Model for Multi-Varieties of Famous Tea Sprouts Based on Deep Learning. *Horticulturae* **2023**, *9*, 819. https://doi.org/10.3390/horticulturae9070819

Academic Editors: Xinchao Wang and Jianyun Ruan

Received: 30 April 2023
Revised: 11 July 2023
Accepted: 13 July 2023
Published: 17 July 2023

1. Introduction

China is known as the home of tea. The country's planting, output, consumption, and export volume of tea are first in the world. The extensive demand for fresh tea leaves requires effective support [1]. Famous tea is a representative of high-quality tea in China. Its raw materials are one sprout and one leaf of a tea tree. Its harvesting is still mainly manual and labor intensive, and there is a shortage of tea collectors [2]. To achieve the

intelligent picking of fresh tea leaf sprouts, researchers use machine vision technology to detect fresh tea leaves. Lei Zhang et al. [3] extracted the R, G, and B components of images of collected fresh tea leaves and then processed the adaptive threshold of the B components. A new component gray diagram was obtained in combination with the G components, and the thresholds were enhanced by segmental transformation, thereby improving the contrast between the tender leaves and the background, and then, the improved watershed function was used to obtain a good division effect. Liang Zhang et al. [4] used Bayesian inference to judge the principles and Bayes methods to build an identification model of the fresh leaf collection status in order to detect purple rose tea tree sprouts in April in real time. Although the above machine learning technology can accurately identify fresh tea leaf sprouts, the identified fresh leaf image background environment is relatively single, and the segmentation accuracy is greatly affected by the characteristics of the fresh tea leaf sprouts. It is often difficult to overcome this shortcoming.

With the rapid development of artificial intelligence technology, the use of deep-learning [5] target detection algorithms, such as Fast R-CNN [6], Faster R-CNN [7], You Only Look Once (YOLO) [8], and Single Shot MultiBox Detector (SSD) [9], etc., are increasingly applied in the agricultural field. In terms of fresh tea leaf sprout recognition, Yatao Li et al. [10] used the YOLO v3 network to detect and identify fresh tea leaf sprouts on an RGB-D image collected with an RGB-D camera and estimated the three-dimensional coordinates of the fresh tea leaf picking position in the corresponding depth chart of the enclosure. It reached 83.18%. Wenkai Xu et al. [11] proposed a detection and classification method for the two-level integration network of the variability domain. This method combined YOLO v3's fast detection capacity and the high-precision classification ability of DenseNet201 to achieve the accurate detection of fresh tea leaves. Yu-Ting Chen et al. [12] detected the OTTL area in a tea tree image through the Faster R-CNN model and then identified the picking point in the OTTL area with the FCN model to determine the three-dimensional coordinates of the picking point. The YOLO model is currently a widely used detection network. It adopts a one-stage algorithm. The network operates quickly, the memory occupation is small, and it has a fast detection speed [13]. Based on inheriting the advantages of the original YOLO model, YOLO v7 [14] has a higher detection accuracy and faster reasoning speed compared to the previous YOLO series models because of its more complex network structure and training techniques. However, because the YOLO v7 model uses only one main convolutional neural network to predict the category and location of different targets, it also improves the speed and makes the recognition accuracy lower. This may lead to more missed inspections and misunderstandings when using YOLO v7 to detect fresh tea leaf images. At the same time, the applicability of the models proposed in the existing literature to fresh sprouts of different varieties of tea is unknown.

Consequently, this study used the YOLO v7 model as the basic framework to research the identification of multiple varieties of fresh tea leaf sprouts and explored the impact of integrating CBAM and ECA mechanisms on YOLO v7 detection accuracy and generalization effects. According to the results of the research, an IMVTS model was proposed to solve the problem of high-precision detection of multiple tea species. In addition, to demonstrate the superiority of the proposed IMVTS model in detection, comparison tests of the IMVTS model with mainstream target detection models (YOLO v3, YOLO v5, FASTER-RCNN, and SSD) and detection tests of the IMVTS model on VOC datasets were designed.

2. Materials and Methods

2.1. Experimental Data Collection and Preparation

2.1.1. Fresh Tea Leaf Image Collection and MVT Dataset Production

At the experimental base of the Tea Research Institute of the Chinese Academy of Agricultural Sciences (Figure 1), a total of 277 fresh leaf images of 3 tea varieties were collected, of which 90 images were ZhongCha108 (ZC108), 150 were ZhongHuangYiHao (ZH), and 37 were ZiJuan (ZJ). The sampling date was 21 September 2022. The collected fresh tea leaf images were made into a dataset of fresh leaves of multiple tea varieties that

could be used to train and verify the network model and were named the MVT dataset. An iQOO Neo3 mobile phone camera was used. The shooting angle was 30~60°, and the shooting distance was 30~50 cm. The images were stored in a JPG format, and the MVT dataset images are shown in Figure 2. The open-source labeling tool Labellmg was used to artificially label the sprout position on the fresh tea leaf images, and the labeled result was saved in the PASCAL VOC format.

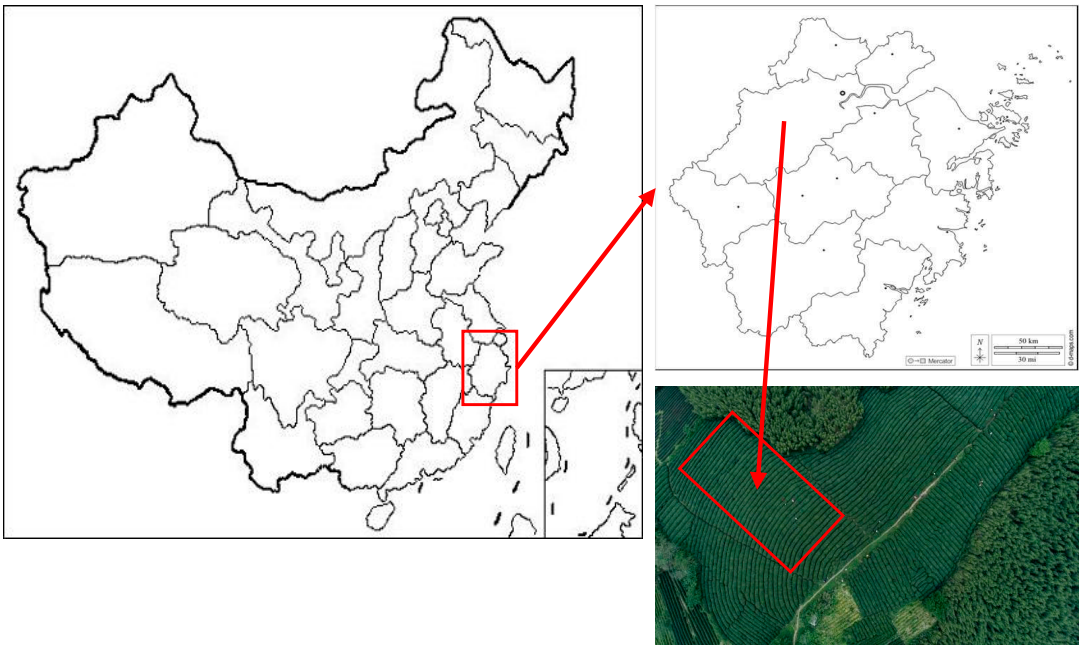

Figure 1. Experimental Base of the Tea Research Institute of the Chinese Academy of Agricultural Sciences.

(**a**) (**b**) (**c**)

Figure 2. MVT dataset images; (**a**) ZC108; (**b**) ZH; (**c**) ZJ.

The images of ZC108, ZH, and ZJ as the research objects are shown in Figure 2a–c. The leaves of ZC108 are long oval in shape, green in color, slightly rumbled on the leaf surface, and flat on the leaf body, and the sprouts are yellowish-green with less velvet. The leaves of ZH are oval in shape, yellowish green in color, slightly elevated on the leaf surface, slightly inflexed on the leaf body, and the sprouts are slender. ZJ is a large-leaved, medium-sprout species. The leaf blade is upwardly slanting, willow-shaped, with an acuminate tip, and purple in color. Its petiole is purple-red in color. These images can also provide data support for future studies of other tea recognition models.

2.1.2. MVT Dataset Division

The 277 obtained images and corresponding labels were divided into training sets and validation sets according to the proportion of training sets: validation sets (=9:1) so that the

model training and validating in the later stage could be performed. To enrich the diversity of samples and improve the robustness of the IMVTS model, the dataset was expanded to 15,000 pieces of the original dataset, with increased or decreased brightness, increased and decreased color saturation, and horizontal flip. The application process is shown in Figure 3. After the enhancement, the number of sprouts of the fresh leaves of the three tea varieties reached 59,337, of which the number of sprouts of ZC108 was 7429, the number of sprouts of ZH was 18,902, and the number of sprouts of ZJ was 33,006.

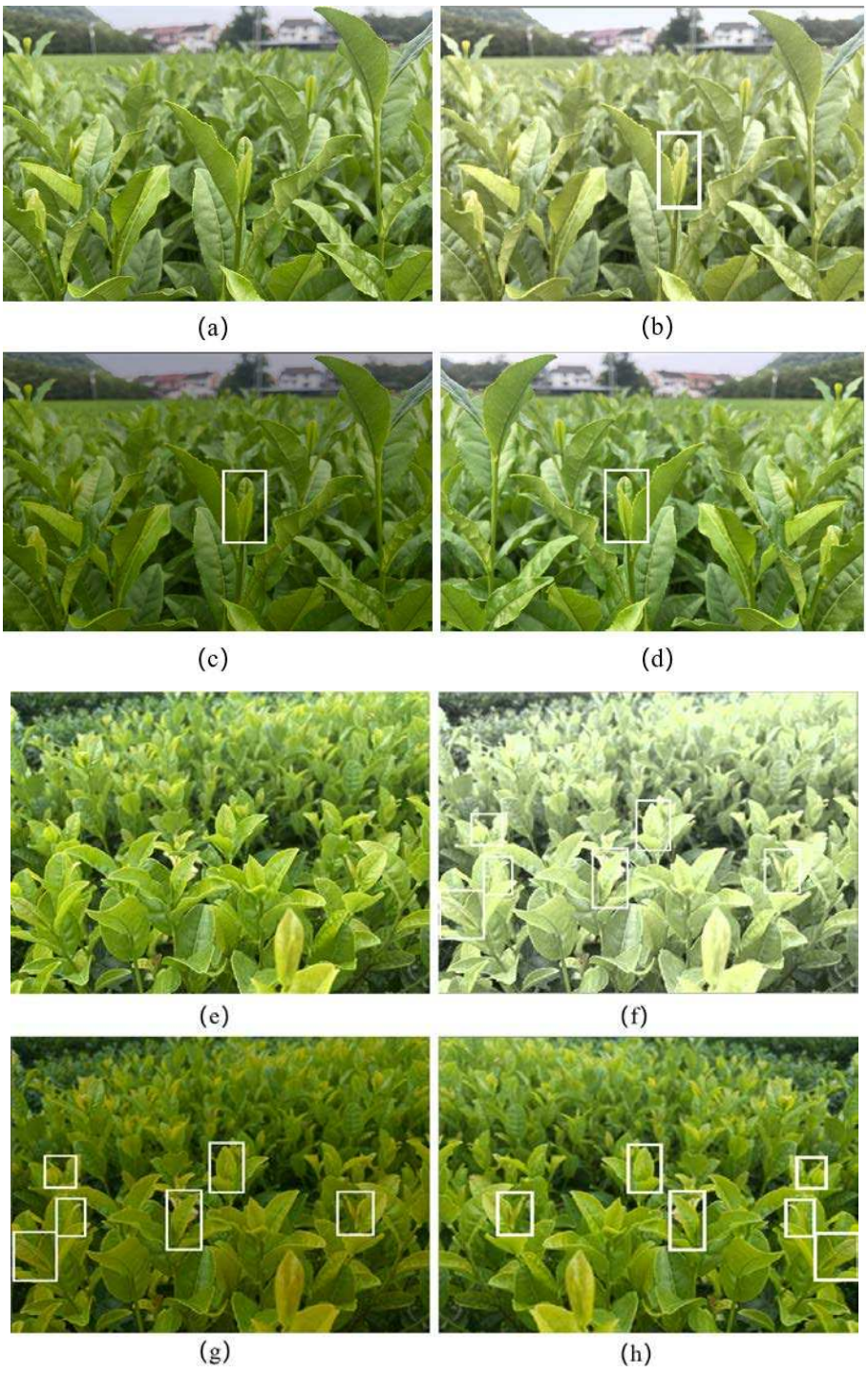

Figure 3. *Cont.*

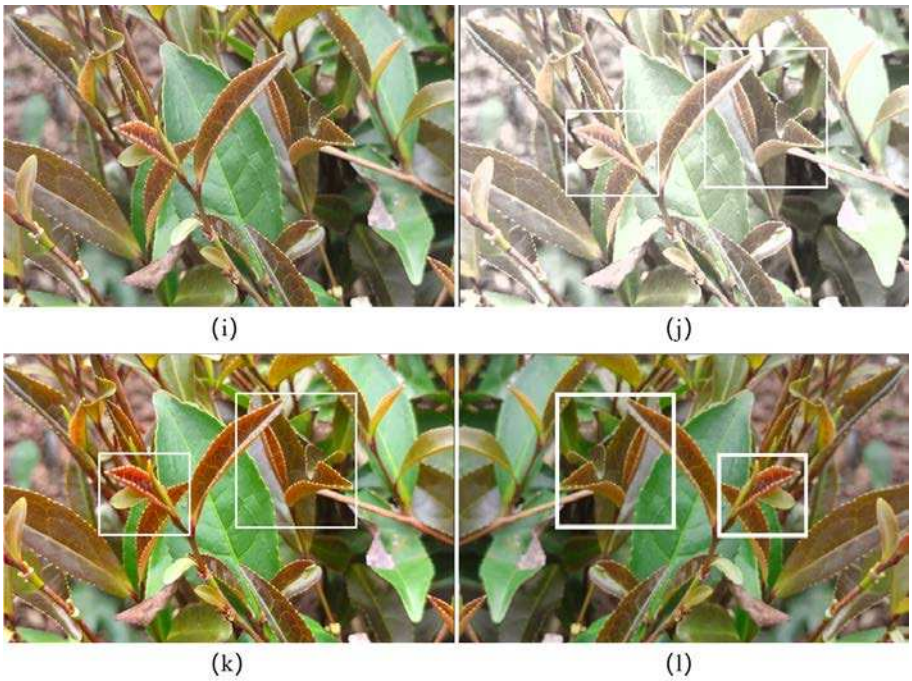

Figure 3. MVT dataset enhancement examples. (**a**,**e**,**i**) Image of primitive fresh tea leaves; (**b**,**f**,**j**) Image of fresh tea leaves with increased or decreased brightness; (**c**,**g**,**k**) Image of fresh tea leaves with increased or decreased color saturation; (**d**,**h**,**l**) Image of fresh tea leaves with the horizontal flip.

2.2. Establishment and Training of the IMVTS Model

2.2.1. Experimental Platform and Environmental Configuration

This study used a workstation equipped with the Ubuntu 18.04 operating system for model training. The CPU was Intel i7 12700F (Shenzhen, China) and the GPU was 3080Ti. The development environment was Pytorch 1.11. The development language was Python, and vs. code software was used for debugging.

2.2.2. Establishment of the IMVTS Model

This study used the YOLO v7 model as the basic framework for the recognition of multiple varieties of fresh tea leaf sprouts; the related research has shown that attention mechanisms [15] such as SENet [16], CBAM [17], and ECA [18] improved the network performance. Therefore, to improve the detection accuracy of YOLO v7's original model on the small target of fresh tea leaves, the effects of adding the CBAM or ECA attention module to YOLO v7 on the detection effect were compared; the final IMVTS network model structure obtained is shown in Figure 4. The IMVTS model mainly includes four parts: input, backbone, head, and output. First, the collected tea leaf images undergo labellmg and random data augmentation, then the tea leaf images are resized into 640 × 640 size RGB images and input to the backbone network The backbone network features the processing of fresh tea leaves with features. Second, the feature information extracted in the backbone network is combined through the characteristics of the head to obtain the characteristics of large, medium, and small sizes. Finally, the characteristics of the characteristic fusion are sent to the REP and Conv module of the head section for detection, and the final result is the output. The workflow of the algorithm is shown in Figure 5. The main network part of the YOLO v7 model is mainly composed of convolution, the extended-ELAN (E-ELAN) module, the MPConv module, and the SPPCSPC module. Among these, the E-ELAN module is based on the original ELAN, changing the calculation block while maintaining the original ELAN's transition layer structure. The network can learn more features by controlling the shortest and longest gradient path. It can resolve the relatively complicated and variable problems that can be solved for the background environment and targets appearing in the MVT dataset to extract more efficient features. The SPPCSPC module

adds parallel MaxPooling operations to a convolution series to obtain different feelings so that the algorithm can adapt to fresh tea leaf images of different resolutions and can make the network speed faster; the accuracy of detecting fresh tea leaf sprouts will also be improved. The main role of the MPConv module is to sample. The experience of the current feature layer is expanded through MaxPooling and then integrated with the normal convolutional fresh tea leaf sprout feature information. It can improve the generalization of the network, suitable for the recognition scene of multiple varieties of tea leaf sprouts [19]. When introducing the attention module, the location information and detail information of the feature information are extracted from the backbone, and there is less semantic information [20]. Feature information is easily lost after processing for small targets such as fresh tea leaf sprouts. To improve the detection accuracy of the YOLO v7 original model for fresh tea leaves, an attention mechanism was added between the backbone and the head. The structure of the attention module is shown in Figure 6. CBAM combines the channel attention mechanism with the spatial attention mechanism. The CBAM module conducts global average pooling and the largest global pooling for the input feature layer, then learns the weight information of each channel through a shared full connection layer and the Sigmoid function. Then, it learns the weight information of each point in the space through a convolutional nucleus of 3 × 3 and the expansion coefficient of 2, and the Sigmoid function. ECA is a channel attention mechanism. The ECA module changes the two full connection layers to one-dimensional convolution. After the Sigmoid function is passed, the channel weight information is obtained. This module avoids the dimension of information and has good cross-channel information acquisition capabilities.

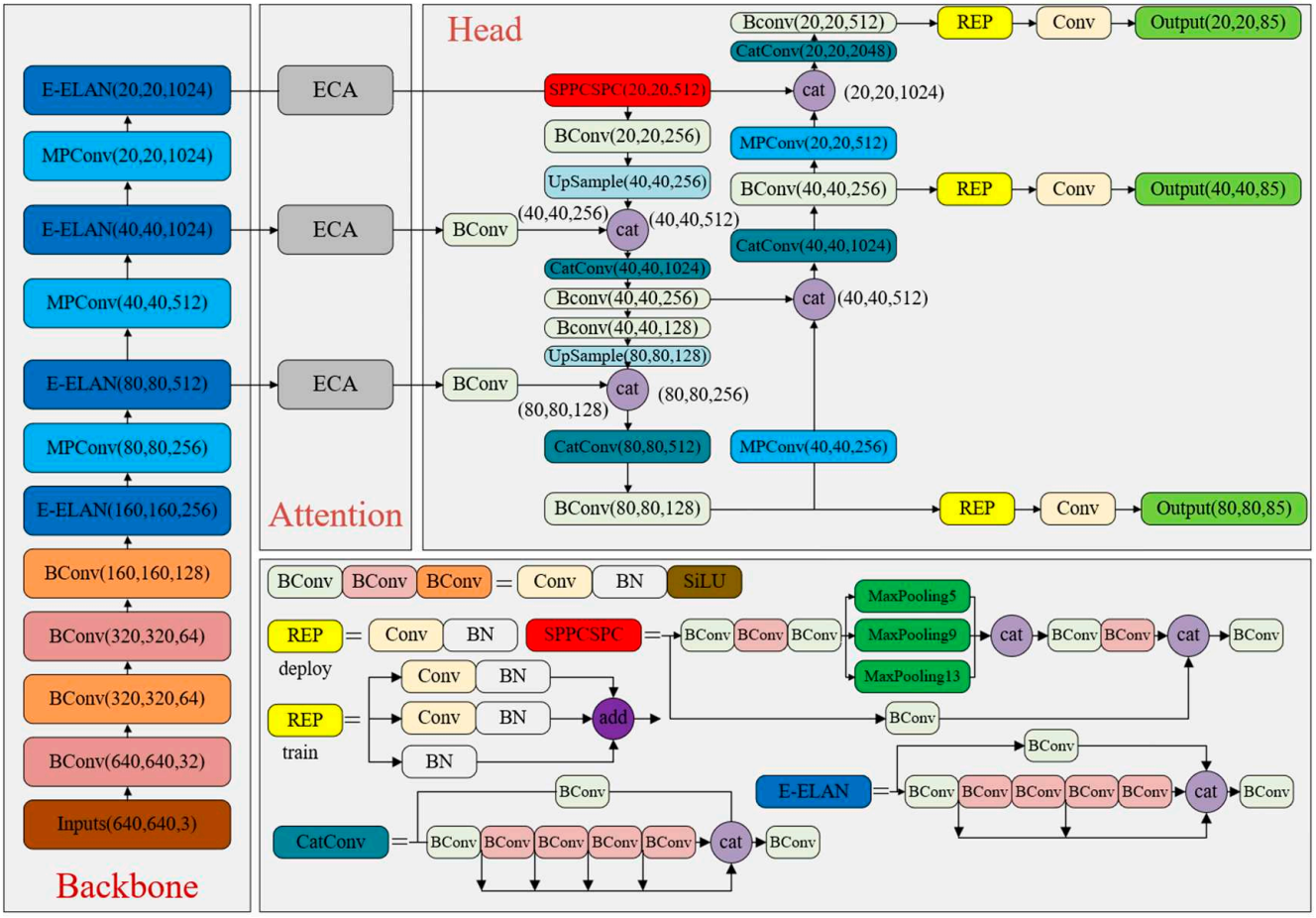

Figure 4. IMVTS model network structure diagram.

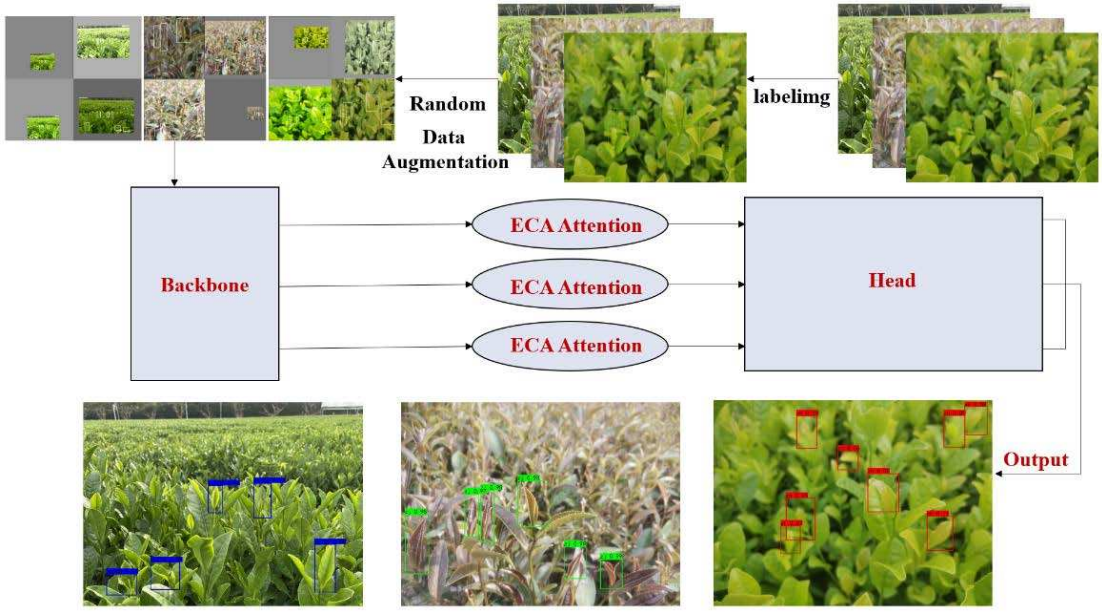

Figure 5. Algorithm workflow diagram.

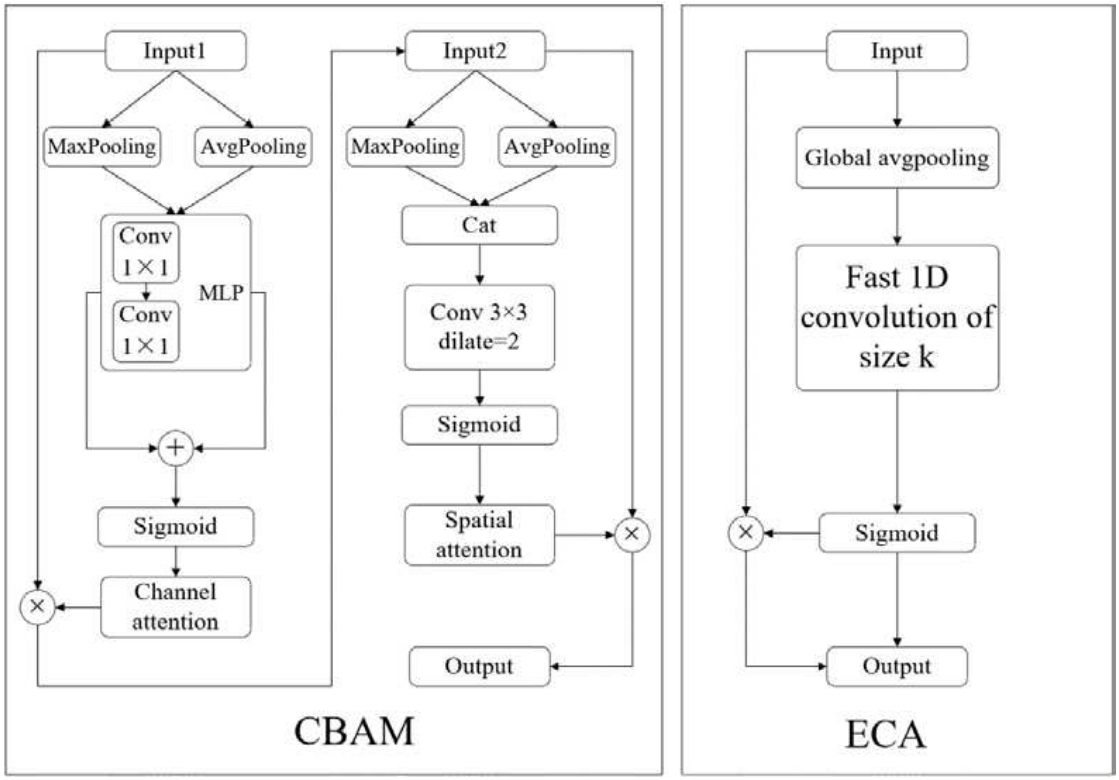

Figure 6. CBAM and ECA module structure diagram.

2.2.3. Training Parameter Settings

When training the original model of YOLO v7 and the IMVTS model, only the thawing training was performed. The thawing training set the total training generation epochs to 500; additionally, the batch size was set to 4, the initial learning rate of the model was set to 0.01, the minimum learning rate was set to 0.0001, and the SGD optimizer was used to optimize the model. The momentum parameters of the SGD optimizer were set to 0.937, and the torque annealing function was used to reduce the learning rate. In the same

environment, the training loss curves of the YOLO v7 original model, YOLO v7+CBAM model, and IMVTS model are shown in Figure 7.

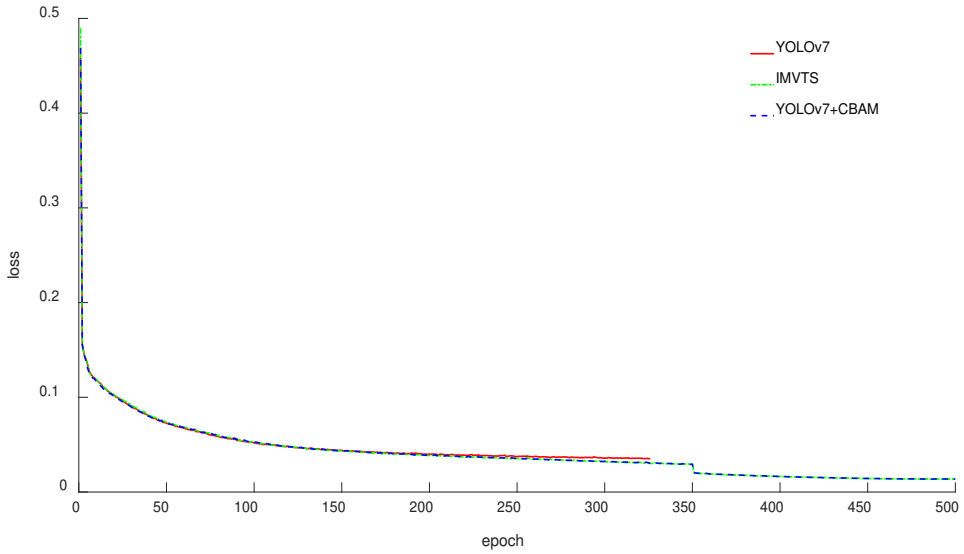

Figure 7. YOLO v7 original model, YOLO v7+CBAM model, and IMVTS model training loss curves.

2.2.4. Model Evaluation Index

To evaluate the detection effect of the IMVTS model, this study used precision (P), recall (R), F1 score, average precision (AP), and mean average precision (mAP) for measurement. Among these, P is the ratio of the number of correctly predicted sprouts to the total number of predicted sprouts in an image, R is the ratio of the number of correctly predicted sprouts to the total number of true sprouts in an image, the F1 score is the equalization of P and R, AP represents the accuracy of each kind of fresh tea leaf sprout recognition, and mAP represents the average value of three kinds of fresh tea leaf sprout recognition. They are calculated as follows (1)–(5):

$$P = \frac{TP}{TP + FP} \times 100\% \tag{1}$$

$$R = \frac{TP}{TP + FN} \times 100\% \tag{2}$$

$$F1 = 2\frac{P \times R}{P + R} \times 100\% \tag{3}$$

$$AP = \int_0^1 P(R)dR \times 100\% \tag{4}$$

$$mAP = \int_1^n \frac{AP_1 + AP_2 + \ldots + AP_n}{n} \tag{5}$$

where TP is the number of correctly predicted sprouts; FP is the number of falsely predicted sprouts; FN is the number of true sprouts that were not predicted as sprouts; and n is the number of fresh tea leaves. The values of the above parameters are obtained by counting and tallying the target detection frames in the validation sets.

3. Results and Discussion

3.1. Model Identification Results and Comparative Analysis

3.1.1. Comparison of YOLO v7 Model, YOLO v7+CBAM Model, and IMVTS Model Recognition Results

The YOLO v7 original model, YOLO v7+CBAM model, and IMVTS model were placed in the same environment for detection. The obtained model evaluation indicators are shown

in Table 1. It can be seen from Table 1 that after adding an attention mechanism module to the YOLO v7 network, the P, R, F1 score, and mAP were improved. The precision value of the IMVTS model was 99.76%, 0.10% higher than the YOLO v7+CBAM and 0.24% higher than the YOLO v7 model. The recall value of the IMVTS model was 97.03%, 0.10% higher than the YOLO v7+CBAM and 2.46% higher than the YOLO v7 model. The F1 score of the IMVTS model was 0.98, as was that of the YOLO v7+CBAM model, which was 0.01 higher than the YOLO v7 model. The mAP value of the IMVTS model was 98.82%, which was 0.02% higher than the YOLO v7+CBAM and 1.36% higher than the YOLO v7 model. In summary, the IMVTS and YOLO v7+CBAM models were better than the detection effect of the YOLO v7 model, and the IMVTS model had the best detection effect. This is because the characteristic information of fresh tea leaf sprouts is easy to lose after processing. After the ECA module is introduced, it uses a dynamic convolution nucleus to perform 1*1 convolution; it can be used to extract feature information in different areas, avoiding the number of channel dimensions caused by learning channel attention information so that the model can more effectively learn the top-level information, improving the position prediction of the fresh tea sprouts, and at the same time, can reduce the model parameters, thereby increasing the model performance. For the CBAM module, although it combines the channel attention mechanism with the space attention mechanism, there is not enough space for the information-rich feature space. For small targets, such as fresh tea leaf sprouts, the actual effect is worse than the additional ECA module.

Table 1. Model performance indicator assessment comparison.

Model	P (%)	R (%)	F1-Score	mAP (%)
YOLO v7	99.52	94.57	0.97	97.46
YOLO v7+CBAM	99.66	96.93	0.98	98.80
IMVTS	99.76	97.03	0.98	98.82

3.1.2. Comparison of IMVTS Model with Mainstream Target Detection Models

To verify the advantages of the IMVTS model for multi-species tea fresh leaf shoot detection, the IMVTS model was compared with four mainstream target detection models (YOLO v3, YOLO v5, FASTER-RCNN, and SSD). The comparison experiments of the models were trained and validated under the MVT dataset. The relevant parameters were kept consistent during the experiment, and the detection effect of the model was evaluated by P, R, F1-score, and mAP, and the results are shown in Table 2. The results show that the IMVTS model proposed in this study improves in P, R, F1 values, and mAP relative to the four mainstream target detection models. Among them, IMVTS improved P by 2.38% and 1.79%, R by 7.02% and 6.31%, F1-score by 0.06 and 0.04, and mAP by 4.88% and 4.37%, respectively, relative to YOLO v3 and YOLO v5. IMVTS has higher detection accuracy than YOLO v3 and YOLO v5 because it not only inherits the advantages of the original YOLO model but also achieves higher detection speed with the same computational resources because it uses a faster convolution operation and a smaller model.

Table 2. Results of the model comparison test.

Model	P (%)	R (%)	F1-Score	mAP (%)
IMVTS	99.76	97.03	0.98	98.82
YOLO v3	97.38	90.01	0.92	93.94
YOLO v5	97.97	90.72	0.94	94.45
FASTER-RCNN	96.84	70.19	0.89	89.28
SSD	99.32	58.22	0.72	85.92

IMVTS improved P by 2.92%, R by 26.84%, F1s by 0.07, and mAP by 9.54% relative to FASTER-RCNN. The reason for the improvement in detection accuracy is that FASTER-RCNN uses resnet50 as the backbone, and its feature map only comes from the top-level

features, while the MVT dataset has small targets, and there are occlusions and blurring between targets, and only the features of the top-level of the network are used to predict the targets in a single way to extract information, which is not conducive to the localization of target frames. For IMVTS compared to SSD, P improved by 0.44%, R improved by 38.81%, F1score value improved by 0.26, and mAP improved by 12.9%. This is because the SSD model adopts a deep learning network of multi-scale characteristic fusion, but the use of low-level feature information is not enough. At the same time, the resolution of the SSD model is also low, resulting in an insufficient ability to recognize the small target SSD model, which is not conducive to conducting small target detection tasks.

3.1.3. Results and Analysis of Ablation Test

In order to verify the effectiveness of the IMVTS model proposed in this study, different optimization strategies (backbone, model size, and attention) were used in this study. An ablation test was conducted, and the comparative results were shown in Table 3. As can be seen from Table 3, the mAP of the original YOLO v7 model was 97.46%, and after the introduction of the ECA attention mechanism, the mAP increased by 1.36% and reached a peak of 98.82%. Therefore, YOLO v7 and ECA are taken as the basic framework to construct the IMVTS model proposed in this study. In addition, the ablation experiments of four mainstream target detection models (YOLO v3, YOLO v5, FASTER-RCNN, and SSD) were also conducted in this study. It can be seen from Table 3 that the IMVTS model (consisting of YOLO v7 and ECA) has the best detection effect.

Table 3. Results of ablation experiments.

Model	Backbone	Model Size	Attention	mAP (%)
YOLO v7		YOLO v7	ECA	98.82
			CBAM	98.80
			NONE	97.46
		YOLO v7_x	ECA	97.86
			CBAM	97.73
			NONE	96.58
YOLO v3			ECA	94.26
			CBAM	94.20
			NONE	93.94
YOLO v5	Cspdarknet	YOLO v5_l	ECA	96.03
			CBAM	95.66
			NONE	94.45
		YOLO v5_x	ECA	95.83
			CBAM	95.72
			NONE	94.51
	Convnext_tiny	YOLO v5_l	ECA	94.28
			CBAM	94.23
			NONE	94.05
		YOLO v5_x	ECA	94.41
			CBAM	94.30
			NONE	94.12
FASTER-RCNN	Resnet50		ECA	90.24
			CBAM	89.76
			NONE	89.28
	Vgg		ECA	87.77
			CBAM	87.59
			NONE	86.33
SSD	Vgg		ECA	88.06
			CBAM	87.24
			NONE	85.92
	Mobilenetv2		ECA	85.42
			CBAM	84.11
			NONE	83.31

3.1.4. IMVTS Model for VOC Dataset Detection Test

To further illustrate the effectiveness of the IMVTS model in practical engineering applications, this study uses the IMVTS model to train and test the VOC dataset, which includes images of birds, boats, buses, etc. The relevant parameters during the experiments were all kept the same as in the previous training of the MVT dataset, and the detection effect of the model was evaluated by P, R, F1-score, and mAP. Furthermore, a comparison test with YOLO v7 was conducted, and the comparison results are shown in Table 4. From Table 4, it can be seen that the IMVTS model has better detection results compared to the original YOLO v7 model.

Table 4. Model comparison results.

Model	P (%)	R (%)	F1-Score	mAP (%)
IMVTS	87.79	72.20	0.79	83.85
YOLO v7	87.60	62.08	0.72	77.90

3.2. Comparison of Model Recognition Effects on the MVT Dataset

To further understand the detection effect of the models for images of fresh leaf sprouts of different varieties of tea. The YOLO v7 and the IMVTS models were used to detect the three different varieties of fresh tea leaves in the selected images. The detection results are shown in Figure 8. It can be seen that the IMVTS model detected more fresh tea leaf sprouts than the YOLO v7 model and had a better detection effect.

Figure 9 shows that when the YOLO v7 original model detects the three varieties of fresh tea leaves, there is a misunderstanding phenomenon. This is because, in the process of generating fresh tea leaf datasets, multiple fresh tea leaves and sprouts often appear in the single picture taken, and these images have problems such as blurry, chaotic positions and overlapping blocks of sprouts. As a result, the selection of the fresh tea leaf sprouts by the frame of artificial labeling is not accurate enough, resulting in error detection of the model. The IMVTS model can effectively reduce the misunderstanding phenomenon, and the specific contrast is as follows.

The results of the original model of YOLO v7, YOLO v7+CBAM, and IMVTS are given in Table 5. In Table 5, it is shown that the AP value of ZC108 can reach up to 99.87%; the AP value of ZJ can reach up to 99.64%; and the AP value of ZH is 96.97%. It can also be seen in Table 2 that compared with the ZC108 and ZJ varieties, the three models have a worse detection effect with ZH. Considering that this study used the same model for all three varieties of fresh tea leaf sprouts, the main reason should be in the images of the fresh tea leaves. Therefore, fresh leaf sprouts and old leaf images of each of the three tea varieties were selected for RGB color gamut analysis. The average and square differences of the RGB of the fresh leaf sprouts and the old leaves of the three tea varieties are shown in Figures 9 and 10. According to Figures 10 and 11, it can be seen that the differences between the three channels of the sprouts and old leaves of ZC108 and the RGB of R, G, and B are 8.33, 30.82, and 31.02, respectively; the differences between the three channels R, G, and B of the square differences of stdRGB are 2.72, 4.79, and 8.04, respectively. The differences between the three channels of the sprouts and old leaves of ZJ and the RGB of R, G, and B are 42.75, 36.52, and 33.76, respectively; the differences between the three channels R, G, and B of the square differences of stdRGB are 15.1, 13.89, and 15.35, respectively. It can be seen that there is a relatively obvious RGB gap between ZC108 and ZJ sprouts and old leaves. It is convenient for the model to distinguish the sprouts and old leaves when the model is detected. The differences between the three channels of the sprouts and old leaves of ZH and the RGB of R, G, and B are 1.34, 1.69, and 5.91, respectively; the differences between the three channels R, G, and B of the square differences of stdRGB are 2.13, 6.11, and 0.14, respectively. It can be seen that the RGB of the fresh leaf sprouts of ZH tea is very low, so the detection accuracy of the model to the fresh leaves of ZH is low.

YOLO v7 IMVTS

(**a**)

YOLO v7 IMVTS

(**b**)

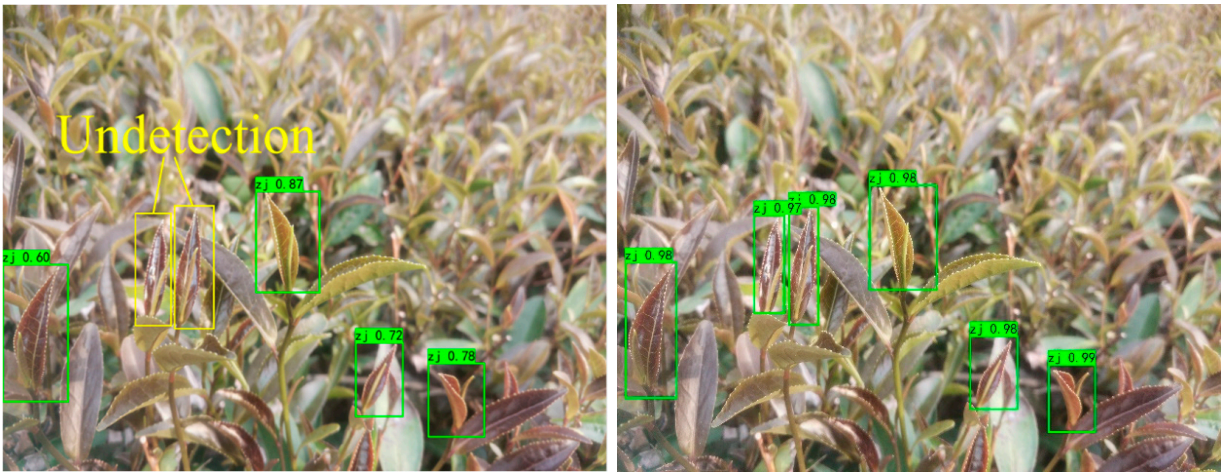

YOLO v7 IMVTS

(**c**)

Figure 8. Comparison of YOLO v7 and IMVTS detection results; (**a**) ZC108; (**b**) ZH; (**c**) ZJ.

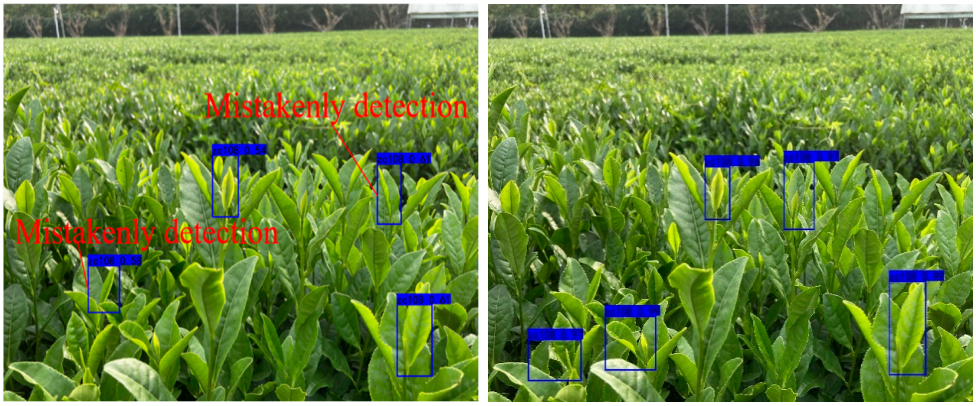

YOLO v7 IMVTS

(**a**)

YOLO v7 IMVTS

(**b**)

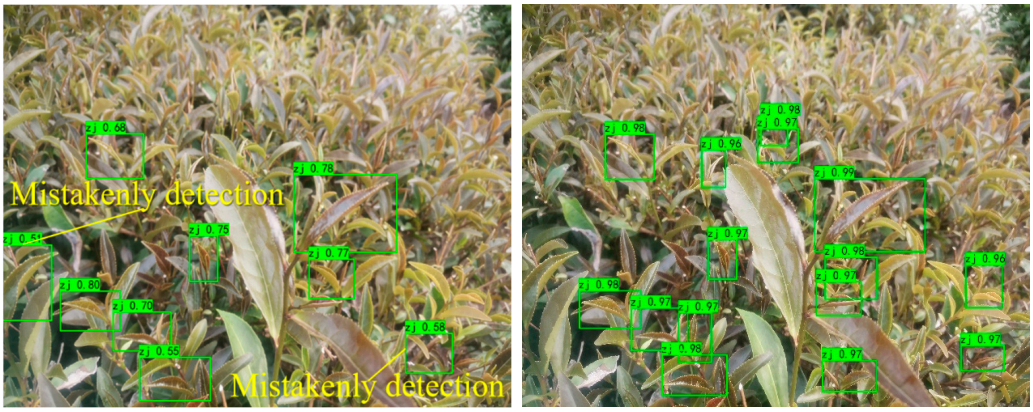

YOLO v7 IMVTS

(**c**)

Figure 9. Errors in the detection of three kinds of fresh tea leaves; (**a**) ZC108; (**b**) ZH; (**c**) ZJ.

Table 5. Comparison of the AP results of different varieties of fresh tea leaves.

Model	ZC108 (AP%)	ZH (AP%)	ZJ (AP%)
YOLO v7	99.79	93.30	99.30
YOLO v7+CBAM	99.87	96.89	99.64
IMVTS	99.87	96.97	99.64

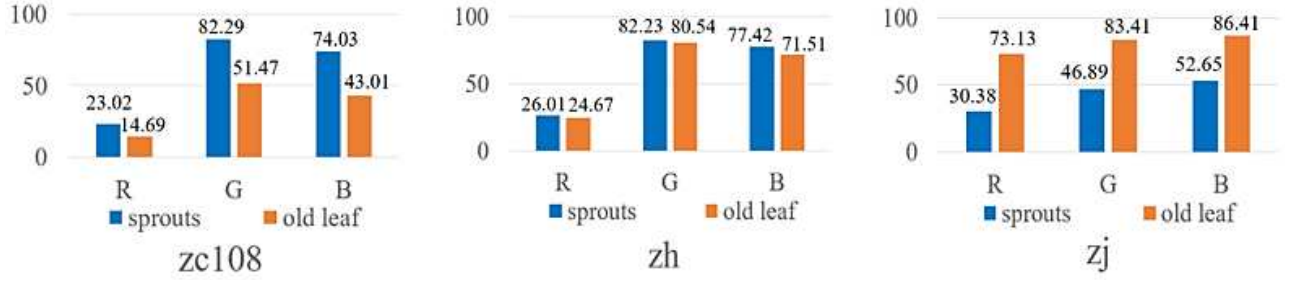

Figure 10. Average RGB of sprouts and old leaves of three varieties of tea.

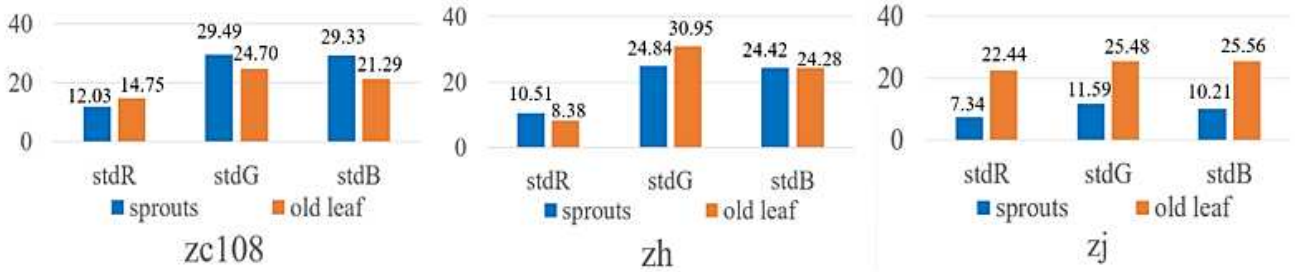

Figure 11. RGB variance stdRGB of sprouts and old leaves of three varieties of tea.

4. Conclusions

This study proposed an identification of multiple varieties of tea sprouts (IMVTS) model for the detection of fresh leaf sprouts of multiple tea species. The model training and validating dataset of multiple varieties of tea (MVT) consisted of images of three representative tea varieties (ZC108, ZH, and ZJ) in Zhejiang Province. To verify the correctness and advantages of the proposed model, IMVTS was compared with YOLO v7 and YOLO v7+CBAM. The results showed that the IMVTS model had the best detection effect, and the mean average precision (mAP) on the MVT dataset was 98.82%, which improved in comparison with YOLO v7 and YOLO v7+CBAM. In addition, this study also conducted comparison tests of the IMVTS model with mainstream target detection models (YOLO v3, YOLO v5, FASTER-RCNN, and SSD) and the IMVTS model on VOC datasets, and the results also demonstrated the superiority of the proposed IMVTS model. The average precision (AP) values of IMVTS for detecting ZC108, ZH, and ZJ tea leaves were 99.87%, 96.97%, and 99.64%, respectively. Among these, the ZH AP value was lower than those of ZJ and ZC108 because the difference in mean RGB and the difference in variance RGB between sprouts and old leaves in ZH images is smaller, and the colors of the object and background are close, making detection more difficult. In summary, the IMVTS model can improve the detection accuracy of fresh leaf sprouts of three varieties of tea, which can meet the requirements for the automatic picking of fresh leaves of the autumn famous tea and provide a basis for the future detection of fresh leaves of additional varieties of autumn tea. Future research will further focus on the improvement and design of the network structure as the IMVTS model detects objects such as ZH that are not clearly distinguished from the background.

Author Contributions: Writing—original draft preparation, R.Z.; methodology and software, C.L.; formal analysis, T.Y.; investigation, J.C.; data curation, Y.L.; supervision, G.L.; project administration, X.H.; writing—review and editing, Z.W. All authors have read and agreed to the published version of the manuscript.

Funding: This research is funded by the National Natural Science Foundation of China (Grant No. 52105284), Science and Technology Program of Meizhou, China (Grant No. 2021A0304004), Postdoctoral Science Foundation of China (Grant No. 2022M722819), and supported by China Agriculture Research System of MOF and MARA, and Key Laboratory of Crop Harvesting Equipment

Technology of Zhejiang Province (Grant No. 2021KZ04). We also thank the anonymous reviewers for their critical comments and suggestions for improving the manuscript.

Institutional Review Board Statement: Not applicable.

Informed Consent Statement: Not applicable.

Data Availability Statement: Data is available on request due to privacy.

Conflicts of Interest: The authors declare no conflict of interest.

References

1. Wang, Z. Design and Experiment of Intelligent Picking Robot for Famous Tea. Ph.D. Thesis, Shenyang University of Technology, Shenyang, China, 2020.
2. Zhou, Y.; Wu, Q.; He, L.; Zhao, R.; Jia, J.; Chen, J.; Wu, C. Design and experiment of intelligent picking robot for famous tea. *J. Mech. Eng.* **2022**, *58*, 12–23.
3. Zhang, L.; Zou, L.; Wu, C.; Jia, J.; Chen, J. Method of famous tea sprout identification and segmentation based on improved watershed algorithm. *Comput. Electron. Agric.* **2021**, *184*, 106108. [CrossRef]
4. Zhang, L.; Zhan, H.; Chen, Y.; Dai, S.; Li, X.; Kenji, I.; Liu, Z.; Li, M. Real-time monitoring of optimum timing for harvesting fresh tea leaves based on machine vision. *Int. J. Agric. Biol. Eng.* **2019**, *12*, 6–9. [CrossRef]
5. Yan, L.; Bengio, Y.; Hinton, G. Deep learning. *Nature* **2015**, *521*, 436–444.
6. Girshick, R. Fast R-CNN. In Proceedings of the 2015 IEEE International Conference on Computer Vision (ICCV), Santiago, Chile, 7–13 December 2015; IEEE: Washington, DC, USA, 2015; pp. 1440–1448.
7. Ren, S.; He, K.; Girshick, R.; Sun, J. Faster R-CNN: Towards real-time object detection with region proposal networks. In Proceedings of the 2015 IEEE Conference on Computer Vision and Pattern Recognition, Boston, MA, USA, 4 June 2015; IEEE: Washington, DC, USA, 2015; pp. 91–99.
8. Redmon, J.; Divvala, S.; Girshick, R. You only look once: Unified, real-time object detection. In Proceedings of the IEEE Conference on Computer Vision and Pattern Recognition, Las Vegas, CA, USA, 8 June 2015; IEEE: Washington, DC, USA, 2016; pp. 779–788.
9. Liu, W.; Anguelov, D.; Erhan, D.; Szegedy, C.; Reed, S.; Fu, C.-Y.; Berg, A.-C. *SSD: Single Shot Multibox Detector. European Conference on Computer Vision*; Springer: Cham, Switzerland, 2016.
10. Li, Y.; He, L.; Jia, J.; Lv, J.; Chen, J.; Qiao, X.; Wu, C. In-field tea shoot detection and 3D localization using an RGB-D camera. *Comput. Electron. Agric.* **2021**, *185*, 106149. [CrossRef]
11. Xu, W.; Zhao, L.; Li, J.; Shang, S.; Ding, X.; Wang, T. Detection and classification of tea buds based on deep learning. *Comput. Electron. Agric.* **2022**, *192*, 106547. [CrossRef]
12. Chen, Y.-T.; Chen, S.-F. Localizing plucking points of tea leaves using deep convolutional neural networks. *Comput. Electron. Agric.* **2020**, *171*, 105298. [CrossRef]
13. Liu, Y.; Cao, X.; Guo, B.; Chen, H.J.; Dai, Z.; Gong, C. Research on detection algorithm about the posture of meat goose in complex scene based on improved YOLO v5. *J. Nanjing Agric. Univ.* **2022**, *32*, 1544–1548.
14. Wang, C.-Y.; Bochkovskiy, A.; Liao, H.-Y.M. YOLOv7: Trainable bag-of-freebies sets new state-of-the-art for real-time object detectors. *arXiv* **2022**, arXiv:2207.02696.
15. Vaswani, A.; Shazier, N.; Parmar, N.; Uszkoreit, J.; Jones, L.; Gomez, A.N.; Kaiser, L.; Polosukhinl, I. Attention is all you need. In Proceedings of the NIPS'17: Proceedings of the 31st International Conference on Neural Information Processing Systems, Long Beach, CA, USA, 4–9 December 2017; pp. 6000–6010.
16. Hu, J.; Shen, L.; Albanie, S.; Sun, G.; Wu, E. Squeeze-and-excitation networks. In Proceedings of the 2018 IEEE/CVF Conference on Computer Vision and Pattern Recognition, Salt Lake City, UT, USA, 18–23 June 2018; IEEE: Washington, DC, USA, 2018; pp. 7132–7141.
17. Woo, S.; Park, J.; Lee, J.-Y. CBAM: Convolutional block attention module. In Proceedings of the 15th European Conference on Computer Vision (ECCV), Munich, Germany, 8–14 September 2018; Springer: Berlin/Heidelberg, Germany, 2018; pp. 3–19.
18. Wang, Q.; Wu, B.; Zhu, P.; Li, P.; Zuo, W.; Hu, Q. ECA-net: Efficient channel attention for deep convolutional neural networks. In Proceedings of the 2020 IEEE/CVF Conference on Computer Vision and Pattern Recognition (CVPR), Seattle, WA, USA, 13–19 June 2022; IEEE: Washington, DC, USA, 2022; pp. 11531–11539.
19. Qi, L.; Gao, J. Small Object Detection Based on Improved YOLOv7. *Comput. Eng.* **2022**, 1000–3428. [CrossRef]
20. Yu, L.; Huang, C.; Tang, J.; Huang, H.; Zhou, Y.; Huang, Y.; Sun, J. Tea Bud Recognition Method Based on Improved YOLOX Model. *Guangdong Agric. Sci.* **2022**, *49*, 49–56.

美国《工程索引》(Ei) 收录期刊
Scopus数据库收录期刊
中文核心期刊　中国科技核心期刊
中国科学引文数据库来源期刊

ISSN 1000-1298
CODEN NUYCA3

农业机械学报

Transactions of the Chinese Society for Agricultural Machinery

专栏主题: 农产品智慧供应链创新技术
专栏主编: 杨信廷 研究员

中国农业机械学会
中国农业机械化科学研究院集团有限公司　主办

2025年
第 56 卷
6

农业机械学报
NONGYE JIXIE XUEBAO

2025 年　第 6 期(第 56 卷)

目　次

农业装备与机械化工程

Transactions of the Chinese Society
for Agricultural Machinery
Vol. 56 No. 6 2025

Contents

Agricultural Equipment and Mechanization Engineering

Agricultural Informatization Engineering

收录情况

★美国《工程索引》(Ei)收录期刊
★美国《化学文摘》(CA)收录期刊
★Scopus 数据库收录期刊
★中文核心期刊
★中国科技核心期刊
★中国科学引文数据库来源期刊
★RCCSE 中国权威学术期刊(A+)

获奖情况

★“中国期刊方阵”双效期刊
★中国农林领域高质量科技期刊分级目录 T1
★中国精品科技期刊
★中国最具国际影响力学术期刊(Top5%)
★中国科协精品科技期刊工程项目资助期刊
★中国机械工业科学技术科技进步二等奖
★中国机械工业集团有限公司优秀科技期刊一等奖

农 业 机 械 学 报
NONGYE JIXIE XUEBAO
2025 年 第 56 卷 第 6 期
(月刊,1957 年创刊)
2025 年 6 月 25 日出版

Transactions of the Chinese Society for Agricultural Machinery
No. 6 Vol. 56 2025
(Monthly, started in 1957)
Published on 25, June 2025

主 管 中国科学技术协会
主 办 中国农业机械学会
中国农业机械化科学研究院集团有限公司
编辑出版 《农业机械学报》编辑部
(地址:北京德外北沙滩 1 号 6 信箱)
邮政编码 100083
主 编 任露泉
印 刷 北京富泰印刷有限责任公司
国内发行 中国邮政集团公司北京报刊发行局
订 购 处 全国各地邮局
国外发行 中国国际图书贸易集团有限公司
(北京 399 信箱)

Responsible Department: China Association for Science and Technology
Sponsored by: Chinese Society for Agricultural Machinery
Chinese Academy of Agricultural Mechanization Sciences Group Co., Ltd.
Published by: Editorial Office of Transactions of the Chinese Society for Agricultural Machinery
Editor in Chief: Ren Luquan
Editorial Office: No. 1 Beishatan, Deshengmen Wai, Beijing 100083, China
Tel: 86-10-64882610/64882231
Fax: 86-10-64867367
http://www.j-csam.org
E-mail: njxb@caams.org.cn
Overseas Distributor: China International Book Trading Corporation
(P. O. Box 399, Beijing, China)

ISSN 1000-1298
CN 11-1964/S
国内邮发代号 2-363 国外发行代号 M289 国内定价 100.00 元

doi:10.6041/j.issn.1000-1298.2025.06.019

水稻收获无人驾驶运粮车粮厢图像轻量化分割模型研究

赵润茂[1,2]　黄嘉涛[1]　满忠贤[1]　罗锡文[1,3]　胡　炼[2,3]　何　杰[1,2]　汪　沛[1,3]　黄培奎[2,3]

（1. 华南农业大学岭南现代农业科学与技术广东省实验室，广州 510642；
2. 农业装备技术全国重点实验室，广州 510642；
3. 华南农业大学南方农业机械与装备关键技术教育部重点实验室，广州 510642）

摘要：针对目前无人驾驶水稻收获机向运粮车转卸稻谷时，依靠收获机和运粮车的北斗定位信息决策卸粮臂位置控制，对靶精度难以保证问题，提出一种粮厢图像视觉分割模型 GTSM，为卸粮臂对靶提供粮厢位置参考信息。在 DeepLabv3 + 结构基础上，使用轻量化主干 ShuffleNetv2 替换 Xception，将 ASPP 模块中空洞卷积替换为深度可分离卷积，然后低秩分解为微因子分解卷积，以减小模型复杂度和提高运行速度；在浅层特征分支引入 SE 通道注意力机制，提高模型对粮厢边缘、纹理等低级特征利用能力。试验结果显示，GTSM 平均交占比和平均像素准确率分别达到 96.06% 和 98.69%，较基准 DeepLabv3 + 分别提升 0.78、0.67 个百分点；同时，模型复杂度明显改善，参数量和内存占用量仅为原来的 1/9，推理速度提高 166%。试验结果表明，提出的 GTSM 兼顾分割精度和推理速度，可为田间运粮车粮厢自动化分割提供参考依据。

关键词：水稻收获；运粮车；无人驾驶；粮厢图像分割；DeepLabv3 +；多机协同作业

中图分类号：S24　　**文献标识码**：A　　**文章编号**：1000-1298(2025)06-0196-09　　**OSID**：

Research on Lightweight Image Segmentation Model for Grain Tank of an Unmanned Grain Cart in Rice Harvesting

ZHAO Runmao[1,2]　HUANG Jiatao[1]　MAN Zhongxian[1]　LUO Xiwen[1,3]　HU Lian[2,3]
HE Jie[1,2]　WANG Pei[1,3]　HUANG Peikui[2,3]

(1. *Guangdong Laboratory for Lingnan Modern Agriculture*, *South China Agricultural University*, *Guangzhou* 510642, *China*
2. *State Key Laboratory of Agricultural Equipment Technology*, *Guangzhou* 510642, *China*
3. *Key Laboratory of Key Technology on Agricultural Machine and Equipment*, *Ministry of Education*, *South China Agricultural University*, *Guangzhou* 510642, *China*)

Abstract: Aiming to address the issue of low targeting accuracy in controlling the unloading arm position during rice transfer from unmanned rice harvesters to grain transport vehicles, which relies on Beidou positioning information of the harvester and transport vehicle, a GTSM network for visual segmentation of grain compartment images was proposed to provide positional reference information for the unloading arm. Based on the DeepLabv3 + architecture, the lightweight ShuffleNetv2 backbone replaced Xception, and the atrous convolutions in the ASPP module were replaced with depthwise separable convolutions, followed by low-rank decomposition into micro-factorized convolutions to reduce model complexity and improve inference speed. Additionally, an SE channel attention mechanism was introduced in the shallow feature branch to enhance the model's ability to utilize low-level features such as grain compartment edges and textures. Experimental results showed that GTSM achieved a mean intersection over union (mIoU) of 96.06% and a mean pixel accuracy (mPA) of 98.69%, representing improvements of 0.78 and 0.67 percentage points, respectively, over the baseline DeepLabv3 +. Meanwhile, model complexity was significantly reduced, with parameter count and memory usage reduced to 1/9 of the original, and inference speed was increased by 166%. These results demonstrated that the proposed GTSM balanced segmentation accuracy and inference speed, providing a reference for automated grain compartment

收稿日期：2025-05-03　修回日期：2025-05-16

基金项目：国家重点研发计划项目(2021YFD2000600)和农业装备技术全国重点实验室(华南农业大学)开放课题项目(SKLAET-202404)

作者简介：赵润茂(1990—)，男，副教授，博士，主要从事水田智能农机装备研究，E-mail：rmzhao@scau.edu.cn

通信作者：胡炼(1984—)，男，研究员，博士，主要从事智能农机装备和无人农场研究，E-mail：lianhu@scau.edu.cn

segmentation in field grain transport vehicles.

Key words: rice harvesting; grain cart; driverless operation; grain tank image segmentation; DeepLabv3 +; multi-vehicle collaboration operation

0　引言

在水稻机械化收获过程中,受粮厢容量限制,收获机需多次往返田间与卸粮点[1]。通过合理配置运粮车转运粮食,可有效提升收获效率[2]。人工驾驶模式下,操作人员通过调整收获机与卸粮臂位置和角度,可使其精准对准运粮车粮厢。而在无人驾驶收获机-运粮车协同作业场景中,卸粮行为完全依赖运粮车与收获机的相对位置决策系统[1],若二者位置控制或卸粮臂定位出现偏差,将直接导致卸粮臂与运粮车粮厢对接失效,致使卸粮任务失败。为实现精准对靶与高效卸粮,要准确感知收获机与运粮车的空间相对位置和姿态,图像分割可有效提取粮厢边界与位置信息,为后续的定位与控制决策提供支撑。

视觉传感器可以感受视野内的语义信息,结合深度学习算法,实现特定目标的分割和提取[3-5]。但是,受推理速度的限制,难以在边缘设备实际应用。为此,部分学者通过网络结构优化[6-11]去除冗余参数,平衡模型分割精度和推理速度,开发适合资源受限等嵌入式设备的部署模型。

基于深度学习的语义分割在田间道路识别、病害分割、作物提取等任务的应用,验证了复杂大田环境下模型分割的有效性及可行性。针对运粮车粮厢颜色与水稻作物颜色相近,卸粮臂出谷过程有大量粉尘影响图像质量,田间光线变化大,粮厢边缘有其它设备导致轮廓不明显的问题,本文基于精度较高的 DeepLabv3 + 模型进行粮厢分割实验。为平衡模型分割准确性与推理速度,满足在嵌入式等轻量化设备的部署,提出一种轻量化运粮车粮厢分割模型(Grain tank segmentation model, GTSM),基于 DeepLabv3 +,选择轻量化的 ShuffleNetv2 替换原网络中的特征提取主干,引入微因子分解卷积替换空间空洞金字塔池化模块(Atrous spatial pyramid pooling,ASPP)中的空洞卷积,以减少模型参数量并提高推理速度;在主干输出浅层特征分支引入通道注意力机制,以提高模型对粮厢边缘特征的提取能力。

1　材料与方法

1.1　运粮车图像获取和标注

在广东省河源市东源县柳城镇万绿智慧无人农场(24.012 180° N,115.118 903° E)采集运粮车图像共 3 891 幅。采样时间为 2024 年 11 月 1—3 日,采样设备为 Redmi K50 Pro 手机,成像分辨率为 4 000 像素 ×3 000 像素,以 jpg 格式保存,图像示例如图 1a 所示,包含运粮车粮厢有稻谷和无稻谷两种情况。经过人工筛选,选取 678 幅图像作为数据集,按照比例 9∶1 划分为训练集和验证集,得到训练集共 610 幅图像,验证集共 68 幅图像。采用 Labelme 对原始图像的运粮车粮厢和背景进行精确划分,像素值分别被标记为 0 和 1,通过可视化操作赋予对应像素颜色值,标签样例如图 1b 所示。

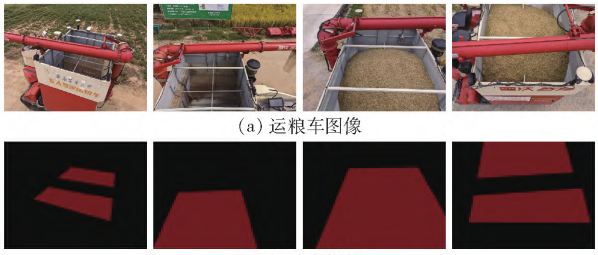

(a) 运粮车图像

(b) 运粮车标签

图 1　运粮车数据集示例

Fig. 1　Grain transport vehicle dataset example

1.2　数据增强

由于较大的图像分辨率影响训练效率,采用等比例缩放并填充图像至 512 像素 ×512 像素。为了提高模型泛化能力,适应复杂田间环境,在训练过程中采用随机样本扩增的方式增加数据量,流程如图 2 所示,包括随机翻转、随机旋转、色域变换和高斯模糊等方法。每种方法触发概率为 50%。其中,随机翻转包括水平和垂直方向,随机旋转有旋转角度 90°、180°或 270°,以解决方向不变性问题;色域

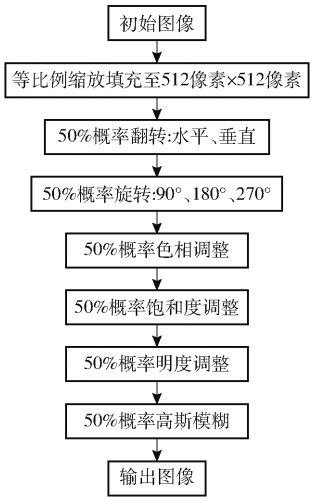

图 2　随机样本扩增流程图

Fig. 2　Random sample augmentation process

变换在 HSV 色彩空间进行，色相调整幅度为 ±10%，饱和度调整幅度为 ±30%，明度调整幅度为 ±25%，可以较好模拟田间复杂光线变化；为模拟农机震动导致成像模糊，设置高斯模糊均值为 0、标准差为 1。数据增强效果如图 3 所示。

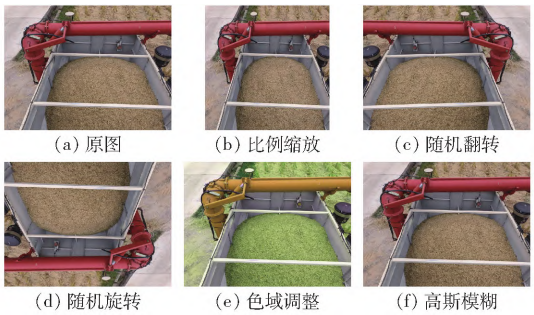

图 3 数据增强效果

Fig. 3 Data augmentation effect

1.3 运粮车粮厢快速分割模型

DeepLabv3 +[12] 为经典语义分割网络架构，包含编码器(Encoder)和解码器(Decoder)两部分。编码阶段先通过特征主干网络 Xception 进行下采样，获得浅层特征送入解码器，在空间金字塔池化模块通过不同膨胀率的空洞卷积和池化操作，利用不同感受野进行多尺度信息提取，获得深层特征。在解码阶段，深层特征经过上采样恢复分辨率后与浅层特征融合，最终通过双线性插值(Bilinear interpolation)上采样后恢复图像原始尺寸，输出像素级分割结果。

得益于包含大量参数的 Xception 特征提取主干[13]和复杂度较高的空间空洞金字塔池化模块[14]，标准的 DeepLabv3 + 网络分割精度高，但也限制了其在轻量化嵌入式设备的部署。因此，为了减少模型参数量、降低计算复杂度，提高推理速度，采用 ShuffleNetv2 作为轻量化特征提取主干，并引入微因子分解卷积，通过低秩分解降低 ASPP 模块参数量。考虑到运粮车粮厢边缘不规则，存在非目标干扰因素，导致边缘分割精度不高的问题，在主干提取低级特征输出后引入 SE 注意力机制，赋予不同通道关注权重，提高模型对颜色、边缘和纹理等浅层特征的学习能力，GTSM 结构如图 4 所示。

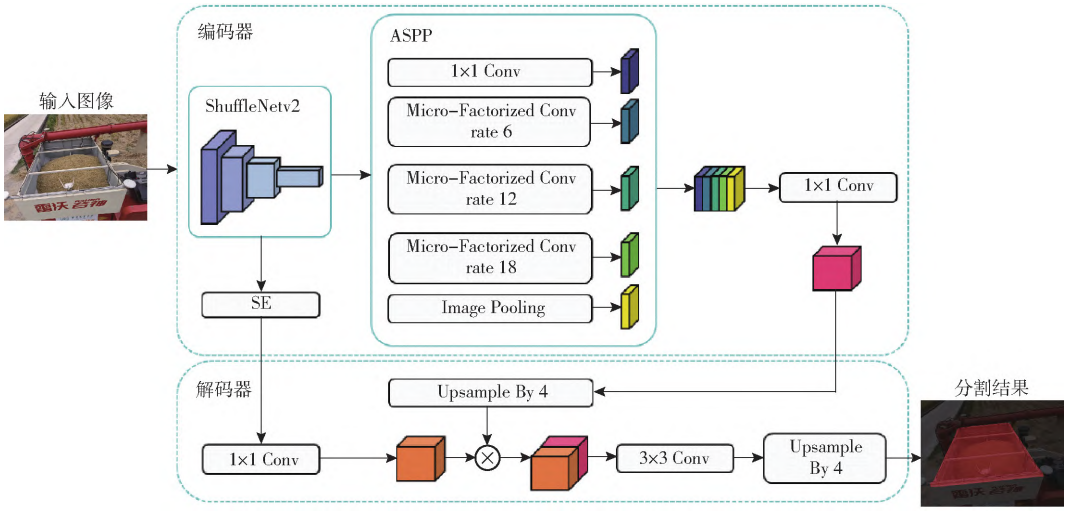

图 4 GTSM 结构

Fig. 4 GTSM structure

1.3.1 ShuffleNetv2 轻量化特征提取主干

ShuffleNetv2[15] 是以模型运行速度为优化对象的轻量级网络架构，旨在保证模型性能的同时大幅减小参数量并加快运算速度。输入图像依次经过第 1 阶段的 3 × 3 卷积核和全局最大池化进行两次下采样，然后重复 3 个相同的单元(stage)进行深层特征提取。每个单元都由 stride 为 1 的基本模块和 stride 为 2 的下采样模块组成，两者结构如图 5 所示，每个模块均含 2 个分支，通过拼接(Concat)后进行通道重排(Channel Shuffle)。经过 5 次下采样后，特征图尺寸变为原来的 1/32，通过 1 × 1 卷积调整通道数为类别数，经过全局池化得到全连接层后分类。

本研究提出将 ShuffleNetv2 模块作为 DeepLabv3 + 轻量化特征提取主干，网络结构及详细参数如表 1 所示。在改进标准 ShuffleNetv2 网络过程中，首先，综合考虑分割精度和计算效率，选择宽度因子为 1.5 的 ShuffleNetv2 作为基准特征提取主干；其次，去除用于调整输出通道数的 1 × 1 卷积、GAP 和 FC，使得特征提取主干的输出通道数为 704；随后，替换 32 倍下采样为 8 倍下采样，即将 Stage3 和 Stage4 中下采样模块的深度卷积 stride 调整为 1；最后，为了扩大感受野，将 Stage3 和 Stage4 中的深度卷积替换为深度膨胀卷积，具体地，Stage3

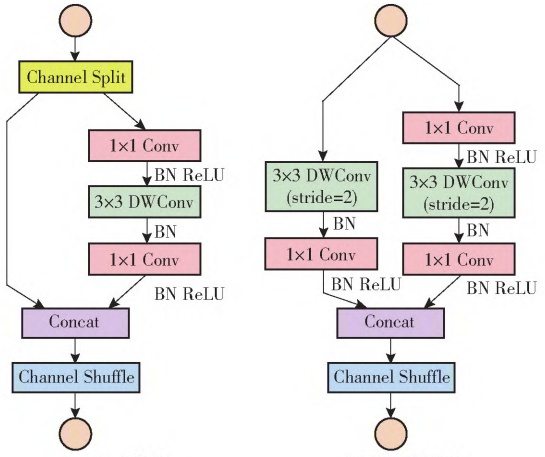

图 5　ShuffleNetv2 模块图

Fig. 5　ShuffleNetv2 module diagram

表 1　ShuffleNetv2 轻量化特征提取主干结构

Tab. 1　Lightweight ShuffleNetv2 feature extraction backbone structure

层	输出尺寸/（像素×像素）	卷积核大小	步长	空洞率	重复次数	输出通道数
Image	512×512					3
Conv1	256×256	3×3	2		1	24
MaxPool	128×128	3×3	2			
Stage2	64×64		2		1	176
	64×64		1		3	
Stage3	64×64		1	2	1	352
	64×64		1	2	7	
Stage4	64×64		1	4	1	704
	64×64		1	4	3	

中的卷积核膨胀率和填充设置为 2，Stage4 中的膨胀率和填充则设置为 4，以确保特征图输出尺寸保持不变。通过上述改进，ShuffleNetv2 作为 DeepLabv3 + 的轻量化特征提取主干，既降低了模型复杂度，又确保了足够语义信息供 ASPP 模块使用，提升了整体性能和效率。

1.3.2　微因子分解卷积和 ASPP 模块优化

微因子分解卷积（Micro-factorized convolution，MFC）由微分解点卷积（Micro-factorized pointwise convolution，MF－PWC）和微分解深度卷积（Micro-factorized depthwise convolution，MF－DWC）两部分组成，通过分解逐点卷积和深度卷积，降低网络连通性，提高计算效率。

微分解深度卷积在空间维度将一个标准卷积核拆分成多个小卷积核，具体表现为分解 $k\times k$ 大小的深度卷积核为 $k\times 1$ 和 $1\times k$，计算量则由 $O(k^2C)$ 降低到了 $O(kC)$，C 为特征通道数，分解过程如图 6 所示。

微分解点卷积将标准 1×1 点卷积因式分解为

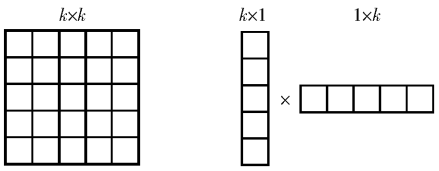

图 6　微分解深度卷积分解

Fig. 6　Micro-factorized depthwise convolution decomposition

2 个自适应点组卷积，中间插入通道重排，进而实现特征通道的压缩与扩展，矩阵分解过程如图 7 所示。计算复杂度由 $O(C^2)$ 变为 $O(2C^2/(RG))$，G 为分组数，R 为压缩因子。为保证计算复杂度降低的同时，使得通道间尽可能连接，应满足关系[16]

$$G=\sqrt{\frac{C}{R}} \tag{1}$$

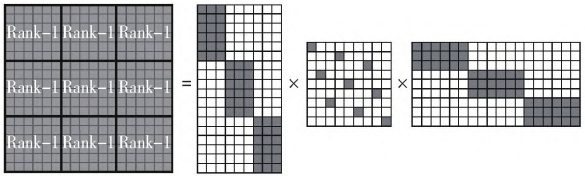

图 7　微分解点卷积矩阵分解

Fig. 7　Micro-factorized pointwise convolution matrix decomposition

ASPP 模块使用不同空洞率的空洞卷积扩展感受野，实现多尺度信息融合，避免了局部特征和全局上下文信息的丢失，然而，不同空洞率的卷积并行排列，增加了模型参数和计算量。为了降低模型复杂度，提高计算效率，在保留空洞卷积空洞率的情况下，将卷积替换为深度可分离卷积，初步减少参数量，再引入微因子分解卷积对深度可分离卷积进行低秩分解，进一步减小模型参数量，降低模型复杂度。

1.3.3　注意力机制

注意力机制用于提升模型对重要特征的关注能力，诸如 SE[11－18]、ECA[19－20]、SAM、CBAM[21－23]、CA[24－25]等注意力机制已经大量应用于识别、分类和分割等任务，取得了显著的效果。为准确分割粮厢边缘，使边缘纹理、颜色特征提取更加高效，本研究在浅层特征分支引入 SE 通道注意力机制。

SE 注意力机制[26]通过自适应调整每个通道的权重，支持网络强化更重要的特征通道，通过压缩、激励和重新加权 3 个阶段实现，其结构如图 8 所示。输入特征图 $X\in\mathbf{R}^{H\times W\times C}$，其中，$H$ 为高度，W 为宽度，C 为通道数。

首先，对每个通道进行全局平均池化，将每个通道的空间信息压缩为一个数值，公式为

$$s_c=F_{sq}(x_c)=\frac{1}{HW}\sum_{i=1}^{H}\sum_{j=1}^{W}x_c(i,j) \tag{2}$$

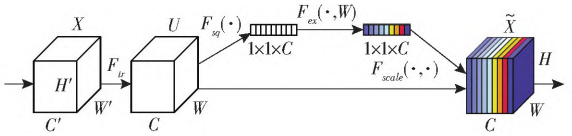

图 8 SE 模块结构

Fig. 8 SE module architecture

得到一个 C 维的向量 $\boldsymbol{s}=(s_1,s_2,\cdots,s_C)$，代表每个通道的全局描述。接下来，通过 2 个全连接层 W_1、W_2对向量 $\boldsymbol{s}$ 进行非线性变换，将每个通道的评分转换为介于 0 到 1 之间的权重，过程表示为

$$z=F_{ex}(\boldsymbol{s},W)=\sigma(W_2\delta(W_1\boldsymbol{s})) \tag{3}$$

式中 σ——Sigmoid 激活函数

δ——ReLU 激活函数

最后，将生成的通道权重与原始特征图对应的每个通道进行逐元素相乘，得到特征图 $\tilde{X}$，表达式为

$$\tilde{X}=F_{\text{scale}}(z_c,x_c)=z_cx_c \tag{4}$$

1.3.4 Dice－Focal 损失函数

为了应对粮厢分割过程正负样本不平衡，缓解粮厢边缘轮廓不规则导致边缘识别和分割效果欠佳的问题，在原有交叉熵损失的基础上，融合 Dice 损失和 Focal 损失。Focal 损失 L_{FL}、Dice 损失 $L_{\text{Dice}(p,g)}$、总损失 L_{total}的计算式为

$$L_{\text{FL}}(p_t)=-\alpha_t(1-p_t)^{\gamma}\lg p_t \tag{5}$$

$$L_{\text{Dice}(p,g)}=1-\frac{2\sum_{i=1}^{N}p_ig_i}{\sum_{i=1}^{N}p_i+\sum_{i=1}^{N}g_i} \tag{6}$$

$$L_{\text{total}}=\lambda_1L_{\text{CE}}+\lambda_2L_{\text{FL}}+\lambda_3L_{\text{Dice}} \tag{7}$$

式中 p_t——模型对真实类别的预测概率

α_t——调节正负样本重要性的平衡因子

γ——聚焦系数，用于调整难易分类样本的权重

p_i——第 i 像素预测为目标类别的概率

g_i——第 i 像素真实标签

L_{CE}——交叉熵损失函数

$\sum_{i=1}^{N}p_ig_i$——预测与真实标签重叠区域

$\sum_{i=1}^{N}p_i+\sum_{i=1}^{N}g_i$——预测与真实标签的总区域

λ_1、λ_2、λ_3——权重

2 结果与讨论

2.1 试验环境

本研究的模型试验均在 64 位 Windows 10 操作系统下进行，内存为 64 GB，显卡为 NVIDIA GeForce RTX 3090，搭载 Intel(R) Core(TM) i9－10980XE CPU 处理器。计算机采用深度学习框架 Pytorch 1.10.0 版本，安装 CUDA 12.6 版本进行并行计算，Python 版本为 3.8。

2.2 评价指标

评价语义分割模型的效果，从性能、推理速度和复杂度等多方面衡量。性能指标采用平均交占比(Mean intersection over union，mIoU)、平均像素准确率(Mean pixel accuracy，mPA)；推理速度用帧速(Frames per second，FPS)来衡量；复杂度包括浮点运算量、参数量(Parameter count)和内存占用量(Model size)，评价模型在嵌入式设备部署的适用性。

2.3 不同注意力机制对比

为了使得模型充分利用粮厢颜色、边缘等低级特征，提升对目标区域的关注度，在浅层特征分支输出添加不同的注意力模块进行对比。表 2 展示了分别将 CA、ECA、SE、SAM、CBAM 注意力机制引入标准 DeepLabv3＋时粮厢分割性能。

表 2 不同注意力机制性能对比

Tab. 2 Comparison of different attention mechanisms

%

添加注意力模块	mIoU	mPA
CA	95.15	97.81
ECA	95.18	98.00
SE	95.39	98.08
SAM	95.24	98.02
CBAM	95.25	97.88

由表 2 可得，加入 CA、ECA、SE、SAM、CBAM 5 种注意力机制，mIoU 相较于标准 DeepLabv3＋模型分别提高 0.05、0.05、0.26、0.11、0.12 个百分点，mPA 分别提高 0.04、0.23、0.31、0.25、0.11 个百分点。相较而言，得益于 SE 注意力模块在捕捉通道信息方面的优势，强化了粮厢边缘、颜色特征表达，从而提高了 DeepLabv3＋模型分割效果，mIoU 和 mPA 分别达到 95.39% 和 98.08%。

2.4 不同模型性能对比

为了评价 GTSM 性能，采用 UNet、DeepLabv3＋、PSPNet 主流语义分割模型，在自建运粮车数据集上采用相同配置参数训练，均添加 Dice－Focal 损失函数。各模型训练过程损失曲线如图 9 所示，损失值随着训练轮次的增加而减小，并趋于收敛，没有发生过拟合现象。在验证集上对比不同模型的 mIoU、mPA、参数量、内存占用量和浮点运算量，结果如表 3 和图 10 所示，图 10 中图像 1～5 分别对应情况：粮厢有稻谷的标准对靶视角、粮厢无稻谷的标准对靶视角、卸粮臂正在出粮、卸粮臂复杂转角和远距离小目标粮厢。

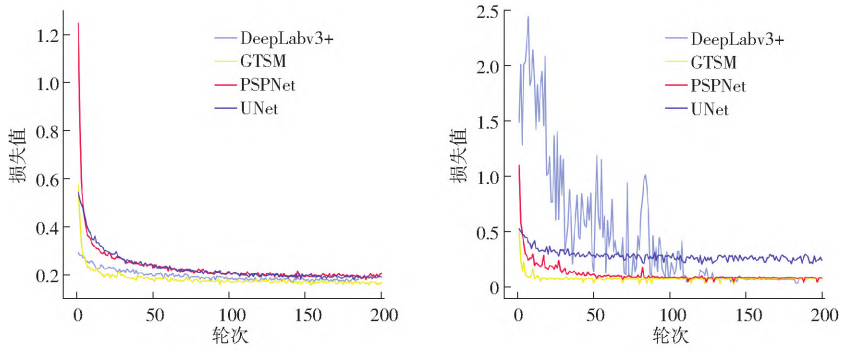

图 9　模型训练损失曲线

Fig. 9　Training loss

表 3　不同模型性能对比

Tab. 3　Comparison of performance of different models

模型	主干网络	平均交占比/%	平均准确率/%	参数量	内存占用量/MB	浮点运算量	推理速度/(f·s^{-1})
UNet	VGG	93. 39	97. 51	2.489×10^{7}	94. 95	$2.258\,4\times10^{11}$	33. 75
DeepLabv3 +	Xception	95. 29	98. 02	5.490×10^{7}	209. 42	$8.342\,0\times10^{11}$	16. 14
PSPNet	ResNet	94. 06	97. 59	4.913×10^{7}	187. 40	$1.944\,0\times10^{11}$	33. 73
GTSM	ShuffleNetv2	96. 07	98. 69	5.620×10^{6}	21. 43	$2.404\,0\times10^{10}$	42. 93

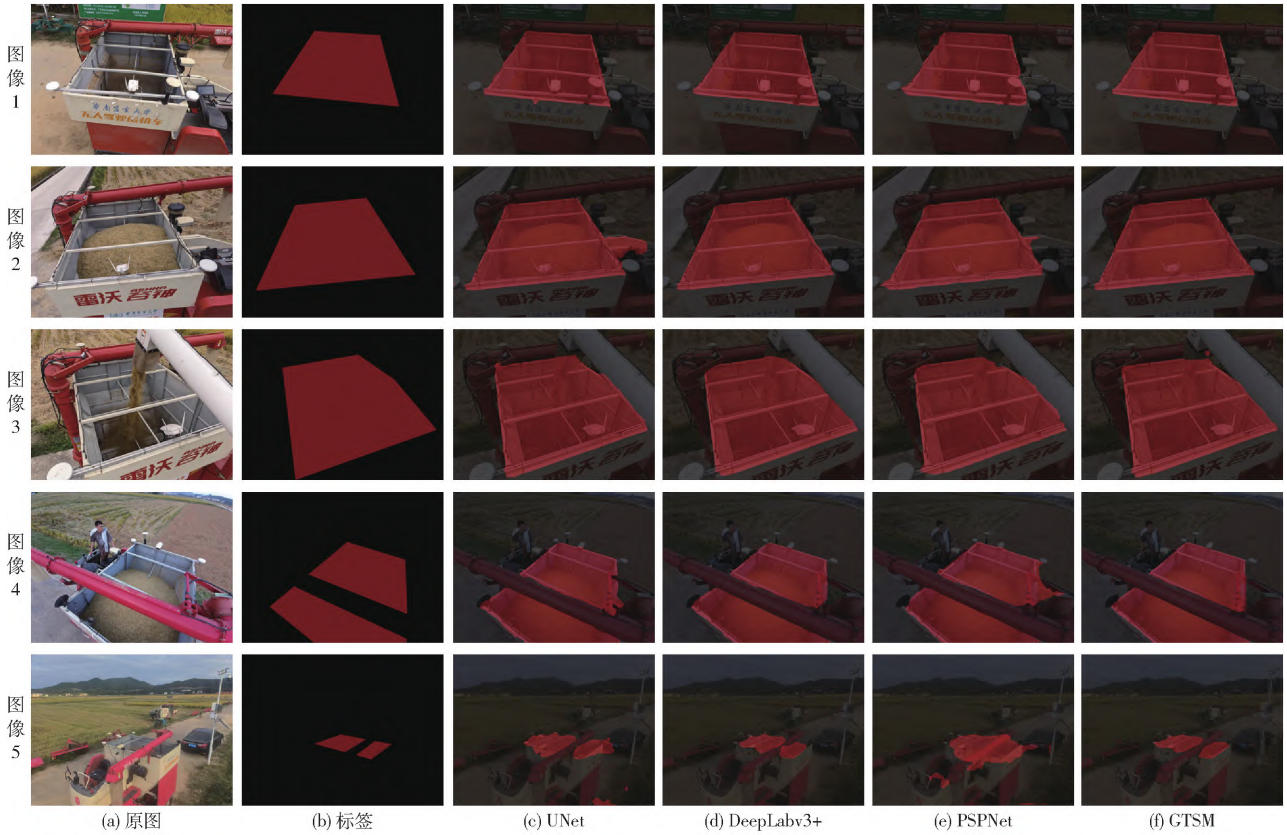

图 10　不同模型分割结果

Fig. 10　Segmentation results of different models

由表 3 可见，GTSM 性能指标表现较好，mIoU 达到 96. 07%，mPA 为 98. 69%，较基准模型 DeepLabv3 + 分别提高 0. 78、0. 67 个百分点，较 UNet 模型分别提高 2. 68、1. 18 个百分点，较 PSPNet 模型分别提高 2. 01、1. 1 个百分点。此外，GTSM 参数量仅 5.62×10^{6}，内存占用量 21. 43 MB，规模远小于其他模型，浮点运算量和推理速度分别为 $2.404\,0\times10^{10}$ 和 42. 93 f/s，相比其他模型复杂度更低，推理速度更快，更适合部署到资源受限的移动设备，提供准确、高效的卸粮目标区域实时检测。

观察图像 1,4 种模型分割效果相近,可以很好分割出粮厢区域;由于图像 2 粮厢中有稻谷,PSPNet 和 UNet 对于粮厢内外稻谷区分能力不足,导致错误识别粮厢外水稻为目标区域;图像 3 中除了 PSPNet,其他模型对于粮厢轮廓分割效果较好,但对白色卸粮臂分割效果稍欠;图像 4 中除了 GTSM,其余模型对于卸粮臂复杂转角分割效果不佳,PSPNet 仍错误划分粮厢外稻杆为目标区域;图像 5 的粮厢是远距离小目标,各模型识别能力不足。综合来看,GTSM 分割效果较好,与基准网络 DeepLabv3 + 相近,说明其在模型参数量大幅减少的情况下仍保持较好分割效果,另外,得益于浅层网络分支引入的通道注意力机制,使模型更适合粮厢轮廓分割,得到平滑分割曲线结果,而对于图像 4 复杂转角和图像 5 等小样本视角,后续可以通过扩充数据集的方式提升模型泛化性能。

2.5 消融试验

为了验证提出的改进方法对于粮厢分割任务的有效性,在自建数据集进行消融试验,并与基准网络 DeepLabv3 + 对比。消融试验结果如表 4 所示,各模型训练参数一致,均添加 Dice - Focal 损失函数。

表 4 消融试验结果

Tab. 4 Ablation experiments

试验序号	Backbone	SE	ASPP	Dw - ASPP	Micro - ASPP	mIoU/%	mPA/%	参数量	内存占用量/MB	浮点运算量	推理速度/(f·s^{-1})
1	Xception	-	√	-	-	95.29	98.02	5.49×10^{7}	209.42	8.342×10^{10}	16.22
2	ShufflNetv2	-	√	-	-	95.95	98.63	1.04×10^{7}	39.62	2.893×10^{10}	45.79
3	ShufflNetv2	-	-	√	-	95.80	98.53	6.08×10^{6}	23.20	2.452×10^{10}	44.38
4	ShufflNetv2	-	-	-	√	95.96	98.61	5.62×10^{6}	21.43	2.404×10^{10}	42.36
5	ShufflNetv2	√	√	-	-	96.10	98.64	1.04×10^{7}	39.62	2.893×10^{10}	42.37
6	ShufflNetv2	√	-	√	-	95.94	98.59	6.08×10^{6}	23.20	2.452×10^{10}	43.82
7	ShufflNetv2	√	-	-	√	96.07	98.69	5.62×10^{6}	21.43	2.404×10^{10}	42.93

注:√表示引入此模块;-表示没有引入此模块;Dw - ASPP 表示使用深度可分离卷积改进 ASPP 模块;Micro - ASPP 表示使用微因子分解卷积改进 ASPP 模块。

表 4 显示,DeepLabv3 + 的特征提取主干由 Xception 替换为轻量化模块 ShuffleNetv2 后,虽然参数量减小 81%,但是模型分割精度没有降低,反而有小幅提高,得益于 ShuffleNetv2 以运行速度为直接优化目标,使得模型复杂度大大降低,计算量减少 65%,推理速度提高 29.57 f/s,达到 45.79 f/s。对比试验 2、5,试验 3、6,以及试验 4、7,SE 注意力机制的加入一定程度上提升了模型分割性能,但没有增加较多的参数,而且对计算复杂度和推理速度没有影响,表明 SE 模块能够很好地捕捉和利用低级特征通道间的相关信息,从而改善分割结果,并保持模型的轻量化。对比试验 2、3、4 和试验 5、6、7,采用深度可分离卷积和微因子分解卷积改进 ASPP 模型后,模型参数量、计算量以及内存占用量逐步减小,但性能指标变化不大,表明深度可分离卷积和微因子分解卷积在不影响 ASPP 模块利用深层特征的情况下,均能够有效降低模型复杂度。对比试验 1、7,改进模型不仅便于在轻量化的嵌入式设备部署,还能够很好地完成粮厢实时检测任务。

3 结论

(1)围绕无人驾驶收获机向运粮车转卸稻谷时,卸粮臂对运粮车粮厢位置精准定位的需求,提出一种 Grain tank segmentation model(GTSM),对运粮车粮厢图像分割。

(2)以运粮车粮厢快速分割为研究目标,针对现有模型复杂度高、推理速度慢的问题,提出轻量化 GCSM 结构。该模型参数量 5.62×10^{6},内存占用量 21.43 MB,仅为基准网络的 1/10,浮点运算量为 2.404×10^{10},平均推理速度达 42.93 f/s,满足轻量化部署和实时性检测需求。

(3)为提高粮厢分割精度,采用 ShuffleNetv2 作为轻量化特征提取主干,在主干浅层特征输出引入 SE 通道注意力,并采用微因子分解卷积对 ASPP 模块低秩分解,进一步降低模型参数量。试验证明,GTSM 性能均高于 UNet、PSPNet 和 DeepLabv3 +,粮厢分割平均交占比达到 96.07%,平均像素精度达到 98.69%,满足田间运粮车粮厢自动化分割需求。

参 考 文 献

[1] 张闻宇,张智刚,张帆,等. 水稻收获转运双机协同自主作业策略与试验[J]. 农业工程学报,2022,38(15):1-9.
ZHANG Wenyu, ZHANG Zhigang, ZHANG Fan, et al. Cooperative autonomous operation strategy and experiment of the rice

harvester together with a rice-transporting vehicle[J]. Transactions of the CSAE,2022,38(15):1 - 9. (in Chinese)
[2] 满忠贤,何杰,刘善琪,等. 智能农机多机协同收获作业控制方法与试验[J]. 农业工程学报,2024,40(1):17 - 26.
MAN Zhongxian,HE Jie,LIU Shanqi,et al. Method and test for operating multi-machine cooperative harvesting in intelligent agricultural machinery[J]. Transactions of the CSAE,2024,40(1):17 - 26. (in Chinese)
[3] DING Y J,YANG W T,ZHANG J J,et al. An improved DeepLabV3 + based approach for disease spot segmentation on apple leaves[J]. Computers and Electronics in Agriculture,2025,231:110041.
[4] ZHANG L,MING L,ZHU X H,et al. Navigation path recognition between rows of fruit trees based on semantic segmentation [J]. Computers and Electronics in Agriculture,2024,216:108511.
[5] 李振东,李云飞,杨立伟,等. 基于改进 UNet 的樱桃树枝直径计算方法[J]. 农业机械学报,2024,55(增刊 1):263 - 269.
LI Zhendong,LI Yunfei,YANG Liwei,et al. Calculation method for cherry branch diameter based on improved UNet[J]. Transactions of the Chinese Society for Agricultural Machinery,2024,55(Supp. 1):263 - 269. (in Chinese)
[6] 杨宁,程巍,张钊源,等. 基于 FPGA 加速的 Mask R - CNN 稻瘟病高通量自适应识别模型研究[J]. 农业机械学报,2024,55(7):298 - 304.
YANG Ning,CHENG Wei,ZHANG Zhaoyuan,et al. Mask R - CNN based on-chip recognition algorithm for rice blast image [J]. Transactions of the Chinese Society for Agricultural Machinery,2024,55(7):298 - 304. (in Chinese)
[7] 顾文娟,魏金,阴艳超,等. 基于改进 DeepLabv3 + 的番茄图像多类别分割方法[J]. 农业机械学报,2023,54(12):261 - 271.
GU Wenjuan,WEI Jin,YIN Yanchao,et al. Multi-category segmentation method of tomato image based on improved DeepLabv3 + [J]. Transactions of the Chinese Society for Agricultural Machinery,2023,54(12):261 - 271. (in Chinese)
[8] 侯文慧,周传起,程炎,等. 基于轻量化 U - Net 网络的果园垄间路径识别方法[J]. 农业机械学报,2024,55(2):16 - 27.
HOU Wenhui,ZHOU Chuanqi,CHENG Yan, et al. Path recognition method of orchard ridges based on lightweight U - Net[J]. Transactions of the Chinese Society for Agricultural Machinery,2024,55(2):16 - 27. (in Chinese)
[9] LIU R,WANG D,CHEN Z,et al. Recognition of tea sprouts based on improved DeepLabV3 + model[J/OL]. Multimed Tools Appl.,2025. https://doi.org/10.1007/s11042 - 024 - 20570 - 8.
[10] SUN J W,ZHOU J,HE Y Q,et al. RL - DeepLabv3 +:a lightweight rice lodging semantic segmentation model for unmanned rice harvester[J]. Computers and Electronics in Agriculture,2023,209:107823.
[11] 曹英丽,赵雨薇,杨璐璐,等. 基于改进 DeepLabv3 + 的水稻田间杂草识别方法[J]. 农业机械学报,2023,54(12):242 - 252.
CAO Yingli,ZHAO Yuwei,YANG Lulu,et al. Weed identification method in rice fielf based on improved DeepLabv3 + [J]. Transactions of the Chinese Society for Agricultural Machinery,2023,54(12):242 - 252. (in Chinese)
[12] CHEN L C,ZHU Y K,PAPANDREOU G,et al. Encoder-decoder with atrous separable convolution for semantic image segmentation[J]. arXiv Preprint,arXiv:1802.02611v3,2018.
[13] CHOLLET F. Xception: deep learning with depthwise separable convolutions[C]// Proceedings of the IEEE Conference on Computer Vision and Pattern Recognition (CVPR),2017:1251 - 1258.
[14] YU F,KOLTUN V. Multi-scale contnxt aggregation by dilated convolutions[J]. arXiv Preprint,arXiv:1511.07122v3,2015.
[15] MA N N,ZHANG X Y,ZHENG H T,et al. ShuffleNet V2: practical guidelines for efficient CNN architecture design[J]. arXiv Preprint,arXiv:1807.11164,2018.
[16] LI Y S,CHEN Y P,DAI X Y,et al. MicroNet: towards image recognition with extremely low FLOP[J]. arXiv Preprint,arXiv: 2011.12289v1,2020.
[17] 赵晋陵,詹媛媛,王娟,等. 基于 SE - UNet 的冬小麦种植区域提取方法[J]. 农业机械学报,2022,53(9):189 - 196.
ZHAO Jinling, ZHAN Yuanyuan, WANG Juan, et al. SE - UNet-based extraction of winter wheat planting areas [J]. Transactions of the Chinese Society for Agricultural Machinery,2022,53(9):189 - 196. (in Chinese)
[18] 武锦龙,吴虹麒,李浩,等. 基于改进 DeepLabV3 + 的荞麦苗期无人机遥感图像分割识别方法研究[J]. 农业机械学报,2024,55(5):186 - 195.
WU Jinlong,WU Hongqi,LI Hao,et al. Segmentation of buckwheat by UAV based on improved lightweight DeepLabv3 + at seedling stage[J]. Transactions of the Chinese Society for Agricultural Machinery,2024,55(5):186 - 195. (in Chinese)
[19] 袁培森,欧阳柳江,翟肇裕,等. 基于 MobileNetV3Small - ECA 的水稻病害轻量级识别研究[J]. 农业机械学报,2024,55(1):253 - 262.
YUAN Peisen,OUYANG Liujiang,ZHAI Zhaoyu,et al. Lightweight identification of rice diseases based on improved ECA and MobileNetV3Small[J]. Transactions of the Chinese Society for Agricultural Machinery,2024,55(1):253 - 262. (in Chinese)
[20] 袁杰,谢霖伟,郭旭,等. 基于改进 YOLO v7 的苹果叶片病害检测方法[J]. 农业机械学报,2024,55(11):68 - 74.
YUAN Jie,XIE Linwei,GUO Xu,et al. Apple leaf disease detection method based on improved YOLO v7[J]. Transactions of the Chinese Society for Agricultural Machinery,2024,55(11):68 - 74. (in Chinese)
[21] 吕继东,翟志强,孟庆建,等. 基于车载成像与深度卷积神经网络的地表残膜识别方法[J]. 农业机械学报,2025,56(5):26 - 37.
LÜ Jidong,ZHAI Zhiqiang,MENG Qingjian,et al. Surface residual film recognition method based on vehicle-mounted imaging and deep convolutional neural networks[J]. Transactions of the Chinese Society for Agricultural Machinery,2025,56(5):26 - 37. (in Chinese)

[22] 王发明,倪昕东,张旗,等. 基于 MobileNetV2 - CBAM 的机收场景下冬小麦成熟期在线分类识别方法[J]. 农业机械学报,2024,55(增刊 1):71 - 80,100.
WANG Faming,NI Xindong,ZHANG Qi,et al. Online classification and identification method of winter wheat maturity under mechanical harvesting scenario based on MobileNetV2 - CBA[J]. Transactions of the Chinese Society for Agricultural Machinery,2024,55(Supp. 1):71 - 80,100. (in Chinese)

[23] 李凯雨,朱昕怡,马浚诚,等. 基于混合扩张卷积和注意力的黄瓜病害严重度估算方法[J]. 农业机械学报,2023,54(2):231 - 239.
LI Kaiyu,ZHU Xinyi,MA Juncheng,et al. Estimation method of leaf disease severity of cucumber based on mixed dilated convolution and attention mechanism[J]. Transactions of the Chinese Society for Agricultural Machinery,2023,54(2):231 - 239. (in Chinese)

[24] 奚小波,丁杰源,翁小祥,等. 基于轻量化 YOLO v5s - MCA 的番茄成熟度检测方法[J]. 农业机械学报,2025,56(3):383 - 391,436.
XI Xiaobo,DING Jieyuan,WENG Xiaoxiang,et al. Tomato maturity detection method based on lightweight YOLO v5s - MCA[J]. Transactions of the Chinese Society for Agricultural Machinery,2025,56(3):383 - 391,436. (in Chinese)

[25] 李尚平,卞俊析,李凯华,等. 基于改进 YOLO v5s 的复杂环境下蔗梢分叉点识别与定位[J]. 农业机械学报,2023,54(11):247 - 258.
LI Shangping,BIAN Junxi,LI Kaihua,et al. Identification and height localization of sugarcane tip bifurcation points in complex environments based on improved YOLO v5s[J]. Transactions of the Chinese Society for Agricultural Machinery,2023,54(11):247 - 258. (in Chinese)

[26] HU J,SHEN L,SUN G,et al. Squeeze-and-excitation network[C]//Proceedings of the IEEE Conference on Computer Vision and Pattern Recognition (CVPR),2018:7132 - 7141.

(上接第 176 页)

[24] LIAN B,PENG J,ZHAN H,et al. Mechanical response of root-reinforced loess with various water contents[J]. Soil and Tillage Research,2019,193: 85 - 94.

[25] SONGÜL G. Soil compaction due to increased machinery intensity in agricultural production: its main causes,effects and management[M]//FIAZ A,MUHAMMAD S. Technology in Agriculture. Rijeka: IntechOpen, 2021.

[26] NIE Y,NI W,LÜ X,et al. Macroscopic mechanical behavior and microstructural evolution of compacted loess in the Chinese Loess Plateau[J]. Soil and Tillage Research,2023,232: 105767.

[27] DA SILVA E E,BAIO F H R,KOLLING D F,et al. Variable-rate in corn sowing for maximizing grain yield[J]. Sci. Rep.,2021,11(1): 10.

[28] 穆璇,吴玉琴. 增湿对斥水土壤压实性的影响研究[J]. 水利水电技术(中英文),2021,52(10): 199 - 208.
MU Xuan,WU Yuqin. Effect of humidification on the compactness of water-repellent soil[J]. Water Resources and Hydropower Engineering,2021,52(10): 199 - 208. (in Chinese)

[29] LAMICHHANE J R,BOIFFIN J,BOIZARD H,et al. Seedbed structure of major field crops as affected by cropping systems and climate: results of a 15-year field trial[J]. Soil and Tillage Research,2021,206: 104845.

[30] 熊乾,高磊,彭新华,等. 黑土区水蚀坡耕地土壤穿透阻力时空变异特征及传递函数[J]. 水土保持学报,2024,38(4): 162 - 169,180.
XIONG Qian,GAO Lei,PENG Xinhua,et al. Spatio-temporal characteristics and pedotransfer of soil penetration resistance in eroded sloping farmland of black soil region[J]. Journal of Soil and Water Conservation,2024,38(4): 162 - 169,180. (in Chinese)

[31] QIU T,LIU C,ZHONG X,et al. Experimental research on the impact of temperature on the adhesion characteristics of soil-structure interface[J]. Geofluids,2020,2020: 6675576.

[32] CHEN X,CRUSE R M,NIU S,et al. Effect of loading time on soil structural failure[J]. Soil and Tillage Research,2019,186: 87 - 93.

美国《工程索引》(Ei) 收录期刊
Scopus数据库收录期刊
中文核心期刊　中国科技核心期刊
中国科学引文数据库来源期刊

ISSN 1000-1298
CODEN NUYCA3

农业机械学报

Transactions of the Chinese Society for Agricultural Machinery

专栏主题: 主要粮油作物高性能播种技术
专栏主编: 廖庆喜 教授　杨丽 教授

中国农业机械学会
中国农业机械化科学研究院集团有限公司　主办

2025年
第 56 卷
9

农业机械学报
NONGYE JIXIE XUEBAO

2025 年　第 9 期(第 56 卷)

目　次

主要粮油作物高性能播种技术专栏

(专栏主编:廖庆喜　杨　丽)

农业信息化工程

农业水土工程

农业生物环境与能源工程

农产品加工工程

车辆与动力工程

机械设计制造及其自动化

Transactions of the Chinese Society for Agricultural Machinery
Vol. 56 No. 9 2025

Contents

AI + Agricultural Frontiers Technology Forum (Part 1)

Agricultural Equipment and Mechanization Engineering

Agricultural Informatization Engineering

doi:10.6041/j.issn.1000-1298.2025.09.024

履带式除草机路径跟踪误差补偿改进型 MPC 控制方法

赵润茂[1,2]　丁帅奇[1,2]　何　杰[1,2]　满忠贤[1,2]　贺子豪[1,2]
阮庆强[1,2]　胡　炼[1,2]　魏正辉[1,2]
(1. 华南农业大学工程学院, 广州 510642; 2. 农业装备技术全国重点实验室, 广州 510642)

摘要: 为解决除草机器人作业受颠簸路面侧滑滑移等外界干扰从而导致路径跟踪上线距离长、直线误差大等问题,提出一种误差补偿的履带式除草机模型预测控制路径跟踪方法。首先基于履带式除草机器人运动学特性建立了线性误差模型,然后设计了以控制增量为状态量的目标函数、控制量与控制增量为约束条件的模型预测控制算法(MPC)。最后针对除草机路径跟踪过程中因左右两侧履带滑移滑转而产生的误差,在系统控制量中进行补偿,进而得出最优控制量。基于 Matlab/Simulink 仿真环境对控制器性能进行验证,结果表明,在速度 1 m/s 下,相对于传统 MPC 控制器,误差补偿型 MPC 控制器在 3 种不同初始状态下上线距离均减少 26% 以上,上线后直线段路径跟踪横向偏差与航向偏差均降低 10% 与 21% 以上。为验证本文所提方法,设计了 4 组除草机路径跟踪试验。相较于传统 MPC 控制器,误差补偿型 MPC 控制器在速度 1 m/s 下,针对初始位置偏差分别为 0.5 m 和 1 m、航向偏差为 0° 的状态,上线距离分别减少 14.5% 和 19.1%。上线后直线段路径跟踪平均横向偏差分别降低 21.05% 和 29.4%,平均航向偏差分别降低 16.7% 和 20.8%。在初始位置偏差 1 m、航向偏差 45° 的状态,上线距离减小 10.1%,上线后直线段路径跟踪平均横向偏差和航向偏差分别降低 18.75% 和 15.7%。在速度 0.5 m/s 下,初始位置偏差 1 m、初始航向角偏差 0° 的状态,上线距离减少 16.2%,上线后直线段路径跟踪平均横向偏差和航向偏差分别降低 21.4% 和 15.2%。误差补偿型 MPC 控制器可以明显减少除草机上线距离,并提升直线段的跟踪精度,为除草机除草作业高精度路径跟踪提供保障。

关键词: 履带式除草机; 模型预测控制; 误差补偿; Matlab/Simulink; 路径跟踪
中图分类号: S220; S24　　**文献标识码**: A　　**文章编号**: 1000-1298(2025)09-0326-09　　**OSID**:

Error Compensation Improved MPC Track-laying Weeding Machine Path Tracking Control Method

ZHAO Runmao[1,2]　DING Shuaiqi[1,2]　HE Jie[1,2]　MAN Zhongxian[1,2]　HE Zihao[1,2]
RUAN Qingqiang[1,2]　HU Lian[1,2]　WEI Zhenghui[1,2]
(1. *College of Engineering, South China Agricultural University, Guangzhou* 510642, *China*
2. *State Key Laboratory of Agricultural Equipment Technology, Guangzhou* 510642, *China*)

Abstract: Aiming to address the problems of long online distance and large straight-line error caused by external disturbances such as side skidding and sliding of the weeding robot on bumpy roads during operation, a model predictive control (MPC) path tracking method with error compensation for tracked weeding robots was proposed. Firstly, a linear error model was established based on the kinematic characteristics of the tracked weeding robot. Then an MPC algorithm with control increment as the state quantity and control quantity and control increment as the constraint conditions was designed. Finally, to compensate for the errors caused by the sliding and slipping of the left and right tracks during the path tracking process of the weeding machine, the compensation was made in the system control quantity, and the optimal control quantity was obtained. The performance of the controller was verified in the Matlab/Simulink simulation environment. The results showed that at a speed of 1 m/s, compared with the traditional MPC controller, the error compensation type MPC controller reduced the online distance by

收稿日期: 2025-04-06　修回日期: 2025-04-16
基金项目: 安徽省重点研究与开发计划项目(2023N06020047)和广东省重点领域研发计划项目(2019B090922001)
作者简介: 赵润茂(1990—),男,副教授,博士,主要从事水田农业机器人研究,E-mail: rmzhao@scau.edu.cn
通信作者: 何杰(1985—),男,副教授,博士,主要从事智能农机装备和无人化农场技术研究,E-mail: hooget@scau.edu.cn

more than 26% under three different initial states, and the lateral deviation and heading deviation of the straight-line path tracking after going online were reduced by more than 10% and 21%, respectively. To verify the proposed method, four groups of weeding machine path tracking experiments were designed. Compared with the traditional MPC controller, the error compensation type MPC controller reduced the online distance by 14.5% and 19.1% respectively when the initial position deviation was 0.5 m and 1 m and the heading deviation was 0° at speed of 1 m/s. The average lateral deviation and heading deviation of the straight-line path tracking after going online were reduced by 21.05% and 29.4%, and 16.7% and 20.8%, respectively. When the initial position deviation was 1 m and the heading deviation was 45°, the online distance was reduced by 10.1%, and the average lateral deviation and heading deviation of the straight-line path tracking after going online were reduced by 18.75% and 15.7%, respectively. At a speed of 0.5 m/s, when the initial position deviation was 1 m and the initial heading deviation was 0°, the online distance was reduced by 16.2%, and the average lateral deviation and heading deviation of the straight-line path tracking after going online were reduced by 21.4% and 15.2%, respectively. The error compensation type MPC controller can significantly reduce the online distance of the weeding machine and improve the tracking accuracy of the straight-line segment, providing a guarantee for high-precision path tracking of the weeding machine during weeding operations.

Key words: tracked weeding machine; model predictive control; error compensation; Matlab/Simulink; path tracking

0　引言

人工除草需要消耗大量的体力、精力,且除草效果不佳。而大量喷洒除草剂虽起到了对杂草的抑制作用,但易造成环境污染,不符合可持续发展理念[1-2]。随着我国农业机械化的快速发展,智能除草机器人是当代农业发展现代化、精细化、智能化的重要体现[3-4]。路径跟踪控制算法作为智能除草机器人导航作业的核心环节,其性能水平直接决定了除草机器人自主导航作业的精度与稳定性,对除草作业的整体效率和质量有着决定性影响。所以探究除草机路径跟踪控制算法具有关键意义。

路径跟踪控制方法主要包括 PID 跟踪控制[5-6]、纯跟踪控制(Pure pursuit control)[7-8]、线性二次型最优控制(Linear quadratic optimal control)[9-10]以及模型预测控制(Model predictive control)[11-12]等。文献[13-14]所设计控制算法均提高了除草机路径跟踪精度,但未考虑滑移滑转问题对控制精度的影响。文献[15-17]均整合了滑动参数补偿机制,但其在线参数估计过程涉及复杂的运算,不仅制约了系统的动态响应能力,还增加了对硬件处理能力的依赖性。文献[18-19]均针对履带式割草机的滑移滑转问题对控制算法进行改进并提升了控制精度,但未进行实时滑移滑转误差补偿。因此,针对履带式车辆路径跟踪过程中存在的滑移滑转问题,进行滑移滑转误差补偿对进一步提升跟踪控制精度至关重要。

本文以履带式除草机器人为研究平台,基于履带式除草机器人运动学模型设计一种基于模型预测的路径跟踪控制算法,结合履带式车辆路径跟踪过程中滑移导致的转向误差,引入误差补偿。针对模型预测路径跟踪控制器进行 Matlab/Simulink 仿真验证,并开展除草机路径跟踪试验,以验证提出方法的可行性。

1　路径跟踪控制器设计

1.1　除草机器人线性误差模型

试验所选用的履带式除草机行进依靠驱动电机带动两侧履带,作业速度一般为 0.5 ~ 1.0 m/s,属于低速行驶车辆,因此可以采用运动学模型设计轨迹跟踪控制器[20-21]。以履带式除草机右转方式为例,构建的运动学模型如图 1 所示,建立平面坐标系 XOY,(x_1, y_1) 为除草机在坐标系中的位置坐标(即控制中心),以 X 正方向为基准逆时针方向与车体之间的夹角 φ 表示车体在坐标系中的航向角,B 为两侧履带之间的距离,R 为瞬时转向半径,当前除草机前进速度 v、瞬时转向半径 R 和转向角速度 ω 都可以通过左右两侧履带速度 v_1 和 v_2 获得。

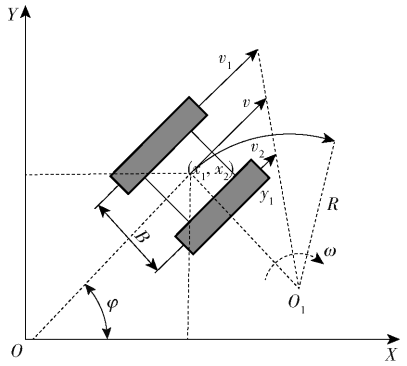

图 1　履带式除草机运动学模型

Fig. 1　Kinematic model of tracked weeding machine

由图 1 可得履带式除草机运动学模型为

$$\begin{bmatrix}\dot{x}\\ \dot{y}\\ \dot{\varphi}\end{bmatrix}=\begin{bmatrix}\cos\varphi & 0\\ \sin\varphi & 0\\ 0 & 1\end{bmatrix}\begin{bmatrix}v\\ \omega\end{bmatrix} \tag{1}$$

由除草机运动学模型可知,$\boldsymbol{X}=(x,y,\varphi)$为除草机状态量,$\boldsymbol{U}=\boldsymbol{u}(v,\omega)$是控制输入。状态空间模型中,输出变量是系统的位置信息,用于导航控制。本文所设计的路径跟踪控制器为 MPC,相比于非线性模型预测控制(NMPC),线性时变模型预测控制(LTV-MPC)算法具有更低的计算复杂度和更快的计算速度,适合实时性较高的应用场景[22-23]。因此,为了确保除草机在路径跟踪中的实时性需求,将车辆的非线性运动模型近似为线性时变模型,其一般形式为

$$\dot{\boldsymbol{X}}=f(\boldsymbol{X},\boldsymbol{u}) \tag{2}$$

将式(2)在$(\boldsymbol{X}_r,\boldsymbol{u}_r)$处采用泰勒级数展开,对方程进行泰勒展开,并忽略高阶项,可以得到线性化后的模型

$$\dot{\boldsymbol{X}}=f(\boldsymbol{X}_r,\boldsymbol{u}_r)+\frac{\partial f(\boldsymbol{X},\boldsymbol{u})}{\partial \boldsymbol{X}}\bigg|_{\substack{\boldsymbol{X}=\boldsymbol{X}_r\\ \boldsymbol{u}=\boldsymbol{u}_r}}(\boldsymbol{X}-\boldsymbol{X}_r)+\frac{\partial f(\boldsymbol{X},\boldsymbol{u})}{\partial \boldsymbol{u}}\bigg|_{\substack{\boldsymbol{X}=\boldsymbol{X}_r\\ \boldsymbol{u}=\boldsymbol{u}_r}}(\boldsymbol{u}-\boldsymbol{u}_r) \tag{3}$$

将公式(2)和公式(3)作差可得新的状态空间模型为

$$\dot{\widetilde{\boldsymbol{X}}}=\boldsymbol{A}\widetilde{\boldsymbol{X}}+\boldsymbol{B}\widetilde{\boldsymbol{u}} \tag{4}$$

联立式(3)、(4)可得离散化后的线性误差模型为

$$\widetilde{\boldsymbol{X}}(k+1)=\boldsymbol{A}_{k,t}\widetilde{\boldsymbol{X}}(k)+\boldsymbol{B}_{k,t}\widetilde{\boldsymbol{u}}(k) \tag{5}$$

其中

$$\widetilde{\boldsymbol{X}}(k)=\begin{bmatrix}x-x_r\\ y-y_r\\ \varphi-\varphi_r\end{bmatrix}\qquad \widetilde{\boldsymbol{u}}(k)=\begin{bmatrix}v_r\\ \omega_r\end{bmatrix}$$

$$\boldsymbol{A}_{k,t}=\begin{bmatrix}1 & 0 & -Tv_r\sin\varphi_r\\ 0 & 1 & Tv_r\cos\varphi_r\\ 0 & 0 & 1\end{bmatrix}$$

$$\boldsymbol{B}_{k,t}=\begin{bmatrix}T\cos\varphi_r & 0\\ T\sin\varphi_r & 0\\ 0 & T\end{bmatrix}$$

式中 T——采样时间

$\boldsymbol{A}_{k,t}$、$\boldsymbol{B}_{k,t}$——线性时变矩阵

$\widetilde{\boldsymbol{X}}(k)$、$\widetilde{\boldsymbol{u}}(k)$——第 k 采样时刻系统的状态量误差和控制量误差

1.2 模型预测轨迹跟踪控制器设计

模型预测控制是一种常用的优化控制算法,MPC 通过预测模型、滚动优化和反馈修正的策略实现控制目标[24-26],因其能够提供较好的实时性和鲁棒性,在车辆路径跟踪中已经得到广泛应用。因此,为了使除草机器人能够快速平稳地跟踪路径,可通过 MPC 的目标函数最优化来实现。由于目标函数转换成标准二次型时存在一定缺陷,导致采样周期内可能出现无解的现象,从而影响控制系统的连续性。所以本文在目标函数中引入松弛因子 ε,目标函数的形式为

$$J(k)=\sum_{k=0}^{N_p}\|\boldsymbol{\eta}(k+i|t)-\boldsymbol{\eta}_{\mathrm{ref}}(k+i|t)\|_{\boldsymbol{Q}}^2+\sum_{k=0}^{N_c-1}\|\Delta\boldsymbol{U}(k+i|t)\|_{\boldsymbol{P}}^2+\rho\varepsilon^2\quad(N_p>N_c>1) \tag{6}$$

式中 $\boldsymbol{Q}$、$\boldsymbol{P}$——权重矩阵 ρ——权重系数

$\boldsymbol{\eta}$、$\boldsymbol{\eta}_{\mathrm{ref}}$——输出状态和参考输出状态量

N_p——预测时域 N_c——控制时域

$\Delta\boldsymbol{U}$——系统控制增量

引入控制量增量 $\Delta\boldsymbol{u}(k)=\boldsymbol{u}(k)-\boldsymbol{u}(k-1)$,对公式的状态量进行增广。设定时刻新的状态量为

$$\boldsymbol{\xi}(k|t)=\begin{bmatrix}\widetilde{\boldsymbol{X}}(k|t)\\ \widetilde{\boldsymbol{u}}(k-1|t)\end{bmatrix} \tag{7}$$

状态空间表达式为

$$\begin{cases}\boldsymbol{\xi}(k+1|t)=\widetilde{\boldsymbol{A}}_{k,t}\boldsymbol{\xi}(k|t)+\widetilde{\boldsymbol{B}}_{k,t}\Delta\boldsymbol{U}(k|t)\\ \boldsymbol{\eta}(k|t)=\widetilde{\boldsymbol{C}}_{k,t}\boldsymbol{\xi}(k|t)\end{cases} \tag{8}$$

其中

$$\widetilde{\boldsymbol{A}}_{k,t}=\begin{bmatrix}\boldsymbol{A}_{k,t} & \boldsymbol{B}_{k,t}\\ \boldsymbol{O}_{2\times3} & \boldsymbol{I}_2\end{bmatrix}\qquad \widetilde{\boldsymbol{B}}_{k,t}=\begin{bmatrix}\boldsymbol{B}_{k,t}\\ \boldsymbol{I}_2\end{bmatrix}$$

$$\widetilde{\boldsymbol{C}}_{k,t}=[\boldsymbol{I}_{N_x}\quad\boldsymbol{O}]$$

式中 $\boldsymbol{I}_2$、$\boldsymbol{I}_{N_x}$——单位向量

$\boldsymbol{O}$——零矩阵

根据文献[11],系统 t 时刻预测模型输出方程为

$$\boldsymbol{Y}(t)=\boldsymbol{\psi}_t\boldsymbol{\xi}(t|t)+\boldsymbol{\Theta}_t\Delta\boldsymbol{U}(t) \tag{9}$$

式中 $\boldsymbol{\psi}_t$——状态量预测参数

$\boldsymbol{\Theta}_t$——控制增量序列预测参数

为了确保履带除草机的控制输入在实际操作中的可行性,本文设计的控制量与控制增量约束条件为

$$\begin{cases}\boldsymbol{u}_{\min}(t+k)\leqslant\boldsymbol{u}(t+k)\leqslant\boldsymbol{u}_{\max}(t+k)\\ \quad(k=0,1,2,\cdots,N_c-1)\\ \Delta\boldsymbol{u}_{\min}(t+k)\leqslant\Delta\boldsymbol{u}(t+k)\leqslant\Delta\boldsymbol{u}_{\max}(t+k)\\ \quad(k=0,1,2,\cdots,N_c-1)\end{cases} \tag{10}$$

MPC 的核心在于通过优化目标函数来寻找到最优的控制输入，使系统在满足约束条件的前提下达到最佳性能[27-28]。为了便于计算，将目标函数转换为标准二次型形式并结合约束条件为

$$\begin{cases} J(\boldsymbol{\xi}(t),\boldsymbol{u}(t-1),\Delta\boldsymbol{U}(t)) = \\ \quad [\Delta\boldsymbol{U}(t)^{\mathrm{T}}\ \varepsilon]^{\mathrm{T}}\boldsymbol{H}_t[\Delta\boldsymbol{U}(t)^{\mathrm{T}}\ \varepsilon]+\boldsymbol{G}_t[\Delta\boldsymbol{U}(t)^{\mathrm{T}}\ \varepsilon] \\ \text{s.t.}\begin{cases}\Delta\boldsymbol{U}_{\min}\leqslant\Delta\boldsymbol{U}_t\leqslant\Delta\boldsymbol{U}_{\max}\\ \boldsymbol{U}_{\min}\leqslant\boldsymbol{A}\Delta\boldsymbol{U}_t+\boldsymbol{U}_t\leqslant\boldsymbol{U}_{\max}\end{cases}\end{cases} \tag{11}$$

其中，正定 Hessian 矩阵 $\boldsymbol{H}=\begin{bmatrix}\boldsymbol{\Theta}^{\mathrm{T}}\boldsymbol{Q}\boldsymbol{\Theta}+\boldsymbol{P} & 0\\ 0 & \rho\end{bmatrix}$，控制增量系数矩阵 $\boldsymbol{G}_t^{\mathrm{T}}=[2\boldsymbol{E}^{\mathrm{T}}\boldsymbol{Q}\boldsymbol{\Theta}\quad 0]$，预测时域内跟踪误差 $\boldsymbol{E}^{\mathrm{T}}=\boldsymbol{\psi}\boldsymbol{\xi}(k)$。

控制系统在完成每个控制周期的求解后，可以得到控制时域内 t 时刻控制输入增量，$\Delta\boldsymbol{U}_t^*=[\Delta\boldsymbol{u}_t^*,\Delta\boldsymbol{u}_{t+1}^*,\cdots,\Delta\boldsymbol{u}_{t+N_c-1}^*]^{\mathrm{T}}$，控制器选用控制序列中第 1 个元素作为实际的输入增量作用于系统中 $\boldsymbol{u}(t)=\boldsymbol{u}(t-1)+\Delta\boldsymbol{u}_t^*$，如此反复循环滚动优化实现除草机的路径跟踪控制。

1.3　滑移滑转误差补偿

履带除草机是通过两侧履带的差速实现转向，转向过程中高速侧履带会受到低速侧履带的拉扯，相反低速侧履带会受到高速侧履带的拖拽，存在高速侧履带的滑转和低速侧履带的滑移，从而导致理论执行的控制量与实际执行的控制量不一致，影响跟踪控制的精度[29-30]。因此需要针对除草机转向过程中因滑转滑移所产生的误差，在路径跟踪控制器中引入误差补偿，提高路径跟踪控制器的精度。

如图 2 所示，以履带除草机的右转方式为例，车辆的转向方式分为 3 种：①左右履带速度方向相同（图 2a）。②左右履带速度方向相反（图 2b）。③左侧履带单方面制动（图 2c）。O_1 为转向中心，v_1' 与 v_2' 分别为左右两侧履带理论线速度，O_1' 为理论转向中心，R'为理论转弯半径。在图 2a 与图 2b 的转向模式下，左侧履带速度大于右侧履带速度，在转向过程中存在左右两侧履带的滑移滑转。在图 2c 的转向模式下，只有左侧的履带单边制动，存在左侧履带的滑转。此时除草机以右侧履带中点为圆心，进行圆周运动。

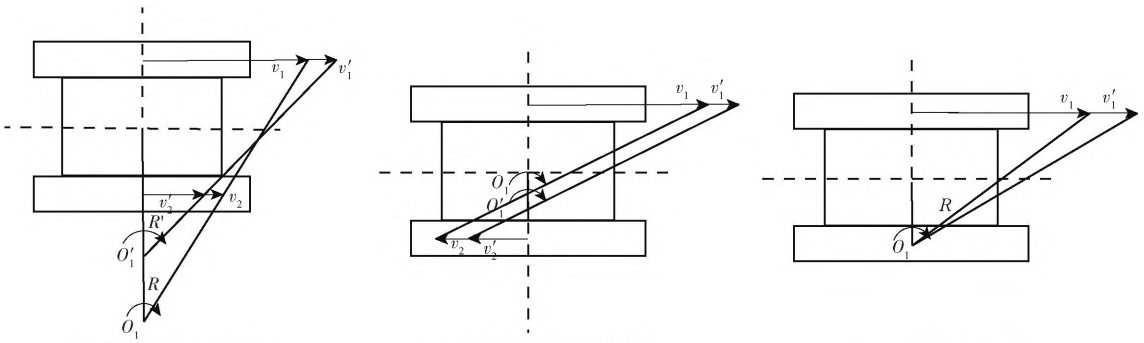

(a) 左右履带速度方向相同　　(b) 左右履带速度方向相反　　(c) 左侧履带单方面制动

图 2　不同转向模式下的履带式车辆滑移滑转图

Fig. 2　Slip and slide diagrams of tracked vehicles under different steering modes

在转向过程中左右两侧履带相对误差 σ_1、σ_2 为

$$\begin{cases}\sigma_1=\dfrac{v_1'-v_1}{v_1'}\\ \sigma_2=\dfrac{v_2'-v_2}{v_2'}\end{cases} \tag{12}$$

履带除草机实际线速度和角速度可以通过传感器实时测量，根据除草机运动学模型，车辆实时线速度与角速度为

$$\begin{cases}v=\dfrac{v_1+v_2}{2}\\ \omega=\dfrac{v_1-v_2}{B}\end{cases} \tag{13}$$

联立式(12)与式(13)可得除草机理论线速度与角速度为

$$\begin{cases}v'=v+\dfrac{\sigma_1v_1'+\sigma_2v_2'}{2}\\ \omega'=\omega+\dfrac{\sigma_2v_2'-\sigma_1v_1'}{B}\end{cases} \tag{14}$$

则除草机线速度与角速度误差可以表示为

$$\begin{cases}v_e=\dfrac{\sigma_1v_1'+\sigma_2v_2'}{2}\\ \omega_e=\dfrac{\sigma_2v_2'-\sigma_1v_1'}{B}\end{cases} \tag{15}$$

以左右两侧履带相对误差表示左右履带滑移率和滑转率，由式(15)可知在设计的模型预测控制器的输出中加入误差补偿

$$\boldsymbol{u}_e=\begin{bmatrix}v_e\\ \omega_e\end{bmatrix}=\begin{bmatrix}\dfrac{\sigma_1v_1'+\sigma_2v_2'}{2}\\ \dfrac{\sigma_2v_2'-\sigma_1v_1'}{B}\end{bmatrix} \tag{16}$$

即在 1.2 节中模型预测控制器得出当前理论控制量 $\boldsymbol{u}'(t)$,与当前所测得实际控制量 $\boldsymbol{u}(t)$ 计算出误差补偿控制量 $\boldsymbol{u}_e(t)$,此时误差补偿后的控制量为 $\boldsymbol{u}_s(t)=\boldsymbol{u}'(t)+\boldsymbol{u}_e(t)$,将 $\boldsymbol{u}_s(t)$ 作为系统控制输出。同时,为了使控制器可以更加稳定工作避免扰动影响,将左右两侧履带相对误差值域设定为 $[-0.1,0.1]$,如图 3 所示。

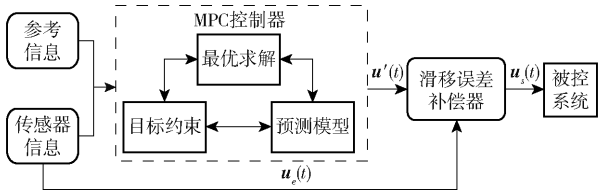

图 3 引入误差补偿的控制流程图

Fig. 3 Control flowchart with error compensation introduced

2 仿真试验

为验证本文所设计的误差补偿型 MPC 路径跟踪控制器的路径跟踪性能,令除草机器人在转向过程中的角速度产生一定的偏差量,模拟履带除草机的滑移滑转误差,采用 Matlab/Simulink 进行仿真试验验证。Matlab/Simulink 模型如图 4 所示。

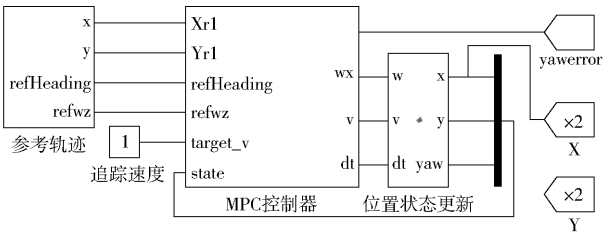

图 4 Matlab/Simulink 模型

Fig. 4 Matlab/Simulink model

仿真试验的参考路径为长度 10 m 的直线,起点坐标为[0,0]、终点为[10 m,0]。分别以速度 1 m/s 进行了 3 种不同初始状态的路径跟踪仿真试验。3 种不同初始状态分别为:①$\boldsymbol{X}=[0\quad 0.5\quad 0]^{\mathrm{T}}$,初始偏差 0.5 m、初始航向偏差 0°。②$\boldsymbol{X}=[0\quad 0\quad 0]^{\mathrm{T}}$,初始偏差 1 m、初始航向偏差 0°。③$\boldsymbol{X}=\left[0\quad 0\quad \frac{\pi}{4}\right]^{\mathrm{T}}$,初始偏差 1 m、初始航向偏差 45°。

当除草机器人位置偏差保持在 ±5 cm 范围内,即达到上线要求。上线距离为除草机器人达到上线状态所走过的距离。控制系统的状态量权重为 $\boldsymbol{Q}=\mathrm{diag}(1,1,0.5)$,控制量权重为 $\boldsymbol{P}=\mathrm{diag}(1,1)$,其余参数如表 1 所示。

不同初始状态下路径跟踪仿真效果如图 5 ~ 7 所示。由图 5a、6a、7a 可以看出,3 种不同初始状态下初始位置偏差较大,在上线初期除草机器人横向速度加快,向目标路径快速靠拢,完成上线进入直线段跟踪。如图 5b、6b、7b 所示,除草机上线初期快速向目标路径靠近,产生了较大的航向偏差。随着接近目标路径,除草机器人纵向速度加快,航向偏差迅速减小。上线过程中相对于传统 MPC 控制器,引入误差补偿的 MPC 控制器上线过程明显更快,上线距离短。从上线后的直线段路径跟踪轨迹可以看出,实时轨迹与目标路径基本重合,由于直线跟踪过程中产生的滑移滑转误差较小,2 种控制器在直线段的路径跟踪效果均良好。

表 1 模型预测控制算法参数

Tab. 1 Parameters of model predictive control algorithm

参数	数值
N_p	25
N_c	15
T/s	0.1
δ/rad	−2 ~ 2
$\Delta\delta$/rad	−0.2 ~ 0.2
ρ	100
ε	10

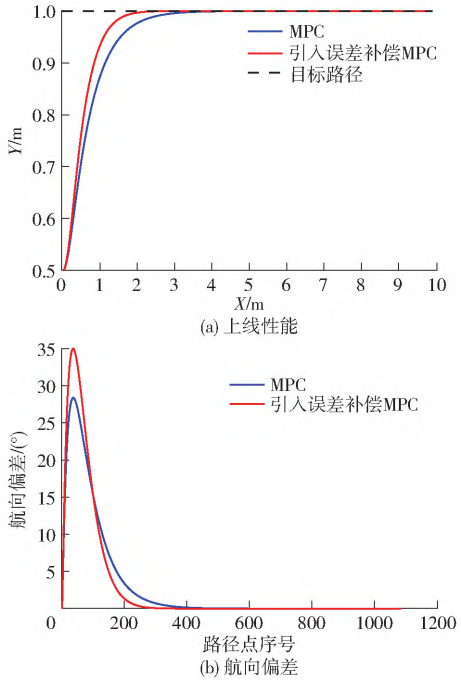

图 5 初始偏差 0.5 m、初始航向偏差 0°路径跟踪性能对比曲线

Fig. 5 Path tracking performance comparison chart when initial deviation was 0.5 m and initial heading angle deviation was 0°

由图 5 ~ 7 可知,引入误差补偿型 MPC 控制器与传统 MPC 控制器分别在 3 种不同初始状态下的仿真结果为:①初始位置偏差 0.5 m、初始航向偏差 0°时,上线距离分别为 1.16、1.57 m,上线距离减少 26.1%。上线后直线段平均横向偏差分别为 0.008、0.01 m,平均横向偏差减小 20%;直线段平

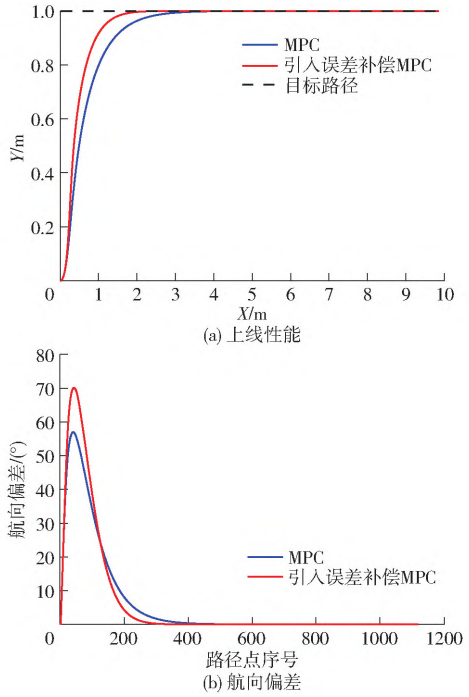

图 6　初始偏差 1 m、初始航向角偏差 0°路径跟踪性能对比曲线

Fig. 6　Path tracking performance comparison chart when initial deviation was 1 m and initial heading angle deviation was 0°

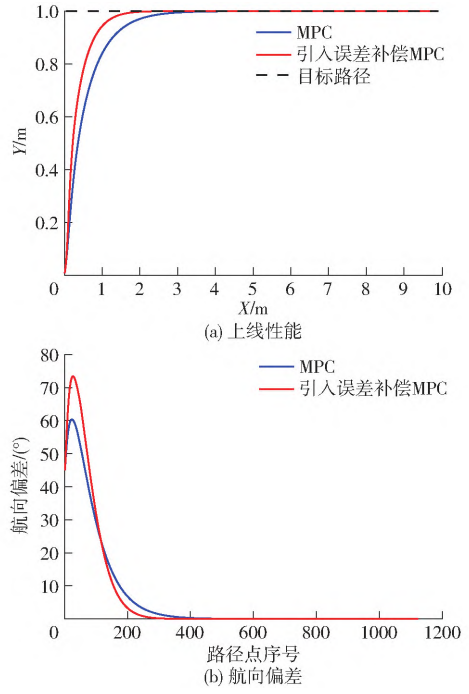

图 7　初始偏差 1 m、初始航向偏差 45°路径跟踪性能对比曲线

Fig. 7　Path tracking performance comparison chart when initial deviation was 1 m and initial heading angle deviation was 45°

均航向偏差分别为 0.11°与 0.14°，平均航向偏差减小 21.4%。②初始位置偏差 1 m、初始航向偏差 0°时，上线距离分别为 1.25、1.79 m，上线距离减少 30.1%。上线后直线段平均横向偏差分别为 0.009、0.01 m，平均横向偏差减小 10%；直线段平均航向偏差分别为 0.13°与 0.17°，平均航向偏差减小 23.5%。③初始位置偏差 1 m、初始航向偏差 45°时，上线距离分别为 1.18、1.64 m，上线距离减少 28.04%。上线后直线段平均横向偏差分别为 0.008、0.01 m，平均横向偏差减小 20%；直线段平均航向偏差分别为 0.11°与 0.14°，平均航向偏差减小 21.4%。由试验结果可知，引入误差补偿的 MPC 在上线与直线段的跟踪性能均得到了提升。

3　实车试验

3.1　试验材料

为验证引入误差补偿的模型预测路径跟踪控制器性能，进行实车试验。试验平台选用油电混合动力履带式除草机器人，由 2 台 12 V/1 000 W 大功率电机驱动履带行驶。机器主要参数如表 2 所示。

表 2　履带式除草机器人参数

Tab. 2　Tracked weeding robot parameters

参数	数值
外形尺寸/(mm × mm × mm)	850 × 900 × 400
轮距 L/mm	600
履带与地面接触面长度 l/mm	700
作业速度/(km·h^{-1})	0 ~ 5
割刀幅宽/mm	550
电机额定电压/V	12
电机功率/W	1 200
最大负载/kg	150
发电机功率/W	1 800

自动导航除草机器人如图 8 所示。主控模块选用 Nuvo－5501 型工控机，配置 melodic 版本的机器人操作系统 ROS（Robot operating system，ubuntu 20.04）。导航定位系统采用北斗定位模块双天线板卡 UM982，定位精度为 2.5 mm，航向精度为 0.2(°)/R_0（R_0 为双天线基线长，取 0.8 m），采用双天线 GNSS 为导航提供位置与航向信息，MTI300 型姿态传感器（IMU）获取姿态信息，具体信息见表 3。工控机通过串口与底盘控制系统通讯，底盘控制系统接收导航下发的运动指令，并将运动指令转换为 PWM 下发给左右电机。

3.2　试验方法

本试验在华南农业大学增城教学科研基地开展。试验条件与仿真试验相同。最后增加速度 0.5 m/s 进行初始状态为 $\boldsymbol{X}=[0\quad 1\quad 0]^{\mathrm{T}}$ 的路径跟踪试验。

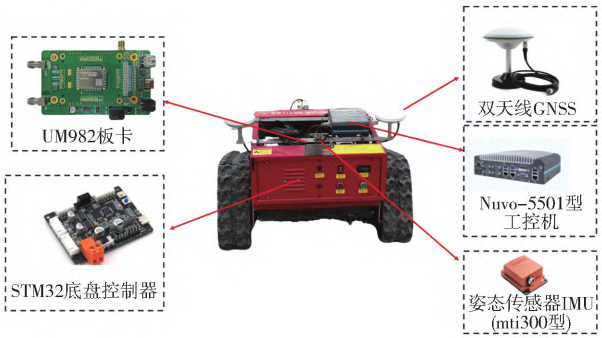

图 8 履带式除草机器人

Fig. 8 Tracked weeding robot

表 3 工控机、GNSS 和 IMU 设备参数

Tab. 3 Industrial personal computer (IPC), GNSS and IMU device parameters

设备	参数	数值/型号
Nuvo - 5501 型工控机	尺寸/(mm × mm × mm)	221 × 173 × 76.2
	处理器	6th - Gen Core i7
	适应温度/(°)	-25 ~ 70
	运行内存/GB	8
	内存/GB	512
GNSS	板卡型号	UM982
	数据更新频率/Hz	10
	PPS 更新频率/Hz	1
	静态水平精度/mm	2.5
	动态水平精度/mm	8
IMU	型号	MTI - 300 - 2A5G4
	翻滚角、俯仰角/(°)	0.2
	航向角/(°)	1.00
	陀螺仪零漂/((°)·h^{-1})	10
	陀螺仪噪声密度/((°)·s^{-1}·Hz$^{-\frac{1}{2}}$)	0.01
	陀螺仪 g-sensitivity/((°)·s^{-1}·g^{-1})	0.003
	加速度计零偏/μg	15
	加速度随机游走/μg	0.01

按照除草机所需的上线性能,将除草机位置调整到目标路径 ±5 cm 范围内,即达到上线要求,上线距离为车辆达到上线状态所走过的距离。记录试验过程中除草机的实时轨迹与航向偏差。试验中的模型预测控制器参数与仿真中相同,试验场地如图 9 所示。

3.3 试验结果与分析

试验结果如图 10 ~ 13 所示。在 4 种不同状态下,除草机初始偏差较大,为向目标路径靠拢,除草机迅速调整航向角,进而产生较大的航向误差。随着逐渐接近目标路径,除草机航向误差迅速减小,完成上线动作,随后进入直线段跟踪阶段。从除草机实时轨迹可以看出,上线过程中因转向产生较大滑移滑转误差,引入误差补偿的 MPC 控制器相对于传统 MPC 的上线过程更快,上线距离更短。在上线后的直线段跟踪过程中,除草机产生的滑移滑转误差较小,2 种控制器作用下除草机在直线段跟踪的实时轨迹与目标路径基本重合。

图 9 除草效果

Fig. 9 Weeding effect diagram

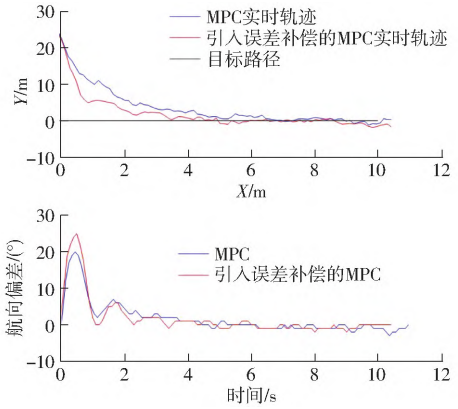

图 10 速度 1 m/s、初始偏差 0.5 m、初始航向偏差 0°路径跟踪性能对比曲线

Fig. 10 Comparison chart of path tracking performance with speed of 1 m/s, initial deviation of 0.5 m, and initial heading deviation of 0°

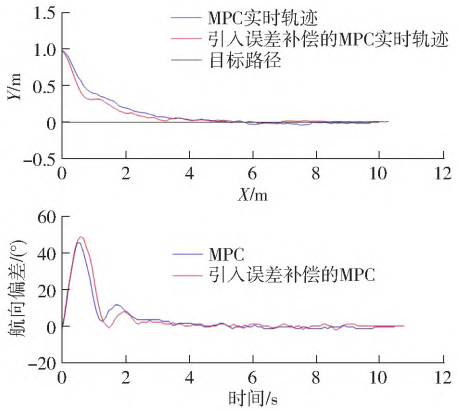

图 11 速度 1 m/s、初始偏差 1 m、初始航向偏差 0°路径跟踪性能对比曲线

Fig. 11 Comparison chart of path tracking performance with speed of 1 m/s, initial deviation of 1 m, and initial heading deviation of 0°

图 10 ~ 13 表明:①速度 1 m/s、初始偏差 0.5 m、初始航向偏差 0°时,误差补偿型 MPC 控制器上线距离与传统 MPC 控制器上线距离分别为 2.46、

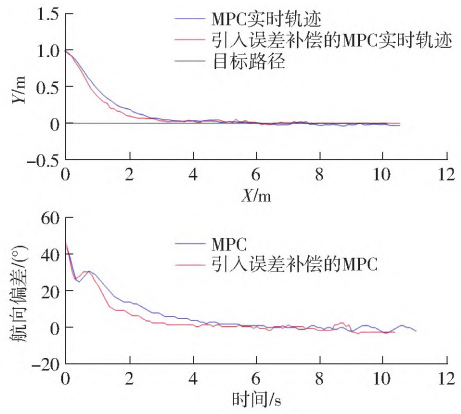

图 12　速度 1 m/s、初始偏差 1 m、初始航向偏差 45°路径跟踪性能对比曲线

Fig. 12　Comparison chart of path tracking performance with speed of 1 m/s, initial deviation of 1 m, and initial heading deviation of 45°

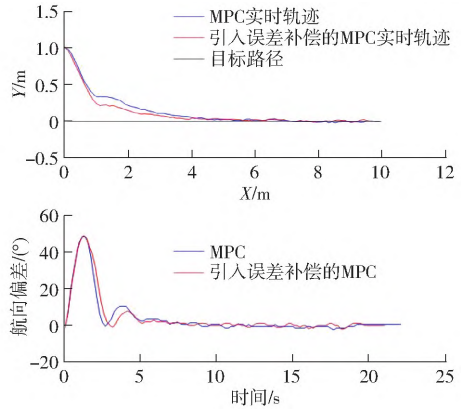

图 13　速度 0.5 m/s、初始偏差 1 m、初始航向偏差 0°路径跟踪性能对比曲线

Fig. 13　Comparison chart of path tracking performance with speed of 0.5 m/s, initial deviation of 1 m, and initial heading deviation of 0°

2.88 m，上线距离减小 14.5%；上线后直线段平均横向偏差分别为 0.015、0.019 m，平均横向偏差减小 21.05%；直线段平均航向偏差分别为 0.65°与 0.78°，平均航向偏差减小 16.7%。②速度 1 m/s、初始偏差 1 m、初始航向偏差 0°时的上线距离分别为 3.15、3.89 m，上线距离减小 19.1%。上线后直线段平均横向偏差分别为 0.012、0.017 m，平均横向偏差减小 29.4%。直线段平均航向偏差分别为 0.57°与 0.72°，平均航向偏差减小 20.8%。③速度 1 m/s、初始偏差 1 m、初始航向角 45°时的上线距离分别为 2.78、3.09 m，上线距离减小 10.1%。上线后直线段平均横向偏差分别为 0.013、0.016 m，平均横向偏差减小 18.75%。直线段平均航向偏差分别为 0.59°与 0.7°，平均航向偏差减小 15.7%。④速度 0.5 m/s、初始偏差 1 m，初始航向偏差 0°时的上线距离分别为 2.89、3.45 m，上线距离减小 16.2%。上线后直线段平均横向偏差分别为 0.011、0.014 m，平均横向偏差减小 21.4%。直线段平均航向偏差分别为 0.5°与 0.59°，平均航向偏差减小 15.2%。在不同状态下上线与直线段路径跟踪中，引入误差补偿的 MPC 控制器通过实时补偿除草机路径跟踪过程产生的滑移滑转误差来提高控制性能，并且直线段跟踪精度也得到了提升。

4　结论

(1)以履带式除草机为研究对象，基于履带式除草机器人运动学特性建立了线性误差模型，设计了控制增量为状态量的目标函数、控制量与控制增量为约束条件的模型预测控制算法。针对除草机路径跟踪过程中因左右两侧履带滑移滑转而产生的误差，在系统控制量中进行补偿，得出最优控制量。

(2)建立了 Matlab/Simulink 仿真模型，试验结果表明，在速度 1 m/s 下，相对于传统 MPC 控制器，误差补偿型 MPC 控制器在 3 种不同初始状态下的上线距离均减少 26% 以上，上线后直线段路径跟踪横向偏差与航向偏差均降低 10% 与 21% 以上。由试验结果可知，引入误差补偿的 MPC 在上线与直线段的路径跟踪性能均有提升。

(3)不同状态下除草机路径跟踪试验结果表明，相较于传统 MPC 控制器，误差补偿型 MPC 控制器在速度 1 m/s 下，针对初始位置偏差分别为 0.5 m 和 1 m、航向偏差 0°的状态，上线距离分别减少 14.5% 和 19.1%。上线后直线段路径跟踪平均横向偏差分别降低 21.05% 和 29.4%，平均航向偏差分别降低 16.7% 和 20.8%。在初始位置偏差 1 m、航向偏差 45°的状态，上线距离减小 10.1%，上线后直线段路径跟踪平均横向偏差和航向偏差分别降低 18.75% 和 15.7%。在速度 0.5 m/s 下，初始位置偏差 1 m、初始航向偏差 0°的状态，上线距离减少 16.2%，上线后直线段路径跟踪的平均横向偏差和航向偏差分别降低 21.4% 和 15.2%。本文设计的误差补偿型 MPC 控制器能有效提升除草机上线段与直线段路径跟踪性能，验证了该控制器在复杂动态环境下的强鲁棒性。

参　考　文　献

[1]　邢钦淞，丁素明，薛新宇，等. 智能田间除草机器人发展现状研究[J]. 中国农机化学报，2022，43(8)：173－181.
XING Qinsong, DING Suming, XUE Xinyu, et al. Research on the development status of intelligent field weeding robot[J].

Journal of Chinese Agricultural Mechanization, 2022, 43(8): 173 - 181. (in Chinese)
[2] 胡炼,刘海龙,何杰,等. 智能除草机器人研究现状与展望[J]. 华南农业大学学报, 2023,44(1):34 - 42.
HU Lian, LIU Hailong, HE Jie, et al. Research progress and prospect of intelligent weeding robot[J]. Journal of South China Agricultural University, 2023, 44(1): 34 - 42. (in Chinese)
[3] 乔清旭,杨晶,袁洪印,等. 浅谈智能化除草机的研究现状及其发展趋势[J]. 农业开发与装备, 2023(1):39 - 41.
[4] 马坚洪,陈学永,江仁伟,等. 智能割草机自主导航关键技术的研究综述[J]. 机电工程技术, 2024,53(7):41 - 45.
MA Jianhong, CHEN Xueyong, JIANG Renwei, et al. Review of the research on the key technologies of autonomous navigation of intelligent lawn mowers[J]. Mechanical and Electrical Engineering Technology, 2024, 53(7): 41 - 45. (in Chinese)
[5] 丁幼春,夏中州,彭靖叶,等. 联合收获机单神经元 PID 导航控制器设计与试验[J]. 农业工程学报, 2020,36(7):34 - 42.
DING Youchun, XIA Zhongzhou, PENG Jingye, et al. Design and experiment of single neuron PID navigation controller for combine harvester[J]. Transactions of the CSAE, 2020, 36(7): 34 - 42. (in Chinese)
[6] DING F, ZHANG W, LUO X, et al. Gain self-adjusting single neuron PID control method and experiments for longitudinal relative position of harvester and transport vehicle[J]. Computers and Electronics in Agriculture, 2023, 213: 108215.
[7] 沈跃,赵莎,张亚飞,等. 基于变前视距离的四轮同步转向农机改进纯跟踪控制[J]. 农业机械学报, 2024,55(3):21 - 28.
SHEN Yue, ZHAO Sha, ZHANG Yafei, et al. Improved pure tracking control of four-wheel synchronous steering agricultural machinery based on variable forward looking distance[J]. Transactions of the Chinese Society for Agricultural Machinery, 2024, 55(3): 21 - 28. (in Chinese)
[8] 张华强,王国栋,吕云飞,等. 基于改进纯追踪模型的农机路径跟踪算法研究[J]. 农业机械学报, 2020,51(9):18 - 25.
ZHANG Huaqiang, WANG Guodong, LÜ Yunfei, et al. Agricultural machinery automatic navigation control system based on improved pure tracking model[J]. Transactions of the Chinese Society for Agricultural Machinery, 2020, 51(9): 18 - 25. (in Chinese)
[9] WANG Z, SUN K, MA S, et al. Improved linear quadratic regulator lateral path tracking approach based on a real-time updated algorithm with fuzzy control and cosine similarity for autonomous vehicles[J]. Electronics, 2022, 11(22): 3703.
[10] YU H, ZHAO C, LI S, et al. Pre-work for the birth of driver-less scraper in the underground mine: the path tracking control based on an lqr controller and algorithms comparison[J]. Sensors, 2021, 21(23): 7839.
[11] HE J, HU L, WANG P, et al. Path tracking control method and performance test based on agricultural machinery pose correction[J]. Computers and Electronics in Agriculture, 2022, 200: 107185.
[12] STANO P, MONTANARO U, TAVERNINI D, et al. Model predictive path tracking control for automated road vehicles: a review[J]. Annual Reviews in Control, 2023, 55: 194 - 236.
[13] 冀杰,贺庆,赵立军,等. 除草机器人自适应快速积分终端滑模跟踪控制技术[J]. 农业机械学报, 2023,54(6):55 - 64.
JI Jie, HE Qing, ZHAO Lijun, et al. Adaptive fast integrating terminal sliding mode tracking control technique for weeding robot[J]. Transactions of the Chinese Society for Agricultural Machinery, 2023, 54(6):55 - 64. (in Chinese)
[14] 贺庆,冀杰,冯伟,等. 割草机器人自适应时域 MPC 路径跟踪控制方法[J]. 智慧农业(中英文), 2024,6(3):82 - 93.
HE Qing, JI Jie, FENG Wei, et al. Adaptive timedomain MPC path following control method for lawn mower robot[J]. Smart Agriculture, 2024, 6(3):82 - 93. (in Chinese)
[15] ZHAO Z, LIU H, CHEN H, et al. Kinematics-aware model predictive control for autonomous high-speed tracked vehicles under the offroad conditions[J]. Mechanical Systems and Signal Processing, 2019, 123:333.
[16] 赵梓烨,刘海鸥,陈慧岩. 分布式电驱动无人高速履带车辆越野环境轨迹预测方法研究[J]. 兵工学报, 2019,40(4): 680 - 688.
ZHAO Ziye, LIU Haiou, CHEN Huiyan. Research on trajectory prediction method for distributed electric drive unmanned high-speed tracked vehicle in off-road environment[J]. Acta Armamentarii, 2019, 40(4): 680 - 688. (in Chinese)
[17] 贾伟健,刘西侠,王可,等. 基于 MPC 的无人履带车辆轨迹跟踪方法研究[J]. 计算机仿真, 2024,41(5):429 - 435.
JIA Weijian, LIU Xixia, WANG Ke, et al. Research on trajectory tracking method for unmanned tracked vehicles based on MPC[J]. Computer Simulation, 2024, 41(5): 429 - 435. (in Chinese)
[18] 赵永春,张庆,尤泳,等. 基于虚拟雷达和两级神经网络的割草机路径跟踪算法[J]. 农业机械学报, 2023,54(4): 222 - 232.
ZHAO Yongchun, ZHANG Qing, YOU Yong, et al. Path tracking algorithm for mower based on virtual radar and two-level neural network[J]. Transactions of the Chinese Society for Agricultural Machinery, 2023, 54(4):222 - 232. (in Chinese)
[19] 赵立军,贾云帆,殷文科,等. 基于模型预测控制的履带式除草机器人设计与试验[J]. 智能化农业装备学报(中英文), 2024,5(4):84 - 94.
ZHAO Lijun, JIA Yunfan, YIN Wenke, et al. Design and experiment of a tracked weeding robot based on model predictive control[J]. Journal of Intelligent Agricultural Machanization, 2024, 5(4):84 - 94. (in Chinese)
[20] 李安楠. 履带车辆路径跟踪算法研究[D]. 昆明:昆明理工大学, 2023.
LI Annan. Research on path tracking algorithm for tracked vehicles[D]. Kunming: Kunming University of Science and Technology, 2023. (in Chinese)

(下转第 354 页)

[18] WEN Changkai, ZHANG Jing, ZHENG Kan, et al. Accelerated verification method for the reliability of the motor drive mechanism of the corn precision seed-metering device[J]. Computers and Electronics in Agriculture, 2023, 212: 108163.
[19] ZENG Zhiwei, CHEN Ying. Simulation of straw movement by discrete element modelling of straw-sweep-soil interaction[J]. Biosystems Engineering, 2019, 180: 25 - 35.
[20] 毕津硕,卢彩云,李洪文,等. 基于最优动态滑切的被动式锯齿圆盘防堵装置设计与试验[J]. 农业机械学报,2025,56(4):118 - 128.
BI Jinshuo, LU Caiyun, LI Hongwen, et al. Design and experiment of anti-blocking device passive sawtooth disc based optimal dynamic sliding cutting[J]. Transactions of the Chinese Society for Agricultural Machinery, 2025, 56(4): 118 - 128. (in Chinese)
[21] 何进,李洪文,陈海涛,等. 保护性耕作技术与机具研究进展[J]. 农业机械学报,2018,49(4):1 - 19.
HE Jin, LI Hongwen, CHEN Haitao, et al. Research progress of conservation tillage technology and machine[J]. Transactions of the Chinese Society for Agricultural Machinery, 2018, 49(4): 1 - 19. (in Chinese)
[22] 齐浩凯. 机械化学复合式玉米除草机设计与试验[D]. 保定:河北农业大学,2022.
QI Haokai. Design and test of mechanochemical composite maize weeder[D]. Baoding: Hebei Agricultural University, 2022. (in Chinese)
[23] 中国农业机械化科学研究院耕作种植机械研究所. 早田中耕追肥机试验方法: JB/T 7864—1999[S]. 北京:中国标准出版社,1999.
[24] 韩豹,郭畅,高英玲,等. 大豆株间除草单体机构及关键部件设计与试验[J]. 农业机械学报,2020,51(6):112 - 121.
HAN Bao, GUO Chang, GAO Yingling, et al. Design and experiment of soybean intra-row weeding monomer mechanism and key components[J]. Transactions of the Chinese Society for Agricultural Machinery, 2020, 51(6): 112 - 121. (in Chinese)

(上接第 334 页)

[21] SUBARI M A, HUDHA K, KADIR Z A, et al. Development of path tracking control of a tracked vehicle for an unmanned ground vehicle[J]. International Journal of Advanced Mechatronic Systems, 2020, 8(4): 136 - 143.
[22] 乔宝山,冯樱,江子旺,等. 基于模型预测控制的智能汽车轨迹跟踪方法比较[J]. 湖北汽车工业学院学报, 2020, 34(2):24 - 28.
QIAO Baoshan, FENG Ying, JIANG Ziwang, et al. Comparison of intelligent vehicle trajectory tracking methods based on model predictive control[J]. Journal of Hubei University of Automotive Industry, 2020, 34(2): 24 - 28. (in Chinese)
[23] WANG Y, BOYD S. Fast model predictive control using online optimization[J]. IEEE Transactions on Control Systems Technology, 2010, 18(2): 267 - 278.
[24] 王玉亮,李汉卿,陈兆英,等. 基于 MPC 的插秧机路径跟踪控制算法研究[J]. 中国农机化学报, 2022, 43(7): 173 - 178.
WANG Yuliang, LI Hanqing, CHEN Zhaoying, et al. Research on path tracking control algorithm of rice transplanter based on MPC[J]. Journal of Chinese Agricultural Mechanization, 2022, 43(7): 173 - 178. (in Chinese)
[25] 迟瑞娟,熊泽鑫,姜龙腾,等. 基于模型预测的插秧机路径跟踪控制算法[J]. 农业机械学报, 2022, 53(11): 22 - 30, 99.
CHI Ruijuan, XIONG Zexin, JIANG Longteng, et al. Path tracking control algorithm of transplanter based on model prediction [J]. Transactions of the Chinese Society for Agricultural Machinery, 2022, 53(11): 22 - 30, 99. (in Chinese)
[26] 徐广飞,陈美舟,苗河泉,等. 基于模型预测控制的农机主从跟随作业控制方法[J]. 农业机械学报, 2020, 51(增刊 2): 11 - 20.
XU Guangfei, CHEN Meizhou, MIAO Hequan, et al. Following operation control method of farmer machinery based on model predictive control[J]. Transactions of the Chinese Society for Agricultural Machinery, 2020, 51(Supp. 2): 11 - 20. (in Chinese)
[27] LI Y H, FAN J K, LIU Y, et al. Path planning and path tracking for autonomous vehicle based on MPC with adaptive dual-horizon-parameters[J]. International Journal of Automotive Technology, 2022, 23(5): 1239 - 1253.
[28] 严国军,贲能军,顾建华,等. 基于 MPC 的无人驾驶拖拉机轨迹跟踪控制[J]. 重庆交通大学学报(自然科学版), 2019, 38(9): 1 - 6.
YAN Guojun, BEN Nengjun, GU Jianhua, et al. Trajectory tracking control of unmanned tractors based on MPC[J]. Journal of Chongqing Jiaotong University(Natural Science Edition), 2019, 38(9): 1 - 6. (in Chinese)
[29] 盖江涛,刘春生,马长军,等. 考虑履带滑转滑移的电驱动履带车辆转向控制[J]. 兵工学报, 2021, 42(10): 2092 - 2101.
GAI Jiangtao, LIU Chunsheng, MA Changjun, et al. Steering control of electrically driven tracked vehicles considering track slip[J]. Journal of Ordnance Engineering, 2021, 42(10): 2092 - 2101. (in Chinese)
[30] 闫清东,张连第,赵毓芹,等. 坦克构造与设计[M]. 北京:北京理工大学出版社, 2007.

美国《工程索引》（Ei）收录期刊
美国《化学文摘》（CA）收录期刊
Scopus数据库收录期刊
中文核心期刊　中国科技核心期刊
中国科学引文数据库来源期刊
RCCSE中国权威学术期刊

ISSN 1000-1298
CODEN NUYCA3

农业机械学报

NONGYE JIXIE XUEBAO

Transactions of the Chinese Society for Agricultural Machinery

第 54 卷

特约专稿

农业装备运维与作业服务管理信息化技术研究进展

赵　博　张巍朋　苑严伟　汪凤珠　周利明　牛　康

ISSN 1000-1298
12
9 771000 129237

2023 12

148

中国农业机械学会主办

全选 显示方式:

> 特约专稿

农业装备运维与作业服务管理信息化技术研究进展
赵博，张巍朋，苑严伟，汪凤珠，周利明，牛康
2023, 54(12):1-26. DOI: 10.6041/j.issn.1000-1298.2023.12.001
摘要 (1466) HTML (0) PDF 8.68 M (1027) 评论 (0) 收藏

> 农业装备与机械化工程

分体组合振动式超级稻精量播种匀种装置设计与试验
朱承天，刘彩玲，李方林，贾旋，曹铭健，王悦伟
2023, 54(12):27-36. DOI: 10.6041/j.issn.1000-1298.2023.12.002
摘要 (1440) HTML (0) PDF 3.90 M (768) 评论 (0) 收藏

荞麦播种机气力集排系统螺旋式增压管设计与试验
付作立，李贵川，李海宇，李旋，宫志超，黄玉祥
2023, 54(12):37-45，69. DOI: 10.6041/j.issn.1000-1298.2023.12.003
摘要 (1227) HTML (0) PDF 2.19 M (722) 评论 (0) 收藏

基于DEM-MFBD的辣椒移栽机取投苗装置设计与试验
侯加林，张二鹏，张康博，李玉华
2023, 54(12):46-57,87. DOI: 410.6041/j.issn.1000-1298.2023.12.004
摘要 (1256) HTML (0) PDF 5.41 M (800) 评论 (0) 收藏

油莎豆排种离散元仿真参数标定与试验
陈永，高晓勋，金鑫，马晓然，胡斌，张秀丽
2023, 54(12):58-69. DOI: 410.6041/j.issn.1000-1298.2023.12.005
摘要 (1104) HTML (0) PDF 3.48 M (784) 评论 (0) 收藏

果园秸秆覆盖机宽幅覆土装置设计与试验
李旭东，臧家俊，高翔，房效东，徐少杰，朱新华
2023, 54(12):70-78，120. DOI: 410.6041/j.issn.1000-1298.2023.12.006
摘要 (1145) HTML (0) PDF 2.87 M (737) 评论 (0) 收藏

油茶林立式螺旋松土除草机设计与试验
许静，刘宝伟，陈平录，王俊南，刘木华
2023, 54(12):79-87. DOI: 410.6041/j.issn.1000-1298.2023.12.007
摘要 (982) HTML (0) PDF 1.86 M (673) 评论 (0) 收藏

大垄宽幅马铃薯中耕机纵横稳定性优化设计与试验
吕金庆，崔鹏飞，竹筱歆，齐钰，杨德秋，孙琪
2023, 54(12):88-96，154. DOI: 410.6041/j.issn.1000-1298.2023.12.008
摘要 (1001) HTML (0) PDF 2.02 M (603) 评论 (0) 收藏

中间集抛后送式双侧斜输烟草培土机设计与试验
罗海峰，张晟，吴明亮，王成伟，何激光，蒋啸虎
2023, 54(12):97-108，165. DOI: 410.6041/j.issn.1000-1298.2023.12.009
摘要 (848) HTML (0) PDF 3.26 M (583) 评论 (0) 收藏

马铃薯联合收获机环形减损集薯升运装置设计与试验
李学强，王兴欢，刘洋，王法明，孟鹏祥，王金梅
2023, 54(12):109-120. DOI: 410.6041/j.issn.1000-1298.2023.12.010
摘要 (957) HTML (0) PDF 2.95 M (733) 评论 (0) 收藏

整秆式甘蔗收获机输送调控系统设计与试验
赖晓，陈佩钟，李尚平，王苗苗，程健华，黄浩然
2023, 54(12):121-128，185. DOI: 410.6041/j.issn.1000-1298.2023.12.011
摘要 (915) HTML (0) PDF 3.09 M (715) 评论 (0) 收藏

手持冲击梳刷式油茶果采摘装置设计与试验
闫锋欣，李许杰，杨永霞，黄国庆，张玉，杨福增
2023, 54(12):129-140. DOI: 410.6041/j.issn.1000-1298.2023.12.012
摘要 (920) HTML (0) PDF 3.18 M (713) 评论 (0) 收藏

扰动下铡草机切碎辊负荷控制器设计与试验
王征，任龙龙，李扬，吴彦强，束钰，宋月鹏
2023, 54(12):141-154. DOI: 410.6041/j.issn.1000-1298.2023.12.013
摘要 (778) HTML (0) PDF 4.49 M (621) 评论 (0) 收藏

棉秆粉碎刀具磨损状态监测系统设计与试验
谢建华，周通，王长云，刘旋峰，蒋永新，张海春
2023, 54(12):155-165. DOI: 410.6041/j.issn.1000-1298.2023.12.014
摘要 (948) HTML (0) PDF 2.36 M (623) 评论 (0) 收藏

不同正导叶几何参数下多级泵作透平功率-流量曲线研究
王世成，杨军虎，徐国斌
2023, 54(12):166-172. DOI: 410.6041/j.issn.1000-1298.2023.12.015
摘要 (774) HTML (0) PDF 1.73 M (573) 评论 (0) 收藏

> 农业信息化工程

基于改进半监督模型的空间异质性农田特征提取研究
陈理，韩毅，杨广，赖有春，郑永军，周宇光
2023, 54(12):173-185. DOI: 410.6041/j.issn.1000-1298.2023.12.016
摘要 (880) HTML (0) PDF 8.06 M (666) 评论 (0) 收藏

基于多时相多参数融合的麦玉轮作小麦产量估算方法
李阳，苑严伟，赵博，王吉中，伟利国，董鑫
2023, 54(12):186-196. DOI: 410.6041/j.issn.1000-1298.2023.12.017
摘要 (906) HTML (0) PDF 3.52 M (621) 评论 (0) 收藏

基于LightGBM的冬小麦产量估测与可解释性研究
王鹏新，王颖，田惠仁，王婕，刘峻明，权文婷
2023, 54(12):197-206. DOI: 410.6041/j.issn.1000-1298.2023.12.018
摘要 (854) HTML (0) PDF 2.46 M (633) 评论 (0) 收藏

基于多物候特征指数的冬小麦分布信息提取
吴喜芳，化仕浩，张莎，谷玲霄，马春艳，李长春
2023, 54(12):207-216. DOI: 410.6041/j.issn.1000-1298.2023.12.019
摘要 (768) HTML (0) PDF 2.85 M (639) 评论 (0) 收藏

无人机多光谱数据可靠性分析与冬小麦产量估算研究
胡田田，赵璐，崔晓路，张俊，李澳旗，王小昌
2023, 54(12):217-225. DOI: 410.6041/j.issn.1000-1298.2023.12.020
摘要 (987) HTML (0) PDF 2.29 M (646) 评论 (0) 收藏

基于冠层光谱和覆盖度的马铃薯叶片钾含量估算方法
马彦鹏，边明博，樊意广，陈志超，杨贵军，冯海宽
2023, 54(12):226-233，252. DOI: 410.6041/j.issn.1000-1298.2023.12.021
摘要 (854) HTML (0) PDF 2.44 M (555) 评论 (0) 收藏

田间茶树冠层三维信息获取及其高度和轮廓表达方法
赵润茂，范国帅，陈建能，武传宇，杜小强，郇晓龙
2023, 54(12):234-241，358. DOI: 410.6041/j.issn.1000-1298.2023.12.022
摘要 (922) HTML (0) PDF 3.00 M (623) 评论 (0) 收藏

基于改进DeepLabv3+的水稻田间杂草识别方法
曹英丽，赵雨薇，杨璐璐，李静，秦列列
2023, 54(12):242-252. DOI: 410.6041/j.issn.1000-1298.2023.12.023
摘要 (1152) HTML (0) PDF 5.72 M (777) 评论 (0) 收藏

基于融合GhostNetV2的YOLO v7水稻籽粒检测
刘庆华，杨欣仪，接浩，孙世诚，梁振伟
2023, 54(12):253-260，299. DOI: 410.6041/j.issn.1000-1298.2023.12.024
摘要 (1053) HTML (0) PDF 2.09 M (696) 评论 (0) 收藏

基于改进DeepLabv3+的番茄图像多类别分割方法
顾文娟，魏金，阴艳超，刘孝保，丁灿
2023, 54(12):261-271. DOI: 410.6041/j.issn.1000-1298.2023.12.025
摘要 (999) HTML (0) PDF 4.06 M (640) 评论 (0) 收藏

基于融合对抗训练的农作物品种信息抽取方法
许鑫，马文政，张浩，马新明，乔红波
2023, 54(12):272-279，337. DOI: 410.6041/j.issn.1000-1298.2023.12.026
摘要 (796) HTML (0) PDF 1.21 M (553) 评论 (0) 收藏

RGB-D SLAM增强现实原木检尺系统构建与测试
范永祥，冯仲科，苏珏颖，韦泽波，申朝永，闫飞口
2023, 54(12):280-287. DOI: 410.6041/j.issn.1000-1298.2023.12.027
摘要 (702) HTML (0) PDF 2.45 M (569) 评论 (0) 收藏

基于Faster-NAM-YOLO的黄瓜霜霉病菌孢子检测
乔琛，韩梦瑶，高苇，李凯雨，朱昕怡，张领先
2023, 54(12):288-307. DOI: 410.6041/j.issn.1000-1298.2023.12.028
摘要 (1074) HTML (0) PDF 4.19 M (691) 评论 (0) 收藏

基于红外热成像和改进YOLO v5的作物病害早期识别
韩鑫，徐衍向，封润泽，刘天旭，白京波，兰玉彬
2023, 54(12):300-307. DOI: 410.6041/j.issn.1000-1298.2023.12.029
摘要 (1028) HTML (0) PDF 2.62 M (665) 评论 (0) 收藏

多尺度自注意力特征融合的茶叶病害检测方法
孙艳歌，吴飞，姚建峰，周棋赢，沈剑波
2023, 54(12):308-315. DOI: 410.6041/j.issn.1000-1298.2023.12.030
摘要 (1000) HTML (0) PDF 2.23 M (663) 评论 (0) 收藏

> 农业水土工程

施氮对中国棉田产量和水分利用效率影响的Meta分析
蔡焕杰，李府阳，赵政鑫，张学桂，刘轩昂，王茂东
2023, 54(12):316-326. DOI: 410.6041/j.issn.1000-1298.2023.12.031
摘要 (883) HTML (0) PDF 1.55 M (615) 评论 (0) 收藏

气候与种植结构变化对温室气体排放及灌溉需水的影响
栾晓波，高子涵，薛静，孙世坤，唐一荷，高飞
2023, 54(12):327-337. DOI: 410.6041/j.issn.1000-1298.2023.12.032
摘要 (897) HTML (0) PDF 5.59 M (625) 评论 (0) 收藏

压力补偿式灌水器补偿腔结构参数对颗粒运动的影响
喻黎明，余家锐，李娜，钟艺，王昌满，赵思懿
2023, 54(12):338-349. DOI: 410.6041/j.issn.1000-1298.2023.12.033
摘要 (864) HTML (0) PDF 3.86 M (537) 评论 (0) 收藏

基于高光谱和机器学习模型的冬小麦土壤含水率监测研究
唐子竣，张威，向友珍，李志军，张富仓，陈俊英
2023, 54(12):350-358. DOI: 410.6041/j.issn.1000-1298.2023.12.034
摘要 (727) HTML (0) PDF 2.45 M (652) 评论 (0) 收藏

> 农业生物环境与能源工程

温室劣苗基质离散元仿真参数标定
王小琴，俞高红，刘霓红，童俊华，王钦源
2023, 54(12):359-366. DOI: 410.6041/j.issn.1000-1298.2023.12.035
摘要 (732) HTML (0) PDF 2.24 M (605) 评论 (0) 收藏

移动式荔枝蓄冷喷淋预冷装置控制系统设计与试验
郭嘉明，蔡威，林济诚，林国鹏，曾志雄，吕恩利
2023, 54(12):367-375. DOI: 410.6041/j.issn.1000-1298.2023.12.036
摘要 (892) HTML (0) PDF 2.08 M (617) 评论 (0) 收藏

> 农产品加工工程

基于属性访问控制模型的果蔬跨链追溯系统设计与实现
杨信廷，李金辉，罗娜，邢斌，孙传恒
2023, 54(12):376-388. DOI: 410.6041/j.issn.1000-1298.2023.12.037
摘要 (717) HTML (0) PDF 4.27 M (540) 评论 (0) 收藏

花生油中黄曲霉毒素B1含量的荧光光谱表征
刘翠玲，殷莺倩，张善哲，孙晓荣，李佳琮，吴静珠
2023, 54(12):389-396，430. DOI: 410.6041/j.issn.1000-1298.2023.12.038
摘要 (909) HTML (0) PDF 2.01 M (591) 评论 (0) 收藏

> 车辆与动力工程

基于QBP-PID的履带式作业机全向调平控制研究
孙泽宇，夏长高，蒋俞，郭逸凡，汪若尘
2023, 54(12):397-406. DOI: 410.6041/j.issn.1000-1298.2023.12.039
摘要 (879) HTML (0) PDF 3.15 M (707) 评论 (0) 收藏

> 机械设计制造及其自动化

基于蚁群算法与人工势场法的移动机器人路径规划
时维国，宁宁，宋存利，宁文静
2023, 54(12):407-416. DOI: 410.6041/j.issn.1000-1298.2023.12.040
摘要 (983) HTML (0) PDF 3.03 M (704) 评论 (0) 收藏

含柔性动平台并联机器人动力学建模方法研究
刘凉，汪博深，冯建峰，赵新华
2023, 54(12):417-430. DOI: 410.6041/j.issn.1000-1298.2023.12.041
摘要 (646) HTML (0) PDF 3.48 M (609) 评论 (0) 收藏

考虑混合间隙的空间并联机构非线性动力学特性分析
陈修龙，郭景尧，王景庆，赵飞跃
2023, 54(12):431-448. DOI: 410.6041/j.issn.1000-1298.2023.12.042
摘要 (630) HTML (0) PDF 5.80 M (597) 评论 (0) 收藏

基于半圆型波纹周期梁的柔顺恒力机构优化设计
刘敏，袁奇，张佳，占金青，吴剑
2023, 54(12):449-458. DOI: 410.6041/j.issn.1000-1298.2023.12.043
摘要 (772) HTML (0) PDF 2.75 M (541) 评论 (0) 收藏

doi:10.6041/j.issn.1000-1298.2023.12.022

田间茶树冠层三维信息获取及其高度和轮廓表达方法

赵润茂[1,2]　范国帅[1]　陈建能[1,2]　武传宇[1,2]　杜小强[1,3]　郇晓龙[1,2]

(1. 浙江理工大学机械工程学院, 杭州 310018; 2. 浙江省种植装备技术重点实验室, 杭州 310018;
3. 农业农村部东南丘陵山地农业装备重点实验室(部省共建), 杭州 310018)

摘要: 茶树的冠层信息是茶树田间管理的重要内容,也是茶叶机械化作业机具设计的重要依据。针对传统的作物冠层信息获取方法费时费力、主观性强且易造成损伤等问题,提出了一种茶树冠层高度和轮廓的获取与估计方法。首先,通过 3D LiDAR 从多个站点采集茶园的点云数据,对原始点云进行姿态矫正、ROI 划分、配准、降噪以及高程归一化预处理,得到高程归一化的茶树点云。其次,通过反距离权重插值法、不规则三角网插值法在不同空间分辨率下生成茶树的冠层高度模型(Canopy height model, CHM),其中,空间分辨率 0.05 m 下不规则三角网插值生成的茶树 CHM 具有较好的插值精度,模型产生的凹坑也相对较少。最后,分别以 90 ~ 100 间的 21 个百分位数提取 CHM 的栅格值作为茶树冠层高度与实测值比较,结果表明,第 98.5 百分位数时估计值最为准确,与真值间的相关系数为 0.88,平均绝对误差为 3.17 cm,均方根误差为 4.16 cm。此外,在高程归一化的茶树点云中提取 20 处冠层断面点云,分别采用椭圆模型、高斯模型和二次多项式模型拟合了冠层轮廓点云,其中,二次多项式模型能更好地反映茶树冠层轮廓特征,点云与拟合曲线间平均最小距离的均值为 2.60 cm,方差为 0.21 cm^2。研究可为茶园现代化管理和茶叶机械化作业机具的设计提供理论支持。

关键词: 茶树; 三维信息; 冠层高度; 冠层轮廓; 激光雷达

中图分类号: S24　　**文献标识码**: A　　**文章编号**: 1000-1298(2023)12-0234-08　　**OSID**:

Describing Height and Outline of Tea Canopy in Natural Field with 3D Sensing

ZHAO Runmao[1,2]　FAN Guoshuai[1]　CHEN Jianneng[1,2]　WU Chuanyu[1,2]　DU Xiaoqiang[1,3]　HUAN Xiaolong[1,2]

(1. *School of Mechanical Engineering, Zhejiang Sci-Tech University, Hangzhou* 310018, *China*
2. *Key Laboratory of Transplanting Equipment and Technology of Zhejiang Province, Hangzhou* 310018, *China*
3. *Key Laboratory of Agricultural Equipment for Hilly and Mountainous Areas in Southeastern China (Co-construction by Ministry and Province), Ministry of Agriculture and Rural Affairs, Hangzhou* 310018, *China*)

Abstract: Canopy information is an important element of tea field management and an important basis for the design of related equipment. Aiming at the traditional methods of obtaining crop canopy information, which are time-consuming, subjective and prone to damage, a method of obtaining and estimating the height and outline of the tea tree canopy was proposed. Firstly, the point cloud data of the tea field was collected from multiple sites by 3D LiDAR, and the original point cloud was pre-processed with attitude correction, ROI selection, alignment, noise reduction, and elevation normalization to obtain the elevation-normalized tea tree point cloud. Secondly, the canopy height model (CHM) of tea trees was generated by inverse distance weight (IDW) and triangulation irregular network (TIN) at different spatial resolutions, among which, the CHM of tea trees generated by IDW at 0.05 m spatial resolution had better interpolation accuracy and the model produced relatively fewer pits. Finally, the raster values of CHM were extracted from 21 percentiles between 90 and 100 as the canopy height of tea trees and compared with the measured values. The results showed that the estimated value was most accurate when the percentile was 98.5, and the correlation coefficient with the true value was 0.88, with an average

收稿日期: 2023-09-15　修回日期: 2023-10-10

基金项目: 国家自然科学基金项目(52105284、32301715)、浙江省“尖兵”研发攻关计划项目(2023C02009)、财政部和农业农村部:国家现代农业产业技术体系项目和中国博士后科学基金项目(2022M722819)

作者简介: 赵润茂(1990—),男,讲师,博士,主要从事农场环境融合感知与农业机器人研究,E-mail: rmzhao@zstu.edu.cn

通信作者: 陈建能(1972—),男,教授,博士生导师,主要从事农业装备及其智能化研究,E-mail: jiannengchen@zstu.edu.cn

absolute error of 3.17 cm, and a root mean square error of 4.16 cm. In addition, totally 20 canopy section point clouds were extracted from the elevation-normalized tea tree point clouds and their outlines were fitted by elliptic, Gaussian and quadratic polynomial models, respectively. The results showed that the quadratic polynomial model could better reflect the characteristics of the tea tree canopy outline, and the mean value of the average minimum distance between the points and the fitted curves was 2.60 cm with a variance of 0.21 cm^2. The research can provide theoretical support for the modern management of tea fields and the design of related equipment.

Key words: tea tree; 3D information; canopy height; canopy outline; LiDAR

0　引言

作物的冠层信息被广泛应用于作物的遗传育种[1]、产量预测[2]、植保管理[3]等方面,对现代农业的发展有重要意义。在早期,作物的冠层信息大多通过人工实地测量获取,此类方法不仅费时费力、主观性强,还容易对作物造成损伤[4]。近年来,随着先进传感器技术在农业领域的应用和发展,快速、准确、无损地获取作物冠层信息成为研究热点。该领域中常用的设备包括相机和激光雷达(Light detection and ranging,LiDAR)等[5-6]。其中,相机受环境光影响较大,通常用于室内获取植株的表型[7-8],而 LiDAR 因扫描范围广且具备较强的抵光性,更适合田间。LUO 等[9]通过随机森林方法对 LiDAR 变量重要性进行排列,建立了作物高度预测模型并估计玉米与大豆的高度,模型的高度预测值与真实值表现出较高的相关性。苏伟等[10]采用地基 LiDAR 获取大田玉米个体植株三维点云数据,通过对叶片进行三角网建模估计了玉米叶面积,与实测值间的均方根误差为 12.69 cm^2,平均绝对百分比误差为 2.38%。管贤平等[11]通过机载 LiDAR 获取大田大豆点云,将植株点云重心在地面上投影,取平均值作为植株茎部与地面的交点,计算得到大豆高度与测量值间的平均相对误差为 5.14%。

我国是世界上最大的茶叶生产国和消费国,茶园面积和茶叶产量均为世界第一,2022 年全国干毛茶总产量高达 3.18×10^6 t,总产值突破 3 180 亿元[12-14]。茶树的冠层信息,不仅是茶树田间管理的重要内容[15-16],也是茶树全程机械化作业机具设计的重要依据,如川崎采茶机所用的割刀为弧形,赵润茂等[17]设计的仿形采茶机采用多把直刀代替弧形割刀贴合茶树冠层。因此,快速准确获取自然环境下茶树的冠层信息对茶产业的发展有重要意义。冠层高度模型(Canopy height model,CHM)是植物冠层点云经空间插值处理后生成的规则格网数据[18],一般由数字高程模型(Digital elevation model,DEM)与数字表面模型(Digital surface model,DSM)作差,或通过归一化后的点云直接插值得到[19]。近年来,CHM 被应用于农作物的高度估计。车荧璞等[20]将 CHM 与超分辨重建相结合,计算了不同生育期玉米的株高,根据重建影像估计的株高与实测值的相关性较好,均方根误差(RMSE)为 3.9 cm。GUO 等[21]通过地面激光扫描(TLS)采集小麦点云并生成 CHM,从中提取了一系列 TLS 衍生指标用于估计不同生长期的小麦高度,然而,需要在小麦播种前采集地面点云。束美艳等[22]对柑橘的 CHM 使用分水岭算法分割单木,有效提取了柑橘的株高以及冠幅投影面积,然而,该方法对低矮、树冠小的植株易产生漏检现象,且不适合密植的茶树。

为快速准确获取茶树冠层信息,本研究首先通过 3D LiDAR 从多个站点采集茶园的三维点云并拼接,处理后得到高程归一化的茶树点云,采用空间插值法生成茶树的冠层高度模型。在此基础上,提出茶树冠层高度和轮廓的估计与分析方法,并对估计结果准确性进行评价。

1　材料与方法

1.1　数据获取

试验地点位于浙江省杭州市余杭区瓶窑镇杭州茶叶试验场(30°24′23″N,119°54′05″E)。所选取的试验田块如图 1 所示,宽度为 6 m,长度为 20 m,含茶树 4 垄,共计长度 80 m,茶垄间距约 1.5 m,茶树的品种为鸠坑种。

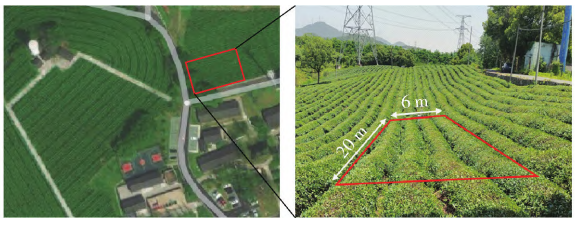

图 1　研究区域

Fig. 1　Study area

1.1.1　冠层高度真值

茶树冠层高度为地面至茶树冠层最高点的距离。于 2023 年 4 月 12 日进行测量,如图 2a 所示,

以茶垄的一端作为起始点,2 m 为间隔距离,将各茶垄划分为 10 个小区域,4 垄茶树共计划分出 40 个小区域。在划分得到的各个小区域中,采用等距取样方法,取各小区域距边线 0.33、0.66、0.99、1.32、1.65 m 处的冠层最高点,使用刻度尺测量高度,取测量平均值作为该小区域内茶树冠层的实测高度。

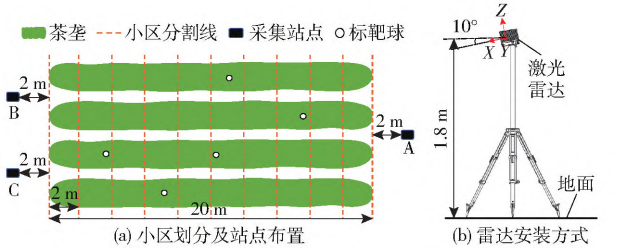

(a) 小区划分及站点布置 (b) 雷达安装方式

图 2 小区划分与设备布局

Fig. 2 Plots division and devices layout

1.1.2 茶园点云采集

上位机操作系统为 Ubuntu 18.04,配置了机器人操作系统(Robot operating system, ROS)、点云库(Point cloud library, PCL)以及开源点云处理软件 CloudCompare,在此基础上进行点云的采集、处理。选用的 LiDAR 为 Livox Mid-40,该 LiDAR 探测距离为 260 m,视场角为圆形 38.4°,点云数据率 100 000 点/s,距离精度 2 cm,角度精度 0.05°,采用非重复扫描方式,随积分时间增长能够获得接近 100% 的视场覆盖率。如图 2a 所示,点云数据的采集先后在 A、B、C 3 个站点进行,采集前在茶园中固定好 5 个标靶球用于后期拼接。LiDAR 的安装方式如图 2b 所示,LiDAR 被安装在三脚架上,安装高度为 1.8 m,俯仰偏置角为 10°,对茶园呈俯视姿态。采集现场如图 3 所示,LiDAR 通过 Ethernet 与上位机通信,由上位机控制数据的采集,在每个站点各记录约 10 s 点云数据。

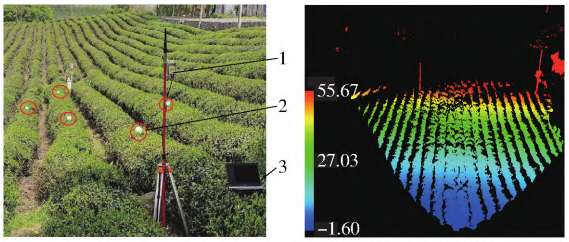

(a) 采集现场 (b) 站点A所采点云

图 3 点云数据采集

Fig. 3 Point cloud acquisition

1. 激光雷达 2. 标靶球 3. 上位机

1.2 点云数据处理

1.2.1 点云姿态矫正

由于 LiDAR 倾斜安装,需要通过点云变换对各站点获取的原始点云进行姿态矫正,点云变换公式为

$$\begin{bmatrix} x \\ y \\ z \end{bmatrix} = \begin{bmatrix} \cos\theta & 0 & \sin\theta \\ 0 & 1 & 0 \\ -\sin\theta & 0 & \cos\theta \end{bmatrix} \begin{bmatrix} x_1 \\ y_1 \\ z_1 \end{bmatrix} \tag{1}$$

式中 θ——LiDAR 安装倾斜角

(x_1, y_1, z_1)——原始点云坐标

(x, y, z)——姿态矫正后点云坐标

1.2.2 ROI 划分

点云数据中包含大量试验茶田外的背景点,这些点并非研究对象,并且会增加后续数据处理的难度,因此将各站点采集得到的点云进行姿态矫正后,使用 CloudCompare 软件对点云进行手动裁切,仅保留试验田块部分作为 ROI 点云。

1.2.3 点云配准

由于从不同站点扫描得到的点云处于不同坐标系下,需要进行点云配准,以实现多站点云的坐标系统一。目前应用最为广泛的点云配准算法为 BESL 等[23]提出的迭代最近点(Iterative closest point,ICP)算法,该算法的实质是以最小二乘法为基础的最优匹配,在目标点云 P 与源点云 Q 间通过重复寻找最邻近点对、解算刚体变换矩阵、应用刚体变换矩阵的步骤,使目标函数经过迭代达到最小,得到最优变换矩阵,目标函数可表示为

$$f(\boldsymbol{R}, \boldsymbol{T}) = \frac{1}{n_c} \sum_{i=1}^{n_c} \| q_i - (\boldsymbol{R} p_i + \boldsymbol{T}) \|^2 \tag{2}$$

式中 $\boldsymbol{R}$——旋转矩阵

$\boldsymbol{T}$——平移向量

n_c——邻近点对的数量

p_i——目标点云 P 中的点

q_i——源点云 Q 中与 p_i 对应的邻近点

ICP 算法虽然能够实现点云间的精确匹配,但对点云的初始位置要求较高,为避免算法陷入局部最优解,通常需要对点云先进行粗配准。首先以布置在茶园环境中的标靶球作为定位点,通过选取同名点的方式,对各站点的 ROI 点云进行粗配准,初步优化点云间的相对位姿,然后再通过 ICP 算法迭代最近点,得到精确配准后的点云。

1.2.4 点云去噪

考虑到噪点在空间中离群分布的特征,研究采用统计滤波对精配准后的点云进行去噪。统计滤波的主要思想是假设点云中任意点与其邻近点的平均距离符合高斯分布,根据均值与标准差确定一个距离阈值,认为阈值外的点为离群点并进行剔除,具体步骤如下:

(1)对精配准后的点云 P 建立 Kd-tree 数据结构,计算 P 中的点 P_m 与其邻近点之间的平均欧氏距

离，邻近点表示为 $P_i(i=1,2,\cdots,k,k\geqslant 1)$，则

$$d_m=\frac{\sum_{i=1}^{k}\sqrt{(x_i-x_m)^2+(y_i-y_m)^2+(z_i-z_m)^2}}{k} \tag{3}$$

式中　d_m——P_m与其邻近点之间的平均欧氏距离

k——邻近点个数

(x_m,y_m,z_m)——点 P_m的坐标

(x_i,y_i,z_i)——点 P_i的坐标

(2)若点云集 P 共包含 n_p个点，则 P 中所有点与其 k 邻域内点的平均欧氏距离的均值 μ_p与标准差 σ_p可表示为

$$\mu_p=\frac{\sum_{m=1}^{n_p}d_m}{n_p} \tag{4}$$

$$\sigma_p=\sqrt{\frac{\sum_{m=1}^{n_p}(d_m-\mu_p)^2}{n_p}} \tag{5}$$

(3)根据标准差与均值设定距离阈值为

$$d_{\max}=\mu_p+\alpha\sigma_p \tag{6}$$

式中　$d_{\max}$——距离阈值　　α——比例系数

(4)对点云集 P 进行遍历，判断遍历到的点与其 k 邻域内点的平均欧氏距离是否大于距离阈值，若大于则将该点剔除，否则保留该点，最终得到降噪后的试验茶垄点云。

1.2.5　地面点分离及点云高程归一化

为将地面点从试验茶垄点云中分离出来，研究采用了布料模拟滤波算法(Clothe simulation filter，CSF)[24-25]，该算法对复杂地形具有较强的适应能力。CSF 算法的思想是先将点云进行翻转，随后假设有一块刚性布料落于翻转后的点云上方，在重力以及布料节点间的相互作用力下，布料的形状近似变化为地表形状，最后根据点云与布料曲面之间的距离实现地面点的提取。在布料模拟过程中，布料形状的变化由外部因素(重力)和内部因素(节点间相互作用力)共同决定，其原理为

$$m\frac{\partial X(t)}{\partial t^2}=F_{ext}(X,t)+F_{int}(X,t) \tag{7}$$

式中　$X(t)$——布料节点在 t 时刻的位置

m——节点质量，取 1

F_{ext}——外部因素

F_{int}——内部驱动因素

在外部因素作用下，布料节点位移 $X(t+\Delta t)$计算公式为

$$X(t+\Delta t)=2X(t)-X(t-\Delta t)+\frac{G}{m}(\Delta t)^2 \tag{8}$$

式中　G——重力常数　　Δt——时间步长

内部因素引起的位移向量计算公式为

$$\boldsymbol{d}=\frac{1}{2}b(\boldsymbol{p}_i-\boldsymbol{p}_0)\boldsymbol{n} \tag{9}$$

其中　$b=\begin{cases}1 & (\text{节点可移动})\\ 0 & (\text{节点不可移动})\end{cases}$

式中　$\boldsymbol{d}$——布料节点的位移向量

b——节点状态

$\boldsymbol{p}_0$——待移动节点的当前位置

$\boldsymbol{p}_i$——p_0相邻节点的位置

$\boldsymbol{n}$——垂直方向上的单位向量

通过 CSF 从试验茶垄点云中分离出地面点后，以地面点为基准，对茶垄点云进行高程归一化，处理过程为用茶垄点云中每个点的 z 坐标值减去最近地面点的 z 坐标值，消除地形对点云高程的影响，得到归一化的茶垄点云。

1.3　冠层高度估计方法

1.3.1　冠层高度模型生成

生成 CHM 的两种方法中，通过 DEM 与 DSM 作差得到 CHM 需要经历 2 次空间插值，会增加信息的损失[26]，因此选择直接对归一化后的茶垄点云插值生成 CHM。空间插值方法有多种，不同插值方法的适用性有所差异，并无绝对的最优方法[27]。其中，反距离权重插值法(Inverse distance weighted，IDW)[28]、不规则三角网插值法(Triangulation irregular network，TIN)[29]是比较有代表性的两种方法。IDW 插值指的是采用一组采样点线性权重组合来判定栅格的像元值，权重主要由已知点和预测点之间的距离决定，权重与距离呈反比关系，IDW 插值得到的预测值为

$$z_{pre_j}=\sum_{i=1}^{n}\frac{1}{d_i^p}z_i\left(\sum_{i=1}^{n}\frac{1}{d_i^p}\right)^{-1} \tag{10}$$

式中　z_{pre_j}——点 j 处的预测值

z_i——第 i 个已知点的值

d_i——已知点 i 与预测点 j 之间的距离

n——参与计算的已知点数量

p——指定的幂值

其中，幂值 p 控制着已知点对内插值的影响，p 越大则预测点受临近点的影响越大，插值结果局部变异越强(模型越不平滑)，相反，p 越小时预测点受远点的影响越大，插值结果整体性更强(模型越平滑)。TIN 插值是另一种被广泛应用的空间插值法，该方法对点云中的所有点进行狄洛尼(Delaunay)三角网构建，构建的原则是三角网中任意一个三角形的外接圆内不存在其他点，最后根据预测点与相邻三角形之间的角度和距离进行插值，与规则格网相比，不

规则三角网精度更高,能更好地反映地形地貌特征,但是算法的复杂度也相对更高。

为使得生成的 CHM 能够更准确地表达茶树的冠层形态,以归一化后的茶垄点云为研究对象,对不同插值方法生成的 CHM 进行比较并择优。具体方法为:从归一化后的茶垄点云中随机抽取 90% 的点云作为插值对象,剩余 10% 的点云用于验证插值精度;利用 2 种不同插值方法(IDW、TIN)生成 CHM,考虑到空间分辨率对插值效果的影响,每种插值方法均采用 6 种空间分辨率(0.01、0.05、0.1、0.15、0.2、0.25 m)分别进行插值;最后,利用验证点云对插值精度进行评价与择优,评价指标为验证点高程与对应插值面高程间的平均绝对误差(Mean absolute error,MAE)、均方根误差(Root mean squared error,RMSE)和粗差率 c。粗差率计算公式为

$$c = \frac{n_e}{n_v} \times 100\% \tag{11}$$

式中 n_v——验证点数量

n_e——误差大于限差(按照拉依达准则,将 3 倍的 E 设为限差)的点数量

1.3.2 冠层高度估计

选择插值效果较好的 CHM 作为高度估计对象,以 2 m 为间隔,将 CHM 中的茶垄分为 40 个小区域,与现场测量时划分的 40 个小区域相对应。CHM 的像素百分位数代表冠层的不同位置,高百分位数代表了冠层上边界,为研究估计茶树冠层高度的最佳百分位数,采用不同百分位数对分离出的小区域进行高度提取,并与对应的真实值进行比较,验证冠层高度估计精度,评价指标为冠层高度估计值与真实值之间的 MAE、RMSE 以及决定系数 R^2。

1.4 冠层轮廓拟合方法

如图 4a 所示,对于剔除地面点且高程归一化后的茶垄点云,在垂直茶垄方向随机选择 5 处断面并提取 1 cm 缓冲区内的点云,如图 4b 所示,5 处断面共得到 20 处茶树冠层的点云。对于各茶树冠层点云,忽略其 X 维度(即假定冠层点云为 YOZ 平面上的二维点云),分别使用椭圆模型、二次多项式模型和高斯模型,以最小二乘法对茶树冠层点云进行拟合,计算点云中各点与拟合曲线的平均最小距离 d_{mean} 以及不同模型下 d_{mean} 的均值与方差,对不同模型的拟合效果进行评价。d_{mean} 的计算公式为

$$d_{mean} = \frac{\sum_{i=1}^{n_E} d_{min_i}}{n_E} \tag{12}$$

式中 d_{min_i}——冠层点云中某点至拟合曲线的最小距离

n_E——冠层点云中点的个数

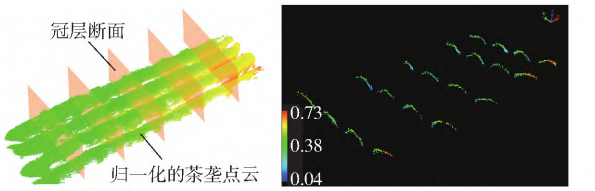

(a) 断面示意图 (b) 冠层断面点云

图 4 茶树冠层断面点云提取

Fig. 4 Extracting point clouds of canopy section

2 结果与分析

2.1 茶园点云预处理结果

图 5 为站点 A 的点云在姿态矫正前后的 Y 坐标轴方向视图,可见经姿态矫正后,LiDAR 安装角度带来的视角倾斜已被消除。

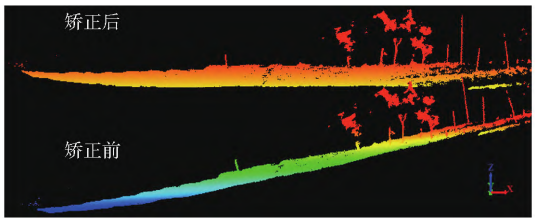

图 5 点云姿态矫正

Fig. 5 Point cloud pose correction

对姿态矫正后的各站点点云进行 ROI 划分选取,得到的 ROI 点云如图 6a 所示,发现受茶垄间相互遮挡的影响,单个站点采集的点云地面点大量缺失,不利于后续点云的高程归一化;对各站 ROI 点云进行粗配准、精配准,得到点云如图 6b 所示。配准前,A、B、C 3 站点 ROI 点云的密度分别为 4 632、7 215、7 005 个/m^2,经配准后点云密度提升至 18 852 个/m^2,点云质量得到提高,地面点云、茶垄点云更为完整。

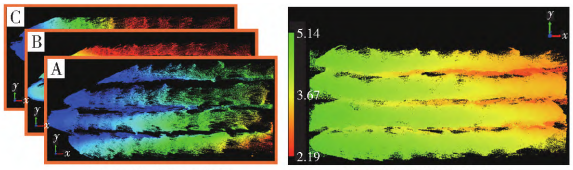

(a) 各站点ROI点云 (b) 配准后的茶垄点云

图 6 点云配准

Fig. 6 Point cloud registration

图 7a 为茶垄点云的局部放大图,发现有大量噪点附着于茶垄表面,这些噪点具有离茶垄主体较远、分布零散的特征。噪点的存在可能会导致冠层高度估计值的偏高,为此对点云进行统计滤波,滤波结果如图 7b 所示,可见大部分噪点已得到剔除。

试验区的茶树种植于山地,茶园地形并不平整,为此首先采用 CSF 算法对点云进行地面点分离,分离结果如图 8a 所示,随后以地面点为基准对茶垄点云进行高程归一化,消除了地形对点云高程的影响,

归一化前后的点云如图 8b 所示。

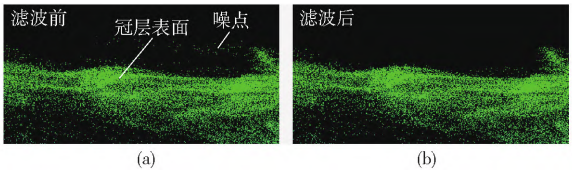

图 7　统计滤波去噪

Fig. 7　Denoising by statistical filtering

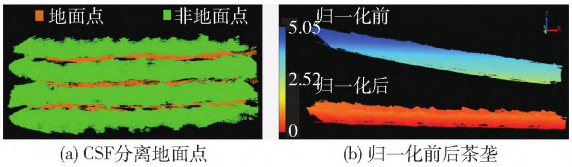

图 8　点云高程归一化

Fig. 8　Normalization of point cloud elevation

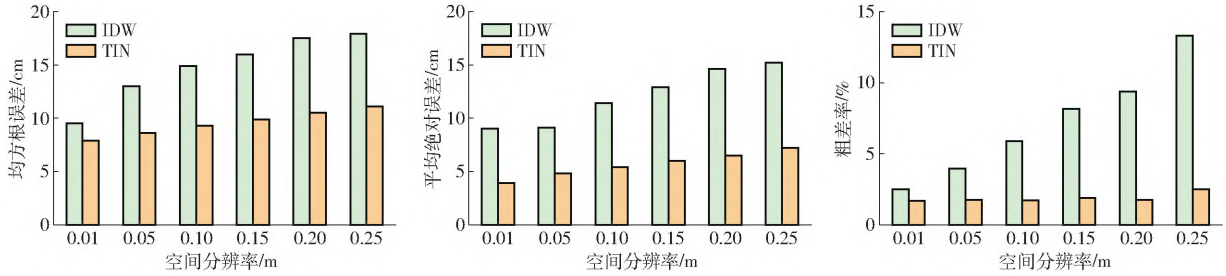

图 9　插值精度验证结果

Fig. 9　Interpolation accuracy verification results

2.2　CHM 插值效果分析

从归一化点云中随机抽取 90% 的点云后，分别通过 IDW、TIN 在 6 个不同空间分辨率下生成 12 个 CHM，随后以剩余的 10% 归一化点云作为验证点云，RMSE、MAE、粗差率作为评估指标，对 CHM 进行插值精度评价，结果如图 9 所示。从图 9 可以看出，在同一空间分辨率下，3 项评价指标均为 TIN 方法生成的 CHM 占据绝对优势，证明 TIN 比 IDW 更适用于生成本研究对象的 CHM。在不同的空间分辨率下，对于 RMSE、MAE 两项评价指标，两种插值法的表现具有一定的相似性，RMSE、MAE 均随着空间分辨率的下降而上升；在粗差率方面，两种插值法的表现有所不同，IDW 方法下的粗差率仍表现为随着空间分辨率的下降而上升，但 TIN 方法下的粗差率受空间分辨率影响较小，始终稳定在 2.5% 以内。

从上述分析看，选择较高的空间分辨率能够获得更高的插值精度，然而，当空间分辨率过高时，CHM 中会出现大量凹坑[30]。凹坑也被称为无效值，是 CHM 图像中黑色的栅格部分，由冠层部分的高程突变造成，对冠层参数的提取有一定影响。如图 10 所示，相比于空间分辨率 0.05 m，空间分辨率 0.01 m 下生成的 CHM 虽然更加精细，但栅格图像中的凹坑占有率较高。综上所述，选择 TIN 方法在空间分辨率 0.05 m 下生成的 CHM 进行后续冠层高度的估计，此时验证点云与对应插值面高程间的 MAE 为 4.8 cm，RMSE 为 8.6 cm。

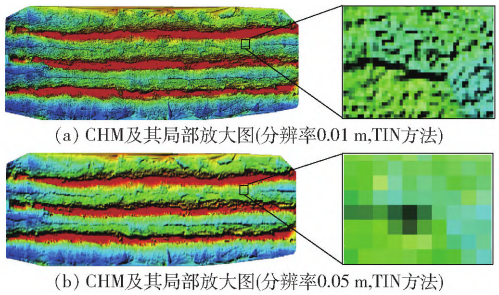

图 10　CHM 中的凹坑

Fig. 10　Pits in CHM

2.3　冠层高度估计结果

根据空间分辨率 0.05 m 下 TIN 生成的 CHM，以 CHM 栅格值的不同百分位数（90 ~ 100 间共计 21 个百分位数）作为上边界估计茶树冠层高度，与冠层高度的实测值进行对比分析，结果如图 11 所示。对于 CHM 中的百分位数，低百分位数表示接近地面部分，高百分位数代表地面以上的植被高度。如图 11a、11b 所示，RMSE、MAE 的变化趋势基本相同，两者先随着百分位数的增加而下降，但在接近第 100 分位数时又迅速升高；如图 11c 所示，决定系数 R^2 在不同百分位数下始终保持在 0.85 以上，表明冠层高度估计值与实测值之间具有良好的相关性，此外，在第 100 分位数时 R^2 有所下降，这与 RMSE、MAE 的变化相符合。上述结果中，高度估计的最佳结果并非出现在第 100 分位数，其主要原因是高度实测时不能保证采样点为实际冠层最高处，这与 LUO 等[9]、王庆等[31]的研究结果相一致。因此，选择 RMSE、MAE 最小的第 98.5 分位数作为高度估计的最佳百分位数，此时冠层高度估计值与实测值之间的关系如图 11d 所示，R^2 为 0.88，MAE 为 3.17 cm，RMSE 为 4.16 cm。

2.4　冠层轮廓拟合结果

图 12a 为椭圆模型、二次多项式模型、高斯模型对某一冠层点云进行曲线拟合的结果，可以看出，冠层点云在二维平面上的整体分布呈弧状，与实际的茶树冠层形状相符，3 种模型拟合出的曲线均能反

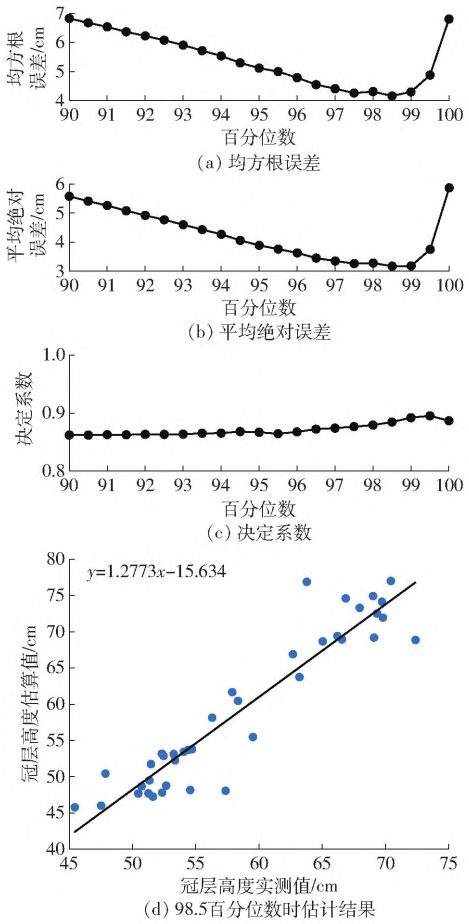

图 11 冠层高度估计结果

Fig. 11 Accuracy assessment of canopy height estimation

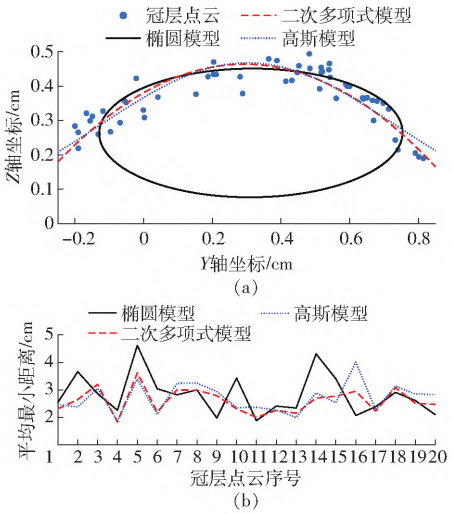

图 12 冠层轮廓拟合结果

Fig. 12 Results of canopy outline fitting

映这一特征。各冠层点云中,点云与拟合曲线的平均最小距离 d_{mean} 如图 12b 所示,计算不同模型下 d_{mean} 的均值 μ、方差 σ^2,结果如下:椭圆模型下 μ 为 2.83 cm,σ^2 为 0.56 cm^2,二次多项式模型下 μ 为 2.60 cm,σ^2 为 0.21 cm^2,高斯模型下 μ 为 2.71 cm,σ^2 为 0.29 cm^2。上述结果表明,相较于椭圆模型、高斯模型,二次多项式模型拟合的曲线能更好地反映茶树冠层的轮廓特征。

3 结论

(1)提出了一种自然环境下茶树三维信息的高通量获取方法,采用 3D LiDAR 从多个站点采集茶园的点云数据,拼接并处理后得到高程归一化的茶树点云。

(2)提出了一种茶树冠层轮廓形状表达方法,在高程归一化的茶树点云的基础上,采用二次多项式拟合冠层断面点云,点云与拟合曲线间平均最小距离的均值为 2.60 cm,方差为 0.21 cm^2。

(3)提出了一种茶树冠层高度估计方法,先采用不规则三角网插值法生成茶树冠层高度模型,在此基础上,以第 98.5 百分位数处的高程作为茶树冠层高度,估计高度与实测值间的决定系数为 0.88,平均绝对误差为 3.17 cm,均方根误差为 4.16 cm。

参 考 文 献

[1] 牛庆林,冯海宽,杨贵军,等. 基于无人机数码影像的玉米育种材料株高和 LAI 监测[J]. 农业工程学报,2018,34(5):73-82.
NIU Qinglin,FENG Haikuan,YANG Guijun,et al. Monitoring plant height and leaf area index of maize breeding material based on UAV digital images[J]. Transactions of the CSAE,2018,34(5): 73-82. (in Chinese)

[2] 向友珍,安嘉琪,赵笑,等. 基于无人机多光谱遥感的大豆生长参数和产量估算[J]. 农业机械学报,2023,54(8): 230-239.
XIANG Youzhen,AN Jiaqi,ZHAO Xiao,et al. Soybean growth parameters and yield estimation based on UAV multispectral remote sensing[J]. Transactions of the Chinese Society for Agricultural Machinery,2023,54(8): 230-239. (in Chinese)

[3] WU J Y,WEN S,LAN Y B,et al. Estimation of cotton canopy parameters based on unmanned aerial vehicle (UAV) oblique photography[J]. Plant Methods,2022,18(1): 129.

[4] 陶惠林,徐良骥,冯海宽,等. 基于无人机高光谱遥感的冬小麦株高和叶面积指数估算[J]. 农业机械学报,2020,51(12): 193-201.
TAO Huilin,XU Liangji,FENG Haikuan,et al. Estimation of plant height and leaf area index of winter wheat based on UAV hyperspectral remote sensing[J]. Transactions of the Chinese Society for Agricultural Machinery,2020,51(12): 193-201. (in Chinese)

[5] 郭庆华,杨维才,吴芳芳,等. 高通量作物表型监测:育种和精准农业发展的加速器[J]. 中国科学院院刊, 2018,33(9): 940-946.
GUO Qinghua,YANG Weicai,WU Fangfang,et al. High-throughput crop phenotyping: accelerators for development of breeding

and precision agriculture[J]. Bulletin of Chinese Academy of Sciences,2018,33(9): 940 - 946. (in Chinese)

[6] 张建,谢田晋,杨万能,等. 近地遥感技术在大田作物株高测量中的研究现状与展望[J]. 智慧农业(中英文),2021,3(1):1 - 15.
ZHANG Jian,XIE Tianjin,YANG Wanneng,et al. Research status and prospect on height estimation of field crop using near-field remote sensing technology[J]. Smart Agriculture,2021,3(1): 1 - 15. (in Chinese)

[7] 徐胜勇,李磊,童辉,等. 基于 RGB - D 相机的黄瓜苗 3D 表型高通量测量系统研究[J]. 农业机械学报,2023,54(7): 204 - 213,281.
XU Shengyong,LI Lei,TONG Hui,et al. High-throughput measurement system for 3D phenotype of cucumber seedlings using RGB - D camera[J]. Transactions of the Chinese Society for Agricultural Machinery,2023,54(7): 204 - 213,281. (in Chinese)

[8] 徐焕良,马仕航,王浩云,等.基于几何模型的绿萝叶片外部表型参数三维估测[J]. 农业机械学报,2020,51(12): 220 - 228.
XU Huanliang, MA Shihang, WANG Haoyun, et al. Three-dimensional estimation of money plant leaf external phenotypic parameters based on geometric model[J]. Transactions of the Chinese Society for Agricultural Machinery,2020,51(12): 220 - 228. (in Chinese)

[9] LUO S Z, LIU W W, ZHANG Y Q, et al. Maize and soybean heights estimation from unmanned aerial vehicle (UAV) LiDAR data[J]. Computers and Electronics in Agriculture, 2021, 182: 106005.

[10] 苏伟,蒋坤萍,郭浩,等. 地基激光雷达提取大田玉米植株表型信息[J]. 农业工程学报,2019,35(10):125 - 130.
SU Wei,JIANG Kunping,GUO Hao,et al. Extraction of phenotypic information of maize plants in field by terrestrial laser scanning[J]. Transactions of the CSAE,2019,35(10): 125 - 130. (in Chinese)

[11] 管贤平,刘宽,邱白晶,等. 基于机载三维激光扫描的大豆冠层几何参数提取[J]. 农业工程学报, 2019, 35(23): 96 - 103.
GUAN Xianping,LIU Kuan,QIU Baijing,et al. Extraction of geometric parameters of soybean canopy by airborne 3D laser scanning[J]. Transactions of the CSAE,2019,35(23): 96 - 103. (in Chinese)

[12] 李杨,董春旺,陈建能,等. 茶叶智能采摘技术研究进展与展望[J]. 中国茶叶,2022,44(7):1 - 9.
LI Yang,DONG Chunwang,CHEN Jianneng,et al. Research progress and prospect of intelligent tea picking technology[J]. China Tea,2022,44(7): 1 - 9. (in Chinese)

[13] 吴敏,郇晓龙,陈建能,等. 融合 2D 激光雷达与航向姿态参考系统的采茶机仿形方法研究与试验[J]. 茶叶科学,2023,43(1):135 - 145.
WU Min,HUAN Xiaolong,CHEN Jianneng,et al. Research and experiment on profiling method of tea picker based on fusion of 2D - LiDAR and attitude and heading reference system[J]. Journal of Tea Science,2023,43(1): 135 - 145. (in Chinese)

[14] 梅宇,张朔. 2022 年中国茶叶生产与内销形势分析[J]. 中国茶叶,2023,45(4):25 - 30.
MEI Yu,ZHANG Shuo. Analysis of China's tea production and domestic sales in 2022[J]. China Tea,2023,45(4): 25 - 30. (in Chinese)

[15] 郑旭霞,王渡丹,李红莉,等. 西湖龙井茶园不同修剪方式效果比较[J]. 中国茶叶,2020,42(11):55 - 59.
ZHENG Xuxia,WANG Dudan,LI Hongli,et al. Comparisons of different pruning applications on Xihu Longjing tea plantations [J]. China Tea,2020,42(11): 55 - 59. (in Chinese)

[16] 王琼琼,孙威江,黄伙水,等. 不同修剪高度对茶树稀土和氟铝含量及品质的研究[J]. 食品安全质量检测学报,2015,6(4):1229 - 1236.
WANG Qiongqiong, SUN Weijiang, HUANG Huoshui, et al. Analysis of rare-earth element, F and Al and biochemical components content in tea plant with different cutting heights[J]. Journal of Food Safety and Quality,2015,6(4): 1229 - 1236. (in Chinese)

[17] 赵润茂,卞贤炳,陈建能,等. 分布控制的乘坐式仿形采茶原型机研制与试验[J]. 茶叶科学,2022,42(2):263 - 276.
ZHAO Runmao,BIAN Xianbing,CHEN Jianneng,et al. Development and test for distributed control prototype of the riding profiling tea harvester[J]. Journal of Tea Science,2022,42(2): 263 - 276. (in Chinese)

[18] 段祝庚,肖化顺,袁伟湘. 基于离散点云数据的森林冠层高度模型插值方法[J]. 林业科学,2016,52(9): 86 - 94.
DUAN Zhugeng,XIAO Huashun,YUAN Weixiang. Comparison of interpolation methods of forest canopy height model using discrete point cloud data[J]. Scientia Silvae Sinicae,2016,52(9): 86 - 94. (in Chinese)

[19] 段祝庚,曾源,赵旦,等. 机载激光雷达森林冠层高度模型凹坑去除方法[J]. 农业工程学报,2014,30(21):209 - 217.
DUAN Zhugeng,ZENG Yuan,ZHAO Dan,et al. Method of removing pits of canopy height model from airborne laser radar[J]. Transactions of the CSAE,2014,30(21): 209 - 217. (in Chinese)

[20] 车荧璞,王庆,李世林,等. 基于超分辨率重建和多模态数据融合的玉米表型性状监测[J]. 农业工程学报,2021,37(20):169 - 178.
CHE Yingpu,WANG Qing,LI Shilin,et al. Monitoring of maize phenotypic traits using super-resolution reconstruction and multimodal data fusion[J]. Transactions of the CSAE, 2021, 37(20): 169 - 178. (in Chinese)

[21] GUO T, FANG Y, CHENG T, et al. Detection of wheat height using optimized multi-scan mode of LiDAR during the entire growth stages[J]. Computers and Electronics in Agriculture, 2019, 165: 104959.

(下转第 358 页)

53(11):379 - 387.
ZHANG Junhua, SHANG Tianhao, CHEN Ruihua, et al. Inversion of soil organic matter content in Yinchuan plain using field spectral fractional-order derivatives combined with spectral optimization index[J]. Transactions of the Chinese Society for Agricultural Machinery, 2022, 53(11):379 - 387. (in Chinese)
[38] 范梅凤,蔡焕杰,李志军. 基于高光谱遥感水分指数的叶片与土壤含水率监测研究[J]. 灌溉排水学报, 2014, 33(增刊1):213 - 217.
FAN Meifeng, CAI Huanjie, LI Zhijun, et al. Monitoring leaf and soil moisture status based on hyperspectral-derived vegetation moisture indices[J]. Journal of Irrigation and Drainage, 2014, 33(Supp. 1):213 - 217. (in Chinese)
[39] 何华,康绍忠,曹红霞. 灌溉施肥部位对玉米同化物分配和水分利用的影响[J]. 西北植物学报, 2003(8):1458 - 1461.
HE Hua, KANG Shaozhong, CAO Hongxia. Effect of fertigation depth on dry matter partition and water use efficiency of corn [J]. Acta Botanica Boreali-occidentalia Sinica, 2003(8):1458 - 1461. (in Chinese)
[40] GUO Jinjin, FAN Junliang, XIANG Youzhen, et al. Maize leaf functional responses to blending urea and slow-release nitrogen fertilizer under various drip irrigation regimes[J]. Agricultural Water Management, 2022, 262:107396.
[41] 夏天,吴文斌,周清波,等. 冬小麦叶面积指数高光谱遥感反演方法对比[J]. 农业工程学报, 2013, 29(3):139 - 147.
XIA Tian, WU Wenbin, ZHOU Qingbo, et al. Comparison of two inversion methods for winter wheat leaf area index based on hyperspectral remote sensing[J]. Transactions of the CSAE, 2013, 29(3):139 - 147. (in Chinese)
[42] HUANG Guangbin, ZHU Qinyu, SIEW C. Extreme learning machine: a new learning scheme of feedforward neural networks [J]. Neurocomputing, 2006, 70: 489 - 501.
[43] 张银,周孟然. 人工神经网络 BP 算法在近红外光谱分析中的应用[J]. 红外, 2006(11):1 - 4.
ZHANG Yin, ZHOU Mengran. Application of artificial neural network BP algorithm in near infrared spectroscopy[J]. Infrared, 2006(11):1 - 4. (in Chinese)
[44] HUANG Guangbin, ZHOU Hongming, DING Xiaojian, et al. Extreme learning machine for regression and multiclass classification[J]. IEEE Transactions on Systems, Man, and Cybernetics, Part B (Cybernetics), 2011, 42(2):513 - 529.
[45] FU Zhaopeng, JIANG Jie, GAO Yang, et al. Wheat growth monitoring and yield estimation based on multi-rotor unmanned aerial vehicle[J]. Remote Sensing, 2020, 12(3):508.

(上接第 241 页)

[22] 束美艳,李世林,魏家玺,等. 基于无人机平台的柑橘树冠信息提取[J]. 农业工程学报,2021,37(1):68 - 76.
SHU Meiyan,LI Shilin,WEI Jiaxi,et al. Extraction of citrus crown parameters using UAV platform[J]. Transactions of the CSAE,2021,37(1): 68 - 76. (in Chinese)
[23] BESL P J, MCKAY N D. A method for registration of 3-D shapes[J]. IEEE Transactions on Pattern Analysis and Machine Intelligence, 1992, 14(2): 239 - 256.
[24] ZHANG W M, QI J B, WAN P, et al. An easy-to-use airborne LiDAR data filtering method based on cloth simulation[J]. Remote Sensing, 2016, 8(6): 501.
[25] SHAO J, ZHANG W M, SHEN A J, et al. Seed point set-based building roof extraction from airborne LiDAR point clouds using a top-down strategy[J]. Automation in Construction, 2021, 126: 103660.
[26] 郝红科. 基于机载激光雷达的森林参数反演研究[D]. 杨凌:西北农林科技大学,2019.
HAO Hongke. Inversion of forest parameters using airborne LiDAR[D]. Yangling: Northwest A&F University, 2019. (in Chinese)
[27] 许子乾. 基于无人机航测与激光雷达技术的林分特征及生物量估测[D]. 南京:南京林业大学,2019.
XU Ziqian. Estimationon stand characteristic parameters and biomass of forest by UAV aerial photogrammetry and LiDAR[D]. Nanjing: Nanjing Forestry University,2019. (in Chinese)
[28] MIKITA T, KLIMANEK M, CIBULKA M. Evaluation of airborne laser scanning data for tree parameters and terrain modelling in forest environment[J]. Acta Universitatis Agriculturae et Silviculturae Mendelianae Brunensis, 2013, 61(5): 1339 - 1347.
[29] HODGSON M E, JENSEN J R, RABER G, et al. An evaluation of Lidar-derived elevation and terrain slope in leaf-off conditions[J]. Photogrammetric Engineering & Remote Sensing, 2005, 71: 817 - 823.
[30] 李明龙. 不同栽培条件对油菜三维结构的影响研究[D]. 武汉:华中农业大学,2022.
LI Minglong. Effects of different cultivation conditions on three-dimensional structure of rapeseed[D]. Wuhan: Huazhong Agricultural University,2022. (in Chinese)
[31] 王庆, 车荧璞, 柴宏红, 等. 基于无人机可见光与激光雷达的甜菜株高定量评估[J]. 农业机械学报,2021,52(3):178 - 184.
WANG Qing,CHE Yingpu,CHAI Honghong,et al. Quantitative evaluation of sugar beet plant height based on UAV - RGB and UAV - LiDAR[J]. Transactions of the Chinese Society for Agricultural Machinery,2021,52(3): 178 - 184. (in Chinese)

agriculture

Impact Factor 3.3
CiteScore 4.9

ISSN 2077-0472

Effect of Microplastic on Bioavailability, Persistence and Toxicity of Pesticide

Volume 15 · Issue 4 February-2 2025

MDPI

agriculture

3.6 Impact Factor | 6.3 CiteScore | 19 days Time to First Decision

Instructions for Authors | Content | Guidelines | About | Search journal articles | Get Alerted

Agriculture, Volume 15, Issue 4

2025 February-2 - 88 articles

Cover Story: While microplastics can reduce the bioavailability of pesticides due to adsorption, they also increase the persistence of pesticides and alter their toxicity. Subsequent desorption, influenced by microplastic types and pesticide hydrophobicity and partitioning, replenishes the pesticides in the soil. This permits the gradual release of pesticides and potential sustained actions on target organisms and non-target organisms. As microplastic pollution increases, the frequency or amount of pesticide applications will need to increase to achieve the desired level of crop protection, resulting in negative costs and environmental impacts. Future studies can quantify how microplastic–pesticide interactions affect target pests to more precisely understand the effects of microplastics on pesticide applications. View this paper

Issues are regarded as officially published after their release is announced to the table of contents alert mailing list .

You may sign up for email alerts to receive table of contents of newly released issues.

PDF is the official format for papers published in both, html and pdf forms. To view the papers in pdf format, click on the "PDF Full-text" link, and use the free Adobe Reader to open them.

Number of Papers 88

Articles (14)

Search | 1 Selected | Most cited

Select all | Export

Systematic Review | 41 Citations | 16,673 Views | 37 Pages

Machine Learning in Sustainable Agriculture: Systematic Review and Research Perspectives

Juan Botero-Valencia, Vanessa García-Pineda, Alejandro Valencia-Arias, Jackeline Valencia, Erick Reyes-Vera, Mateo Mejía-Herrera and Ruber Hernández-García

Agriculture **2025**, *15*(4), 377; https://doi.org/10.3390/agriculture15040377 - 11 February 2025

Machine learning (ML) has revolutionized resource management in agriculture by analyzing vast amounts of data and creating precise predictive models. Precision agriculture improves agricultural productivity and profitability while reducing costs and... Show more

Full Article →

Article | 14 Citations | 1,923 Views | 21 Pages

LCDDN-YOLO: Lightweight Cotton Disease Detection in Natural Environment, Based on Improved YOLOv8

Haoran Feng, Xiqu Chen and Zhaoyan Duan

Agriculture **2025**, *15*(4), 421; https://doi.org/10.3390/agriculture15040421 - 17 February 2025

To address the challenges of detecting cotton pests and diseases in natural environments, as well as the similarities in the features exhibited by cotton pests and diseases, a Lightweight Cotton Disease Detection in Natural Environment (LCDDN-YOLO) a... Show more

Full Article →

Review | 12 Citations | 4,929 Views | 31 Pages

Review of Methods and Models for Potato Yield Prediction

Magdalena Piekutowska and Gniewko Niedbała

Agriculture **2025**, *15*(4), 367; https://doi.org/10.3390/agriculture15040367 - 9 February 2025

This article provides a comprehensive overview of the development and application of statistical methods, process-based models, machine learning, and deep learning techniques in potato yield forecasting. It emphasizes the importance of integrating di... Show more

Full Article →

Article | 10 Citations | 1,648 Views | 24 Pages

Estimating Canopy Chlorophyll Content of Potato Using Machine Learning and Remote Sensing

Xiaofei Yang, Hao Zhou, Qiao Li, Xueliang Fu and Honghui Li

Agriculture **2025**, *15*(4), 375; https://doi.org/10.3390/agriculture15040375 - 11 February 2025

Potato is a major food crop in China. Its development and nutritional state can be inferred by the content of chlorophyll in its canopy. However, the existing study on applying feature extraction and optimization algorithms to determine the canopy SP... Show more

Full Article →

Article | 7 Citations | 2,299 Views | 19 Pages

Evaluation of Weed Infestations in Row Crops Using Aerial RGB Imaging and Deep Learning

Plamena D. Nikolova, Boris I. Evstatiev, Atanas Z. Atanasov and Asparuh I. Atanasov

Agriculture **2025**, *15*(4), 418; https://doi.org/10.3390/agriculture15040418 - 16 February 2025

One of the important factors negatively affecting the yield of row crops is weed infestations. Using non-contact detection methods allows for a rapid assessment of weed infestations' extent and management decisions for practical weed control. T... Show more

Full Article →

Article | 7 Citations | 2,262 Views | 24 Pages

Research on a Potato Leaf Disease Diagnosis System Based on Deep Learning

Chunhui Zhang, Shuai Wang, Chunguang Wang, Haichao Wang, Yingjie Du and Zheying Zong

Agriculture **2025**, *15*(4), 424; https://doi.org/10.3390/agriculture15040424 - 18 February 2025

Potato is the fourth largest food crop in the world. Disease is an important factor restricting potato yield. Disease detection based on deep learning has strong advantages in network structure, training speed, detection accuracy, and other aspects.... Show more

Full Article →

Article | 6 Citations | 2,563 Views | 23 Pages

Sweet Potato Yield Prediction Using Machine Learning Based on Multispectral Images Acquired from a Small Unmanned Aerial Vehicle

Kriti Singh, Yanbo Huang, Wyatt Young, Lorin Harvey, Mark Hall, Xin Zhang, Edgar Lobaton, Johnie Jenkins and Mark Shankle

Agriculture **2025**, *15*(4), 420; https://doi.org/10.3390/agriculture15040420 - 17 February 2025

Accurate prediction of sweet potato yield is crucial for effective crop management. This study investigates the use of vegetation indices (VIs) extracted from multispectral images acquired by a small unmanned aerial vehicle (UAV) throughout the growi... Show more

Full Article →

Article | 4 Citations | 1,143 Views | 16 Pages

A Variable-Threshold Segmentation Method for Rice Row Detection Considering Robot Travelling Prior Information

Jing He, Wenhao Dong, Qingneng Tan, Jianing Li, Xianwen Song and Runmao Zhao

Agriculture **2025**, *15*(4), 413; https://doi.org/10.3390/agriculture15040413 - 15 February 2025

Accurate rice row detection is critical for autonomous agricultural machinery navigation in complex paddy environments. Existing methods struggle with terrain unevenness, water reflections, and weed interference. This study aimed to develop a robust... Show more

Full Article →

Article | 4 Citations | 1,649 Views | 21 Pages

The Development of a Sorting System Based on Point Cloud Weight Estimation for Fattening Pigs

Luo Liu, Yangsen Ou, Zhenan Zhao, Mingxia Shen, Ruqian Zhao and Longshen Liu

Agriculture **2025**, *15*(4), 365; https://doi.org/10.3390/agriculture15040365 - 8 February 2025

As large-scale and intensive fattening pig farming has become mainstream, the increase in farm size has led to more severe issues related to the hierarchy within pig groups. Due to genetic differences among individual fattening pigs, those that grow... Show more

Full Article →

Article | 4 Citations | 2,878 Views | 15 Pages

In-Field Phenotyping Using the Low-Cost and Open Access Fluorescence PhotosynQ Multispeq Sensor Together with NDVI: A Case Study with Durum Wheat

Adrian Gracia-Romero, Joel Segarra, Fatima Zahra Rezzouk, Nieves Aparicio, Shawn C. Kefauver and José Luis Araus

Agriculture **2025**, *15*(4), 385; https://doi.org/10.3390/agriculture15040385 - 12 February 2025

Durum wheat production is concentrated in Mediterranean climate regions, making it essential to develop cultivars that adapt to its changing conditions, including water and heat stress. In this regard, photosynthetic capacity estimates may help impro... Show more

Full Article →

Article | 4 Citations | 1,176 Views | 20 Pages

A Minority Sample Enhanced Sampler for Crop Classification in Unmanned Aerial Vehicle Remote Sensing Images with Class Imbalance

Jiapei Cheng, Liang Huang, Bohui Tang, Qiang Wu, Meiqi Wang and Zixuan Zhang

Agriculture **2025**, *15*(4), 388; https://doi.org/10.3390/agriculture15040388 - 12 February 2025

Deep learning techniques have become the mainstream approach for fine-grained crop classification in unmanned aerial vehicle (UAV) remote sensing imagery. However, a significant challenge lies in the long-tailed distribution of crop samples. This imb... Show more

Full Article →

Article | 3 Citations | 1,784 Views | 15 Pages

Portable Machine with Embedded System for Applying Granulated Fertilizers at Variable Rate

Igor Rodrigues Quintão, Domingos Sárvio Magalhães Valente, André Luiz de Freitas Coelho, Daniel Marçal de Queiroz, Marconi Ribeiro Furtado Junior, Flora Maria de Melo Villar and Pedro Henrique de Moura Rodrigues

Agriculture **2025**, *15*(4), 361; https://doi.org/10.3390/agriculture15040361 - 8 February 2025

Coffee production in mountainous regions faces significant challenges to mechanization, particularly in management and fertilization. Fertilizer application remains largely manual, reducing accuracy and failing to meet the demands of variable-rate ap... Show more

Full Article →

Article | 3 Citations | 1,754 Views | 25 Pages

A Semi-Supervised Diffusion-Based Framework for Weed Detection in Precision Agricultural Scenarios Using a Generative Attention Mechanism

Ruiheng Li, Xuaner Wang, Yuzhuo Cui, Yifei Xu, Yuhao Zhou, Xuechun Tang, Chenlu Jiang, Yihong Song, Hegan Dong and Shuo Yan

Agriculture **2025**, *15*(4), 434; https://doi.org/10.3390/agriculture15040434 - 19 February 2025

The development of smart agriculture has created an urgent demand for efficient and accurate weed recognition and detection technologies. However, the diverse and complex morphology of weeds, coupled with the scarcity of labeled data in agricultural... Show more

Full Article →

Article | 1,296 Views | 16 Pages

RF-YOLOv7: A Model for the Detection of Poor-Quality Grapes in Natural Environments

Changyong Li, Shunchun Zhang and Zhijie Ma

Agriculture **2025**, *15*(4), 387; https://doi.org/10.3390/agriculture15040387 - 12 February 2025

This study addresses the challenges of detecting inferior fruits in table grapes in natural environments, focusing on subtle appearance differences, occlusions, and fruit overlaps. We propose an enhanced green grape fruit disease detection model name... Show more

Full Article →

agriculture

IMPACT FACTOR 3.6

CITESCORE 6.3

Article

A Variable-Threshold Segmentation Method for Rice Row Detection Considering Robot Travelling Prior Information

Jing He, Wenhao Dong, Qingneng Tan, Jianing Li, Xianwen Song and Runmao Zhao

MDPI

https://doi.org/10.3390/agriculture15040413

agriculture

MDPI

Article

A Variable-Threshold Segmentation Method for Rice Row Detection Considering Robot Travelling Prior Information

Jing He [1,2], Wenhao Dong [1], Qingneng Tan [1], Jianing Li [1], Xianwen Song [1] and Runmao Zhao [2,3,*]

[1] School of Mechanical and Electrical Engineering, Guangdong Polytechnic of Industry and Commerce, Guangzhou 510642, China; hejing_1127@163.com (J.H.); dwh1012@163.com (W.D.); 0001250431@gdgm.edu.cn (Q.T.); pn088sci@163.com (J.L.); 18922205385@139.com (X.S.)
[2] Guangdong Provincial Key Laboratory for Agricultural Artificial Intelligence (GDKL-AAI), Guangzhou 510642, China
[3] Key Laboratory of the Ministry of Education of China for Key Technologies for Agricultural Machinery and Equipment for Southern China, South China Agricultural University, Guangzhou 510642, China
* Correspondence: rmzhao@scau.edu.cn

Abstract: Accurate rice row detection is critical for autonomous agricultural machinery navigation in complex paddy environments. Existing methods struggle with terrain unevenness, water reflections, and weed interference. This study aimed to develop a robust rice row detection method by integrating multi-sensor data and leveraging robot travelling prior information. A 3D point cloud acquisition system combining 2D LiDAR, AHRS, and RTK-GNSS was designed. A variable-threshold segmentation method, dynamically adjusted based on real-time posture perception, was proposed to handle terrain variations. Additionally, a clustering algorithm incorporating rice row spacing and robot path constraints was developed to filter noise and classify seedlings. Experiments in dryland with simulated seedlings and real paddy fields demonstrated high accuracy: maximum absolute errors of 59.41 mm (dryland) and 69.36 mm (paddy), with standard deviations of 14.79 mm and 19.18 mm, respectively. The method achieved a 0.6489° mean angular error, outperforming existing algorithms. The fusion of posture-aware thresholding and path-based clustering effectively addresses the challenges in complex rice fields. This work enhances the automation of field management, offering a reliable solution for precision agriculture in unstructured environments. Its technical framework can be adapted to other row crop systems, promoting sustainable mechanization in global rice production.

Keywords: rice row detection; variable-threshold segmentation; prior information; multi-sensors

Academic Editor: José Lima

Received: 6 January 2025
Revised: 9 February 2025
Accepted: 14 February 2025
Published: 15 February 2025

Citation: He, J.; Dong, W.; Tan, Q.; Li, J.; Song, X.; Zhao, R. A Variable-Threshold Segmentation Method for Rice Row Detection Considering Robot Travelling Prior Information. *Agriculture* **2025**, *15*, 413. https://doi.org/10.3390/agriculture15040413

1. Introduction

Rice is one of the three most important staple crops worldwide, predominantly grown in the Asian monsoon region. In addition to its significant water requirements, which make efficient water management crucial for sustainable production [1,2], rice cultivation also plays a vital role in rural livelihoods, economic stability, and cultural practices, particularly in the Asian monsoon region [3]. However, rice production still involves numerous processes and remains labor-intensive. During the mid-term management phase of paddy fields (including operations such as weeding, fertilization, and pesticide application), the mechanization level remains notably low at merely 16.84% [4]. The primary machinery used for tasks such as fertilization and pest control in rice fields is the highland gap sprayer, which requires the operator to remain vigilant to prevent the tires from damaging the rice plants. Similarly, rice weeding machines must also be operated carefully to avoid

crushing the rice crops. Therefore, in complex agricultural environments, the rapid and accurate identification of rice rows is crucial in enhancing the automation of field management. This rice row recognition is essential in achieving automatic tracking and control in agricultural machinery.

Currently, both domestic and international scholars primarily focus on crop row recognition using ultrasonic sensors, visual sensors, and LiDAR. Ultrasonic waves exhibit significant energy attenuation during atmospheric propagation, accompanied by lower ranging accuracy and limited directivity. Additionally, their performance is susceptible to temperature variations. These inherent limitations make ultrasonic technology generally unsuitable as a standalone solution for environmental perception applications requiring high precision [5]. However, it remains applicable in scenarios with relaxed accuracy requirements, such as obstacle detection in parking assistance systems [6]. Visual sensors, while providing abundant information, face challenges due to the uncontrollable nature of agricultural environments, such as fluctuations in light intensity [7]. Despite the development of various algorithms to interpret environmental information, the results vary significantly depending on the environment, crop type, sensor choice, and algorithm used [8–13]. LiDAR has emerged as a prominent technology in precision agriculture (PA) due to its high ranging accuracy, excellent real-time performance, and strong anti-interference capabilities [14–21]. LiDAR systems are typically classified as either two-dimensional (2D) or three-dimensional (3D), based on their scanning mechanisms. While 3D LiDAR systems are expensive, 2D LiDAR systems offer simpler structures, faster detection speeds, and lower costs, making them more commonly used in research [22–25].

In complex agricultural environments, uneven terrain can cause significant bumps during vehicle movement. However, 2D LiDAR, lacking height information, struggles to fully reconstruct the terrain and may suffer from data distortion or false readings. To address this challenge, many researchers have incorporated additional sensors for posture correction, enabling the generation of 3D point cloud maps of crops. For example, Colaço et al. combined 2D LiDAR and GNSS to create a scanning system capable of generating 3D models of citrus trees, including the canopy volume and height [26]. Miguel Garrido et al. installed a total station, IMU, and multiple 2D LiDAR sensors oriented in different directions on a vehicle. Due to the limitations of single-directional LiDAR for crop detection, they employed the ICP algorithm to fuse point cloud data from different directions, thereby enhancing the accuracy and reliability of the resulting 3D point clouds [27]. Similarly, David et al. fused data from a total station, IMU, and 2D LiDAR sensors to generate 3D point clouds for the clustering of individual maize seedlings at various growth stages. In semi-structured environments, their crop detection system achieved a 100% detection rate. However, their approach did not account for the crop shape and struggled to filter out noise from weeds and other obstacles [28].

The paddy field environment in Southern China is highly complex, characterized by varying water and soil depths across different fields [29]. The presence of water layers in paddy fields presents significant challenges for visual identification systems through two primary mechanisms: (1) specular reflections from water surfaces [30] and (2) the chromatic and morphological characteristics of weeds, which closely resemble those of rice seedlings. These coexisting factors substantially compromise the reliability of computer vision-based weed detection in submerged agricultural environments. Additionally, the uneven hard bottom layer of paddy fields causes frequent posture changes in field operation machinery [31]. When a 2D LiDAR is mounted on a mobile platform, the reconstructed environmental data often suffer from inaccuracies in height information. To address these challenges, this study presents a 3D information acquisition system that integrates 2D LiDAR, an attitude and heading reference system (AHRS), and a global navigation satellite

system (GNSS). Furthermore, a variable-threshold segmentation method is proposed, along with a rice row classification technique based on prior information.

2. Materials and Methods

2.1. Three-Dimensional Point Cloud Acquisition and Preprocessing

2.1.1. LiDAR and AHRS Sensor Coordinate Calibration

Coordinate calibration, as illustrated in Figure 1, involves three coordinate systems: the LiDAR coordinate system ($O_lX_lY_lZ_l$), the vehicle coordinate system ($O_VX_VY_VZ_V$), and the geodetic coordinate system ($O_WX_WY_WZ_W$). In this system, the X_W and Y_W coordinates are derived from the Gaussian–Krüger projection transformation within the WGS-84 geocentric coordinate system, while the Z_W coordinate represents elevation information (the elevation is adjusted by subtracting the installation height).

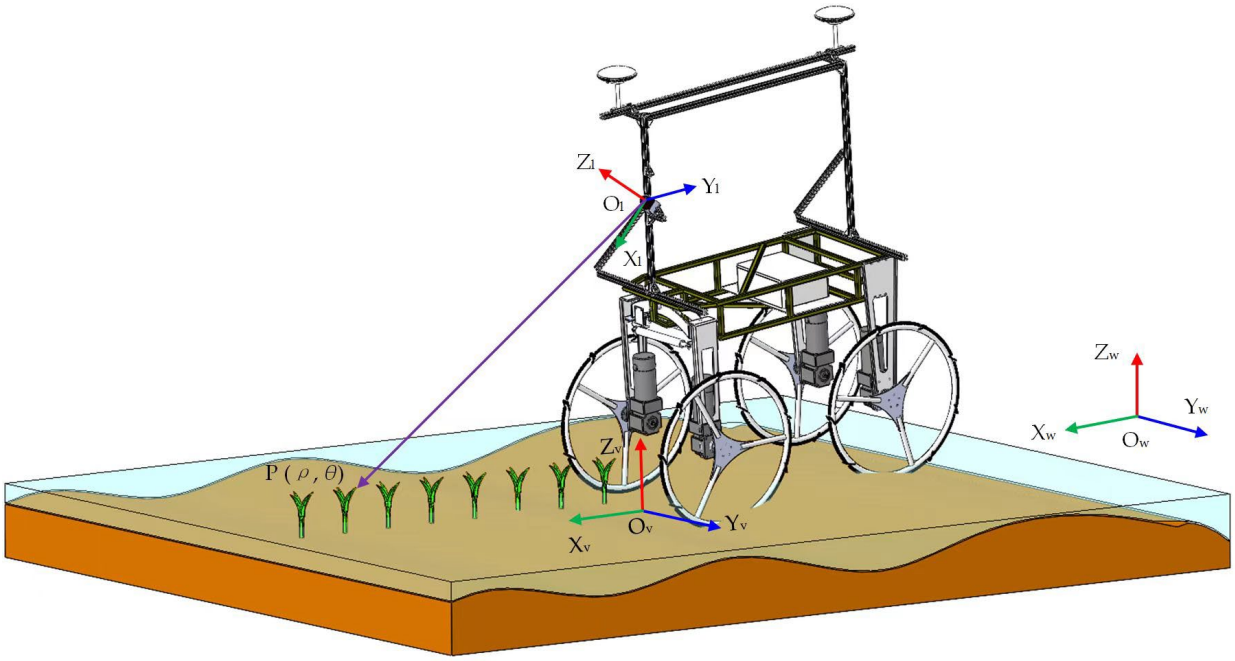

Figure 1. Schematic representation of acquisition process.

Assuming that the robot is a rigid body, the vehicle coordinate system is defined with the point projected by the main GNSS antenna onto the ground as the origin (O_V).

(1) Conversion of LiDAR Coordinate System to Vehicle Coordinate System

Assume that a LiDAR scanning point $P(\rho, \theta)$ corresponds to the point $P_l = [cos\theta * \rho;\ sin\theta * \rho;\ 0]$ in the LiDAR coordinate system and the point $P_V = [X_V; Y_V; Z_V]$ in the vehicle coordinate system. Let the origin of the LiDAR coordinate system, denoted by O_l, be projected onto the vehicle coordinate system at O_l', while O_v is the origin of the vehicle coordinate system. Therefore, the transformation from the LiDAR coordinate system to the vehicle coordinate system can be described as

$$P_V = \begin{bmatrix} 1 & 0 & 0 \\ 0 & cos\varphi & sin\varphi \\ 0 & -sin\varphi & cos\varphi \end{bmatrix} * \begin{bmatrix} cos(-a) & 0 & -sin(-a) \\ 0 & 1 & 0 \\ sin(-a) & 0 & cos(-a) \end{bmatrix} * P_l + \begin{bmatrix} d_{x23}; d_{y23}; H_l \end{bmatrix}^T \quad (1)$$

where d_{x23} and d_{y23} are the installation distances of O_l' and O_v in the X_V axis and Y_V axis directions, respectively, in mm; α is the angle between the LiDAR and the vertical line (Z_V), in deg; φ is the angle between the LiDAR and the horizontal line (Y_V), in deg.

(2) Conversion of the Vehicle Coordinate System to the Geodetic Coordinate System

The attitude and heading reference system (AHRS) is installed at the center of the front section of the vehicle to accurately measure the vehicle's roll (a_x) and pitch (a_y) angles. The dual-antenna GNSS system provides the heading angle (a_z). The comprehensive rotation matrix ${}^{W}R_{V}$, which transforms the vehicle coordinate system to the geodetic coordinate system, can be derived from the global roll–pitch–heading (RPH) matrix (Equation (2)). Assuming that the origin of the vehicle coordinate system, O_V, corresponds to the point O_{W_V} in the geodetic coordinate system, and O_{W_G} denotes the current position as determined by the GNSS, the relationship between O_{W_V} and O_{W_G} is as shown in Equation (3).

$$\begin{aligned} {}^{W}R_{V} &= R_{Z}^{T} * R_{Y}^{T} * R_{X}^{T} \\ &= \begin{bmatrix} cosa\_ycosa\_z & -cosa\_xsina\_z + cosa\_zsina\_xsina\_y & sina\_xsina\_z + cosa\_xcosa\_zsina\_y \\ cosa\_ysina\_z & cosa\_xcosa\_z + sina\_xsina\_ysina\_z & -sina\_xcosa\_z + cosa\_xsina\_ysina\_z \\ -sina\_y & cosa\_ysina\_x & cosa\_xcosa\_y \end{bmatrix} \end{aligned} \tag{2}$$

$$O_{W\_V} = O_{W\_G} + {}^{W}R_{V} * (O_V - O_G) \tag{3}$$

As shown in Equation (4), the point in the vehicle coordinate system is transformed to the corresponding point in the geodetic coordinate system.

$$\begin{bmatrix} X_W \\ Y_W \\ Z_W \end{bmatrix} = \begin{bmatrix} X_V \\ Y_V \\ Z_V \end{bmatrix} * {}^{W}R_{V} + O_{W\_V} \tag{4}$$

2.1.2. Outlier Elimination Based on the Pauta Criterion

The teleoperated robotic vehicle was navigated through uneven, weed-free, and weed-covered dryland (where simulated rice seedlings were pre-planted with 300 mm row spacing) to conduct sensor data pre-collection for algorithm development and parameter calibration, as illustrated in Figure 2.

(**a**) uneven, weed-free dryland

(**b**) uneven, weed-covered dryland

Figure 2. Data pre-collection environment.

Sharp edges and reflective surfaces can cause the misalignment of the LiDAR beam, resulting in "ghost points" [32], also known as outliers. As illustrated in Figure 3, the LiDAR data are converted from polar to Cartesian coordinates, which may introduce rough spots. These points typically deviate along the X_l-axis direction. To eliminate the influence of outliers, the Pauta criterion (also known as the 3σ criterion) is employed for detection and judgment.

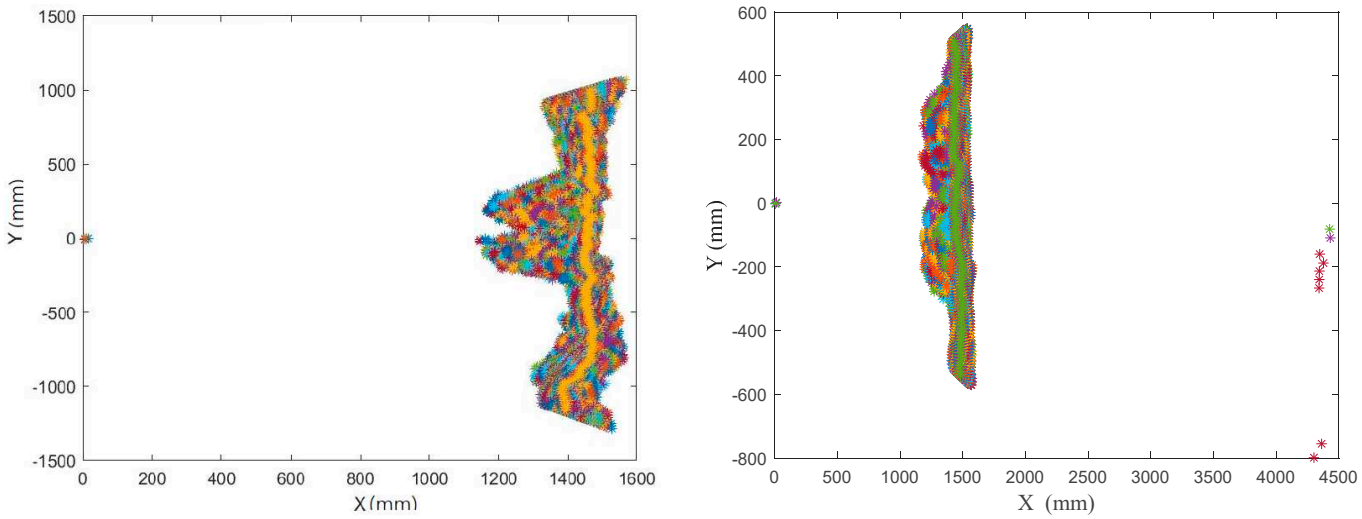

(**a**) uneven, weed-free dryland (scanning range = ±40°, sampling time = 56 s)

(**b**) uneven, weed-covered dryland (scanning range = ±20°, sampling time = 47.2 s)

Figure 3. Conversion from polar coordinates to Cartesian coordinates.

The 3D point cloud data are reconstructed by fusing information from the LiDAR, AHRS, and GNSS sensors. Figure 4a,b display the 3D point cloud, including outliers (in red box and circles). The presence of outliers reduces the clarity of the environmental information. Figure 4c,d presents the 3D point cloud after outlier removal using the Pauta criterion, where different colors of solid points correspond to the varying height values of objects within the environment. The results demonstrate that the rice rows and ground features are clearly discernible, and the proposed method effectively mitigates the influence of outliers.

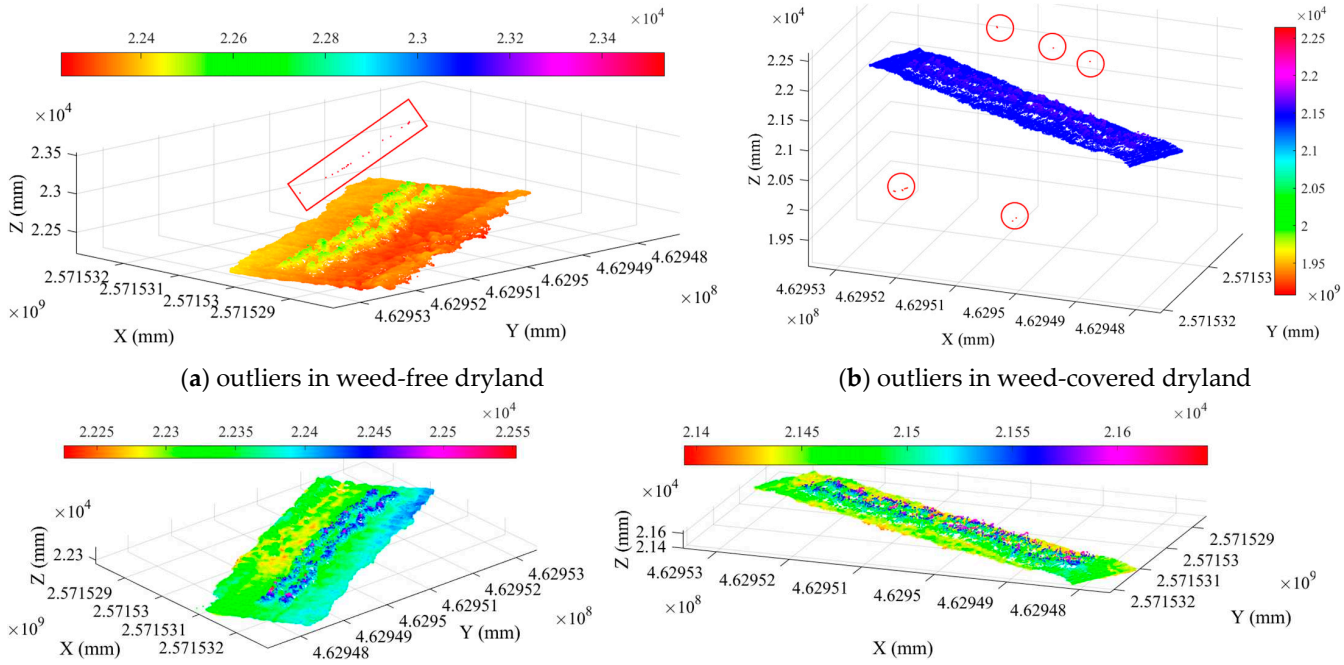

(**a**) outliers in weed-free dryland

(**b**) outliers in weed-covered dryland

(**c**) point cloud after outlier removal in weed-free dryland

(**d**) point cloud after outlier removal in weed-covered land

Figure 4. Point cloud data pre-processing.

2.2. Rice Row Recognition Method Based on Multi-Sensor Information

2.2.1. Variable-Threshold Object Segmentation Method Based on Posture Perception

Accurate object segmentation is a critical prerequisite for obstacle segmentation and recognition. Commonly employed object segmentation methods, such as plane fitting [33–35], often rely on simplifying assumptions about the environment. However, point cloud data, after outlier removal, more accurately reflect real field conditions. The height variations of individual data points are influenced by several factors, including the terrain and environmental conditions, which complicates the establishment of a fixed threshold for segmentation. To address this challenge, we propose a variable-threshold object segmentation method based on posture perception. This approach adapts the segmentation threshold dynamically, accommodating the variability in the field conditions and improving the segmentation accuracy.

As shown in Figure 5, due to the uneven hard layer of the paddy field, the robot's posture undergoes frequent changes. Equation (5) is employed to correct the robot's posture and mitigate the impact of posture variations on object segmentation. Using trigonometric relationships, the distance between the i-th LiDAR scanning line and the robot's position can be calculated as $L\_X = H_l * tan\beta$, where $\beta = 90^\circ - \alpha$. Within the same LIDAR frame, the maximum height difference between the ground point cloud and the LiDAR scanning center point is given by

$$Z\_cha(i) = L\_Y * tan(a\_x1) \tag{5}$$

where $L\_Y = abs\left(tan\theta * \frac{H_l}{cos\beta}\right)$, and θ represents the LiDAR's field of view angle, while a_x1 is the roll angle of the LiDAR scanning position. A certain distance exists between the current measured roll angle position of the robot and a_x1.

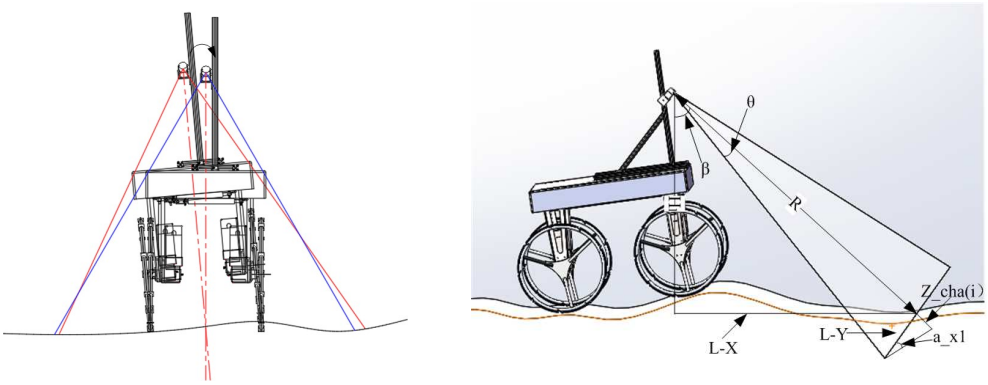

(**a**) Vehicle posture (**b**) Automatic threshold setting

Figure 5. Schematic diagram of automatic threshold setting. Note: red and blue solid lines indicate LiDAR scanning boundaries under different poses.

In general, the closer the LiDAR frame is to the LiDAR scanning line, the smaller the corresponding roll angle error. Based on this observation, we propose using an exponential smoothing model for data prediction. The exponential smoothing model is an enhanced version of the moving average model, with the key feature that the weight of the data increases as the data points grow closer in time, with the most recent data receiving the highest weight. Therefore, the exponential smoothing model is chosen for data prediction [36]. The smoothing equation is expressed as

$$a\_x1 = k_a * a\_x(i) + k_a * (1 - k_a) * a\_x(i-1) + \cdots k_a * (1 - k_a)^9 * a\_x(i-9) \tag{6}$$

where K_a is the smoothing coefficient (with $0 < K_a < 1$). In the exponential smoothing model, the smoothing coefficient α directly determines the trade-off between prediction

sensitivity and stability. According to [37,38], when handling time series with significant fluctuations, moderate smoothing (α = 0.3–0.5) is generally recommended to balance noise suppression and trend responsiveness. Considering the large fluctuations in the data, K_a is set to 0.5.

If the value of a_x1 is close to zero, it indicates that the ground is nearly flat. Conversely, if the value is significant, it suggests that the ground is uneven and there is a height difference within the LiDAR frame scanning area. By using trigonometric relationships to calculate the maximum possible height difference, the threshold $Z\_T(i)$ is determined as in Equation (7):

$$Z\_T(i) = mean(Z_w(i,:)) + Z\_cha(i) \tag{7}$$

where $Z_w(i,:)$ represents the height data of the ground point cloud, in mm.

To further validate the advantages of the proposed variable-threshold segmentation method, a set of comparative experiments was designed to evaluate its performance against conventional fixed-threshold segmentation, with the results presented in Figure 6. A comparative analysis of Figure 6a,b reveals that, while the fixed-threshold algorithm demonstrates limited efficacy in terrain segmentation by failing to completely isolate rice seedlings from the background, the proposed variable-threshold segmentation method successfully extracts two distinct rice seedling rows in the weed-free dryland. Equation (7) can only classify ground and non-ground point clouds, and it fails to segment seedlings from weeds in the weed-covered field (Figure 7a). To address this limitation, Equation (7) was enhanced by integrating the height differential between weeds and seedlings (where weeds exhibit lower vertical profiles than seedlings), yielding Equation (8) for complete seedling segmentation. The segmentation performance of Equation (8) in weed-covered scenarios is demonstrated in Figure 7b.

$$Z\_T(i) = mean(Z_w(i,:)) + Z\_cha(i) + PTh \tag{8}$$

where PTh represents the pass-through filter coefficient. Considering the emergence height of rice seedlings, the PTh value should satisfy $PTh \leq 40$ for directly seeded fields and $PTh \leq 140$ for transplanted fields. In this study, PTh is set to 30.

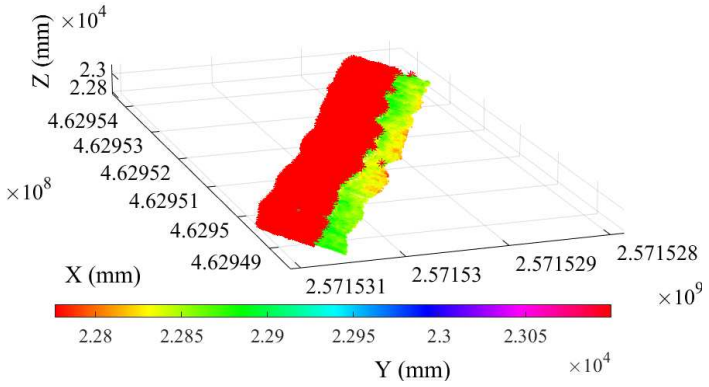

(**a**) Fixed-threshold method (without Z_cha(i) term) for segmentation of weed-free dataset

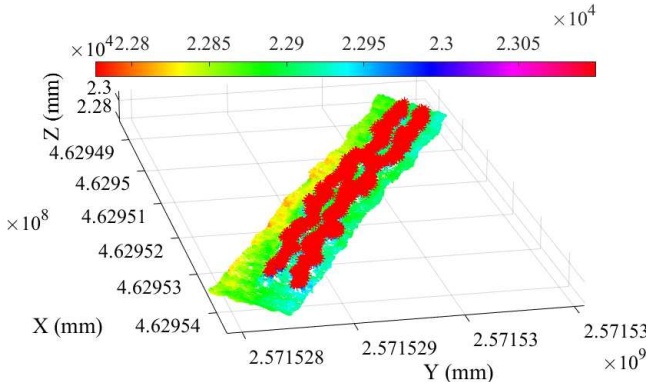

(**b**) Variable-threshold method (with Z_cha(i) term) for segmentation of weed-free dataset

Figure 6. Comparative analysis of the proposed variable-threshold method (the non-ground points are marked with red asterisks (*)).

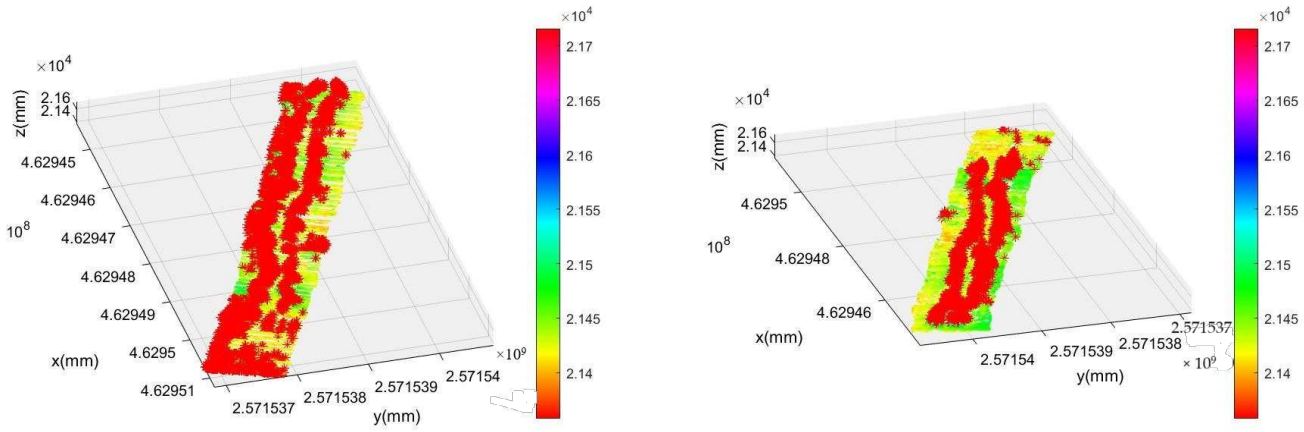

(**a**) Variable-threshold method (with *PTh* term) for segmentation of weed-covered dataset (before)

(**b**) Variable-threshold method (with *PTh* term) for segmentation of weed-covered dataset (after)

Figure 7. Comparative analysis of the proposed variable-threshold method on the weed-covered dataset.

2.2.2. Rice Row Cluster Method Based on Prior Information

(1) Extraction of the Center Point of Rice Rows

In a given LiDAR frame, there are significant positional differences between rice rows in the geodetic coordinate system. Based on this characteristic, the non-ground point cloud data for each LiDAR frame are classified to extract the center point. The specific steps are as follows.

- Threshold Setting

The threshold T_{lidar} is determined based on the mathematical model derived in Equation (9). In this equation, the LiDAR's angular resolution is 0.36° (HOKUYO's URG-04LX), $line\_space$ represents the row spacing of the rice rows, and $w\_l \in [0,1]$ is the proportional coefficient. The row spacing parameter (line_space) can be dynamically set to 25 or 30 cm depending on the seeder type, while incorporating a row spacing variation coefficient w_l to quantify field-level fluctuations caused by mechanical vibrations and terrain undulations.

$$T_{lidar} = \frac{line\_space * w\_l}{L\_Y} * \frac{abs(\theta)}{0.36} = \frac{line\_space * w\_l}{abs\left(tan\theta * \frac{H_L}{cos\beta}\right)} * \frac{abs(\theta)}{0.36} \quad (9)$$

- Data Classification

The non-ground point cloud data are classified by calculating their spatial characteristics and comparing them with the threshold T_{lidar}. This results in the classification of the data points into distinct groups.

- Center Point Extraction

If the classified point cloud data contain multiple rice rows, the center point of each cluster is identified by extracting the midpoint within each category.

If only one category is identified, the midpoint of the entire non-ground point cloud data is set as the center point.

(2) Center Point Classification Based on Robot Travelling Path

In seedling row recognition, positional relationships are commonly utilized for clustering [11]. As shown in Figure 8, the red dots represent the non-ground point data that

have been denoised and processed to extract the center points from the LiDAR data, while the yellow route represents the robot's travelling path, which separates two rows of rice. Additionally, the autonomous robot is equipped with a GNSS system. Based on this setup, a classification method is proposed that leverages the relationship between the rice rows and the robot's travelling path (prior information).

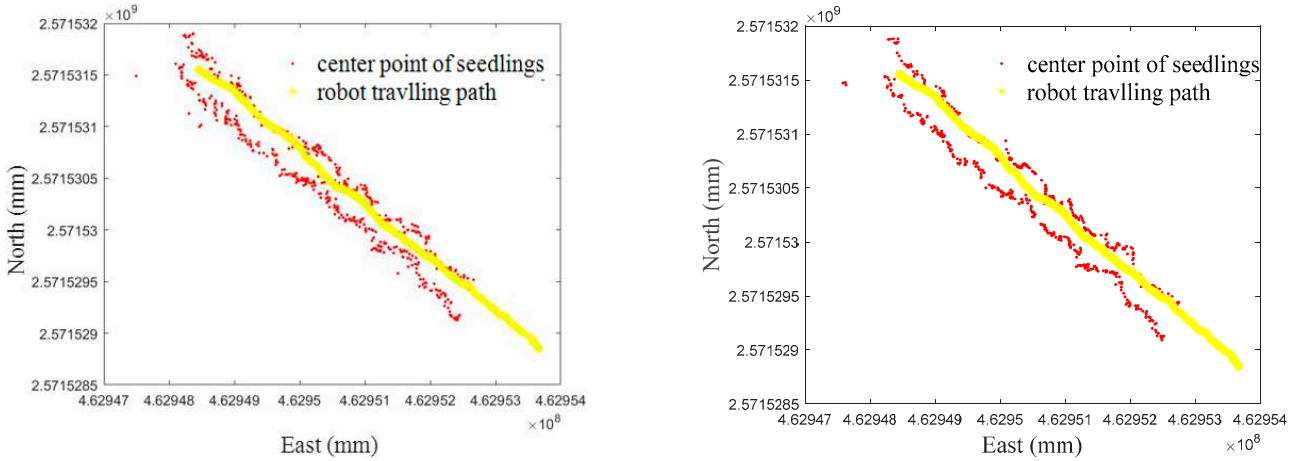

(**a**) Non-ground point (**b**) Center point ($w\_l = 0.75$)

Figure 8. Center point extraction.

- Horizontal Distance Calculation

First, in the same frame, the horizontal distance in the vehicle coordinate system between the center point of the rice row and the robot's travelling path is computed. This distance is denoted as dis. In this study, the origin of the vehicle coordinate system is defined as the point where the main GNSS antenna projects onto the ground. Therefore, the robot's travelling path serves as the origin of the vehicle coordinate system at different data acquisition times. If a point in the vehicle coordinate system is represented by (X_V, Y_V, Z_V), the distance is given by

$$dis = Y_V \tag{10}$$

- Point Clustering

Next, the center points are clustered using Equation (11). Here, $line\_space$ denotes the rice row spacing, and $label$ is the variable representing the category label. Simultaneously, the variable $label\_num\_sum$ is used to count the number of center points in each category.

$$label = ceil\left(\frac{dis - line\_space * 0.5}{line\_space}\right) \tag{11}$$

- Elimination of Small Weed Interference

While the point cloud data have already been processed to remove outliers and low weeds, some weeds that are comparable in height to rice may still remain. To further enhance the accuracy of rice row recognition, a second round of denoising is performed before fitting the rice rows. Given that rice is planted in rows, the number of center points within each clustering category is significantly greater than that of small-weed areas. A threshold value $T_{number} = mean(label\_num\_sum)$ is set. When the number of points within a cluster exceeds this threshold, the region is classified as a rice row. Otherwise, the area is considered noisy and is removed. Finally, as shown in Figure 9, the data corresponding to the X_w and Y_w axes of the seedling cluster are extracted.

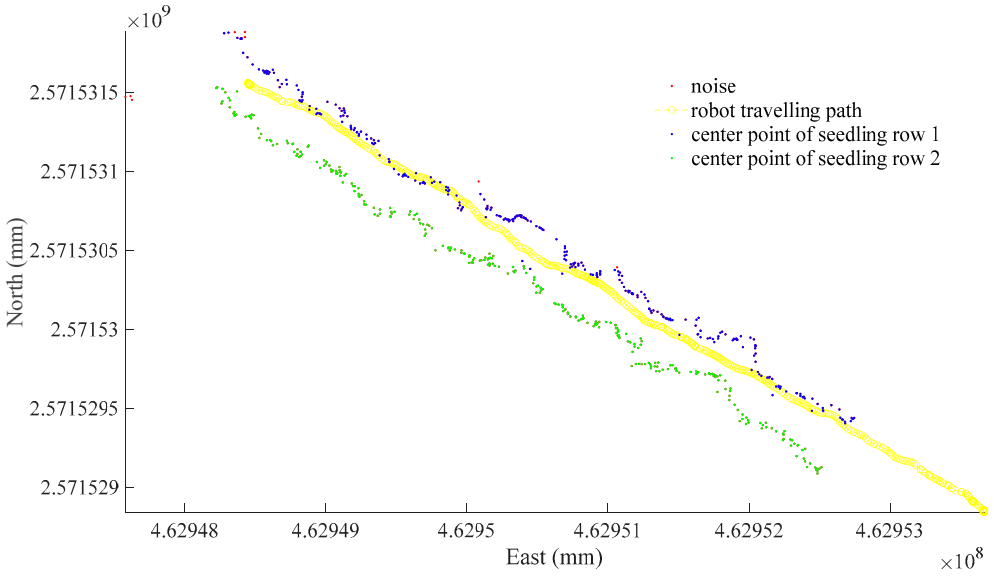

Figure 9. Center point clustering.

3. Experiment and Discussion

In order to verify the effectiveness of the algorithm, we used the robot to conduct validation experiments on sloped terrain (Figure 10d), in dryland (Figure 3a), and in a paddy field (Figure 10e). The experimental platform and environment are shown in Figure 10a. The data collection was composed of HOKUYO's URG-04LX 2D LiDAR (10 Hz, ambient light resistance: 10,000 Lx or less), XSENS' MTI-300 AHRS (10 Hz), and RTK-GNSS (10 Hz), etc. The sensor data acquisition system was i processed in the multithreaded software platform developed in LabVIEW 2015 (National Instruments, Austin, TX, USA. As shown in Figure 10b, a customized software architecture was specifically designed to handle parallel data processing from multiple sensor channels. The development environment operated on a Windows-based laptop (Core i5-7200U, 8GB DDR4 RAM), which provided sufficient computational resources for real-time data acquisition and processing tasks. The installation height of the 2D LiDAR was 1220 mm, with the angle α between the installation angle and Z_v axis being 54.5°, and the angle φ between the installation angle and Y_v axis was 1.744°. The field of view angle was $\theta \in [-10^o, 12^o]$, the installation height was $H_l = 1220$ mm, the proportional coefficient $w\_l = 0.75$, and the rice planting row spacing was 300 mm. According to Equation (9), the clustering threshold was $T_{lidar} \approx [23.54, 23.65]$. Therefore, in the experiment, the value of T_{lidar} was set to 24.

During the experiment, the data collection platform moved in a straight line along the rice rows. The forward speeds of the experimental platform in the simulated and field environments were approximately 0.2 m/s and 1 m/s, respectively. The experimental site was located at the Zengcheng Experimental Base of South China Agricultural University in Guangzhou, China.

The rice row recognition results based on the robot's travelling path are shown in Figure 11. In this figure, the yellow symbol represents the vehicle's position in the geodetic coordinate system, obtained via the GNSS. The red asterisk (*) symbol indicates the manually measured position using the CTI RTK-DGPS I70. The solid points in various colors correspond to the center points of different objects: red points represent the center points of noisy areas, while blue and green points denote the center points of the rice rows. After clustering, the center points are fitted into straight lines using the robust regression method. Different line types represent the fitted results of different rice rows. The results indicate

that the manually measured rice positions predominantly lie on the fitted straight lines of the rice rows.

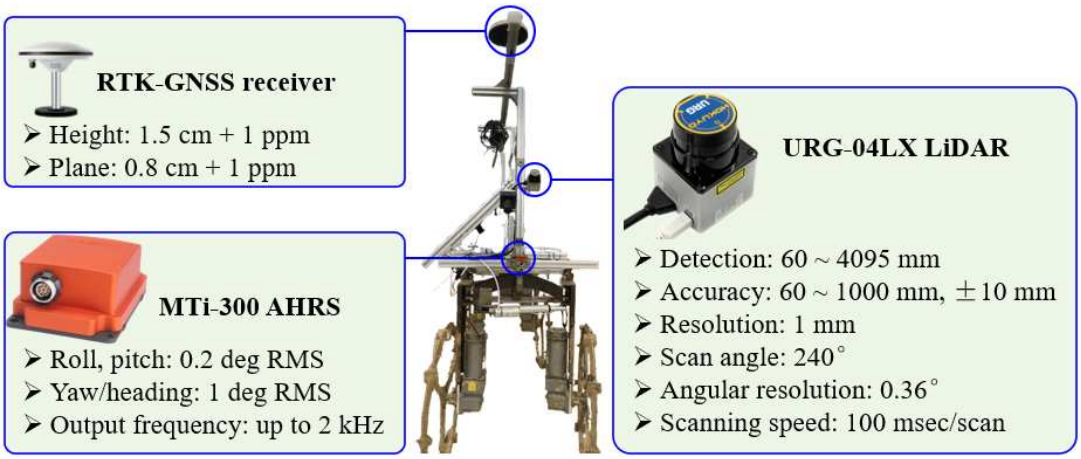

(**a**) Rice seedling row recognition robot

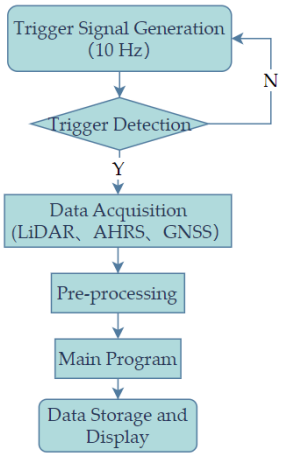

(**b**) Flowchart of multi-threaded synchronous acquisition

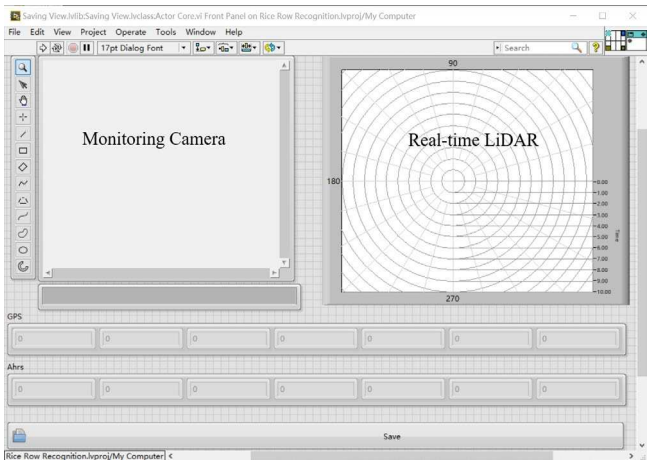

(**c**) Customized software GUI

(**d**) Experimental setup of simulated seedling on sloped terrain (sampling time = 17.8 s)

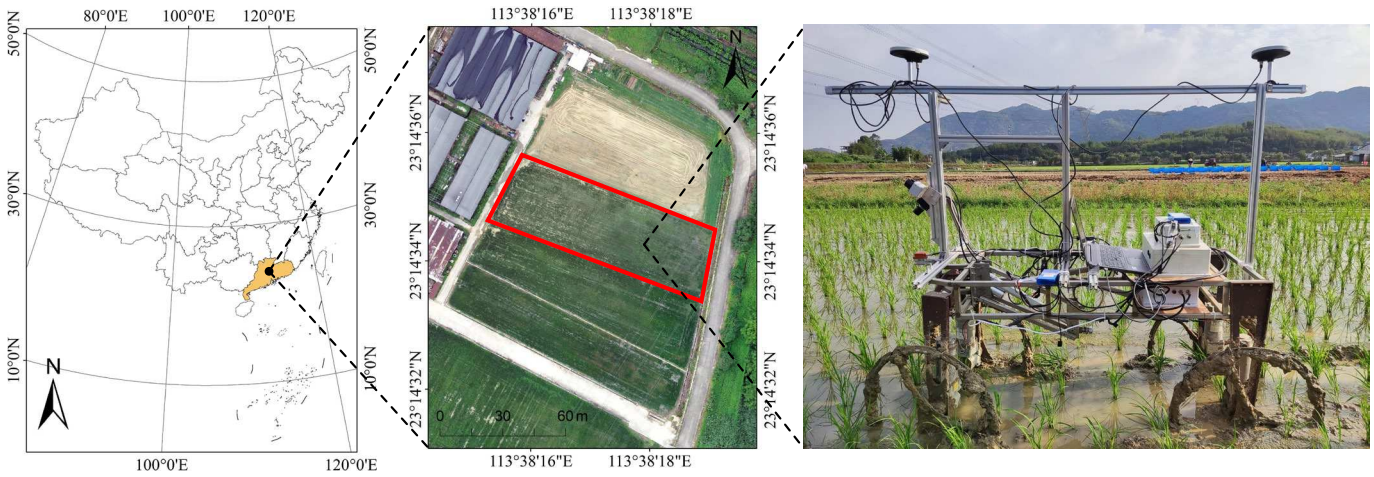

(**e**) Paddy field environment (sampling time = 55 s)

Figure 10. Experimental data collection platform and experimental environment.

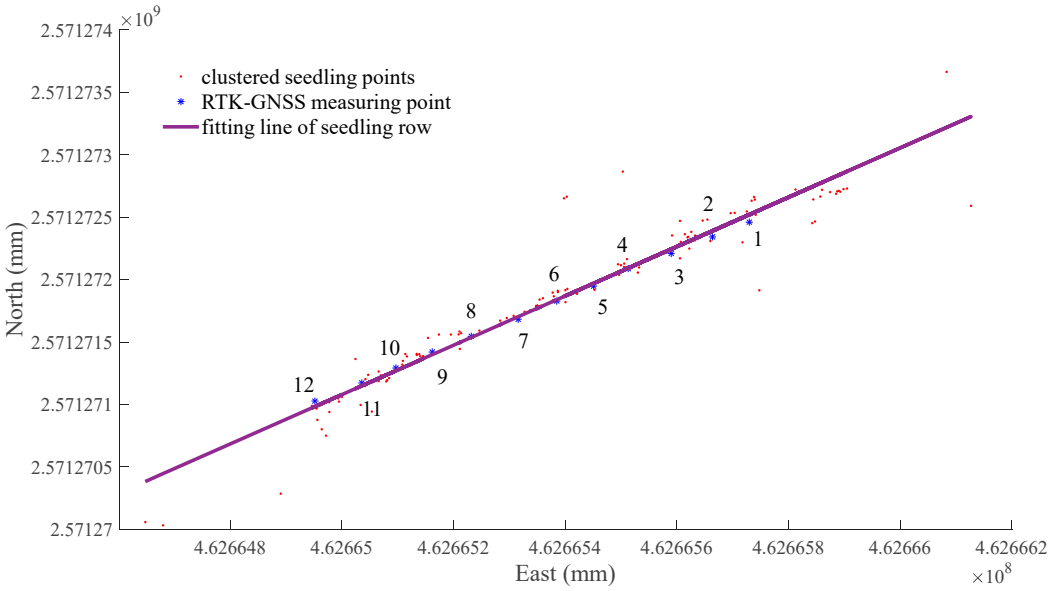

(**a**) Simulated seedling row detection on sloped terrain

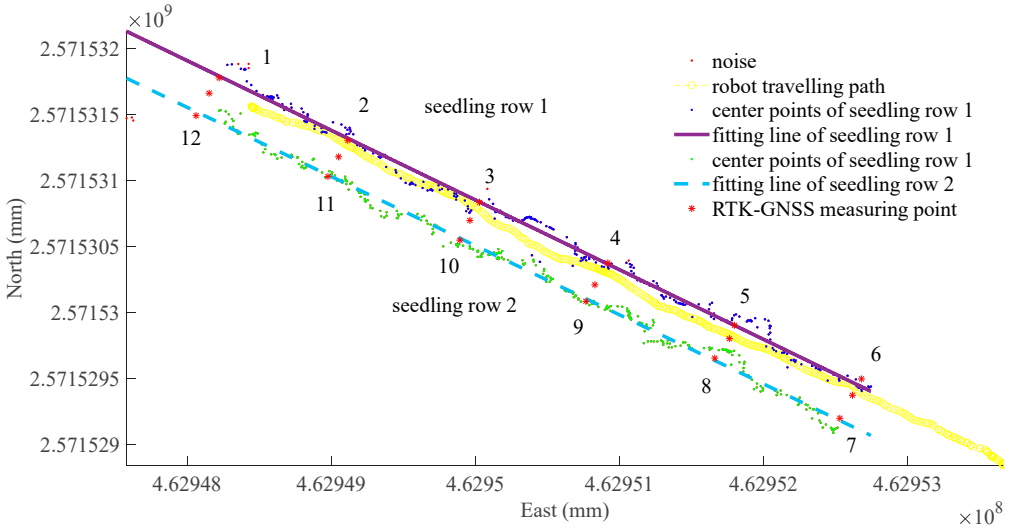

(**b**) Simulated seedling row detection in dryland

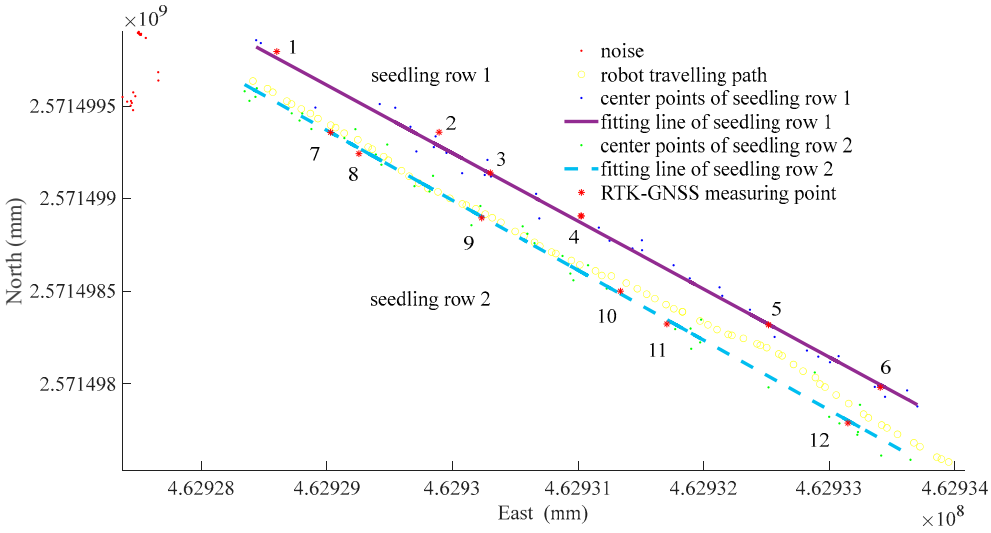

(**c**) Seedling row detection in paddy field

Figure 11. Seedling row detection experiments. Note: numbers 1–12 are indexes of RTK-GNSS measuring points.

In order to further evaluate the accuracy of the fitting rice line, the error ε_l was defined as the vertical distance from the RTK-GNSS measurement value to the fitting line. On the sloped terrain, the simulated seedling row fitting results were as shown in Figure 11a, where the linear equation for seedling rows is $y = 1.9756{*}x + 1657242002.64$. In the dryland, the simulated seedling row fitting results were as shown in Figure 11b, where the linear equations for seedling rows 1 and 2 are $y = -0.53 * x + 2817020373.78$ and $y = -0.524 * x + 2814010460.1$, respectively. In the paddy field, the fitting results of the seedling rows were as shown in Figure 11c. The linear equations for seedling rows 1 and 2 are $y = -0.3672 * x + 2741494099.49$ and $y = -0.3777 * x + 274637039.18$, respectively. The error analysis results of seedling position recognition are shown in Table 1, where the maximum absolute error, minimum absolute error, and standard deviation on sloped terrain are shown to be 27.42 mm, 1.81 mm, and 7.66 mm, respectively; the maximum absolute error, minimum absolute error, and standard deviation in the dryland are 59.41 mm, 0.86 mm, and 14.79 mm, respectively; and the maximum error, minimum error, and standard deviation in the paddy field are 69.36 mm, 0.53 mm, and 19.18 mm, respectively.

Table 1. Seedling position recognition results.

Seedling position recognition on sloped terrain	RTK-GNSS measuring point	1	2	3	4	5	6
	absolute error (mm)	27.42	21.82	15.86	1.81	9.72	5.03
	RTK-GNSS measuring point	7	8	9	10	11	12
	absolute error (mm)	9.40	4.12	9.67	9.86	10.09	19.55
Seedling position recognition in dryland	RTK-GNSS measuring point	1	2	3	4	5	6
	absolute error (mm)	15.18	14.70	0.86	10.57	4.89	59.41
	RTK-GNSS measuring point	7	8	9	10	11	12
	absolute error (mm)	27.04	10.87	13.31	16.59	16.41	16.09
Seedling position recognition in paddy field	RTK-GNSS measuring point	1	2	3	4	5	6
	absolute error (mm)	32.60	69.36	4.28	33.79	3.34	13.81
	RTK-GNSS measuring point	7	8	9	10	11	12
	absolute error (mm)	7.01	0.53	27.66	13.48	21.69	13.17

The experimental results demonstrate that fusing data from LiDAR, AHRS, and GNSS enables the accurate reconstruction of 3D point cloud data. Furthermore, the straight lines fitted to the point cloud data effectively represent the positional information of the rice rows. The standard deviations under the two conditions are 14.79 mm and 19.18 mm, respectively. Notably, the position errors at point 6 in the simulated environment and at point 2 in the real environment are relatively large. The occurrence of significant errors can be attributed to the following factors. The objective of this study was to estimate the straight lines of seedling rows, thereby providing a reference path for robot navigation. Consequently, we employed a robust regression method to fit the positioning points of seedlings. The main characteristic of this method lies in its ability to identify and disregard potential points with a strong influence that deviate from the model structure, thereby ensuring the fitting effect of in-structure points. As a result, significant statistical errors may occur for individual outlier points (point 6 in the simulated environment and point 2 in the paddy field). For the task of robot navigation operations, it is beneficial to ignore individual outlier seedling points when fitting the straight line, as it aids in maintaining and controlling the stability of the heading. Therefore, future compensation is not necessary. Furthermore, the reference points used in this study correspond to the actual positions of the rice seedlings.

However, due to variations in the soil's bottom layer during the planting process, the precise positioning of seedlings—when transplanted or sown by machinery—inevitably deviates from the ideal straight-line path of the entire row. This inherent deviation can be attributed to the uneven nature of the field's bottom layer, which affects the accurate alignment of the seedlings. To further evaluate the performance of the proposed algorithm, a comparative analysis was conducted against the crop row identification methods proposed in [38,39]. The quantitative comparison results are presented in Table 2.

Table 2. Comparison of three algorithms for rice seedling centerline extraction.

Algorithm Type	Mean Angular Error (°)	Mean Processing Time (ms)
Proposed (paddy field)	0.6489	50.67
[38]	3.14	192.52
[39]	1.124	20.1

Note: The angular error metric is defined as the angle between the ground-truth line fitted to seedling positions and the estimated line derived by the proposed algorithm, ensuring consistent evaluation criteria with the referenced methods.

As evidenced in Table 2, the proposed algorithm achieves a significant improvement in angular accuracy, outperforming both [38] (by 79.3%) and [39] (by 42.3%). While the computational time of our method (50.67 ms per iteration) is moderately higher than that of [39], it successfully fulfills the real-time processing requirement for LiDAR data acquisition at 10 Hz. Furthermore, it should be noted that the current implementation leaves room for hardware optimization to enhance the computational efficiency.

4. Conclusions

This study presents a robust framework for rice row detection in complex paddy environments. Firstly, a multi-sensor fusion system integrating 2D LiDAR, AHRS, and RTK-GNSS was developed to reconstruct 3D point clouds, effectively compensating for height distortions caused by the uneven terrain. Secondly, the proposed variable-threshold segmentation method, dynamically adjusted through posture perception, demonstrated superior adaptability to field variations compared to fixed-threshold approaches. By incorporating robot travelling path constraints and prior information about the rice row spacing, the clustering algorithm successfully filtered out weed interference and achieved accurate seedling localization. Experimental validation across sloped land, dryland, and submerged paddy fields confirmed the method's reliability, with standard deviations below 20 mm and angular errors under 0.65°, outperforming existing techniques. These results highlight the method's potential to enhance the autonomous navigation accuracy in real-world agricultural operations. Future research will focus on optimizing the computational efficiency through hardware acceleration and integrating MEMS-IMU with stereo visual odometry to address GNSS-denied scenarios. Additionally, extending this framework to diverse crop types and multi-robot coordination systems will further advance precision agriculture technologies.

Author Contributions: Conceptualization, J.H. and R.Z.; methodology, J.H.; software, J.H.; validation, W.D., Q.T. and X.S.; data curation, J.L. and Q.T.; writing—original draft preparation, J.H.; writing—review and editing, R.Z.; project administration, R.Z.; funding acquisition, J.H. All authors have read and agreed to the published version of the manuscript.

Funding: This work was supported by the Characteristic Innovation Projects of Ordinary Universities in Guangdong Province (No.2024KTSCX398) and the Guangdong Polytechnic of Industry and Commerce Scientific Research Project (No. 2024-ZKT-05, No. 2023-gc-04) and funded by the Science and Technology Planning Project of Guangdong Province (No. 2021B1212040009).

Data Availability Statement: The data will be made available upon reasonable request by the corresponding author.

Acknowledgments: The authors would like to express their gratitude to the Guangdong Polytechnic of Industry and Commerce, the Guangdong Provincial Key Laboratory for Agricultural Artificial Intelligence, Key Laboratory of the Ministry of Education of China for Key Technologies for Agricultural Machinery and Equipment for Southern China, and the reviewers who provided helpful suggestions for this manuscript.

Conflicts of Interest: The authors declare no conflicts of interest.

References

1. Dehghanpir, S.; Bazrafshan, O.; Nadi, S.; Jamshidi, S. Assessing the sustainability of Agricultural Water Use Based on Water Footprints of wheat and rice production. In *Sustainability and Water Footprint*; Springer: Cham, Switzerland, 2024; Volume 10, pp. 57–82.
2. Bwire, D.; Saito, H.; Sidle, R.C.; Nishiwaki, J. Water management and hydrological characteristics of paddy-rice fields under alternate wetting and drying irrigation practice as climate smart practice: A review. *Agronomy* **2024**, *14*, 1421. [CrossRef]
3. Zhang, L.; Zhang, F.; Zhang, K.; Liao, P.; Xu, Q. Effect of agricultural management practices on rice yield and greenhouse gas emissions in the rice–wheat rotation system in China. *Sci. Total Environ.* **2024**, *916*, 170307. [CrossRef]
4. Peng, S.; Zheng, C.; Yu, X. Progress and challenges of rice ratooning technology in China. *Crop Environ.* **2023**, *2*, 5–11. [CrossRef]
5. Chen, Q. *China Agricultural Mechanization Yearbook*; China Agricultural Science and Technology Press: Beijing, China, 2020.
6. He, Y.; Jiang, H.; Fang, H.; Wang, Y.; Liu, Y. Research progress of intelligent obstacle detection methods of vehicles and their application on agriculture. *Trans. Chin. Soc. Agric. Eng.* **2018**, *34*, 21–32.
7. Ji, Y.; Xu, H.; Zhang, M.; Li, S.; Cao, R.; Li, H. Design of Point Cloud Acquisition System for Farmland Environment Based on LiDAR. *Trans. Chin. Soc. Agric. Mach.* **2019**, *50*, 1–7.
8. Ji, C.; Zhou, J. Current Situation of Navigation Technologies for Agricultural Machinery. *Trans. Chin. Soc. Agric. Mach.* **2014**, *45*, 44–54.
9. Zhang, Q.; Chen, M.E.S.; Li, B. A visual navigation algorithm for paddy field weeding robot based on image understanding. *Comput. Electron. Agric.* **2017**, *143*, 66–78. [CrossRef]
10. Kaizu, Y.; Imou, K. A dual-spectral camera system for paddy rice seedling row detection. *Comput. Electron. Agric.* **2008**, *63*, 49–56. [CrossRef]
11. Zhang, X.; Li, X.; Zhang, B.; Zhou, J.; Tian, G.; Xiong, Y.; Gu, B. Automated robust crop-row detection in maize fields based on position clustering algorithm and shortest path method. *Comput. Electron. Agric.* **2018**, *154*, 165–175. [CrossRef]
12. Jing, G.; Yang, X.; Wang, Z.; Liu, H. Crop rows detection based on image characteristic point and particle swarm optimization-clustering algorithm. *Trans. Chin. Soc. Agric. Eng.* **2017**, *33*, 165–170.
13. Choi, K.H.; Han, S.K.; Han, S.H.; Park, K.H.; Kim, K.S.; Kim, S. Morphology-based guidance line extraction for an autonomous weeding robot in paddy fields. *Comput. Electron. Agric.* **2015**, *113*, 266–274. [CrossRef]
14. Wang, S.; Dai, X.; Xu, N.; Zhang, P. Overview on Environment Perception Technology for Unmanned Ground Vehicle. *J. Chang. Univ. Sci. Technol. (Nat. Sci. Ed.)* **2017**, *40*, 1–6.
15. Chateau, T.; Debain, C.; Collange, F.; Trassoudaine, L.; Alizon, J. Automatic guidance of agricultural vehicles using a laser sensor. *Comput. Electron. Agric.* **2000**, *28*, 243–257. [CrossRef]
16. Barawid, O.C., Jr.; Mizushima, A.; Ishii, K.; Noguchi, N. Development of an Autonomous Navigation System using a Two-dimensional Laser Scanner in an Orchard Application. *Biosyst. Eng.* **2007**, *96*, 139–149. [CrossRef]
17. Hiremath, S.A.; Van Der Heijden, G.W.; Van Evert, F.K.; Stein, A.; Ter Braak, C.J. Laser range finder model for autonomous navigation of a robot in a maize field using a particle filter. *Comput. Electron. Agric.* **2014**, *100*, 41–50. [CrossRef]
18. Zhang, Y.; Zhou, J. Laser radar based orchard trunk detection. *J. China Agric. Univ.* **2015**, *20*, 249–255.
19. Hämmerle, M.; Höfle, B. Effects of reduced terrestrial LiDAR point density on high-resolution grain crop surface models in precision agriculture. *Sensors* **2014**, *14*, 24212–24230. [CrossRef]
20. Keightley, K.E.; Bawden, G.W. 3D volumetric modeling of grapevine biomass using Tripod LiDAR. *Comput. Electron. Agric.* **2010**, *74*, 305–312. [CrossRef]
21. Xue, J.; Dong, S.; Fan, B. Detection of Obstacles Based on Information Fusion for Autonomous Agricultural Vehicles. *Trans. Chin. Soc. Agric. Mach.* **2018**, *49*, 36–41.
22. Peng, Y.; Qu, D.; Zhong, Y.; Xie, S.; Luo, J.; Gu, J. The obstacle detection and obstacle avoidance algorithm based on 2-D LiDAR. In Proceedings of the 2015 IEEE International Conference on Information and Automation, Lijiang, China, 8–10 August 2015; IEEE: New York, NY, USA, 2015.

23. Malavazi, F.B.P.; Guyonneau, R.; Fasquel, J.B.; Lagrange, S.; Mercier, F. LiDAR-only based navigation algorithm for an autonomous agricultural robot. *Comput. Electron. Agric.* **2018**, *154*, 71–79. [CrossRef]
24. Liu, W.; Li, W.; Feng, H.; Xu, J.; Yang, S.; Zheng, Y.; Liu, X.; Wang, Z.; Yi, X.; He, Y.; et al. Overall integrated navigation based on satellite and lidar in the standardized tall spindle apple orchards. *Comput. Electron. Agric.* **2024**, *216*, 108489. [CrossRef]
25. Liu, Y.; He, Y.; Noboru, N. Development of a collision avoidance system for agricultural airboat based on laser sensor. *J. Zhejiang Univ. (Agric. Life Sci.)* **2018**, *44*, 431–439.
26. Colaço, A.F.; Trevisan, R.G.; Molin, J.P.; Rosell-Polo, J.R.; Escolà, A. A Method to Obtain Orange Crop Geometry Information Using a Mobile Terrestrial Laser Scanner and 3D Modeling. *Remote Sens.* **2017**, *9*, 763. [CrossRef]
27. Garrido, M.; Paraforos, D.S.; Reiser, D.; Vázquez Arellano, M.; Griepentrog, H.W.; Valero, C. 3D Maize Plant Reconstruction Based on Georeferenced Overlapping LiDAR Point Clouds. *Remote Sens.* **2015**, *7*, 17077–17096. [CrossRef]
28. Reiser, D.; Vázquez-Arellano, M.; Paraforos, D.S.; Garrido-Izard, M.; Griepentrog, H.W. Iterative individual plant clustering in maize with assembled 2D LiDAR data. *Comput. Ind.* **2018**, *99*, 42–52. [CrossRef]
29. Zhao, R.; Hu, L.; Luo, X.; Zhou, H.; Du, P.; Tang, L.; He, J.; Mao, T. A novel approach for describing and classifying the unevenness of the bottom layer of paddy fields. *Comput. Electron. Agric.* **2019**, *162*, 552–560. [CrossRef]
30. He, J.; Zang, Y.; Luo, X.; Zhao, R.; He, J.; Jiao, J. Visual detection of rice rows based on Bayesian decision theory and robust regression least squares method. *Int. J. Agric. Biol. Eng.* **2021**, *14*, 199–206. [CrossRef]
31. Hu, L.; Lin, C.; Luo, X.; Yang, W.; Xu, Y.; Zhou, H.; Zhang, Z. Design and experiment on auto leveling control system of agricultural implements. *Trans. Chin. Soc. Agric. Eng.* **2015**, *31*, 15–20.
32. Balduzzi, M.A.; Van der Zande, D.; Stuckens, J.; Verstraeten, W.W.; Coppin, P. The Properties of Terrestrial Laser System Intensity for Measuring Leaf Geometries: A Case Study with Conference Pear Trees (*Pyrus communis*). *Sensors* **2011**, *11*, 1657–1681. [CrossRef]
33. Li, B.; Fang, Z.; Ren, J. Extraction of Building's Feature from Laser Scanning Data. *Geomat. Inf. Sci. Wuhan Univ.* **2003**, *28*, 65–70.
34. Guan, Y.L.; Liu, S.T.; Zhou, S.J.; Zhang, L.; Lu, T. Robust Plane Fitting of Point Clouds Based On TLS. *J. Geod. Geodyn.* **2011**, *31*, 80–83.
35. Reiser, D.; Miguel, G.; Arellano, M.V.; Griepentrog, H.W.; Paraforos, D.S. Crop row detection in maize for developing navigation algorithms under changing plant growth stages. In Proceedings of the Robot 2015: Second Iberian Robotics Conference, Lisbon, Portugal, 19–21 November 2015; Springer: Cham, Switzerland, 2016.
36. Wang, C. Selection of smoothing coefficient via exponential smoothing algorithm. *J. North Univ. China (Nat. Sci. Ed.)* **2006**, *27*, 4. [CrossRef]
37. Li, S.; Liu, K. Quadric Exponential Smoothing Model with Adapted Parameter and Its Applications. *Syst. Eng. Theory Pract.* **2004**, *24*, 94–99.
38. Zhang, S.; Ma, Q.; Cheng, S.; An, D.; Yang, Z.; Ma, B.; Yang, Y. Crop row detection in the middle and late periods of maize under sheltering based on solid state LiDAR. *Agriculture* **2022**, *12*, 2011. [CrossRef]
39. Yang, Y.; Ma, Q.; Chen, Z.; Wen, X.; Zhang, G.; Zhang, T.; Dong, X.; Chen, L. Real-time extraction of the navigation lines between sugarcane ridges using LiDAR. *Trans. Chin. Soc. Agric. Eng.* **2022**, *38*, 8. [CrossRef]

agronomy

IMPACT FACTOR 3.7

CITESCORE 5.2

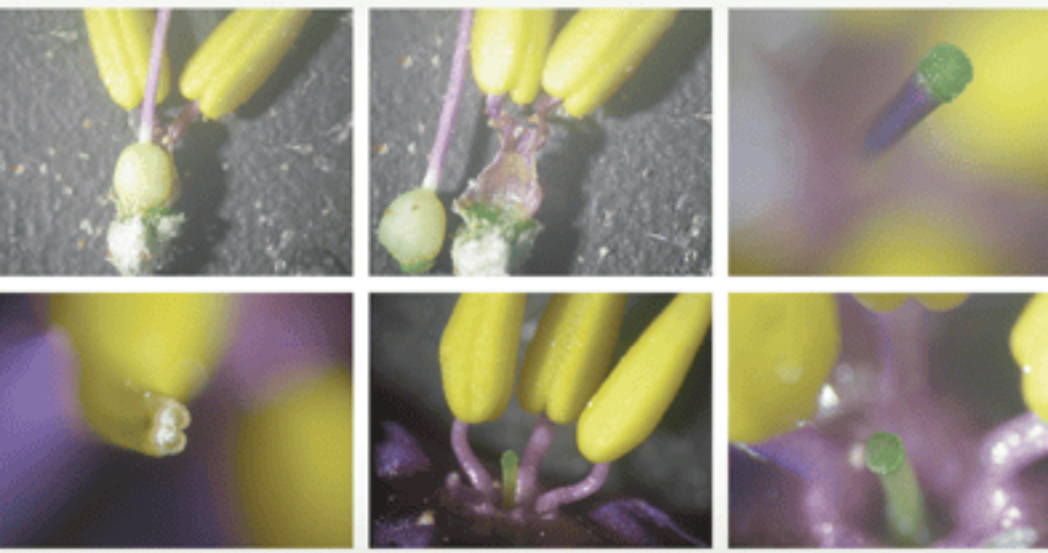

Reproductive Biology of the Australian Bush Tomato *Solanum orbiculatum*

Volume 13 · Issue 11 | November 2023

MDPI

mdpi.com/journal/agronomy
ISSN 2073-4395

agronomy

3.4 Impact Factor | 6.7 CiteScore | 17 days Time to First Decision

Agronomy, Volume 13, Issue 11

2023 November - 186 articles

Cover Story: *Solanum orbiculatum* ssp. *orbiculatum* is an edible bush tomato endemic to Australia. Plants of this species are potentially self-compatible but are unable to carry out spontaneous autogamy. The flowers are protogynous with a floral structure and morphology that can encourage cross pollination as the stigma is exserted above the anther's tips. This study will contribute to understanding the evolution and systematic relationships of species. Furthermore, understanding the reproductive biology of this species is also of interest for cultivated tomato breeding. View this paper

Number of Papers 186

Articles (26)

Search | 1 Selected

Select all | Export | Most recent

Article | 4 Citations | 1,895 Views | 14 Pages

A Proposal for Lodging Judgment of Rice Based on Binocular Camera

Yukun Yang, Chuqi Liang, Lian Hu, Xiwen Luo, Jie He, Pei Wang, Peikui Huang, Ruitao Gao and Jiehao Li

Agronomy **2023**, *13*(11), 2852; https://doi.org/10.3390/agronomy13112852 - 20 November 2023

Rice lodging is a crucial problem in rice production. Lodging during growing and harvesting periods can decrease rice yields. Practical lodging judgment for rice can provide effective reference information for yield prediction and harvesting. This ar... Show more

Full Article →

Article | 16 Citations | 3,362 Views | 17 Pages

Modeling Callus Induction and Regeneration in Hypocotyl Explant of Fodder Pea (*Pisum sativum* var. *arvense* L.) Using Machine Learning Algorithm Method

Aras Türkoğlu, Parisa Bolouri, Kamil Haliloğlu, Barış Eren, Fatih Demirel, Muhammet İslam Işık, Magdalena Piekutowska, Tomasz Wojciechowski and Gniewko Niedbała

Agronomy **2023**, *13*(11), 2835; https://doi.org/10.3390/agronomy13112835 - 17 November 2023

A comprehensive understanding of genetic diversity and the categorization of germplasm is important to effectively identify appropriate parental candidates for the goal of breeding. It is necessary to have a technique of tissue culture that is both e... Show more

Full Article →

Review | 16 Citations | 6,047 Views | 24 Pages

Field Phenotyping Monitoring Systems for High-Throughput: A Survey of Enabling Technologies, Equipment, and Research Challenges

Huali Yuan, Minghan Song, Yiming Liu, Qi Xie, Weixing Cao, Yan Zhu and Jun Ni

Agronomy **2023**, *13*(11), 2832; https://doi.org/10.3390/agronomy13112832 - 17 November 2023

High-throughput phenotype monitoring systems for field crops can not only accelerate the breeding process but also provide important data support for precision agricultural monitoring. Traditional phenotype monitoring methods for field crops relying... Show more

Full Article →

Article | 6 Citations | 2,534 Views | 14 Pages

Fixed Spraying Systems Application in Citrus Orchards: Nozzle Type and Nozzle Position Effects on Droplet Deposition and Pest Control

Chen Chen, Xinyu Xue, Qingqing Zhou, Wei Gu, Songchao Zhang and Chundu Wu

Agronomy **2023**, *13*(11), 2828; https://doi.org/10.3390/agronomy13112828 - 16 November 2023

Pesticide application is an essential means of controlling plant diseases and pests in citrus orchards. In recent years, fixed spraying systems have gradually been used as alternatives to traditional sprayers and manual sprayers in some hilly citrus... Show more

Full Article →

Article | 10 Citations | 3,664 Views | 21 Pages

Integration of Vis–NIR Spectroscopy and Machine Learning Techniques to Predict Eight Soil Parameters in Alpine Regions

Chuanli Jiang, Jianyun Zhao and Guorong Li

Agronomy **2023**, *13*(11), 2816; https://doi.org/10.3390/agronomy13112816 - 15 November 2023

Visible and near-infrared spectroscopy (Vis–NIR, 350–1100 nm) has great potential for predicting soil properties. However, current research on the hyperspectral prediction of soil parameters in agricultural areas of alpine regions and the... Show more

Full Article →

Article | 20 Citations | 5,927 Views | 19 Pages

Evaluation of Variable Application Rate of Fertilizers Based on Site-Specific Management Zones for Winter Wheat in Small-Scale Farming

Yuefan Wang, Yifan Yuan, Fei Yuan, Syed Tahir Ata-Ul-Karim, Xiaojun Liu, Yongchao Tian, Yan Zhu, Weixing Cao and Qiang Cao

Agronomy **2023**, *13*(11), 2812; https://doi.org/10.3390/agronomy13112812 - 13 November 2023

China is currently experiencing a severe issue of excessive fertilization. Variable rate fertilization (VRF) technology is key to solving this issue in precision agriculture, and one way to implement VRF is through management zone (MZ) delineation. T... Show more

Full Article →

Article | 5 Citations | 3,326 Views | 19 Pages

Estimation of Agronomic Characters of Wheat Based on Variable Selection and Machine Learning Algorithms

Dunliang Wang, Rui Li, Tao Liu, Chengming Sun and Wenshan Guo

Agronomy **2023**, *13*(11), 2808; https://doi.org/10.3390/agronomy13112808 - 13 November 2023

Wheat is one of the most important food crops in the world, and its high and stable yield is of great significance for ensuring food security. Timely, non-destructive, and accurate monitoring of wheat growth information is of great significance for o... Show more

Full Article →

Article | 3 Citations | 1,729 Views | 27 Pages

Clustering and Segmentation of Adhesive Pests in Apple Orchards Based on GMM-DC

Yunfei Wang, Shuangxi Liu, Zhuo Ren, Bo Ma, Junlin Mu, Linlin Sun, Hongjian Zhang and Jinxing Wang

Agronomy **2023**, *13*(11), 2806; https://doi.org/10.3390/agronomy13112806 - 13 November 2023

The segmentation of individual pests is a prerequisite for pest feature extraction and identification. To address the issue of pest adhesion in the apple orchard pest identification process, this research proposed a pest adhesion image segmentation m... Show more

Full Article →

Article | 7 Citations | 5,555 Views | 23 Pages

Feasibility of Detecting Sweet Potato (*Ipomoea batatas*) Virus Disease from High-Resolution Imagery in the Field Using a Deep Learning Framework

Fanguo Zeng, Ziyu Ding, Qingkui Song, Jiayi Xiao, Jianyu Zheng, Haifeng Li, Zhongxia Luo, Zhangying Wang, Xuejun Yue and Lifei Huang

Agronomy **2023**, *13*(11), 2801; https://doi.org/10.3390/agronomy13112801 - 13 November 2023

The sweet potato is an essential food and economic crop that is often threatened by the devastating sweet potato virus disease (SPVD), especially in developing countries. Traditional laboratory-based direct detection methods and field scouting are co... Show more

Full Article →

Article | 3 Citations | 2,601 Views | 21 Pages

Enhancing Crop Mapping Precision through Multi-Temporal Sentinel-2 Image and Spatial-Temporal Neural Networks in Northern Slopes of Tianshan Mountain

Xiaoyong Zhang, Yonglin Guo, Xiangyu Tian and Yongqing Bai

Agronomy **2023**, *13*(11), 2800; https://doi.org/10.3390/agronomy13112800 - 12 November 2023

Northern Slopes of Tianshan Mountain (NSTM) in Xinjiang hold significance as a principal agricultural hub within the region's arid zone. Accurate crop mapping across vast agricultural expanses is fundamental for intelligent crop monitoring and... Show more

Full Article →

Article | 3 Citations | 1,973 Views | 16 Pages

Combining Gaussian Process Regression with Poisson Blending for Seamless Cloud Removal from Optical Remote Sensing Imagery for Cropland Monitoring

Soyeon Park and No-Wook Park

Agronomy **2023**, *13*(11), 2789; https://doi.org/10.3390/agronomy13112789 - 10 November 2023

Constructing optical image time series for cropland monitoring requires a cloud removal method that accurately restores cloud regions and eliminates discontinuity around cloud boundaries. This paper describes a two-stage hybrid machine learning-based... Show more

Full Article →

Article | 6 Citations | 1,750 Views | 23 Pages

Study on the Influence of Grooved-Wheel Working Parameters on Fertilizer Emission Performance and Parameter Optimization

Jinfeng Wang, Ruidong Wang, Jinyan Ju, Yuling Song, Zuodong Fu, Tenghui Lin, Guoqing Chen, Rui Jiang and Zhentao Wang

Agronomy **2023**, *13*(11), 2779; https://doi.org/10.3390/agronomy13112779 - 8 November 2023

The grooved-wheel fertilizer machine is one of the most widely used pieces of fertilization equipment. However, detailed information on the fertilizer filling status and the mechanism of particle interactions during the operation of the grooved wheel... Show more

Full Article →

Article | 1 Citations | 2,072 Views | 15 Pages

Collaborative Wheat Lodging Segmentation Semi-Supervised Learning Model Based on RSE-BiSeNet Using UAV Imagery

Hongbo Zhi, Baohua Yang and Yue Zhu

Agronomy **2023**, *13*(11), 2772; https://doi.org/10.3390/agronomy13112772 - 6 November 2023

Lodging is a common natural disaster during wheat growth. The accurate identification of wheat lodging is of great significance for early warnings and post-disaster assessment. With the widespread use of unmanned aerial vehicles (UAVs), large-scale w... Show more

Full Article →

Review | 19 Citations | 4,538 Views | 26 Pages

Technologies and Equipment of Mechanized Blossom Thinning in Orchards: A Review

Xiaohui Lei, Quanchun Yuan, Tao Xyu, Yannan Qi, Jin Zeng, Kai Huang, Yuanhao Sun, Andreas Herbst and Xiaolan Lyu

Agronomy **2023**, *13*(11), 2753; https://doi.org/10.3390/agronomy13112753 - 31 October 2023

Orchard thinning can avoid biennial bearing and improve fruit quality, which is a necessary agronomic section in orchard management. The existing methods of artificial fruit thinning and chemical spraying are no longer suitable for the development of... Show more

Full Article →

Article | 12 Citations | 4,001 Views | 22 Pages

Multiscale Inversion of Leaf Area Index in Citrus Tree by Merging UAV LiDAR with Multispectral Remote Sensing Data

Weicheng Xu, Feifan Yang, Guangchao Ma, Jinhao Wu, Jiapei Wu and Yubin Lan

Agronomy **2023**, *13*(11), 2747; https://doi.org/10.3390/agronomy13112747 - 31 October 2023

The LAI (leaf area index) is an important parameter describing the canopy structure of citrus trees and characterizing plant photosynthesis, as well as providing an important basis for selecting parameters for orchard plant protection operations. By... Show more

Full Article →

Article | 6 Citations | 2,829 Views | 14 Pages

Semantic Segmentation of Portuguese Agri-Forestry Using High-Resolution Orthophotos

Tiago G. Morais, Tiago Domingos and Ricardo F. M. Teixeira

Agronomy **2023**, *13*(11), 2741; https://doi.org/10.3390/agronomy13112741 - 30 October 2023

The *Montado* ecosystem is an important agri-forestry system in Portugal, occupying about 8% of the total area of the country. However, this biodiverse ecosystem is threatened due to factors such as shrub encroachment. In this context, the development... Show more

Full Article →

Article | 2 Citations | 2,467 Views | 18 Pages

Method and Experiments for Acquiring High Spatial Resolution Images of Abnormal Rice Canopy by Autonomous Unmanned Aerial Vehicle Field Inspection

Qiangzhi Zhang, Xiwen Luo, Lian Hu, Chuqi Liang, Jie He, Pei Wang and Runmao Zhao

Agronomy **2023**, *13*(11), 2731; https://doi.org/10.3390/agronomy13112731 - 29 October 2023

The yield and quality of rice are closely related to field management. The automatic identification of field abnormalities, such as diseases and pests, based on computer vision currently mainly relies on high spatial resolution (HSR) images obtained... Show more

Full Article →

Article | 3 Citations | 2,529 Views | 13 Pages

Unravelling the Complexities of Genotype-Soil-Management Interaction for Precision Agriculture

Svend Christensen and Signe M. Jensen

Agronomy **2023**, *13*(11), 2727; https://doi.org/10.3390/agronomy13112727 - 29 October 2023

The knowledge of interactions among crop genotypes, soil types, and crop management is essential for precision agriculture. This paper explores these interactions through the analysis of 27 years of winter wheat trials, with 276 unique varieties test... Show more

Full Article →

Article | 12 Citations | 2,346 Views | 16 Pages

Win-Former: Window-Based Transformer for Maize Plant Point Cloud Semantic Segmentation

Yu Sun, Xindong Guo and Hua Yang

Agronomy **2023**, *13*(11), 2723; https://doi.org/10.3390/agronomy13112723 - 29 October 2023

Semantic segmentation of plant point clouds is essential for high-throughput phenotyping systems, while existing methods still struggle to balance efficiency and performance. Recently, the Transformer architecture has revolutionized the area of compu... Show more

Full Article →

Editorial | 1 Citations | 2,056 Views | 7 Pages

Precision Operation Technology and Intelligent Equipment in Farmland

Jun Ni

Agronomy **2023**, *13*(11), 2721; https://doi.org/10.3390/agronomy13112721 - 29 October 2023

Precision operation technology and intelligent equipment in farmland is centered on farmland cultivation, planting, management, harvesting, and other operations [...]

Full Article →

Article | 7 Citations | 2,785 Views | 19 Pages

Identifying the Spatio-Temporal Change in Winter Wheat–Summer Maize Planting Structure in the North China Plain between 2001 and 2020

Bo Yang, Jinglei Wang, Shenglin Li and Xiuqiao Huang

Agronomy **2023**, *13*(11), 2712; https://doi.org/10.3390/agronomy13112712 - 27 October 2023

Tracking winter wheat–summer maize distribution is crucial for the management of agricultural water resources in the water-scarce North China Plain (NCP). However, the spatio-temporal change in planting structure that has occurred during the la... Show more

Full Article →

Article | 11 Citations | 3,464 Views | 20 Pages

Multi-Plant Disease Identification Based on Lightweight ResNet18 Model

Li Ma, Yuanhui Hu, Yao Meng, Zhiyi Li and Guifen Chen

Agronomy **2023**, *13*(11), 2702; https://doi.org/10.3390/agronomy13112702 - 27 October 2023

Deep-learning-based methods for plant disease recognition pose challenges due to their high number of network parameters, extensive computational requirements, and overall complexity. To address this issue, we propose an improved residual-network-bas... Show more

Full Article →

Article | 17 Citations | 3,101 Views | 20 Pages

Evaluating the Efficacy of Sentinel-2B and Landsat-8 for Estimating and Mapping Wheat Straw Cover in Rice–Wheat Fields

Muhammad Sohail Memon, Shuren Chen, Yaxiao Niu, Weiwei Zhou, Osama Elsherbiny, Runzhi Liang, Zhiqiang Du and Xiaohu Guo

Agronomy **2023**, *13*(11), 2691; https://doi.org/10.3390/agronomy13112691 - 26 October 2023

Sustainable agriculture and soil conservation methods are integral to ensuring food safety and mitigating environmental impacts worldwide. However, crop residue/straw serves many vital functions from tillage to harvest, so that quantifying the approp... Show more

Full Article →

Review | 20 Citations | 4,411 Views | 18 Pages

Anti-Drift Technology Progress of Plant Protection Applied to Orchards: A Review

Shaobo Li, Jianping Li, Shaomeng Yu, Pengfei Wang, Hongjie Liu and Xin Yang

Agronomy **2023**, *13*(11), 2679; https://doi.org/10.3390/agronomy13112679 - 25 October 2023

In orchard plant protection application, an anti-drift strategy can effectively reduce drift in the non-target area, reduce spray drift in the environment, and avoid spray leakage and overspraying. To clarify the future development direction of orcha... Show more

Full Article →

Article | 21 Citations | 2,279 Views | 16 Pages

Calibration of Small-Grain Seed Parameters Based on a BP Neural Network: A Case Study with Red Clover Seeds

Xuejie Ma, Mengjun Guo, Xin Tong, Zhanfeng Hou, Haiyang Liu and Haiyan Ren

Agronomy **2023**, *13*(11), 2670; https://doi.org/10.3390/agronomy13112670 - 24 October 2023

In order to enhance the accuracy of discrete element numerical simulations in the processing of small-seed particles, it is essential to calibrate the parameters of seeds within the discrete element software. This study employs a series of physical t... Show more

Full Article →

Article | 19 Citations | 4,012 Views | 23 Pages

Improved YOLOv7-Tiny Complex Environment Citrus Detection Based on Lightweighting

Bo Gu, Changji Wen, Xuanzhi Liu, Yingjian Hou, Yuanhui Hu and Hengqiang Su

Agronomy **2023**, *13*(11), 2667; https://doi.org/10.3390/agronomy13112667 - 24 October 2023

In complex citrus orchard environments, light changes, branch shading, and fruit overlapping impact citrus detection accuracy. This paper proposes the citrus detection model YOLO-DCA in complex environments based on the YOLOv7-tiny model. We used dep... Show more

Full Article →

agronomy

IMPACT FACTOR 3.4

CITESCORE 6.7

Article

Method and Experiments for Acquiring High Spatial Resolution Images of Abnormal Rice Canopy by Autonomous Unmanned Aerial Vehicle Field Inspection

Qiangzhi Zhang, Xiwen Luo, Lian Hu, Chuqi Liang, Jie He, Pei Wang and Runmao Zhao

Special Issue

Unmanned Farms in Smart Agriculture

Edited by

Prof. Dr. Zhiyan Zhou and Prof. Dr. Lian Hu

MDPI

https://doi.org/10.3390/agronomy13112731

agronomy

MDPI

Article

Method and Experiments for Acquiring High Spatial Resolution Images of Abnormal Rice Canopy by Autonomous Unmanned Aerial Vehicle Field Inspection

Qiangzhi Zhang [1,2], Xiwen Luo [1,2], Lian Hu [1,2], Chuqi Liang [1,2], Jie He [1,2], Pei Wang [1,2] and Runmao Zhao [1,2,*]

[1] Key Laboratory of the Ministry of Education of China for Key Technologies for Agricultural Machinery and Equipment for Southern China, South China Agricultural University, Guangzhou 510642, China
[2] Guangdong Laboratory for Lingnan Modern Agriculture, Guangzhou 510642, China
* Correspondence: zhrm_2007@163.com; Tel.: +86-13926112654

Abstract: The yield and quality of rice are closely related to field management. The automatic identification of field abnormalities, such as diseases and pests, based on computer vision currently mainly relies on high spatial resolution (HSR) images obtained through manual field inspection. In order to achieve automatic and efficient acquisition of HSR images, based on the capability of high-throughput field inspection of UAV remote sensing and combining the advantages of high-flying efficiency and low-flying resolution, this paper proposes a method of "far-view and close-look" autonomous field inspection by unmanned aerial vehicle (UAV) to acquire HSR images of abnormal areas in the rice canopy. First, the UAV equipped with a multispectral camera flies high to scan the whole field efficiently and obtain multispectral images. Secondly, abnormal areas (namely areas with poor growth) are identified from the multispectral images, and then the geographical locations of identified areas are positioned with a single-image method instead of the most used method of reconstruction, sacrificing part of positioning accuracy for efficiency. Finally, the optimal path for traversing abnormal areas is planned through the nearest-neighbor algorithm, and then the UAV equipped with a visible light camera flies low to capture HSR images of abnormal areas along the planned path, thereby acquiring the "close-look" features of the rice canopy. The experimental results demonstrate that the proposed method can identify abnormal areas, including diseases and pests, lack of seedlings, lodging, etc. The average absolute error (AAE) of single-image positioning is 13.2 cm, which can meet the accuracy requirements of the application in this paper. Additionally, the efficiency is greatly improved compared to reconstruction positioning. The ground sampling distance (GSD) of the acquired HSR image can reach 0.027 cm/pixel, or even smaller, which can meet the resolution requirements of even leaf-scale deep-learning classification. The HSR image can provide high-quality data for subsequent automatic identification of field abnormalities such as diseases and pests, thereby offering technical support for the realization of the UAV-based automatic rice field inspection system. The proposed method can also provide references for the automatic field management of other crops, such as wheat.

Keywords: unmanned aerial vehicle (UAV); rice canopy; abnormal area; single-image positioning; high spatial resolution (HSR); autonomous field inspection; diseases and pests

Citation: Zhang, Q.; Luo, X.; Hu, L.; Liang, C.; He, J.; Wang, P.; Zhao, R. Method and Experiments for Acquiring High Spatial Resolution Images of Abnormal Rice Canopy by Autonomous Unmanned Aerial Vehicle Field Inspection. *Agronomy* **2023**, *13*, 2731. https://doi.org/10.3390/agronomy13112731

Academic Editor: Yanbo Huang

Received: 10 October 2023
Revised: 25 October 2023
Accepted: 25 October 2023
Published: 29 October 2023

1. Introduction

Rice is one of the most important food crops in China and even in the world. Its production affects the food security of the country [1–3], and the yield and quality of rice are closely related to field management [4,5]. In recent years, in order to improve the efficiency and quality of field management, researchers in the agricultural field have developed various types of automatic equipment (such as self-driving agricultural machinery,

agricultural UAVs, etc.) to perform management actions such as fertilization and pesticide application [6–8]. However, field management decisions are currently mainly made through manual field inspections. In order to detect diseases and pests, water and fertilizer management problems, and other issues in time, agricultural experts regularly observe the rice fields according to the established route. Generally, they first look at the whole from a distance, find abnormalities, then look closer at the details and record. Manual field inspection is not only labor-intensive and inefficient but also depends on experience and has high subjectivity.

With the mature development of UAV and sensor technology and the popularization of agricultural UAVs, UAVs can be equipped with various sensors for multi-modal and high-throughput field inspection [8,9], and those equipped with multispectral cameras are now especially widely used to achieve precision agriculture [10–13]. Compared with manual field inspection, the advantages of UAV field inspection are shown in Table 1. In addition, the development of artificial intelligence technology provides a "brain" for field management decision making [14], among which the development of computer vision technology provides technical means for automatically identifying abnormal conditions in the field, such as diseases and pests [15–22].

Table 1. Comparison between manual field inspection and UAV field inspection.

Manual Field Inspection	UAV Field Inspection
High labor intensity, low efficiency, and low frequency	Easy to automate, high efficiency, and high frequency
Visual observation, limited field of view, and high subjectivity	Machine recognition, wide field of view, and high objectivity
Difficult to go to the ground in the middle and later stages of crop growth	Available in the whole growth period of crops
Difficult to record and trace	Easy to record and trace

Su et al. [23] proposed a method for identifying wheat yellow rust by learning from multispectral UAV imagery, and the experimental results indicated that (1) good classification performance (with an average precision, recall, and accuracy of 89.2%, 89.4%, and 89.3%) was achieved; (2) the top three vegetation indices (VIs) for separating healthy and yellow rust infected wheat plants were the Ratio Vegetation Index (RVI), Normalized Difference Vegetation Index (NDVI), and Optimized Soil-Adjusted Vegetation Index (OSAVI), while the top two spectral bands were Near-Infrared (NIR) and Red. A high-throughput method for above-ground estimation of biomass in rice using multispectral imagery captured at different scales of the crop was proposed by Devia et al. [24], in which seven VIs were calculated to model the relationship, and the results have shown that the proposed approach was able to estimate the biomass of large areas of the crop with an average correlation of 0.76. Kim et al. [25] used the VI extracted from UAV multispectral imagery for crop damage assessment after chemical exposure, and the results demonstrated that the NDVI was capable of reflecting the plant response to chemical exposure and was feasible as an alternative for crop monitoring, damage assessment after chemical exposure, and yield prediction. Wang et al. [12] studied the estimation of the nitrogen status of paddy rice at the vegetative phase using UAV-based multispectral imagery and found an index-based model which correlated well with the N-index values. Many studies have shown that the VI based on UAV multispectral remote sensing images can be used to monitor the growth status of rice and other crops [10–13,23–26]. However, there is a contradiction in the low-altitude remote sensing of UAVs: by flying high, the efficiency is high, but the image spatial resolution is low; by flying low, the image spatial resolution is high, but the efficiency is low. In addition, multispectral remote sensing has the problem of the same spectrum and foreign objects (namely different abnormalities with the same appearance in remote sensing images), which makes it difficult to discriminate different abnormalities [26].

Therefore, exploring how to efficiently inspect the field to acquire rich and useful data for determining whether crop growth exhibits abnormal conditions and even identifying specific types of abnormalities is the objective of this study.

State-of-the-art large-scale deep learning frameworks have been tested by Rahman et al. [15] to investigate the effectiveness in rice plant disease and pest identification from images collected from real-life environments, while they proposed a novel two-stage light-weight Convolutional Neural Network (CNN) highly effective for mobile device based rice plant disease and pest detection, which could be an effective tool for farmers in a remote environment. Chen et al. [16] have combined the DenseNet and inception module to achieve an average predicting accuracy of no less than 94.07% in the public dataset. Shrivastava et al. [17] used VGG16 for classifying the diseases from the 1216 images of seven classes and achieved 93.11% accuracy. Patil et al. [18] proposed a novel multi-modal data fusion framework to diagnose rice diseases using the numerical features extracted from agro-meteorological data collected from sensors and the visual features extracted from the captured rice images, and the experimental results demonstrated that the proposed framework outperformed the outcome of unimodal frameworks. For rapid detection of nutrient stress, Anami et al. [19] used VGG16 for different biotic and abiotic stress detection in rice, while Wang et al. [20] combined CNN and reinforcement learning for NPK detection. Dey et al. [21] have evaluated the performance of CNN-based pre-trained models for the efficient detection of biotic stressed rice leaves caused by two fungal diseases, one insect pest, and three abiotic stressed leaves caused by NPK deficiency by using both public and field data collected, respectively, from laboratory and real field conditions. Hu et al. [22] proposed a rice pest identification method based on a CNN and migration learning, which effectively improved the recognition accuracy of pest images and significantly reduced the number of model parameters. From the above literature, it can be seen that significant achievements have been made in the automatic identification of field abnormalities, such as diseases and pests, based on visible light images [15–22,26]. However, the training and application of the recognition model all rely on HSR images, currently mainly obtained manually, which is not only inefficient but also labor-intensive. Therefore, the automatic acquisition of HSR images is also the starting point of this research.

In general, UAVs have been widely used in the field of agriculture, and UAVs equipped with multispectral cameras have greatly improved the efficiency of field inspections. However, if UAVs fly high, the image spatial resolution will be low, and if UAVs fly low, the efficiency will be low. In addition, automatic recognition relies on HSR images. If we can simulate the method of manual field inspection, "first view far then look close", and combine the advantages of high-flying and low-flying, or specifically, first preliminarily identify abnormal areas efficiently at a high altitude and then accurately identify abnormal areas at a low altitude, both efficiency and precision can be achieved. Based on the above idea, we propose an automatic field inspection system, as shown in Figure 1. Based on this system, a method for acquiring HSR images of rice canopy abnormal areas by autonomous UAV field inspection is proposed in this paper. First, the UAV equipped with a multispectral camera flies high to scan the whole field efficiently and obtain multispectral images. Secondly, abnormal areas (namely areas with poor growth) are identified from the multispectral images, and then the geographical locations of identified abnormal areas are positioned with a single-image method instead of the most used method of reconstruction, sacrificing part of positioning accuracy for efficiency. Finally, the optimal path for traversing abnormal areas is planned through the nearest-neighbor algorithm, and then the UAV equipped with a visible light camera flies low to capture HSR images of abnormal areas along the planned path.

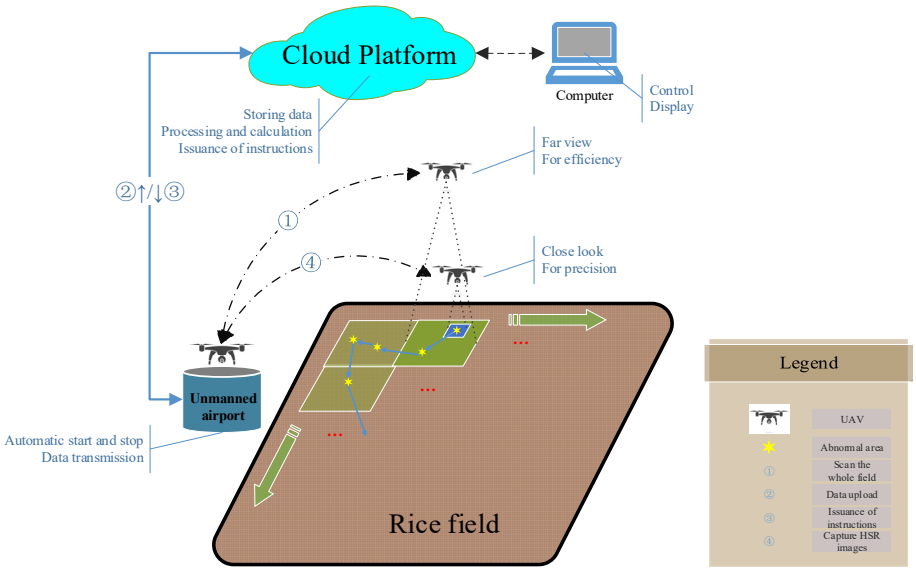

Figure 1. Automatic field inspection system.

2. Materials and Methods

The natural rice field environment is very complex, and it is necessary to reduce background disturbances such as soil. In addition, the jointing booting stage and heading and flowering stage are the main control periods for rice diseases and pests [27], and VIs during this period are also relatively stable [28]. Therefore, the method in this paper is mainly applied to the jointing booting stage and heading and flowering stage of rice. According to previous research results, the NDVI has a strong linear or exponential relationship with the leaf area index (LAI), biomass, leaf chlorophyll content, etc. [25,29], which means the NDVI can be used to judge the growth status of crops. The main processing flow of the method in this paper is shown in Figure 2: far view with multispectral UAV; identification of abnormal areas; positioning of the center point of the abnormal area; path planning; and close look with visible light UAV.

2.1. Far View with Multispectral UAV

A UAV equipped with a multispectral camera, GNSS, IMU, and gimbal is used to perform an aerial orthophoto scanning at a high altitude on the target field, as shown in Figure 3, and the position and orientation information obtained from GNSS and IMU is recorded in the multispectral images for positioning. A multispectral image taken by DJI Phantom 4 Multispectral (P4M) is shown in Figure 4, including visible light (RGB), blue (B), green (G), red (R), red edge (RE), and NIR.

2.2. Identification of Abnormal Areas

Abnormal conditions such as diseases and pests, lack of fertilizer, lodging, etc., usually lead to poor crop growth [30], and the main purpose of field inspection is to find abnormalities. Therefore, the idea of this paper is to regard the area with poor growth as a suspicious abnormal area and then accurately identify the area at a low altitude to achieve both efficiency and precision. As one of the most widely used VIs currently, the NDVI is used to judge the growth status of rice in this paper [31,32]. In actual production, due to noise interference from soil, leaf variations, shadows, etc., in the natural rice field environment, the abnormality of the rice canopy, especially the early symptoms of diseases and pests, usually appears as scattered points rather than blocks in the low-spatial-resolution NDVI obtained at a high altitude, which makes it difficult to extract effective regional features from the NDVI [26]. To address this problem, from the perspective of probability and statistics, this paper first identifies the abnormal points from the NDVI and then counts the dense areas of abnormal points to identify the abnormal areas. As such, the identification

of abnormal areas is transformed into the detection of abnormal point-dense areas in the NDVI. Based on the above idea, this paper proposes a method for identifying abnormal areas based on the NDVI. The detailed process is shown in Figure 5:

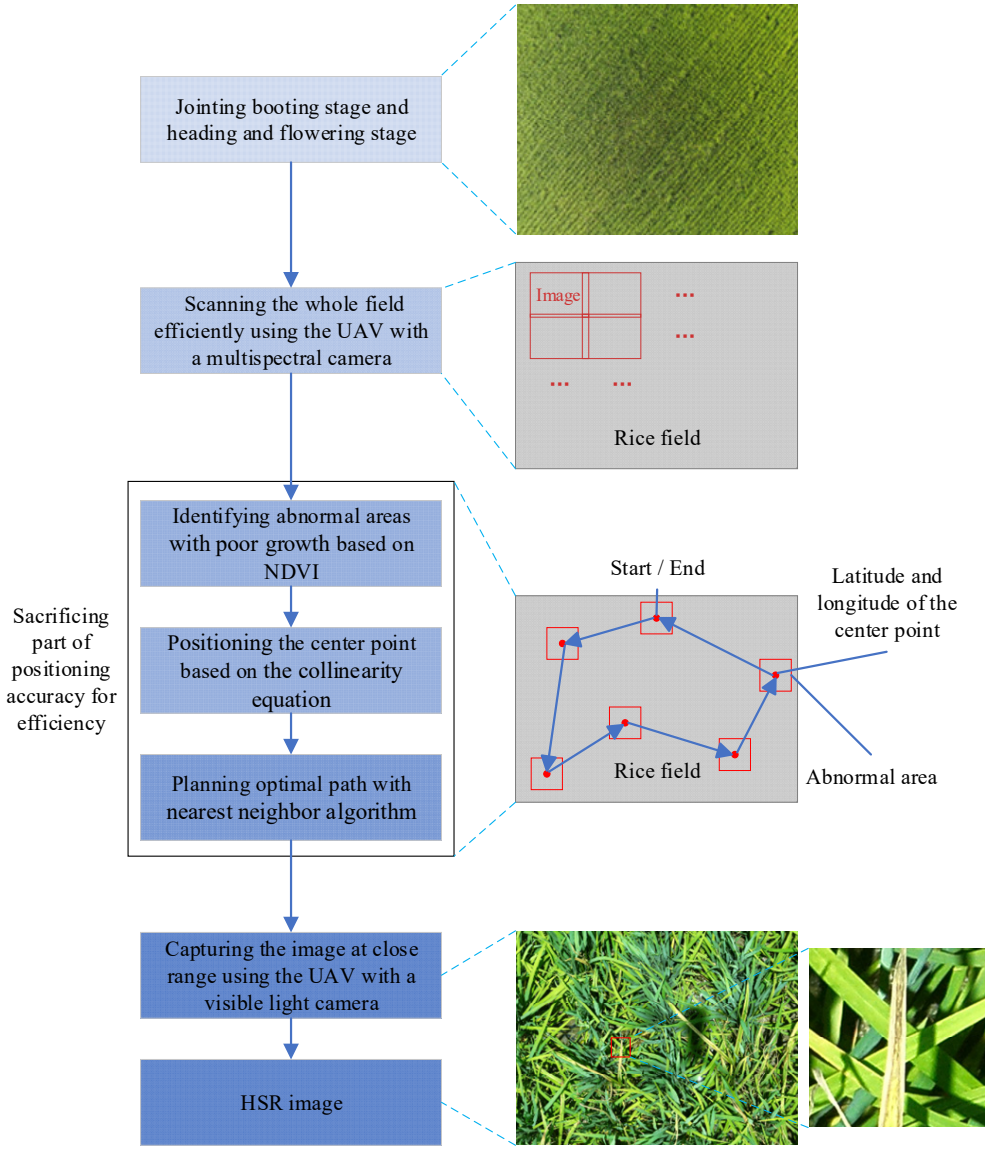

Figure 2. The main processing flow of the proposed method.

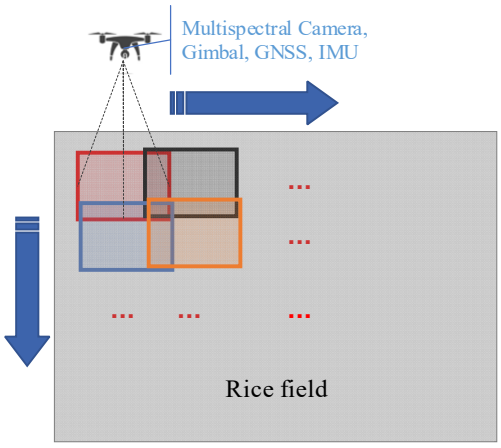

Figure 3. Orthophoto scanning.

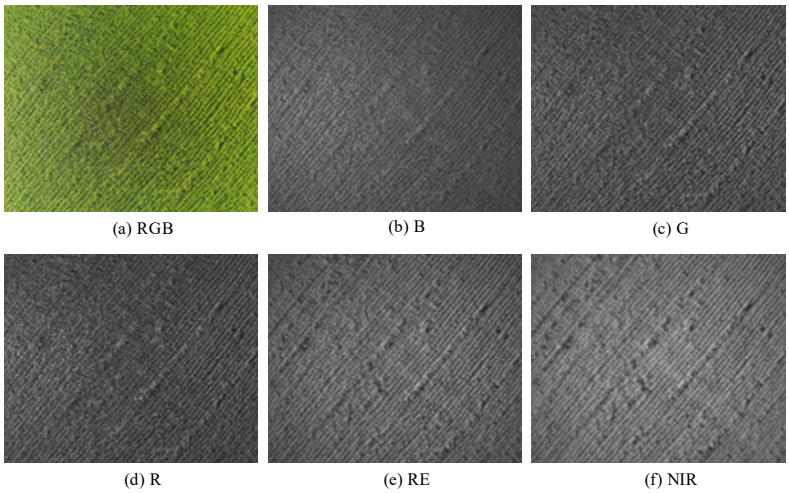

Figure 4. Multispectral image (GSD: 1.59 cm/pixel, resolution: 1600 × 1300, and size: 25 m × 20 m).

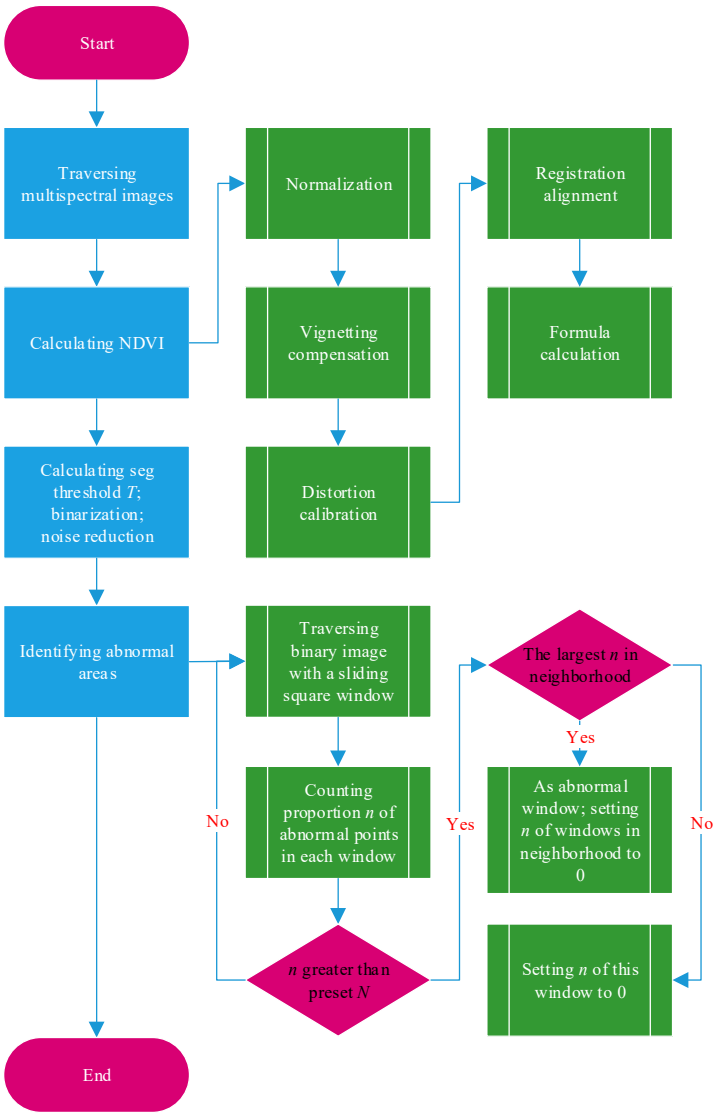

Figure 5. Flow chart of the method for identifying abnormal areas.

1. The multispectral images obtained are traversed to calculate NDVIs with Equation (1) [32]. One of the results is shown in Figure 6b.

$$\mathrm{NDVI} = \frac{\mathrm{NIR} - \mathrm{R}}{\mathrm{NIR} + \mathrm{R}} \tag{1}$$

2. In actual production, due to many factors such as different varieties, different growth periods, different management, and different row spacing and plant spacing, it is impossible to obtain a fixed segmentation threshold T, used to judge an NDVI lower than T as poor growth. Through the statistical analysis of the NDVI, it is found that the histogram of the rice canopy NDVI basically conforms to the bell curve shown in Figure 7, which reminds us of the normal distribution. As a strict mathematical distribution is not required in the engineering application of this paper, it can be assumed that the rice canopy NDVI is approximately normally distributed.

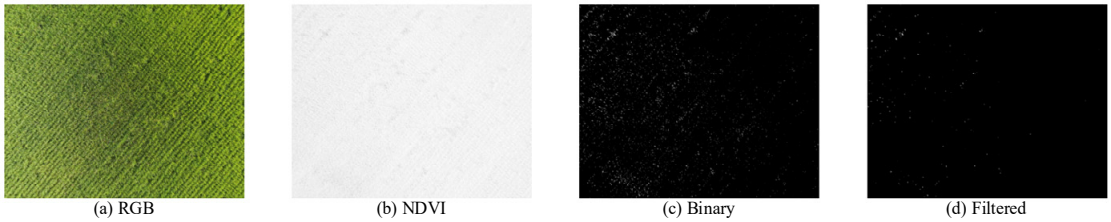

(a) RGB (b) NDVI (c) Binary (d) Filtered

Figure 6. Example of image processing (GSD: 1.59 cm/pixel, resolution: 1600 × 1300, and size: 25 m × 20 m).

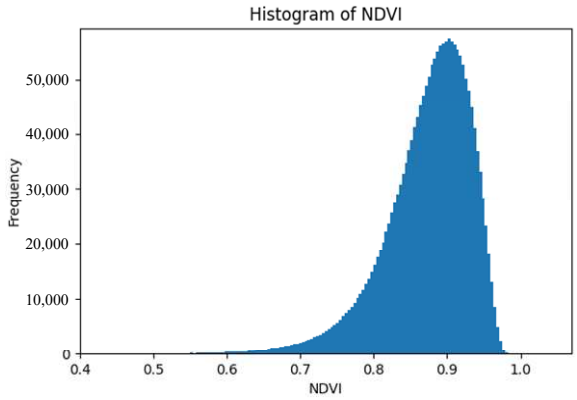

Figure 7. Histogram of rice canopy NDVI (natural field, variety: Xiangya Xiangzhan, growth stage: jointing booting stage).

Normal distribution, also known as Gaussian distribution, is a natural phenomenon, and many events are normally distributed, which is why it is very important in the fields of mathematics, physics, engineering, etc. If the random variable X follows a normal distribution, it can generally be recorded as follows:

$$X \sim N(\mu, \sigma^2) \tag{2}$$

Its probability density function is as follows:

$$f(x) = \frac{1}{\sigma\sqrt{2\pi}} e^{-\frac{(x-\mu)^2}{2\sigma^2}} \tag{3}$$

where μ is the mathematical expectation value (namely mean value), which determines the location of the distribution; σ is the standard deviation, which determines the magnitude of the distribution.

Assuming that there are n points $(x_1, x_2, \cdots, x_n)$ subject to a normal distribution, the mean value μ and standard deviation σ are, respectively:

$$\mu = \sum_{i=1}^{n} x_i / n \tag{4}$$

$$\sigma = \sqrt{\sum_{i=1}^{n} (x_i - \mu)^2 / n} \tag{5}$$

In outlier detection based on normal distribution, points outside the value region $\mu \pm 3\sigma$ can be marked as outliers [33].

As the above normal distribution theory, $\mu - 3\sigma$ can be adaptively used as the segmentation threshold T for abnormal point detection. In other words, points (namely pixels) with an NDVI less than T are judged as abnormal points with poor growth, thereby obtaining a binary image. One of the binary images is shown in Figure 6c.

3. Based on the characteristics of random noise, the median filter is used to filter the above binary images to reduce the noise interference caused by soil, shadows, etc. [34]. One of the results is shown in Figure 6d.
4. Each filtered binary image is traversed with a sliding square window of 1 m^2 and 50% overlap, while the proportion n of abnormal points in the window is counted. The 1 m^2 square window can be calculated with the GSD (namely, the actual physical distance each pixel represents).
5. A preset discrimination threshold, N, is used to discriminate between normal and abnormal windows. If $n > N$, the window is judged as abnormal, while the corresponding area is recorded as an abnormal area with poor growth. Since adjacent abnormal areas are usually caused by the same reason, the neighborhood method is used for deduplication, as shown in Figure 5, to reduce the same adjacent abnormal areas and improve the system efficiency. As a result, only one abnormal area with the largest proportion, n, is retained in the same neighborhood.

2.3. Positioning of the Center Point of the Abnormal Area

In agricultural remote sensing, the current most used positioning method is using photogrammetry technology to reconstruct a two-dimensional (2D) map and then perform positioning (such as DJI Terra) [35]. However, this method requires high along-track and cross-track overlap in the orthophoto scanning mentioned in Section 2.1. The generated large volume of data and the intensive computational requirements for reconstruction require high-performance computers or even computer clusters for processing, which is not only time-consuming but also currently requires human involvement. In addition, the efficiency of data acquisition and map reconstruction in the reconstruction method is insufficient to support high-frequency field inspections of large farms.

In aerial photogrammetry, the collinearity equation is one of the fundamental formulas that describes the mathematical relationship between the object point, image point, and projection center (typically the lens center), stating that they lie on the same line [36]:

$$x - x_o = -f \frac{a_1(X_A - X_s) + b_1(Y_A - Y_s) + c_1(Z_A - Z_s)}{a_3(X_A - X_s) + b_3(Y_A - Y_s) + c_3(Z_A - Z_s)} \tag{6}$$

$$y - y_o = -f \frac{a_2(X_A - X_s) + b_2(Y_A - Y_s) + c_2(Z_A - Z_s)}{a_3(X_A - X_s) + b_3(Y_A - Y_s) + c_3(Z_A - Z_s)} \tag{7}$$

where (x, y) are the image point coordinates in the image plane; x_o, y_o, and f are the internal orientation parameters of the camera; (X_s, Y_s, Z_s) are the object space coordinates of the camera position; (X_A, Y_A, Z_A) are the object space coordinates of the object point; a_i, b_i, and c_i $(i = 1, 2, 3)$ are the nine direction cosines, composed of the three exterior orientation angle parameters ψ, ω, and κ of the image, as shown in Equation (8).

$$R = \begin{bmatrix} \cos\psi & 0 & -\sin\psi \\ 0 & 1 & 0 \\ \sin\psi & 0 & \cos\psi \end{bmatrix} \begin{bmatrix} 1 & 0 & 0 \\ 0 & \cos\omega & -\sin\omega \\ 0 & \sin\omega & \cos\omega \end{bmatrix} \begin{bmatrix} \cos\kappa & -\sin\kappa & 0 \\ \sin\kappa & \cos\kappa & 0 \\ 0 & 0 & 1 \end{bmatrix} = \begin{bmatrix} a_1 & a_2 & a_3 \\ b_1 & b_2 & b_3 \\ c_1 & c_2 & c_3 \end{bmatrix} \quad (8)$$

Among these parameters, x_o, y_o, and f are fixed camera parameters; X_s, Y_s, and Z_s can be measured by GNSS; and ψ, ω, and κ can be measured by IMU. If Z_A (namely, the elevation) is known, the object point (X_A, Y_A) corresponding to the image point (x, y) can be obtained by the collinearity Equations (6) and (7). In other words, single-image positioning can be achieved by combining the digital elevation model (DEM) and the collinearity equation.

In order to reduce data volume and computational requirements and improve the overall efficiency and automation performance of the system, the positioning approach in this paper is to sacrifice part of positioning accuracy for system efficiency. First, the orthophoto scanning mentioned in Section 2.1 is performed with low overlap; secondly, taking advantage of prior knowledge that the rice canopy is approximately flat [37], the position and orientation information recorded in the orthophoto is used to achieve single-image positioning based on the above theory. In this paper, the center point p of the abnormal area is chosen as the positioning point. The reducing overlap schematic diagram and the single-image positioning schematic diagram are shown in Figure 8a,b, respectively. The detailed process of single-image positioning is shown in Figure 9:

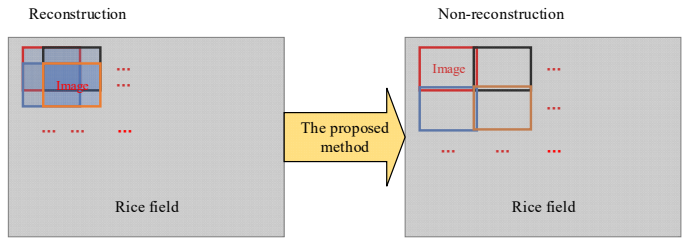

(a) Reducing overlap

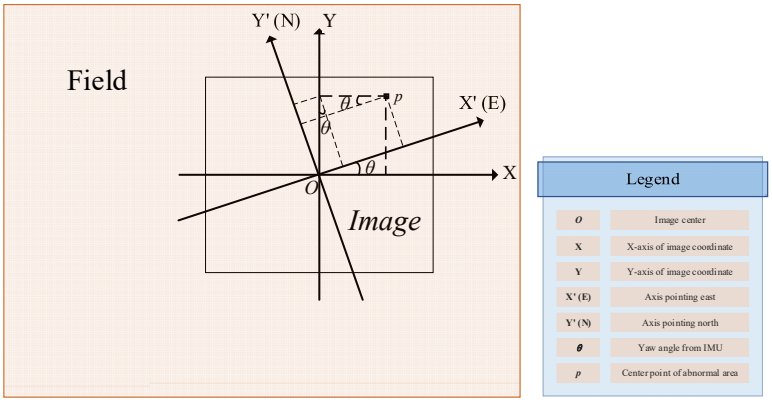

(b) Single-image positioning

Figure 8. Reducing overlap and single-image positioning.

1. As shown in Figure 10, the GSD is calculated as follows using the flight height h and camera parameters:

$$\text{GSD} = \frac{\text{flight height } h \times \text{sensor size}}{\text{focal length} \times \text{image size}} \quad (9)$$

2. Based on the GSD, the coordinates (x, y) of the center point p in the Cartesian coordinate system XOY with the image center point O as the origin are calculated:

$$x = \text{image plane coordinate in } x \text{ direction} \times \text{GSD} \quad (10)$$

$$y = \text{image plane coordinate in } y \text{ direction} \times \text{GSD} \quad (11)$$

3. The coordinates (x', y') of the center point p in the northeast Cartesian coordinate system X′OY′ with the image center point O as the origin are calculated with the yaw angle θ from the orientation information recorded in the image:

$$x' = x\cos\theta + y\sin\theta \tag{12}$$

$$y' = y\cos\theta - x\sin\theta \tag{13}$$

where Y′(N) and X′(E) in Figure 8b point to the true north (N) and true east (E) directions, respectively. In general, the coordinates in the non-northeast coordinate system are mapped to the northeast coordinate system using only the yaw angle θ.

4. From the recorded position information in the image, the latitude and longitude of the image center point O are obtained, and the corresponding projected coordinates (x_o, y_o) can be obtained by applying the Gauss–Krüger projection [38]. Therefore, the projected coordinates of the center point p can be calculated as $(x_o + x', y_o + y')$. Finally, the latitude and longitude of point p can be obtained by performing the inverse Gauss–Krüger projection.

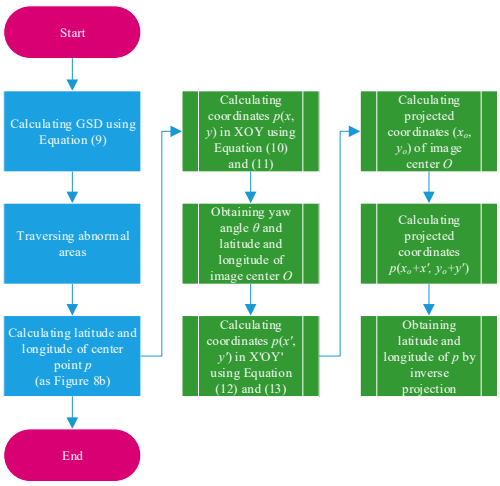

Figure 9. Flow chart of single-image positioning.

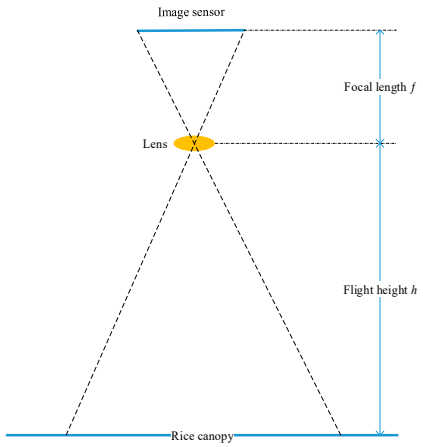

Figure 10. GSD schematic diagram.

2.4. Path Planning

Since there are usually multiple identified and positioned abnormal areas in natural fields, it is necessary to plan a path to efficiently traverse these areas. This is a typical traveling salesman problem (TSP), which belongs to the class of NP-complete problems [39].

There is no perfect algorithm that can solve the optimal path in polynomial time. The mathematical description of TSP is as follows:

$$G(V,\ E) \tag{14}$$

$$V = \{1, 2, \cdots, n\} \tag{15}$$

$$E = \{(i, j)|i, j \in V\} \tag{16}$$

where G is a complete undirected graph composed of n vertices; V is the set of vertices; and E is the set of edges. The objective is to find an optimal vertex arrangement $l = (v_1,\ v_2,\ \cdots,\ v_n,\ v_1)$ that minimizes the following:

$$f(l) = \sum_{k=1}^{n} d_{v_k v_{k+1}} \tag{17}$$

where $d_{v_k v_{k+1}}$ is the edge weight from vertex v_k to vertex v_{k+1}.

In order to reduce computational complexity, this paper adopts a simple nearest-neighbor algorithm to solve the approximate optimal path [40]. Although the nearest-neighbor algorithm is straightforward, it does not guarantee finding the optimal path. The algorithm flow is illustrated in Figure 11. Starting from the initial vertex v_1, at each step, the nearest unvisited vertex is selected as the next destination vertex v_{k+1}, until all vertices have been visited once before finally returning to the initial vertex v_1. Here, the distance (namely the edge weight $d_{v_k v_{k+1}}$) is defined as the Euclidean distance of the Gauss–Krüger projected coordinates, which is calculated as Equation (18).

$$d_{v_k v_{k+1}} = \sqrt{(x_{k+1} - x_k)^2 + (y_{k+1} - y_k)^2} \tag{18}$$

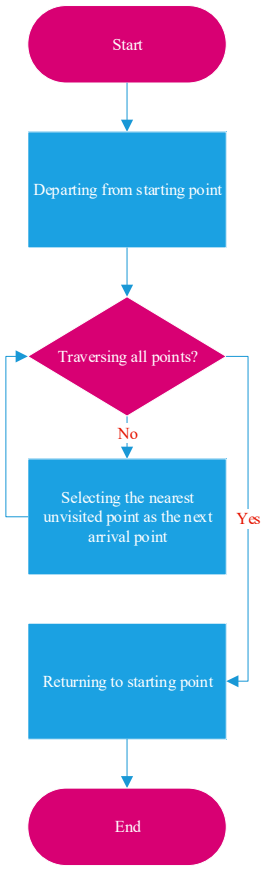

Figure 11. Nearest-neighbor algorithm.

2.5. Close Look with Visible Light UAV

Finally, a UAV equipped with a visible light camera, GNSS, IMU, and gimbal is used to autonomously fly along the planned path and capture HSR images of the abnormal areas at close range, as shown in Figure 12. GNSS is used for navigation and positioning to the center of the abnormal area, while IMU and gimbal control the shooting angle. In order to obtain rich visual features, it is preferable to use a high-definition telephoto camera.

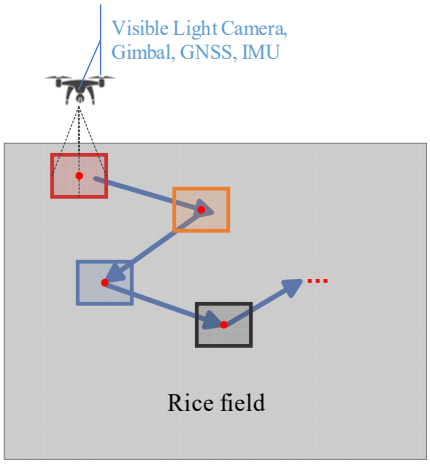

Figure 12. Low-flying waypoint shooting.

3. Results

3.1. Experiments

To verify the feasibility and effectiveness of the proposed method, the entire process was implemented using the Python programming language. Experiments were conducted in the Simiao Rice Modern Agricultural Industrial Park (as shown in Figure 13), Zhucun Street, Zengcheng District, Guangzhou City, Guangdong Province, China, using DJI UAVs P4M and Mavic 3 Thermal (M3T) (as shown in Figure 14 and introduced in Table 2). The rice varieties included 19 Xiang and Xiangya Xiangzhan. In addition, the experiments took place from 1 May to 30 June 2023, between 10:00 a.m. and 04:00 p.m., under clear weather conditions with no wind or a light breeze.

Table 2. Function introduction of P4M and M3T.

UAV	Camera					Gimbal (Ctrl Pitch)	GNSS (RTK) Psn Accuracy		IMU Bias	
	Type	FOV (°)	Focal Len (mm)	Image Resolution	Sensor Size (mm)		Planar	Elevation	ACCL	Gyro
P4M	MS	62.7	5.74	1600 × 1300	4.96 × 3.72	[−90°, +30°]	1.0 cm +1 ppm	1.5 cm +1 ppm	0.002	0.001
M3T	VL	15	30	4000 × 3000	6.4 × 4.8	[−90°, +35°]	1.0 cm +1 ppm	1.5 cm +1 ppm	0.002	0.001

M3T is equipped with 3 cameras (wide-angle camera, telephoto camera, and thermal imaging camera), and the M3T camera introduced in Table 2 refers to the telephoto camera. MS—multispectral; VL—visible light; FOV—field of view; len—length; ctrl—controllable; psn—positioning; and ACCL—accelerometer.

Experimental procedures and parameter settings were as follows:

1. Utilizing the mapping aerial photography function of P4M, the experimental fields were orthographically scanned (camera parameters are introduced in Table 2) at a flight height of 30 m with 10% overlap of both along track and cross track. The gimbal pitch angle was set to −90°, capturing multispectral images at equidistant intervals with a time interval of 2 s.

2. Following the steps outlined in the *P4 Multispectral Image Processing Guide* (https://dl.djicdn.com/downloads/p4-multispectral/20200717/P4_Multispectral_Image_Processing_Guide_EN.pdf, accessed on 1 April 2023), the NDVI was calculated to identify abnormal areas using the proposed method. The size of the median filter was set to 5×5, the discrimination threshold N was set to 2%, and the size of the deduplication neighborhood was set to 9×9 (i.e., only one abnormal area was retained within a range of 2 m).
3. The geographical location of the center point of the identified abnormal area was determined using the single-image positioning method proposed in this paper, followed by path planning using the nearest-neighbor algorithm.
4. Finally, the planned path and photography actions were executed using the waypoint flight function of M3T, with a flight height of 5 m, flight speed of 5 m/s, and a telephoto camera selected (camera parameters are introduced in Table 2).

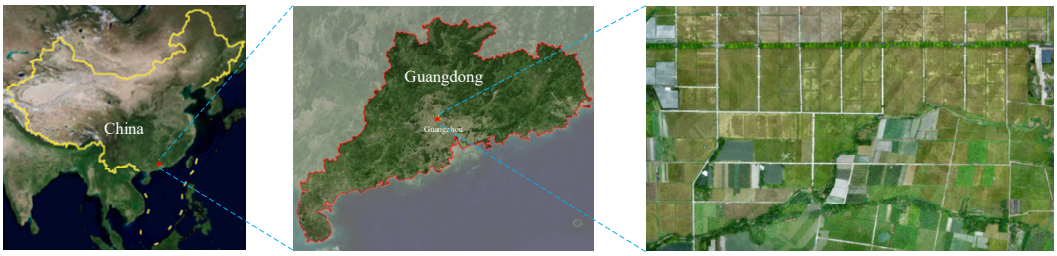

Figure 13. Geographical location of the experimental area.

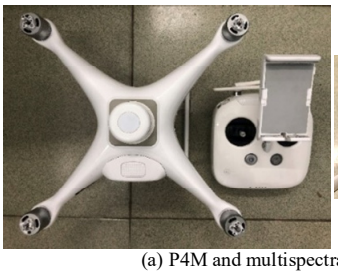

(a) P4M and multispectral camera

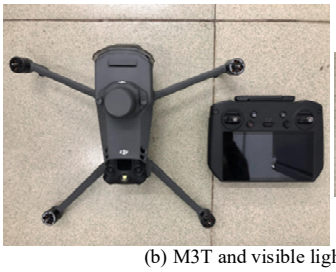

(b) M3T and visible light camera

Figure 14. P4M and M3T.

In addition, to verify the accuracy of single-image positioning, an experiment was conducted at the Huashan District Football Field of South China Agricultural University, Tianhe District, Guangzhou City, Guangdong Province, China, as shown in Figure 15. A self-made 1 m $\times$ 1 m black-and-white positioning board was used as a marker. The latitude and longitude of the center point of the positioning board were measured as the true coordinates using the Huace Zhonghui i70 intelligent RTK receiver (planar accuracy: $\pm(2.5 + 0.5 \times 10^{-6} \times D)$ mm and elevation accuracy: $\pm(5 + 0.5 \times 10^{-6} \times D)$ mm). At a flight height of 30 m, the P4M UAV was moved to position the positioning board in different locations within the images (center, sides, corners, etc.). A total of 30 images were captured, and the proposed single-image positioning method was used to calculate the latitude and longitude of the center point of the positioning board. The results were compared with the true coordinates to calculate the AAE. Furthermore, 10 positioning

boards were placed on the football field, and the center point coordinates were measured as the true coordinates, also using the Huace Zhonghui i70 intelligent RTK receiver. The P4M UAV performed mapping aerial photography three times at a flight height of 30 m (80% along-track overlap, 70% cross-track overlap, and -90° of gimbal pitch angle, capturing images at equidistant intervals with a time interval of 2 s). The DJI Terra software (Version 3.6.0) was used to reconstruct three 2D maps, then 30 center point coordinates of the black-and-white positioning boards were determined on the 2D maps and compared with the true coordinates to calculate the AAE.

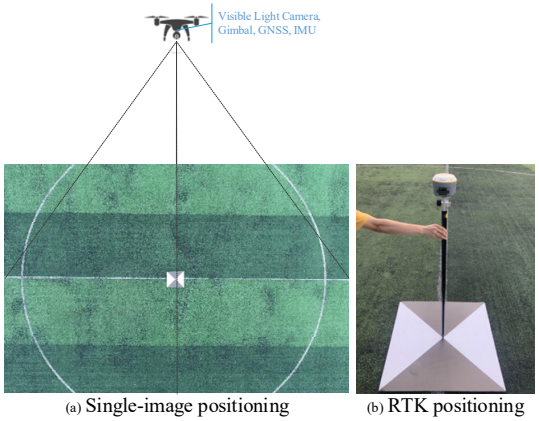

(a) Single-image positioning (b) RTK positioning

Figure 15. Single-image positioning and RTK positioning.

3.2. Experimental Results

Some identification results of abnormal areas are shown in Figure 16.

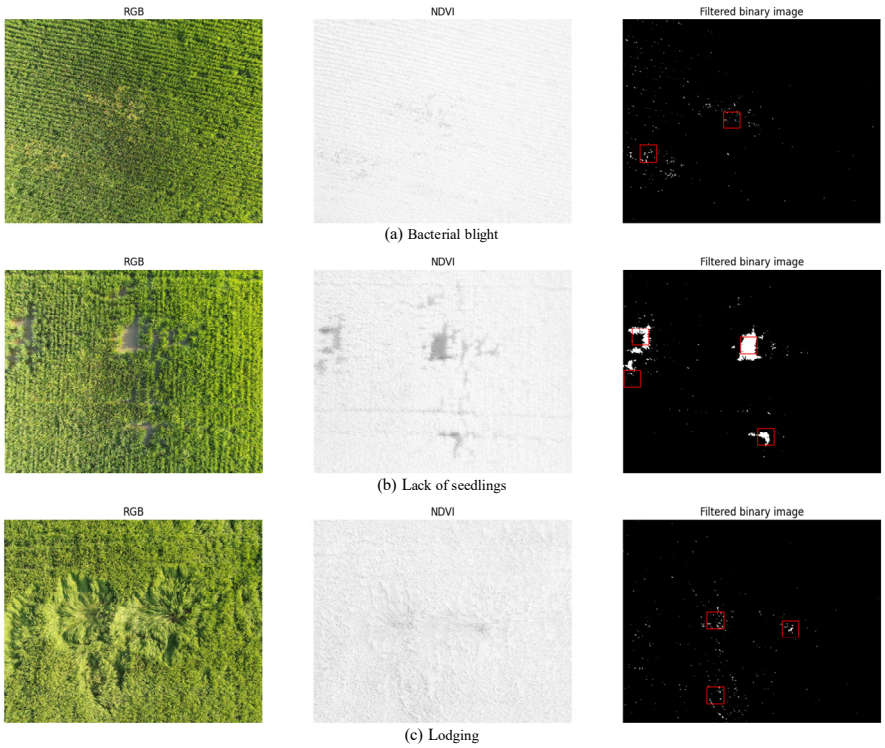

(a) Bacterial blight

(b) Lack of seedlings

(c) Lodging

Figure 16. Identification results of abnormal areas (marked by red box).

The planned path obtained during the experiment conducted in the field shown in Figure 17 is depicted by the red dashed line in the figure. In addition, the blue dots represent the center points of the identified abnormal areas, "Start & End" indicates the takeoff and landing points of the UAV, and the arrows indicate the direction of the path.

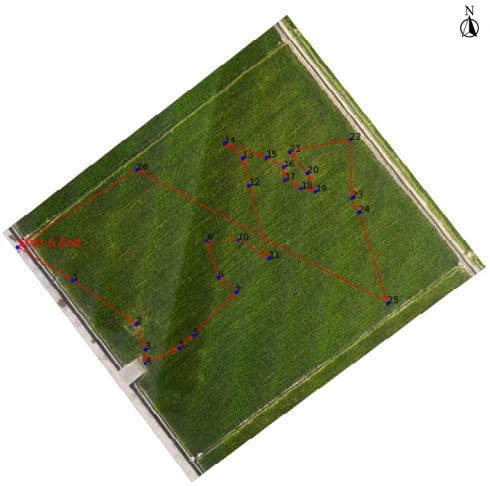

Figure 17. Example of path planning.

Some HSR images of abnormal areas captured by M3T are shown in Figure 18.

(a) Lack of seedlings (b) Lodging (c) Disease

Figure 18. HSR images of abnormal areas.

4. Discussion

The experimental results indicate that the proposed method successfully identifies abnormal areas, including symptomatic diseases and pests, lack of seedlings, lodging, etc. As shown in Figure 16, bacterial blight, lack of seedlings, and lodging are depicted, and only one abnormal area with the largest proportion n is retained within a 2 m range, demonstrating the feasibility and effectiveness of the method. Additionally, by adjusting the discrimination threshold N, the sensitivity of abnormal detection can be controlled. A smaller N value increases sensitivity but may result in misidentification of non-abnormal areas, reducing system efficiency. Conversely, a larger N value decreases sensitivity and may lead to missed detection of early abnormalities. The size of the deduplication neighborhood can be adjusted to retain only one abnormal area with the largest proportion n within a certain range, thereby controlling the number and density of abnormal areas that require low-altitude traversal.

In the approximately flat football field, the AAE of the single-image positioning method proposed in this paper is 13.2 cm, while the AAE of the reconstruction positioning is 4.3 cm. In the application of this paper, the real size of abnormal areas is usually much larger than 13.2 cm, indicating that the positioning accuracy meets the requirements of the application. Generally, the efficiency and accuracy comparison between single-image positioning and reconstruction positioning are shown in Table 3. Although there is a slight loss in positioning accuracy within an acceptable range, the flight efficiency is greatly improved, the number of images is significantly reduced, and the time-consuming process of reconstruction is eliminated, which proves the feasibility and effectiveness of single-image positioning.

Table 3. Efficiency and accuracy comparison between single-image positioning and reconstruction positioning.

UAV	FH and GSD	Captured Area (mu/img)	Method	Overlap		Flight Eff (s/mu)	No. of Imgs (imgs/mu)	Recon Time (s/mu)	AAE of Psn (cm)
				Along Track (%)	Cross Track (%)				
P4M	30 m 1.59 cm/pixel	0.80	Recon	80	70	53.88	20.41	53.84	4.3
			Sgl-img	10	10	4.00	1.44	\	13.2

The reconstruction time is measured in HP ZBook 15 G6 (64.0 GB RAM, Intel(R) Core(TM) i7-9750H CPU @ 2.60 GHz); 1 mu ≈ 666.67 m^2. FH—flight height; Sgl-img—single-image; Recon—reconstruction; eff—efficiency; No.—number; and psn—positioning.

According to Equation (9) and Table 2, GSDs of the Figures 16 and 18 are 1.59 cm/pixel and 0.027 cm/pixel, respectively, which indicates that the spatial resolution is greatly improved when flying at a lower altitude compared to a higher altitude. At the leaf and canopy scale, many studies have shown that it is possible to accurately capture diseases and pests damage characteristics on rice leaves by acquiring HSR images [26]. In addition, the input image size for most used deep-learning classification models is 224 pixels × 224 pixels [15–22], and the width of mature rice leaves typically ranges from 2 cm to 3 cm [41]. If extracting an image patch of 224 pixels × 224 pixels from the HSR images obtained by the proposed method, the rice leaf will occupy approximately 74 to 111 pixels, accounting for about 1/3 to 1/2 of the image patch. Therefore, we can extract image patches from the HSR images without downsampling to perform even leaf-scale deep-learning classification and identify specific types of diseases and pests.

5. Conclusions

In summary, the proposed method in this paper enables autonomous field inspection by UAVs to acquire HSR images of abnormal areas in the rice canopy. The HSR images can provide high-quality data for subsequent automatic identification of field abnormalities such as diseases and pests, thereby offering technical support for the realization of the UAV-based automatic rice field inspection system. The experimental results demonstrate that the proposed method can identify abnormal areas, including diseases and pests, lack of seedlings, lodging, etc. The AAE of single-image positioning is 13.2 cm, which meets the accuracy requirements of the application in this paper. Additionally, the efficiency is greatly improved compared to reconstruction positioning. The GSD of the acquired HSR image can reach 0.027 cm/pixel, or even smaller, which meets the resolution requirements of even leaf-scale deep-learning classification.

The proposed method in this paper can also provide references for the automatic field management of other crops, such as wheat. Additionally, the method for identifying and positioning abnormal areas in this paper can provide targeted objectives for other field operations, such as ground-based crop phenotyping, thereby reducing workload and labor intensity.

In future research work, we will study the automatic identification of diseases and pests based on HSR images captured by UAVs, which will provide further technical support for the realization of the UAV-based automatic rice field inspection system. Additionally, we will explore the feasibility and effectiveness of applying the proposed method to other crops, such as wheat and peanuts.

Author Contributions: Conceptualization, Q.Z., X.L., L.H. and J.H.; methodology, Q.Z., X.L., L.H. and J.H.; software, Q.Z. and C.L.; validation, Q.Z. and C.L.; formal analysis, Q.Z.; investigation, Q.Z.; resources, Q.Z., X.L., L.H., J.H., P.W. and R.Z.; data curation, Q.Z., X.L., L.H., C.L. and J.H.; writing—original draft preparation, Q.Z.; writing—review and editing, Q.Z., X.L., L.H., J.H., P.W. and R.Z.; visualization, Q.Z., L.H., C.L., J.H., P.W. and R.Z.; supervision, X.L., L.H., J.H., P.W. and R.Z.; project administration, X.L. and L.H.; funding acquisition, X.L. and L.H. All authors have read and agreed to the published version of the manuscript.

Funding: This research was funded by the Laboratory of Lingnan Modern Agriculture Project (NT2021009) and the Science and Technology Planning Project of Guangdong Province (2021B1212040009).

Data Availability Statement: The data that support this study will be shared upon reasonable request to the corresponding author.

Acknowledgments: We would like to thank our partners at the Zengcheng Simiao Rice Modern Agricultural Industrial Park and the Zengcheng Teaching Base of South China Agricultural University for their help and support in field management and machine maintenance.

Conflicts of Interest: The authors declare no conflict of interest.

References

1. Brolley, M. Rice security is food security for much of the world. *Rice Today Int. Rice Res. Inst. (IRRI) DAPO Box* **2015**, *7777*, 30–32.
2. Durand-Morat, A.; Nalley, L.L.; Thoma, G. The implications of red rice on food security. *Glob. Food Secur.* **2018**, *18*, 62–75. [CrossRef]
3. Khan, M.I.R.; Palakolanu, S.R.; Chopra, P.; Rajurkar, A.B.; Gupta, R.; Iqbal, N.; Maheshwari, C. Improving drought tolerance in rice: Ensuring food security through multi-dimensional approaches. *Physiol. Plant.* **2021**, *172*, 645–668. [CrossRef] [PubMed]
4. Deng, N.; Grassini, P.; Yang, H.; Huang, J.; Cassman, K.G.; Peng, S. Closing yield gaps for rice self-sufficiency in China. *Nat. Commun.* **2019**, *10*, 1725. [CrossRef] [PubMed]
5. Zhang, H.; Hou, D.P.; Peng, X.L.; Shao, S.M.; Jing, W.J.; Gu, J.F.; Liu, L.J.; Wang, Z.Q.; Liu, Y.Y.; Yang, J.C. Optimizing integrative cultivation management improves grain quality while increasing yield and nitrogen use efficiency in rice. *J. Integr. Agric.* **2019**, *18*, 2716–2731. [CrossRef]
6. Hamza, A.; Riaz, F.; Abid, S.; Raza, U.; Holderbaum, W.; Chowdhry, B.S. A Comprehensive Study of the Role of Self-Driving Vehicles in Agriculture: A Review. In Proceedings of the 2023 7th International Multi-Topic ICT Conference (IMTIC), Jamshoro, Pakistan, 10–12 May 2023; pp. 1–7.
7. Barrile, V.; Simonetti, S.; Citroni, R.; Fotia, A.; Bilotta, G. Experimenting agriculture 4.0 with sensors: A data fusion approach between remote sensing, UAVs and self-driving tractors. *Sensors* **2022**, *22*, 7910. [CrossRef] [PubMed]
8. Mogili, U.M.R.; Deepak, B. Review on application of drone systems in precision agriculture. *Procedia Comput. Sci.* **2018**, *133*, 502–509. [CrossRef]
9. Maes, W.H.; Steppe, K. Perspectives for remote sensing with unmanned aerial vehicles in precision agriculture. *Trends Plant Sci.* **2019**, *24*, 152–164. [CrossRef]
10. Jiang, J.; Wu, Y.; Liu, Q.; Liu, Y.; Cao, Q.; Tian, Y.; Zhu, Y.; Cao, W.; Liu, X. Developing an efficiency and energy-saving nitrogen management strategy for winter wheat based on the UAV multispectral imagery and machine learning algorithm. *Precis. Agric.* **2023**, *24*, 2019–2043. [CrossRef]
11. Yu, F.; Jin, Z.; Guo, S.; Guo, Z.; Zhang, H.; Xu, T.; Chen, C. Research on weed identification method in rice fields based on UAV remote sensing. *Front. Plant Sci.* **2022**, *13*, 1037760. [CrossRef]
12. Wang, Y.P.; Chang, Y.C.; Shen, Y. Estimation of nitrogen status of paddy rice at vegetative phase using unmanned aerial vehicle based multispectral imagery. *Precis. Agric.* **2022**, *23*, 1–17. [CrossRef]
13. Stavrakoudis, D.; Katsantonis, D.; Kadoglidou, K.; Kalaitzidis, A.; Gitas, I.Z. Estimating rice agronomic traits using drone-collected multispectral imagery. *Remote Sens.* **2019**, *11*, 545. [CrossRef]
14. Jha, K.; Doshi, A.; Patel, P.; Shah, M. A comprehensive review on automation in agriculture using artificial intelligence. *Artif. Intell. Agric.* **2019**, *2*, 1–12. [CrossRef]
15. Rahman, C.R.; Arko, P.S.; Ali, M.E.; Khan, M.A.I.; Apon, S.H.; Nowrin, F.; Wasif, A. Identification and recognition of rice diseases and pests using convolutional neural networks. *Biosyst. Eng.* **2020**, *194*, 112–120. [CrossRef]
16. Chen, J.; Zhang, D.; Nanehkaran, Y.A.; Li, D. Detection of rice plant diseases based on deep transfer learning. *J. Sci. Food Agric.* **2020**, *100*, 3246–3256. [CrossRef] [PubMed]
17. Shrivastava, V.K.; Pradhan, M.K.; Thakur, M.P. Application of pre-trained deep convolutional neural networks for rice plant disease classification. In Proceedings of the 2021 International Conference on Artificial Intelligence and Smart Systems (ICAIS), Coimbatore, India, 25–27 March 2021; pp. 1023–1030.
18. Patil, R.R.; Kumar, S. Rice-fusion: A multimodality data fusion framework for rice disease diagnosis. *IEEE Access* **2022**, *10*, 5207–5222. [CrossRef]
19. Anami, B.S.; Malvade, N.N.; Palaiah, S. Deep learning approach for recognition and classification of yield affecting paddy crop stresses using field images. *Artif. Intell. Agric.* **2020**, *4*, 12–20. [CrossRef]
20. Wang, C.; Ye, Y.; Tian, Y.; Yu, Z. Classification of nutrient deficiency in rice based on CNN model with Reinforcement Learning augmentation. In Proceedings of the 2021 International Symposium on Artificial Intelligence and its Application on Media (ISAIAM), Xi'an, China, 21–23 May 2021; pp. 107–111.
21. Dey, B.; Haque, M.M.U.; Khatun, R.; Ahmed, R. Comparative performance of four CNN-based deep learning variants in detecting Hispa pest, two fungal diseases, and NPK deficiency symptoms of rice (*Oryza sativa*). *Comput. Electron. Agric.* **2022**, *202*, 107340. [CrossRef]

22. Hu, P. A Rice Pest Identification Method Based on a Convolutional Neural Network and Migration Learning. *J. Circuits Syst. Comput.* **2023**, *32*, 2350089. [CrossRef]
23. Su, J.; Liu, C.; Coombes, M.; Hu, X.; Wang, C.; Xu, X.; Li, Q.; Guo, L.; Chen, W.H. Wheat yellow rust monitoring by learning from multispectral UAV aerial imagery. *Comput. Electron. Agric.* **2018**, *155*, 157–166. [CrossRef]
24. Devia, C.A.; Rojas, J.P.; Petro, E.; Martinez, C.; Mondragon, I.F.; Patiño, D.; Rebolledo, M.C.; Colorado, J. High-throughput biomass estimation in rice crops using UAV multispectral imagery. *J. Intell. Robot. Syst.* **2019**, *96*, 573–589. [CrossRef]
25. Kim, H.; Kim, W.; Kim, S.D. Damage assessment of Rice crop after toluene exposure based on the vegetation index (VI) and UAV multispectral imagery. *Remote Sens.* **2020**, *13*, 25. [CrossRef]
26. Zheng, Q.; Huang, W.; Xia, Q.; Dong, Y.; Ye, H.; Jiang, H.; Chen, S.; Huang, S. Remote Sensing Monitoring of Rice Diseases and Pests from Different Data Sources: A Review. *Agronomy* **2023**, *13*, 1851.
27. Bewke, G.B. Review on integrated pest management of important disease and insect pest of rice (*Oryzae sativa* L.). *World Sci. News* **2018**, *100*, 184–196.
28. Zhang, K.; Ge, X.; Shen, P.; Li, W.; Liu, X.; Cao, Q.; Zhu, Y.; Cao, W.; Tian, Y. Predicting rice grain yield based on dynamic changes in vegetation indexes during early to mid-growth stages. *Remote Sens.* **2019**, *11*, 387. [CrossRef]
29. Goswami, S.; Gamon, J.; Vargas, S.; Tweedie, C. Relationships of NDVI, Biomass, and Leaf Area Index (LAI) for six key plant species in Barrow, Alaska. *PeerJ PrePrints* **2015**, *3*, e913v1. [CrossRef]
30. Nie, L.; Peng, S. Rice production in China. In *Rice Production Worldwide*; Springer: Cham, Switzerland, 2017; pp. 32–52. [CrossRef]
31. Zhang, Z.; Zhu, L. A Review on Unmanned Aerial Vehicle Remote Sensing: Platforms, Sensors, Data Processing Methods, and Applications. *Drones* **2023**, *7*, 398.
32. Rouse, J.W., Jr.; Haas, R.H.; Deering, D.W.; Schell, J.A.; Harlan, J.C. *Monitoring the Vernal Advancement and Retrogradation (Green Wave Effect) of Natural Vegetation*; No. E75-10354; NASA CR: Clear Lake, TX, USA, 1974.
33. Han, J.; Kamber, M.; Pei, J. Outlier detection. Data mining: Concepts and techniques. In Proceedings of the 2013 International Conference on Machine Intelligence and Research Advancement, Katra, India, 21–23 December 2013; pp. 543–584.
34. Hwang, H.; Haddad, R.A. Adaptive median filters: New algorithms and results. *IEEE Trans. Image Process.* **1995**, *4*, 499–502. [CrossRef]
35. Rueda-Ayala, V.P.; Peña, J.M.; Höglind, M.; Bengochea-Guevara, J.M.; Andújar, D. Comparing UAV-based technologies and RGB-D reconstruction methods for plant height and biomass monitoring on grass ley. *Sensors* **2019**, *19*, 535. [CrossRef]
36. Wolf, P.R.; Dewitt, B.A.; Wilkinson, B.E. *Elements of Photogrammetry: With Applications in GIS*; McGraw-Hill: New York, NY, USA, 2000.
37. Katul, G.G.; Leuning, R.; Kim, J.; Denmead, O.T.; Miyata, A.; Harazono, Y. Estimating CO_2 source/sink distributions within a rice canopy using higher-order closure model. *Bound.-Layer Meteorol.* **2001**, *98*, 103–125. [CrossRef]
38. Deakin, R.E.; Hunter, M.N.; Karney, C.F.F. The gauss-krüger projection. In Proceedings of the 23rd Victorian Regional Survey Conference, Warrnambool, VIC, Australia, 10–12 September 2010; pp. 1–20.
39. Hoffman, K.L.; Padberg, M.; Rinaldi, G. Traveling salesman problem. *Encycl. Oper. Res. Manag. Sci.* **2013**, *1*, 1573–1578.
40. Abdulkarim, H.A.; Alshammari, I.F. Comparison of algorithms for solving traveling salesman problem. *Int. J. Eng. Adv. Technol.* **2015**, *4*, 76–79.
41. Wangpan, T.; Taka, T.; Tangjang, S. On-farm Diversity of Indigenous Rice (*Oryza Sativa* L.) Landraces in Border of Eastern Himalaya. *Pertanika J. Trop. Agric. Sci.* **2018**, *41*, 393–410.

美国《工程索引》(Ei) 收录期刊
Scopus数据库收录期刊
中文核心期刊 中国科技核心期刊
中国科学引文数据库来源期刊

ISSN 1000-1298
CODEN NUYCA3

农业机械学报

Transactions of the Chinese Society for Agricultural Machinery

专栏主题: 无人化智慧农场
专栏主编: 罗锡文 院士 胡炼 研究员

中国农业机械学会
中国农业机械化科学研究院集团有限公司 主办

2025年
第 56 卷
2

农业机械学报
NONGYE JIXIE XUEBAO

2025 年　第 2 期(第 56 卷)

目　次

农业装备与机械化工程

农业信息化工程

农业水土工程

农业生物环境与能源工程

农产品加工工程

车辆与动力工程

机械设计制造及其自动化

Transactions of the Chinese Society
for Agricultural Machinery
Vol. 56 No. 2 2025

Contents

Agricultural Equipment and Mechanization Engineering

Agricultural Informatization Engineering

Agricultural Soil and Water Engineering

Agricultural Bio-environment and Energy Engineering

Agricultural Products Processing

Vehicle and Power Engineering

Mechanical Design & Manufacturing and Automation

doi:10.6041/j.issn.1000-1298.2025.02.024

支撑式水田平地机结构设计与试验

陈高隆[1]　胡　炼[1,2]　汪　沛[1,2]　赵润茂[1,2]　冯达文[1]　田　力[1]
黄志铖[1]　陈禹琦[1]　王靖霆[1]
(1.华南农业大学工程学院,广州 510642;2.农业装备技术全国重点实验室,广州 510642)

摘要:水田平整是水稻生产不可或缺的环节。为了改善水田平地机对坑洼硬底层的适应性,进一步提高作业性能,设计了支撑式水田平地机。根据平地铲工作原理,对平地铲高度调节机构进行运动学分析;在此基础上,设计了平地铲及其高度调节机构。设计了支撑杆结构,研究了支撑杆对平地铲运动特性的影响。开展了有/无支撑杆对比试验和水田平整试验。对比试验结果表明,有支撑杆的平地铲在试验全程高度变化幅度减少 15% 以上,在田面凸起位置高度变化幅度减少 30% 以上,同时,平地铲高度变化次数减少。表明有支撑杆平地铲更有利于平地铲高度控制,更适用于坑洼硬底层作业。0.21 hm^2 的水田平整试验结果表明,平整后田面高度标准差 S_d 为 21.66 mm,田面高度相对平整基准高度绝对偏差不大于 30 mm 的测量点占比 ρ 为 86.54%;总面积为 1.89 hm^2 的 2 块水田平整试验结果表明,平整后 S_d 分别为 26.02 mm 和 27.43 mm,ρ 分别为 80.53% 和 81.03%。全部试验田块经平整后的 S_d 均小于 30 mm,且 ρ 均高于 80%,达到了水田平整要求,验证了支撑式水田平地机结构设计有效性,可为坑洼硬底层水田机械化平整提供装备支撑。

关键词:水田平整;平地机;支撑杆;农田地形
中图分类号:S222.5+1　　**文献标识码**:A　　**文章编号**:1000-1298(2025)02-0252-09　　**OSID**:

Structural Design and Test of Supported Paddy-field Leveling Machine

CHEN Gaolong[1]　HU Lian[1,2]　WANG Pei[1,2]　ZHAO Runmao[1,2]　FENG Dawen[1]
TIAN Li[1]　HUANG Zhicheng[1]　CHEN Yuqi[1]　WANG Jingting[1]
(1. *College of Engineering, South China Agricultural University, Guangzhou* 510642, *China*
2. *State Key Laboratory of Agricultural Equipment Technology, Guangzhou* 510642, *China*)

Abstract: The leveling of paddy fields is an indispensable part of rice production. Aiming to improve the adaptability of existing leveling machines to the bumpy hard bottom layer of paddy fields and further enhance the operational performance, the supported paddy-field leveling implement was developed. Firstly, according to the working principle of the leveling shovel, the height adjustment mechanism of the leveling shovel was kinematically analyzed. On this basis, the leveling shovel and its height adjustment mechanism were designed. Secondly, the supported rod structure was designed, and the influence of the supported rods on the motion characteristics of the leveling shovel was studied. Finally, a comparison test with/without supported rods and a paddy-field leveling test were carried out. The results of the comparison test showed that the amplitude of height change of the leveling shovel with the supported rods was reduced by more than 15% throughout the test, and reduced by more than 30% in the convex position of the field surface. Meanwhile, the number of height changes of the leveling shovel was reduced. It showed that the leveling shovel with supported rods was more conducive to the height control of leveling shovels and was more suitable for the operation of bumpy hard bottom layer of paddy fields. The leveling test results for 0.21 hm^2 of paddy field showed that the standard deviation (S_d) of the topography height was 21.66 mm, and the proportion (ρ) of points ($|h_i - \bar{h}| \leqslant 30$ mm, where h_i indicated the height of each measuring point, and $\bar{h}$ indicated the average height of all measuring points.)

收稿日期:2024-10-09　修回日期:2024-11-11
基金项目:新一代人工智能国家科技重大专项(2021ZD0110902)和国家自然科学基金项目(32071913、32101623)
作者简介:陈高隆(1995—),男,博士生,主要从事精准作业研究,E-mail:dbalong@163.com
通信作者:赵润茂(1990—),男,副教授,主要从事农业机器人研究,E-mail:rmzhao@scau.edu.cn

was 86.54%. The test results for two paddy fields with a total area of 1.89 hm^2 showed that the standard deviations S_d for the two fields were 26.02 mm and 27.43 mm, and the proportions ρ were 80.53% and 81.03%, respectively. After leveling, the standard deviation S_d in all test fields was less than 30 mm, and the proportion ρ was higher than 80%, which met the requirements of paddy-field leveling, and verified the structural advantages and design validity of the supported paddy-field leveling machine. This can provide equipment support for mechanized leveling of paddy fields with bumpy hard bottom layer.

Key words: paddy-field leveling; leveling machine; supported rods; field topography

0　引言

在全球范围内,水田占耕地总面积的9%[1],在粮食生产方面发挥着至关重要作用[2],特别是在东亚、东南亚和南亚以及非洲部分地区[3]。水稻是三大粮食作物之一,全球大部分水稻(75%)在水田环境下种植[4]。水稻生产灌溉方式以漫灌和淹灌为主,不平整农田会导致水资源利用率低[5]。通过改善农田平整度不仅可以节约水稻生产用水,提高灌溉效率与灌水均匀度[6-9],还可以提高土地利用率、稻种发芽率、杂草防治效率、作物成熟均匀度和作物产量,以及减少肥药施用量[10-15]。综上所述,水田平整是水稻生产必不可少的环节。由于水田旱平机械受土质、土壤含水率与降雨季节应用限制,因此,水田平整机械更有利于在多季稻地区争抢农时。

目前,诸多研究者研制了水田平整机械。LUO等[16]研制了以乘坐式水稻插秧机为配套动力的水田激光平地机,但其更适用于小面积农田,如华南地区。碎片化和不平整农田会阻碍机械化生产与降低农业生产效率[17]。诸多国家已开展农田改造措施,如“小农大田”和“高标准农田建设”[18-22]。单块农田面积呈增大趋势,这促使以拖拉机为配套动力的平整机械成为主流。严乙桉等[23]根据拖拉机后桥结构,设计了挂接支座以连接平整机具与拖拉机,但挂接支座无法兼容不同型号拖拉机。胡炼等[24]研制了1PJ-4.0型水田激光平地机,提高了平整机具与不同型号拖拉机连接的通用性,但平整机具控制响应迟滞且调节速度低。基于此,HU等[25]进一步研制了激光控制旋刮式水田平地机,提高了平整机具控制的动态响应性能。上述平整机具机架与拖拉机三点悬挂固连,形成一个刚体,机具机架自由度与拖拉机一致,平地铲高度调节通过额外增加的独立自由度实现。当以拖拉机前轮为转动点,后轮行驶至凸起地形时,平地铲高度变化幅度大于凸起地形高度。若平地铲高度无法及时调节,会导致出现挖坑和堆土现象。拖拉机与平地铲之间距离越大,这种现象更为明显。

现有水田平整机具与拖拉机三点悬挂装置固接。当拖拉机行驶于坑洼硬底层下,平地铲高度变化幅度增大,这增加了平整控制系统作业难度。为了解决现有水田平地机对坑洼硬底层适应性差的问题,本文设计支撑式水田平地机关键部件结构,研究支撑杆对平地铲高度变化的影响,并开展有/无支撑杆对比性能和水田平整试验,以验证平地机作业效果。

1　整机结构与工作原理

1.1　整机结构

支撑式水田平地机整机结构如图1所示,主要由机架、支撑杆、平地铲和高度调节机构等组成。机架包括前梁、后梁和后梁臂等结构。高度调节机构由平行连杆和液压油缸等组成,其分别与平地铲和机架连接。液压油缸伸缩动作可实现平地铲高度调节。支撑杆安装在机架前梁上,且安装间距根据配套拖拉机后轮轮距进行调节,以保证支撑杆沿后轮轮辙路径移动。

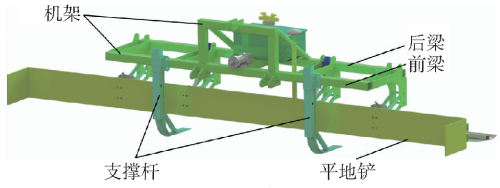

(a) 整机视图

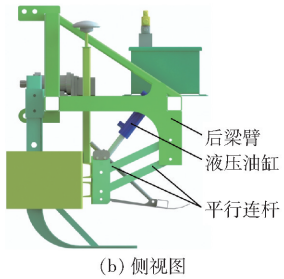

(b) 侧视图

图1　支撑式水田平地机

Fig. 1　Supported paddy-field leveling machine

1.2　工作原理

如图2a所示,支撑式水田平整机具与拖拉机三点悬挂转动连接。机具机架高度不受拖拉机高度变化影响。为实现平地铲高度自动控制,根据旱田平整机械地轮的支撑仿形原理[26],提出了支撑式水田平地机设计方案。如图2所示,机具因自重下降使支撑杆支撑于水田硬底层。平整作业前,根据水田地形高度信息计算平整基准高度。平整作业中,支

撑杆在坑洼不平的硬底层移动,使平地铲高度在作业中偏离平整基准高度[27]。当农田田面和平整基准高度一致时(图 2a),平地铲不挖泥且不卸泥;当农田田面高于平整基准高度时(图 2c),平地铲铲运高于平整基准高度的泥浆;当农田田面低于基准高度时(图 2b),平地铲卸泥填坑。支撑式水田平地机对农田田面进行“挖高填低”作业,以提高水田田面平整度。

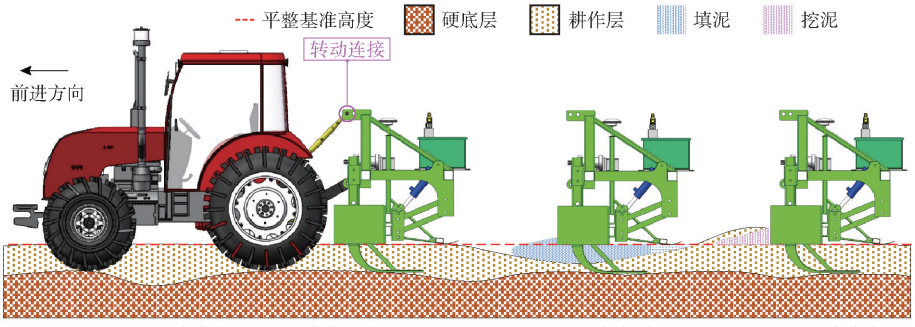

(a) 地形高度与平整基准高度一致 (b) 地形高度低于平整基准高度 (c) 地形高度高于平整基准高度

图 2 水田平地机工作原理

Fig. 2 Working principle of paddy-field leveling machine

2 关键部件设计与运动学建模

2.1 平地铲

根据平地铲结构和作业参数,设计平行连杆尺寸和安装位置。通过建立平地铲运动学模型,对液压油缸选型并设计其安装位置。如图 3 所示,平地铲结构参数包括高度(h_S)与宽度(b_S),设定 h_S 为 0.3 m 与 b_S 为 5 m。如图 4 所示,平地铲工作参数包括调节行程(h_A)和极限位置(最高位 $ABC'D'$ 和最低位 $ABC''D''$)。由于支撑杆在硬底层上移动,调节行程主要由硬底层地形高度决定。参照文献[28]获取华南农业大学教学科研基地水田(3.33 hm^2)硬底层地形高度数据。结果表明水田硬底层地形高度变化幅值约为 0.3 m,则设定该值为平地铲调节行程。平地铲极限位置主要由干涉情况和水田耕作层深度共同决定。平地铲最高位设置需确保平地铲不与机架干涉,设定平地铲处于最高位时与机架底部保留一定距离(h_{UI}),设定 h_{UI} 为 0.02 m。平地铲最低位设置需确保平地铲不与支撑杆干涉,且满足水田浅耕作层区域的作业需求。当平地铲处于最低位时,设定平地铲与支撑杆保留一定距离(h_{BI})。由于单次旋耕作业深度为 0.15 ~ 0.18 m[29],设定 h_{BI} 为 0.1 m。

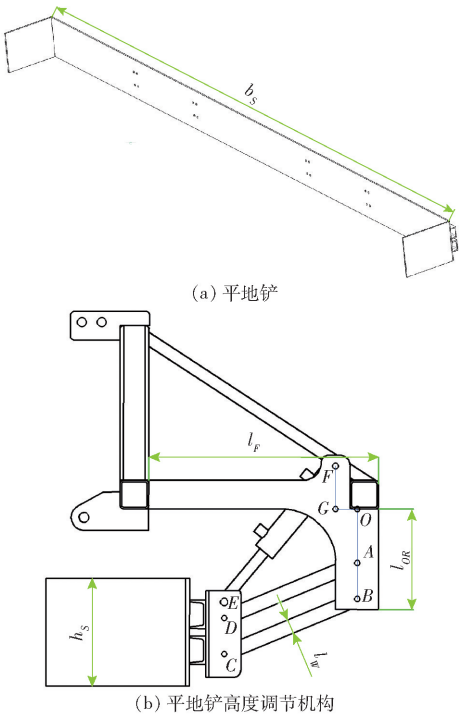

(a) 平地铲

(b) 平地铲高度调节机构

图 3 平地铲及其高度调节机构

Fig. 3 Leveling shovel and its height adjustment mechanism

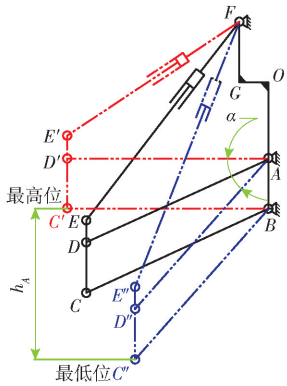

图 4 平地铲高度调节原理

Fig. 4 Adjustment principle of leveling shovel height

平地铲结构和工作参数决定平行连杆尺寸和安装位置。图 3b 和图 4 为高度调节机构示意图和平地铲调节原理图。点 O 为机架后梁的底端点。点 A、B、C 和点 D 为平行连杆的转动点,且点 C'、点 C'' 和点 D'、点 D''分别为点 C 和点 D 的不同位置。点 F 和点 E 分别为液压油缸上连接点和下连接点,且点 E'为点 E 不同位置。

为保证机架后梁臂不破坏平整后的田面,后梁

臂长度 l_{OR}需满足

$$\begin{cases} l_{OR} \leqslant h_S + h_{UI} \\ l_{OR} \geqslant l_{OB} \end{cases} \tag{1}$$

式中　l_{OB}——后梁底端与连接点 B 的距离，m

为保证高度调节机构满足作业需求，设定平地铲处于最高位时 AD'垂直于 OB，则平行连杆需满足

$$\begin{cases} l_{AD} \leqslant l_F \\ h_A = l_{AD}\sin\alpha \\ l_W > l_{AB}\cos\alpha \end{cases} \tag{2}$$

式中　l_{AD}——点 A 和点 D 间距离，m

l_F——机架前梁和后梁距离，m

α——平地铲从最高位运动至最低位时连杆 AD 转角，(°)

l_W——连杆 AD 宽度，m

l_{AB}——点 A 和点 B 距离，m

通过建立平地铲运动学模型，对液压油缸选型并设计其安装位置。如图 5 所示，以机架后梁底端点 O 为原点建立平面坐标系。

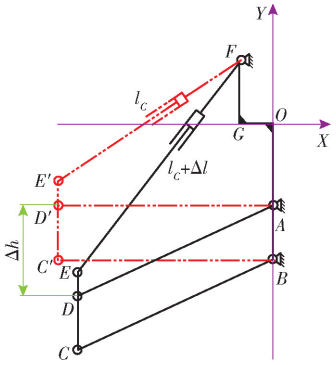

图 5　平面坐标系

Fig. 5　Plane coordinate system

以点 F 为圆心与油缸长度为半径，建立油缸下连接点 $E(x_1, y_1)$运动轨迹为

$$(x_1 + l_{OG})^2 + (y_1 - l_{GF})^2 = (l_C + \Delta l)^2 \tag{3}$$

式中　l_{OG}——油缸上连接点 F 距离机架后梁底端点 O 横向距离，m

l_{GF}——油缸上连接点 F 距离机架后梁底端点 O 纵向距离，m

l_C——油缸初始长度，m

Δl——油缸伸长量，m

以点 A 为圆心与 l_{AD}为半径，建立点 $D(x_2, y_2)$运动轨迹为

$$x_2^2 + (y_2 + l_{OA})^2 = l_{AD}^2 \tag{4}$$

式中　l_{OA}——原点 O 与点 A 间距离，m

点 E 与点 D 相对位置关系为

$$\begin{cases} x_1 = x_2 \\ y_1 - y_2 = l_{DE} \end{cases} \tag{5}$$

式中　l_{DE}——连接点 E 与点 D 的距离，m

连接点 $D(x_2, y_2)$和平地铲调节高度 Δh 的关系为

$$-y_2 = l_{OA} + \Delta h \tag{6}$$

结合式(3)～(6)得到平地铲运动学模型，即油缸伸缩量 Δl 与平地铲调节高度 Δh 的关系为

$$l_{AD}^2 - \Delta h^2 - 2l_{OG}\sqrt{l_{AD}^2 - \Delta h^2} + l_{OG}^2 + (l_{DE} - l_{OA} - l_{GF} - \Delta h)^2 = (l_C + \Delta l)^2 \tag{7}$$

根据式(7)可对液压油缸选型并设计其安装位置。

2.2　支撑杆仿形性能分析

如图 6 所示，水田平整机具以拖拉机前轮为转动点，后轮行驶至凸起地形时，平地铲高度变化幅度 h_C 大于凸起地形高度 h_T。若平地铲高度无法及时调节，会导致出现挖坑和堆土现象。拖拉机与平地铲之间距离越大，这种现象更为明显，如图 7 中，$l_2 > l_3 > l_1$。

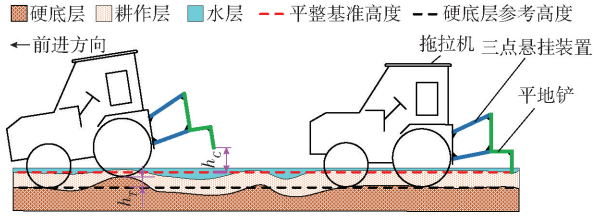

图 6　平地铲高度变化幅度

Fig. 6　Amplitude of height change of leveling shovel

如图 8 所示，本文设计的支撑杆支撑平整机具沿着硬底层地形运动。平地铲高度变化幅度主要受硬底层地形影响。因此，当支撑杆和平地铲的相对高度保持不变时，平地铲高度轨迹(h_P)与硬底层地形高度具有一致性。

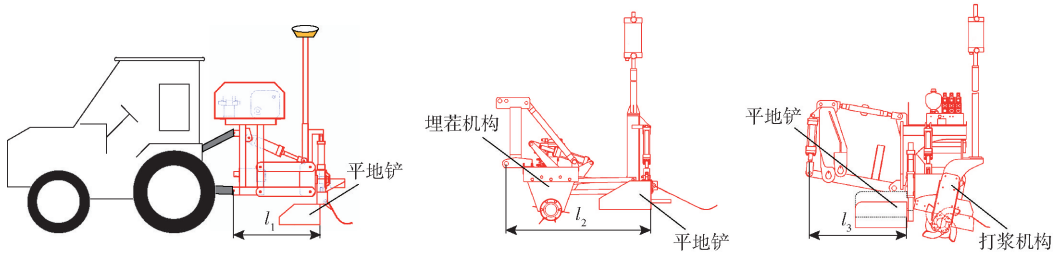

(a) 文献[25]平地机　(b) 文献[30]埋茬平地机　(c) 文献[31]平地打浆机

图 7　水田平地机

Fig. 7　Paddy-field leveling machines

以机架底端为起算点，支撑杆长度 h_R 需满足

$$h_R = h_{UI} + h_S + h_A + h_{BI} \tag{8}$$

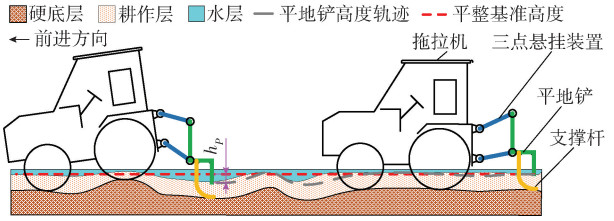

图 8 支撑杆仿形性能

Fig. 8 Profiling performance of supported rods

3 有/无支撑杆对比试验

3.1 材料与方法

如图 9 所示，于 2022 年 10 月在华南农业大学教学科研基地开展试验。为验证支撑杆具有减少平地铲高度变化幅度与次数的优势，设计了有支撑杆和无支撑杆对比试验。为保证有/无支撑杆对比试验行驶路径一致，选取局部存在凸起地形的旱田，先开展有支撑杆试验使支撑杆在旱田中生成移动轨迹，再沿此轨迹开展无支撑杆试验。在试验中，平地铲姿态仅受农田地形起伏影响，且不与田面接触，保证平地铲不搬运土方且不消除支撑杆移动轨迹。水田硬底层是由于长期水分管理、耕作和土壤压实而形成具有较大承载能力的紧实土层，其平整度差，呈不规则坑洼状，坑洼大小不一，深浅不等。所选旱田经历了水稻收获作业、多次干湿循环和农机碾压后，已发生土壤固结现象，仅表层因拖拉机胎花作用而形成浅薄松土，以保证拖拉机多次行驶的试验地形相同。因此，旱田局部凸起地形与硬质特征同水田硬底层一致，可保证试验结果有效性。以雷沃欧豹 M804 型拖拉机为配套动力悬挂平整机具，平整机具主要技术参数如表 1 所示。此外，按照拖拉机后轮轮距安装支撑杆，保证支撑杆沿着后轮轮辙移动。全球导航卫星系统（Global navigation satellite system，GNSS）接收器安装于平地铲上方，将显控终端作为数据采集平台且以频率 10 Hz 采集平地铲高度信息。对比试验分别以速度 0.8、1.0、1.2 m/s 开

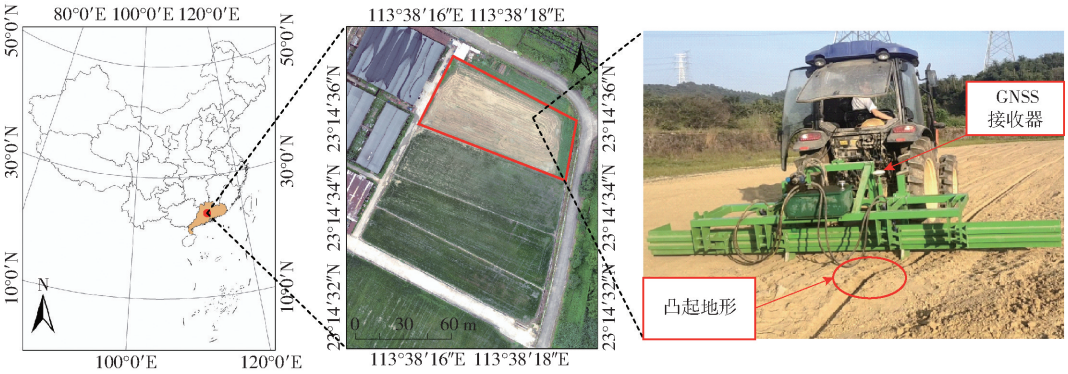

图 9 有/无支撑杆对比试验的试验地点

Fig. 9 Test site for comparison test with/without support rods

表 1 平整机具主要技术参数

Tab. 1 Main technical parameters of leveling implement

参数	数值
整机尺寸（长×宽×高）/（mm×mm×mm）	5 000×1 050×1 300
机具质量/kg	600
平地铲幅宽/m	5
平地铲高度/m	0.3
平地铲质量/kg	217
土壤切削角/(°)	90
铲调节幅度/m	0.3

3.2 结果与分析

由显控终端采集的平地铲高度经 Matlab R2023a 处理结果如图 10 所示。

由图 10 可知，有支撑杆和无支撑杆平地铲高度曲线变化趋势具有一致性，二者主要差异在于曲线峰值（区域 A）。无支撑杆曲线峰值明显高于有支撑杆，这是由于拖拉机经过凸起地形使拖拉机俯仰角变化造成的。表 2 为两组在 3 种速度下高度峰值。

由表 2 可知，有/无支撑杆对比试验的行驶路径一致条件下，3 种速度下曲线峰值差分别为 82.59、55.79、47.59 mm。相比于无支撑杆，有支撑杆平地铲在 3 种速度下高度变化幅度分别减少 52.45%、37.45% 和 31.98%。

为了分析平地铲在试验全程的高度变化，进一步对高度分布进行统计，如图 11 所示。与有支撑杆平地铲相比，无支撑杆高度分布中离群点明显较多。在 3 种速度下，有支撑杆平地铲高度变化标准差（σ）比无支撑杆分别减少 15.09%、17.82% 和 31.75%，表明在试验全程有支撑杆平地铲高度变化幅度小。

除了曲线峰值，两条曲线差异还表现在曲线极点数量（区域 B）。放大图 10 区域 B 位置曲线，如图 12 所示。

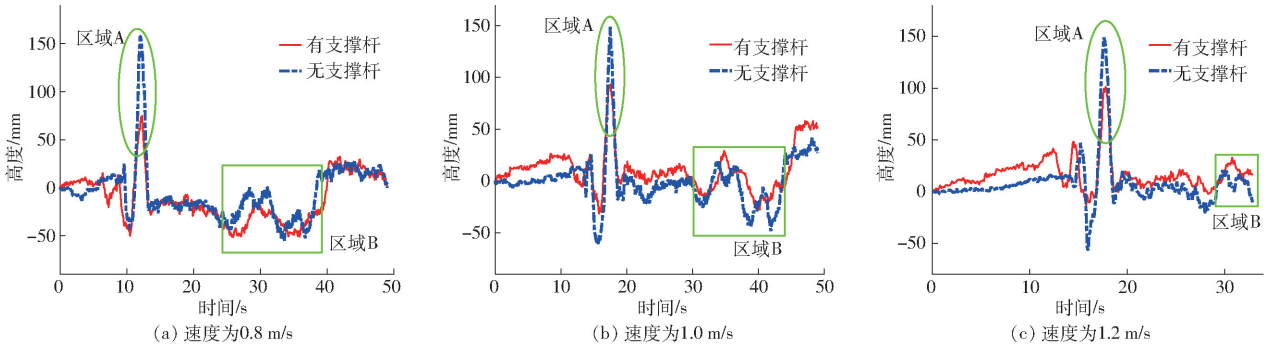

(a) 速度为0.8 m/s　(b) 速度为1.0 m/s　(c) 速度为1.2 m/s

图 10　平地铲高度变化曲线

Fig. 10　Leveling shovel height change curves

表 2　3 种速度下平地铲高度变化峰值

Tab. 2　Peaks of leveling shovel height change at three travelling speeds

速度/(m·s^{-1})	高度峰值/mm	
	有支撑杆	无支撑杆
0.8	74.86	157.45
1.0	93.19	148.98
1.2	101.23	148.82

不考虑测量噪声情况下，无支撑杆平地铲高度变化曲线极值点比有支撑杆多。当有支撑杆平地铲高度呈“∧”形变化时，无支撑杆平地铲高度呈“M”形变化；当有支撑杆平地铲高度呈“∨”形变化时，无支撑杆平地铲高度呈“W”形变化。这是由于拖拉机前后轮依次经过凸起或凹陷地形时，其俯仰角出现正负值交替，导致无支撑杆平地铲高度变化曲线呈“W”和“M”形波动。此外，当“∧”和“∨”形峰值和谷值越大，无支撑杆平地铲高度“W”和“M”曲线的中间极值点越大。因此，在平整作业中，有支撑杆平地铲高度变化次数减少。

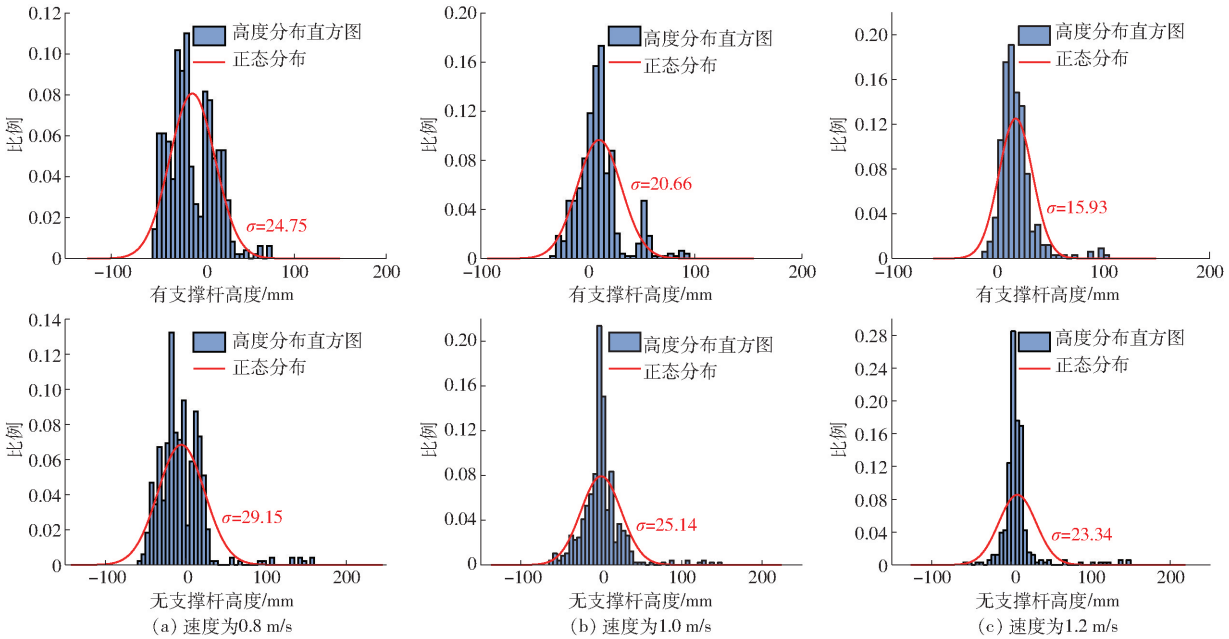

(a) 速度为0.8 m/s　(b) 速度为1.0 m/s　(c) 速度为1.2 m/s

图 11　平地铲高度分布

Fig. 11　Height distribution of leveling shovels

上述试验结果表明，在坑洼硬底层地形下，支撑式水田平地机可减少平地铲高度变化幅度和次数。通过减少平地铲高度变化幅度，可减少执行元件伸缩量与伸缩至极限状态的次数。通过减少平地铲高度变化次数，可减少执行元件伸缩频次，降低液压系统工作负荷，提高平地机作业性能。因此，支撑式水田平地机更适用于坑洼硬底层作业。此外，通过降低执行元件伸缩量和伸缩频次，可减少控制时间和频次，有效提高高速精准平整作业可靠性。

4　水田平整试验

4.1　材料与方法

平整机具主要技术参数如表 1 所示。如图 13 所示，农田平整控制系统主要由 GNSS 接收器和显控终端组成。平整作业前，通过显控终端来设定平整基准高度。平整作业中，GNSS 接收器检测平地铲实时高度信息并传输至显控终端，显控终端处理高度信息并下发控制信号至液压系统来驱动执行元

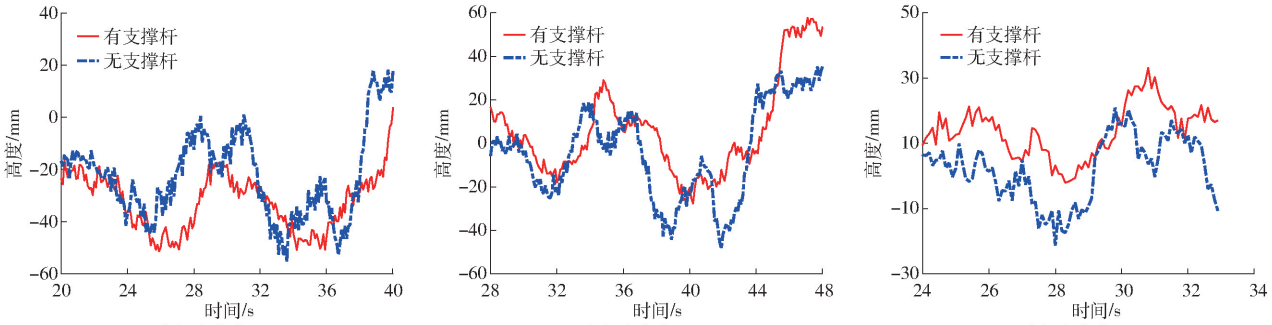

(a) 速度为0.8 m/s (b) 速度为1.0 m/s (c) 速度为1.2 m/s

图 12 区域 B 的放大视图

Fig. 12 Enlarged view of area B

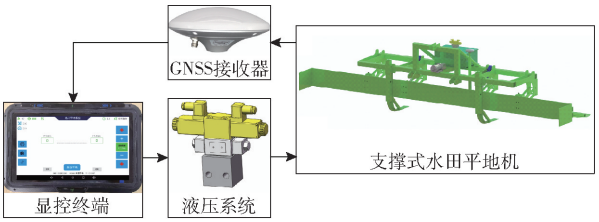

图 13 农田平整控制系统

Fig. 13 Leveling control system

件,保证实时调节平地铲运动至平整基准高度。

如图 14 所示,于 2023 年 3 月在华南农业大学教学科研基地和湖南省益阳市大通湖区分别开展田间试验。如表 3 所示,2 次试验在农田面积、农田前茬作物、农田准备方式和配套动力机械方面具有差异性。为分析支撑式水田平地机的作业效果,采用便携式激光雷达(Light detection and ranging, LiDAR)系统(金景科技,精度:20 mm)(图 14d)来获取农田平整前后地形点云数据。

4.2 结果与分析

将便携式 LiDAR 系统采集的原始数据,经 InertialExplorer 和 Scanlook PC 处理生成三维点云数据,且采用 CloudCompare 对点云数据按照高度值进行渲染,渲染结果如图 15 所示。平整前农田田面地形高度差在 100 mm 内,且旋耕作业产生间隔分布的曲线凸起和凹陷地貌。平整作业改善了农田地形高度差异,并解决了凸起和凹陷间隔分布问题,表明平整作业可实现“挖高填低”效果,而图 15b 中局部地形偏高(红色区域)的主要原因是旋耕作业后耕作层土壤软硬不一,导致平整作业后耕作层土壤发生不同程度的沉降。

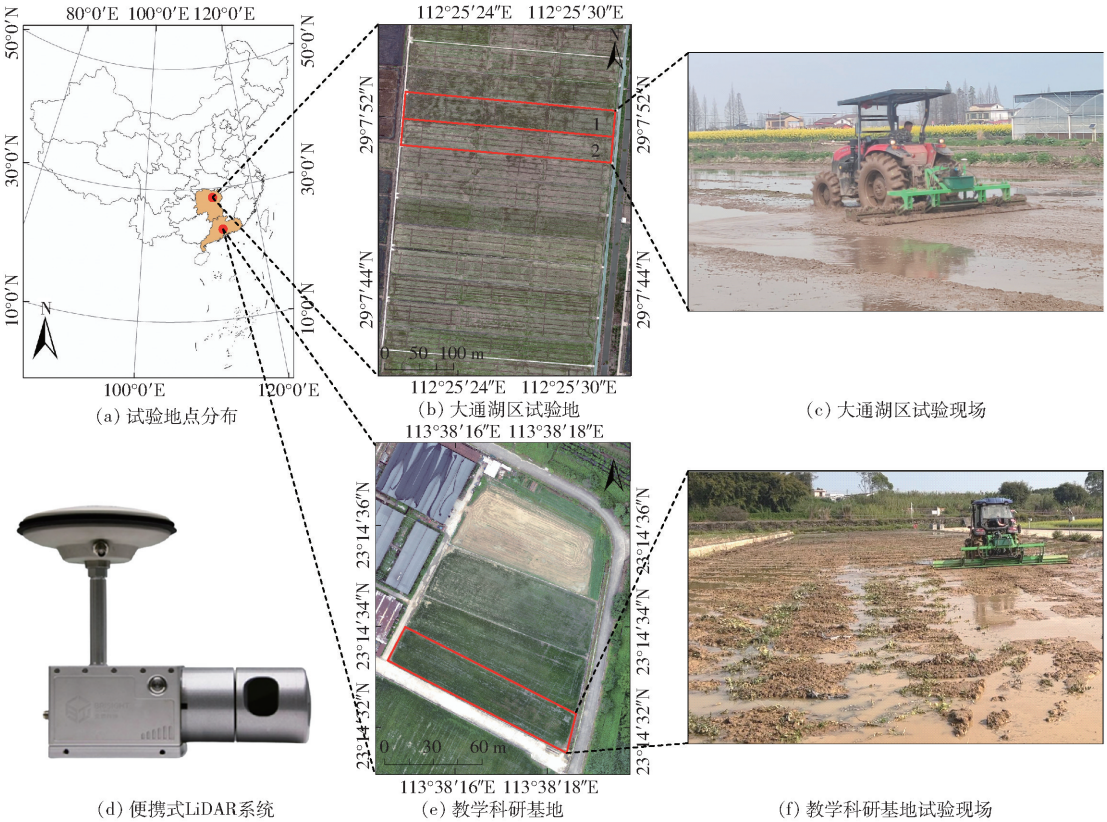

(a) 试验地点分布 (b) 大通湖区试验地 (c) 大通湖区试验现场

(d) 便携式LiDAR系统 (e) 教学科研基地 (f) 教学科研基地试验现场

图 14 水田平整试验的试验地点与过程

Fig. 14 Test site and process of paddy field leveling test

表 3　水田平整试验条件

Tab. 3　Test conditions of paddy field leveling test

地点	农田序号	农田面积/hm²	前茬作物	农田准备	配套动力
广州	1	0.21	荷兰豆	旋耕	雷沃欧豹 M804 型拖拉机
湖南	1	0.90	油菜	小并大推土、旋耕	东方红 LY1004 型拖拉机
	2	0.99			

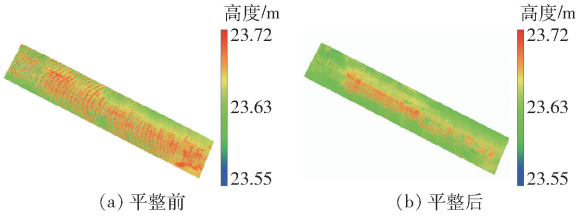

(a) 平整前　(b) 平整后

图 15　广州 1 号田地形数据渲染结果

Fig. 15　Rendering results of topographic data for field 1 in Guangzhou City

以农田田面地形高度标准差 S_d[32-33]与农田田面高度相对平整基准高度绝对偏差不大于 30 mm 测量点占比 ρ[30, 34]评价农田平整质量。平整作业后，农田田面地形高度标准差 S_d 为 21.66 mm，ρ 为 86.54%，表明支撑式水田平地机可改善田面平整情况。与文献[24]进行对比，文献[24]水田面积为 0.25 hm²，平整后 S_d 为 26.40 mm，且 ρ 为 69.40%。在水田面积相近情况下，本研究 0.21 hm² 水田平整后 S_d 与 ρ 指标均优于文献[24]。

湖南省益阳市大通湖区的试验田块平整前后原始测量数据经 InertialExplorer、Scanlook PC 和 CloudCompare 进行依次处理，结果如图 16 所示。平整前农田地形沿长边方向存在严重高度差异，其中 2 号田地形高度差约 300 mm，1 号田地形高差则次之。平整作业减少了农田在长边方向的地形高度差异。田块渲染图颜色层次减少，单色覆盖率和均匀性高表明农田平整后农田田面具有良好的平整度。

采用指标 S_d 和 ρ 评价农田平整质量，统计 2 块试验田平整质量。湖南试验田块 1 平整后 S_d 为 26.02 mm，ρ 为 80.53%；湖南试验田块 2 平整后 S_d 为 27.43 mm，ρ 为 81.03%。由此可知，平整后 S_d 均小于 30 mm，且 ρ 均大于 80%，达到了水田平整要求，验证了支撑式水田平地机结构设计有效性。与文献[24]进行对比，本文水田面积比文献[24]大 3.8 倍情况下，S_d 与文献[24]基本一致，且 ρ 均高于文献[24]的 10%以上。

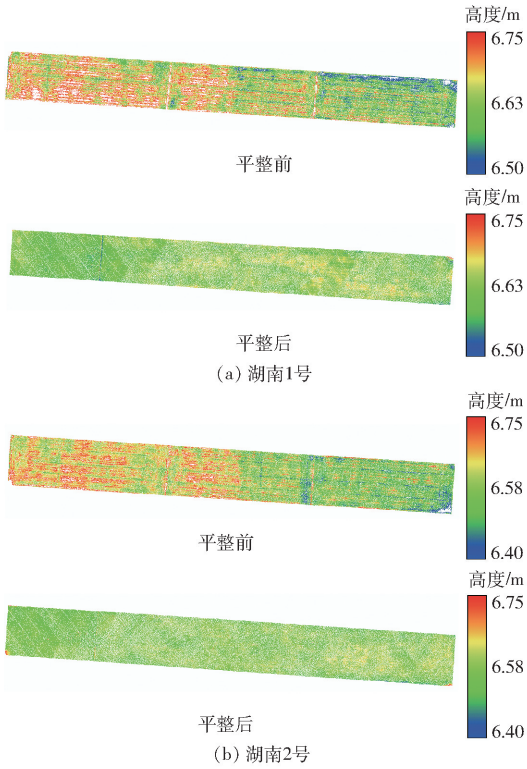

(a) 湖南1号　(b) 湖南2号

图 16　田地形数据渲染结果

Fig. 16　Rendering results of topographic data

5　结论

(1)通过水田平整试验结果验证了支撑式水田平地机的结构设计有效性。由支撑式水田平地机进行水田平整试验，0.21 hm² 水田平整后田面高度标准差 S_d 为 21.66 mm，田面高度相对平整基准高度的绝对偏差不大于 30 mm 的测量点占比 ρ 为 86.54%；总面积为 1.89 hm² 的 2 块水田平整后 S_d 分别为 26.02 mm 和 27.43 mm，ρ 分别为 80.53% 和 81.03%。试验田块经平整后 S_d 均小于 30 mm，且 ρ 均高于 80%，达到了水田平整要求。

(2)有/无支撑杆对比试验结果表明，支撑式水田平地机减少了平地铲高度变化幅度和次数，可提高平地铲高度控制精度，更适用于坑洼硬底层作业。相比于无支撑杆，有支撑杆平地铲在试验全程高度变化幅度减少 15%以上，在田面凸起位置高度变化幅度减少 30%以上，且平地铲高度变化次数减少。

参　考　文　献

[1] LIU Yalong, GE Tida, GROENIGEN K J V, et al. Rice paddy soils are a quantitatively important carbon store according to a global synthesis[J]. Communications Earth & Environment, 2021, 2(1): 1-9.

[2] MACLEAN J L, DAWE D C, HARDY B, et al. Rice almanac: source book for the most important economic activity on earth [M]. Third edition. UK: CABI, 2002.

[3] PAN Jinhua, WANG Jin, ZHUANG Shunyao. Higher soil carbon and nitrogen sequestration in rice than non-rice soils following land reclamation[J]. Soil and Tillage Research, 2024, 237: 105963.

[4] NAWAZ A, REHMAN A U, REHMAN A, et al. Increasing sustainability for rice production systems[J]. Journal of Cereal Science, 2022, 103: 103400.
[5] SINGH M, SIDHU H S, SINGH Y, et al. Performance evaluation of automatic vis-à-vis manual topographic survey for precision land levelling[J]. Precision Agriculture, 2020, 21(2): 300 - 310.
[6] SOUSA P L D, DEDRICK A R, CLEMMENS A J, et al. Effect of furrow elevation differences on level-basin performance[J]. American Society of Agricultural and Biological Engineers, 1995, 38(1): 153 - 158.
[7] RAJPUT T B S, PATEL N. Enhancement of field water use efficiency in the Indo-Gangetic Plain of India[J]. Irrigation and Drainage, 2005, 54(2): 189 - 203.
[8] SINGH N K, SINGH J B, SINGH A K, et al. Feasibility of laser land leveling in rice-wheat systems of the Central Indo-Gangetic Plains[J]. International Journal of Pure & Applied Bioscience, 2018, 6(6): 167 - 171.
[9] 魏新华, 王庆壮, 吉鑫, 等. 基于混合扩张状态观测器的农田平地机液压系统反步滑模控制研究[J]. 农业机械学报, 2024, 55(7): 37 - 46.
WEI Xinhua, WANG Qingzhuang, JI Xin, et al. Backstepping sliding mode control for hydraulic system in farmland leveller based on hybrid extended state observer[J]. Transactions of the Chinese Society for Agricultural Machinery, 2024, 55(7): 37 - 46. (in Chinese)
[10] SHEIKH A T, MUGERA A, PANDIT R, et al. The adoption of laser land leveler technology and its impact on groundwater use by irrigated farmland in Punjab, Pakistan[J]. Land Degradation & Development, 2022, 33(12): 2026 - 2038.
[11] LATIF A, SHAKIR A S, RASHID M U. Appraisal of economic impact of zero tillage, laser land levelling and bed-furrow interventions in Punjab, Pakistan[J]. Journal of Engineering and Applied Sciences, 2013, 13: 65 - 81.
[12] JAT M L, SINGH Y, GILL G, et al. Advances in soil science: laser-assisted precision land levelling impacts in irrigated intensive production systems of South Asia[M]. New York: CRC Press, 2015: 323 - 352.
[13] BAKAR B A, AHMAD M T, GHAZALI M S S, et al. Leveling-index based variable rate seeding technique for paddy[J]. Precision Agriculture, 2020, 21(4): 729 - 736.
[14] CHEN Gaolong, HU Lian, LUO Xiwen, et al. A review of global precision land-leveling technologies and implements: current status, challenges and future trends[J]. Computers and Electronics in Agriculture, 2024, 220: 108901.
[15] 罗锡文, 胡炼, 何杰, 等. 中国大田无人农场关键技术研究与建设实践[J]. 农业工程学报, 2024, 40(1): 1 - 16.
LUO Xiwen, HU Lian, HE Jie, et al. Key technologies and practice of unmanned farm in China[J]. Transactions of the CSAE, 2024, 40(1): 1 - 16. (in Chinese)
[16] LUO Xiwen, ZHAO Zuoxi, LI Qing, et al. Study on leveling control for a paddy laser leveler[C]//2007 ASAE Annual Meeting Presentation, 2007.
[17] NGUYEN V H, BALINGBING C, SANDRO J, et al. Precision land leveling for sustainable rice production: case studies in Cambodia, Thailand, Philippines, Vietnam, and India[J]. Precision Agriculture, 2022, 23(5): 1633 - 1652.
[18] SHARIFI A, GORJI M, ASADI H, et al. Land leveling and changes in soil properties in paddy fields of Guilan Province, Iran [J]. Paddy and Water Environment, 2014, 12(1): 139 - 145.
[19] BARUAH S, MOHANTY S, ROLA A C. Small Farmers Large Field (SFLF): a synchronized collective action model for improving the livelihood of small farmers in India[J]. Food Security, 2022, 14(2): 323 - 336.
[20] 陈正, 刘瀛弢, 贺德俊, 等. 中国高标准农田建设现状与发展趋势[J]. 农业工程学报, 2023, 39(18): 1 - 8.
CHEN Zheng, LIU Yingtao, HE Dejun, et al. Current situation and development trend of well-facilitated farmland construction in China[J]. Transactions of the CSAE, 2023, 39(18): 1 - 8. (in Chinese)
[21] 罗纨, 王嘉诚, 贾忠华, 等. 稻麦轮作高标准农田控制排水对排水与氮素输出削减效果模拟[J]. 农业机械学报, 2024, 55(4): 272 - 279, 311.
LUO Wan, WANG Jiacheng, JIA Zhonghua, et al. Simulation of effect of controlled drainage on reducing drainage and nitrogen output from high standard farmland in rice and wheat rotation area[J]. Transactions of the Chinese Society for Agricultural Machinery, 2024, 55(4): 272 - 279, 311. (in Chinese)
[22] 袁翠霞, 赵春江, 任艳敏, 等. 基于 U - Net 网络的高标准农田道路识别方法[J]. 农业机械学报, 2023, 54(5): 163 - 169, 218.
YUAN Cuixia, ZHAO Chunjiang, REN Yanmin, et al. Recognition method of high-standard farmland road based on U - Net [J]. Transactions of the Chinese Society for Agricultural Machinery, 2023, 54(5): 163 - 169, 218. (in Chinese)
[23] 严乙桉, 罗锡文, 资双飞, 等. 基于 50 马力轮式拖拉机的水田激光平地机设计与试验[C]//创新农业工程科技 推进现代农业发展——中国农业工程学会 2011 年学术年会, 2011.
[24] 胡炼, 罗锡文, 林潮兴, 等. 1PJ - 4.0 型水田激光平地机设计与试验[J]. 农业机械学报, 2014, 45(4): 146 - 151.
HU Lian, LUO Xiwen, LIN Chaoxing, et al. Development of 1PJ - 4.0 laser leveler installed on a wheeled tractor for paddy field[J]. Transactions of the Chinese Society for Agricultural Machinery, 2014, 45(4): 146 - 151. (in Chinese)
[25] HU Lian, XU Yi, HE Jing, et al. Design and test of tractor-attached laser-controlled rotary scraper land leveler for paddy fields[J]. Journal of Irrigation and Drainage Engineering, 2020, 146(4): 04020002.
[26] 胡炼, 杜攀, 罗锡文, 等. 悬挂式多轮支撑旱地激光平地机设计与试验[J]. 农业机械学报, 2019, 50(8): 15 - 21.
HU Lian, DU Pan, LUO Xiwen, et al. Design and experiment on multi-wheel support laser land leveler hanging on tractor [J]. Transactions of the Chinese Society for Agricultural Machinery, 2019, 50(8): 15 - 21. (in Chinese)

(下转第 274 页)

SUN Liang, LIU Bing, CHEN Xuan, et al. Design of differential transplanting mechanism for zigzag wide-narrow row rice pot seedlings[J]. Transactions of the CSAE, 2017, 33(17): 18 - 27. (in Chinese)

[22] ZHOU L, YU J Q, WANG Y, et al. A study on the modelling method of maize-seed particles based on the discrete element method[J]. Powder Technology, 2020, 374: 353 - 376.

[23] TANG Han, GUAN Tianyuan, XU Fudong, et al. Test on adsorption posture and seeding performance of the high-speed precision dual-chamber maize metering device based on the seed characteristics[J]. Computers and Electronics in Agriculture, 2024, 216: 108471.

[24] 衣淑娟,陈涛,李衣菲,等. 正负气压-型孔轮组合式谷子穴播排种器设计与试验[J]. 农业机械学报,2021,52(6):83 - 94.
YI Shujuan, CHEN Tao, LI Yifei, et al. Design and test of millet hill-drop seed-metering device with combination of positive-negative pressure and hole wheel[J]. Transactions of the Chinese Society for Agricultural Machinery, 2021, 52(6): 83 - 94. (in Chinese)

[25] 中国农业机械化科学研究院. 农业机械设计手册:上册[M]. 北京:中国农业科学技术出版社,2007.

[26] 郭鹏,郑效帅,王东伟,等. 气力辅助充种式花生精量排种器设计与试验[J]. 农业机械学报,2024,55(3):64 - 74.
GUO Peng, ZHENG Xiaoshuai, WANG Dongwei, et al. Design and experiment of precision seed metering device with pneumatic assisted seed-filling for peanut[J]. Transactions of the Chinese Society for Agricultural Machinery, 2024, 55(3): 64 - 74. (in Chinese)

[27] 刘瑞,刘忠军,刘立晶,等. 玉米扰动辅助充种高速气吸式排种器设计与试验[J]. 农业机械学报,2022,53(9):50 - 59.
LIU Rui, LIU Zhongjun, LIU Lijing, et al. Design and experiment of corn high speed air suction seed metering device with disturbance assisted seed-filling[J]. Transactions of the Chinese Society for Agricultural Machinery, 2022, 53(9): 50 - 59. (in Chinese)

[28] 史嵩,刘虎,位国建,等. 基于 DEM - CFD 的驱导辅助充种气吸式排种器优化与试验[J]. 农业机械学报,2020,51(5):54 - 66.
SHI Song, LIU Hu, WEI Guojian, et al. Optimization and experiment of pneumatic seed metering device with guided assistant filling based on EDEM CFD[J]. Transactions of the Chinese Society for Agricultural Machinery, 2020, 51(5): 54 - 66. (in Chinese)

(上接第 260 页)

[27] ZHAO Runmao, HU Lian, LUO Xiwen, et al. A novel approach for describing and classifying the unevenness of the bottom layer of paddy fields[J]. Computers and Electronics in Agriculture, 2019, 162: 552 - 560.

[28] TU Tuanpeng, HE Jie, LUO Xiwen, et al. Methods and experiments for collecting information and constructing models of bottom-layer contours in paddy fields[J]. Computers and Electronics in Agriculture, 2023, 207: 107719.

[29] 孙永健, 郑洪帧, 徐徽, 等. 机械旱直播方式促进水稻生长发育提高产量[J]. 农业工程学报, 2014, 30(20): 10 - 18.
SUN Yongjian, ZHENG Hongzhen, XU Hui, et al. Mechanical dry direct-sowing modes improving growth, development and yield of rice[J]. Transactions of the CSAE, 2014, 30(20): 10 - 18. (in Chinese)

[30] 杜攀. 浮动悬挂式激光平地机设计与试验研究[D]. 广州: 华南农业大学, 2019.
DU Pan. Design and experimental study of the floating suspended laser grader[D]. Guangzhou: South China Agricultural University, 2019. (in Chinese)

[31] ZHOU Hao, HU Lian, LUO Xiwen, et al. Design and test of laser-controlled paddy field levelling-beater[J]. International Journal of Agricultural and Biological Engineering, 2020, 13(1): 57 - 65.

[32] 刘刚, 林建涵, 司永胜, 等. 激光控制平地系统设计与试验分析[J]. 农业机械学报, 2006, 37(1): 71 - 74.
LIU Gang, LIN Jianhan, SI Yongsheng, et al. Development and experiment on laser controlled leveling system[J]. Transactions of the Chinese Society for Agricultural Machinery, 2006, 37(1): 71 - 74. (in Chinese)

[33] 汪沛, 冯达文, 陈高隆, 等. 农田精准平整过程中三维地形实时测量方法研究[J]. 农业机械学报, 2023, 54(3): 41 - 48.
WANG Pei, FENG Dawen, CHEN Gaolong, et al. Real-time 3D terrain measurement method and experiment in farmland leveling[J]. Transactions of the Chinese Society for Agricultural Machinery, 2023, 54(3): 41 - 48. (in Chinese)

[34] 胡炼, 彭靖怡, 赖桑愉, 等. 基于 BDS 和 IMU 的挖掘机铲斗位姿测量方法与试验[J]. 农业工程学报, 2022, 38(23): 12 - 19.
HU Lian, PENG Jingyi, LAI Sangyu, et al. Method and experiments of excavator bucket position and attitude measurement using BDS and IMU[J]. Transactions of the CSAE, 2022, 38(23): 12 - 19. (in Chinese)

国家出版基金项目

“十四五”时期国家重点出版物出版专项规划项目

智慧农业关键技术集成与应用系列丛书

大田无人化智慧农场

Unmanned Smart Farm for Field Crops Production

罗锡文　胡　炼◎主编

中国农业大学出版社
China Agricultural University Press

内 容 简 介

无人化智慧农场是智慧农业的主要实现方式，是一个多学科交叉的应用领域，涉及农业工程、车辆工程、控制工程、计算机科学与技术、机器人工程等，并融合了自动驾驶、机器视觉、深度学习、遥感信息和农机-农艺融合等前沿技术。

本书的作者为高校从事智慧农业方向的教师、科研人员和研究生，依托“无人化智慧农场”团队的教研与推广实践，全面详细地介绍了大田无人化智慧农场的技术体系，内容涵盖了从农场规划建设至运行维护所涉及的各个环节，重点阐述支撑农场高效生产的智能农机装备的相关理论与方法，特别是线控底盘、卫星定位、路径规划、导航控制、自动避障和多机协同等。本书适合作为现代农业研究人员和应用技术人员的参考资料，也可作为农业工程、智慧农业和车辆工程等相关专业研究生、本科生和专科生的学习资料。

图书在版编目(CIP)数据

大田无人化智慧农场/罗锡文，胡炼主编. --北京：中国农业大学出版社，2024.12.

ISBN 978-7-5655-3346-4

Ⅰ.S126

中国国家版本馆 CIP 数据核字第 2024JS6117 号

书　　名　大田无人化智慧农场

Datian Wurenhua Zhihui Nongchang

作　　者　罗锡文　胡　炼　主编

总 策 划　王笃利　丛晓红　张秀环　　责任编辑　刘　聪　石　华　蔡恩嘉

策划编辑　刘　聪　石　华　　封面设计　中通世奥图文设计中心

出版发行　中国农业大学出版社

社　　址　北京市海淀区圆明园西路 2 号　　邮政编码　100193

电　　话　发行部 010-62733489，1190　　读者服务部 010-62732336

编辑部 010-62732617，2618　　出　版　部 010-62733440

网　　址　http://www.caupress.cn　　E-mail cbsszs@cau.edu.cn

经　　销　新华书店

印　　刷　涿州市星河印刷有限公司

版　　次　2024 年 12 月第 1 版　2024 年 12 月第 1 次印刷

规　　格　185 mm×260 mm　16 开本　23.5 印张　509 千字

定　　价　128.00 元

编 委 会

目录

农业全程无人化作业试验系列成果

智能农机

技 | 术 | 路 | 线 | 图 1.0版

庞春霖 ◎主编

电子科技大学出版社
University of Electronic Science and Technology of China Press

图书在版编目（CIP）数据

智能农机技术路线图 ： 1.0 版 / 庞春霖主编 . — 成都 ： 电子科技大学出版社， 2022.6

ISBN 978-7-5647-9245-9

Ⅰ . ①智… Ⅱ . ①庞… Ⅲ . ①智能技术—应用—农业机械化 Ⅳ . ① S23

中国版本图书馆 CIP 数据核字（2021）第 195247 号

智能农机技术路线图 1.0 版

ZHINENG NONGJI JISHU LUXIANTU 1.0 BAN

庞春霖 主编

总 策 划　周 涛 杜 倩

执行策划　段 勇 杨雅薇

责任编辑　段 勇

助理编辑　杨雅薇

出版发行　电子科技大学出版社

成都市一环路东一段 159 号电子信息产业大厦九楼　邮编 610051

主　　页　www.uestcp.com.cn

服务电话　028-83203399

邮购电话　028-83201495

印　　刷　四川煤田地质制图印刷厂

成品尺寸　170 mm×240 mm

印　　张　23.5

字　　数　365 千字

版　　次　2022 年 6 月第 1 版

印　　次　2022 年 6 月第 1 次印刷

书　　号　ISBN 978-7-5647-9245-9

定　　价　108.00 元

指导委员会

主　任

钟志华

副主任

罗锡文　陈学庚　张洪程　李　骏　邵安林　李言荣　龙　腾　兰玉彬　瞿国春
洪暹国　陈俊宝

委　员（按照姓氏笔画）

丁艳锋　王云飞　王志勤　向　勇　何小龙　陈有方　李斯华　张兆田　苏　波
李荣利　李　红　吴建会

编委会

主　编

庞春霖

副主编

黄胜操

章节主编（按照章节顺序）

张　楠　王国业　傅秀清　冯雪松　胡　炼　康　陈　胡耀光　邱惠君　孙　坤

参编人员（按照姓氏笔画顺序）

于合龙　于志威　王　帅　王　伟　王　进　王　林　王　恒
王　辉　王　淼　王　儒　王升升　王兴伟　王晓鹏　王景立
王蓬勃　尤　杨　毛黎明　叶　聪　叶大鹏　田大永　冯绍晰
龙翔宇　许　旻　刘　亮　刘　超　刘永东　刘军帅　刘雨童
刘贵敬　刘继凯　江发潮　安华明　齐江涛　阮炜涛　任哲平
孙卫东　孙战胜　吴　华　李　由　李　杨　李永胜　李向前
李政平　李保忠　李恒欣　李晓宇　李家坤　李德芳　张　昆
张　博　张　瑶　张胜利　张振乾　张德晖　陈　星　陈　胜
陈　磊　陈伟元　陈芸芳　陈洪涛　陈露瑶　杨大芳　杨国来
贡　军　吴　琼　宋　琦　沈　超　肖建峰　何晓龙　周　全
周　君　周　祥　苗　霖　郑书河　屈龙涛　范永豪　明书聪
季　山　季宇杰　金时超　周朋朋　郑思仪　周彩云　姚　坤
俞　轶　赵　杨　赵凯旋　赵润茂　钟贵华　姚轶溥　闻敬谦
高一平　袁发骏　黄　川　黄　亮　龚　奘　鹿　斌　梁冬晗
崔红杰　逯益夏　韩　帅　韩玉玺　谢　勇　谢　斌　谢瑞华
葛　畅　温长吉　董光阳　曾宇斐　雷治国　翁海勇　解晓琳
甄晓阳　翟　艺

CONTENT 目录

四、科研成果

证书号第5605395号

发明专利证书

发明名称：一种夹剪收一体化的紧凑双臂式茶叶行间采收装置及方法

发 明 人：赵润茂;俞焘杰;陈建能;贾江鸣;武传宇;贺磊盈

专 利 号：ZL 2022 1 0167838.4

专利申请日：2022年02月23日

专利权人：浙江理工大学

地 址：310018 浙江省杭州市下沙高教园区2号大街928号

授权公告日：2022年11月25日　　授权公告号：CN 114467492 B

国家知识产权局依照中华人民共和国专利法进行审查，决定授予专利权，颁发发明专利证书并在专利登记簿上予以登记。专利权自授权公告之日起生效。专利权期限为二十年，自申请日起算。

专利证书记载专利权登记时的法律状况。专利权的转移、质押、无效、终止、恢复和专利权人的姓名或名称、国籍、地址变更等事项记载在专利登记簿上。

局长
申长雨

国家知识产权局

2022年11月25日

其他事项参见续页

证 书 号 第 5605395 号

专利权人应当依照专利法及其实施细则规定缴纳年费。本专利的年费应当在每年 02 月 23 日前缴纳。未按照规定缴纳年费的，专利权自应当缴纳年费期满之日起终止。

申请日时本专利记载的申请人、发明人信息如下：

申请人：

浙江理工大学

发明人：

赵润茂；俞焘杰；陈建能；贾江鸣；武传宇；贺磊盈

中华人民共和国国家版权局
计算机软件著作权登记证书

证书号： 软著登字第16787645号

软 件 名 称： 无人驾驶运粮车粮仓智能视觉定位系统 V1.0

著 作 权 人： 华南农业大学

权利取得方式： 原始取得

权 利 范 围： 全部权利

登 记 号： 2025SR2131447

根据《计算机软件保护条例》和《计算机软件著作权登记办法》的规定，经中国版权保护中心审核，对以上事项予以登记。

2025年11月03日

证书号第5784708号

发明专利证书

发明名称：一种基于压电驱动的精确配比小流量在线混药方法

发　明　人：郑俊杰;赵润茂;陈建能;贾江鸣;魏义坤;熊永森

专　利　号：ZL 2022 1 0360902.0

专利申请日：2022年04月07日

专利权人：浙江理工大学

地　　址：310018 浙江省杭州市经济技术开发区白杨街道2号大街928号

授权公告日：2023年03月14日　　授权公告号：CN 114667984 B

国家知识产权局依照中华人民共和国专利法进行审查，决定授予专利权，颁发发明专利证书并在专利登记簿上予以登记。专利权自授权公告之日起生效。专利权期限为二十年，自申请日起算。

专利证书记载专利权登记时的法律状况。专利权的转移、质押、无效、终止、恢复和专利权人的姓名或名称、国籍、地址变更等事项记载在专利登记簿上。

局长
申长雨

国家知识产权局
2023年03月14日

其他事项参见续页

证书号第5784708号

专利权人应当依照专利法及其实施细则规定缴纳年费。本专利的年费应当在每年04月07日前缴纳。未按照规定缴纳年费的，专利权自应当缴纳年费期满之日起终止。

申请日时本专利记载的申请人、发明人信息如下：

申请人：

浙江理工大学

发明人：

郑俊杰;赵润茂;陈建能;贾江鸣;魏义坤;熊永森

证书号第8314353号

专利公告信息

发明专利证书

发 明 名 称：一种夹拔式采摘与回收茶叶的采摘收集臂及其工作方法

专 利 权 人：浙江理工大学

地　　址：310018 浙江省杭州市下沙高教园区2号大街928号

发　明　人：王翔;赵润茂;陈建能;武传宇;郇晓龙;吴敏

专　利　号：ZL 2023 1 1015173.6　　授权公告号：CN 116941421 B

专利申请日：2023年08月14日　　授权公告日：2025年09月30日

申请日时申请人：浙江理工大学

申请日时发明人：王翔;赵润茂;陈建能;武传宇;郇晓龙;吴敏

国家知识产权局依照中华人民共和国专利法进行审查，决定授予专利权，并予以公告。

专利权自授权公告之日起生效。专利权有效性及专利权人变更等法律信息以专利登记簿记载为准。

局长

申长雨

国家知识产权局

2025年09月30日

广东省科学技术厅

粤科函产字〔2025〕272号

广东省科学技术厅关于认定2024年度广东省工程技术研究中心的通知

各地级以上市科技局，各有关单位:

根据《广东省工程技术研究中心管理办法》（粤科规范字〔2022〕12号）和《广东省科学技术厅关于组织申报2024年度广东省工程技术研究中心的通知》（粤科函产字〔2024〕1096号），经组织申报、专家评审和网上公示及复核，现认定广东省智慧能源技术与应用工程技术研究中心等554家单位为2024年度广东省工程技术研究中心（简称“工程中心”，名单见附件）。有关事项通知如下:

一、工程中心是构建以企业为主体、市场为导向、产学研用深度融合的技术创新体系的重要科研平台。各工程中心要加大科研投入和条件建设，加强技术攻关和协同合作，加速成果转化和人才培养，在推进现代化产业体系建设、促进产业科技互促双强中发挥支撑作用。

二、鼓励各地市科技管理部门积极研究并制定配套支持政

策，指导和服务工程中心进一步提高自主创新能力，推动工程中心高质量发展。

三、工程中心实行网络化管理，相关信息发布及过程管理依托“广东省工程技术研究中心创新服务平台”（www.gdetrc.net）实施，请2024年度认定通过的工程中心于2025年3月15日前登录该平台进行注册备案。后续工程中心如发生依托单位更名、所属地或工程中心主任变更及资格撤销等情况，请通过服务平台进行相关操作。

附件：2024年度广东省工程技术研究中心认定名单

广东省科学技术厅

2025年2月21日

公开方式：主动公开

附件

2024年度广东省工程技术研究中心认定名单

序号	工程中心名称	依托单位	所在地市
1	广东省Mini LED新型显示工程技术研究中心	广州市鸿利显示电子有限公司	广州市
2	广东省新能源汽车充电设备及管理系统（万城万充）工程技术研究中心	广州万城万充新能源科技有限公司	广州市
3	广东省智慧能源技术与应用工程技术研究中心	广东电网能源投资有限公司	广州市
4	广东省综合智慧能源工程技术研究中心	广州发展集团股份有限公司	广州市
5	广东省生物质能复合应用工程技术研究中心	广州环峰能源科技股份有限公司	广州市
6	广东省光伏电站AI智慧运维工程技术研究中心	广东省电力开发有限公司	广州市
7	广东省户用储能及其控制系统工程技术研究中心	广州疆海科技有限公司	广州市
8	广东省高效燃气输配工程技术研究中心	广州东部发展燃气有限公司	广州市
9	广东省汽车座椅舒适系统线束工程技术研究中心	广州市信征汽车零件有限公司	广州市
10	广东省新能源汽车动力总成自动化成套装备工程技术研究中心	广州市创智机电设备有限公司	广州市
11	广东省汽车电器分配系统（整车线束）工程技术研究中心	广州新李汽车零部件有限公司	广州市
12	广东省智能大屏应用工程技术研究中心	广州欢网科技有限责任公司	广州市
13	广东省新一代信息技术与数字化应用（科城数科）工程技术研究中心	科学城（广州）数字科技集团有限公司	广州市
14	广东省民航数字经济工程技术研究中心	广州民航信息技术有限公司	广州市
15	广东省效果营销工程技术研究中心	省广营销集团有限公司	广州市

序号	工程中心名称	依托单位	所在地市
118	广东省节能建筑工程质量检测工程技术研究中心	广东惠和工程检测有限公司	广州市
119	广东省公路数智化养护工程技术研究中心	广东和立交通养护科技有限公司	广州市
120	广东省智能认知与行为决策工程技术研究中心	华南理工大学	广州市
121	广东省集成电路设计自动化工程技术研究中心	广东工业大学	广州市
122	广东省无人系统群体智能应用工程技术研究中心	中山大学	广州市
123	广东省毫米波太赫兹器件与系统工程技术研究中心	广东大湾区空天信息研究院	广州市
124	广东省人工智能赋能智慧物流工程技术研究中心	暨南大学	广州市
125	广东省新型显示工程技术研究中心	广东聚华新型显示研究院	广州市
126	广东省空天飞行器工程技术研究中心	广东空天科技研究院（南沙）	广州市
127	广东省近海基础设施韧性提升工程技术研究中心	广州航海学院	广州市
128	广东省无人化智慧农场工程技术研究中心	华南农业大学	广州市
129	广东省聚集诱导发光工程技术研究中心	广东省大湾区华南理工大学 聚集诱导发光高等研究院	广州市
130	广东省智慧设施农业工程技术研究中心	广东省农业科学院设施农业研究所	广州市
131	广东省未来植源性化妆品创制工程技术研究中心	中新国际联合研究院	广州市
132	广东省粤北地方家禽健康养殖工程技术研究中心	广东科贸职业学院	广州市
133	广东省高性能纸用功能材料工程技术研究中心	广东轻工职业技术大学	广州市

广东省工程技术研究中心认定申请书

中心名称： 广东省无人化智慧农场工程技术研究中心

研究开发方向： 农业技术

所属领域： 农业装备(农业机械、设备及材料等)

依托单位： 华南农业大学

联合共建单位：

通信地址： 广东省广州市天河区五山路483号

邮政编码： 510642

联 系 人： 胡炼

联系电话： 15915767370

申报日期： 2024-09-17

广 东 省 科 学 技 术 厅

2024年7月制

一、申报单位基本情况

依托单位	华南农业大学			
法人代表	薛红卫		法人代码	
主管部门				
通信地址	广东省广州市天河区五山路483号			
邮政编码	510642		传真	
单位性质	高等院校		申报单位类型	高校/科研院所/医院
联系人	胡炼		联系电话	
电子邮件	lianhu@scau.edu.cn			
经济类型	高等院校			
成立时间	1952-07-01			
注册资本	311733.00万人民币			
职工总数	3380			
工程技术人员数	2360			
市（区）级科研平台建设情况	否	批准成立名称		
		批准成立时间		
		获得资助金额	（万元）	
其他研发机构建设情况：	市（区）级科研平台：	否		
	省级科研平台：	是	成立名称：南方农业机械与装备关键技术教育部重点实验室 成立时间：2006-05-01	
	国家级科研平台：	是	成立名称：农业装备技术全国重点实验室 成立时间：2022-11-30	
	其他			
“专精特新”企业建设情况：	省级专精特新中小企业：	否		
	国家级专精特新“小巨人”企业：	否		
是否上市公司：	否			

依托单位和联合共建单位分工

序号	单位名称	分工

二、依托单位上一年度经济效益与研究开发经费情况

上一年度经济效益（企业需填写）			
项目		单位	数额
全年总产值		万元	0
其中：新产品产值		万元	
主营业务收入额		万元	0
其中：新产品销售额		万元	
高技术服务收入额		万元	
全年总出口额		万美元	
其中：新产品出口		万美元	
研究开发经费情况			
研究开发经费投入合计		万元	5227.00
研发经费占全年总销售额比重		%	
经费来源	企业税前从销售额中提取	万元	
	政府拨款	万元	4727.00
	横向合作	万元	500.00
	其他	万元	
研究开发经费支出合计		万元	3000.00
经费支出	基建投入	万元	0
	仪器设备购置	万元	550.00
	材料费	万元	900.00
	测试化验加工外协费	万元	650.00
	人员费	万元	100.00
	知识产权费	万元	60.00
	差旅费	万元	300.00
	会议费	万元	40.00
	其他	万元	400.00

三、工程中心人员情况表

工程中心研究开发人员情况			
项目			人数
研究开发人员数量70	职称：	高级职称	60
		中级职称	10
		初级职称	0
	学历：	博士	69
		硕士	1
		本科	0
		大专	0
		其他	0

工程中心主任										
序号	姓名	性别	年龄	职称	职务	学历	现从事专业	在中心承担的任务	所在单位	签名
1	罗锡文	男		教授	重点实验室主任	硕士研究生	农业工程	主持工程中心的建设	华南农业大学工程学院	

中心主要研究人员										
序号	姓名	性别	年龄	职称	职务	学历	现从事专业	在中心承担的任务	所在单位	签名
1	胡炼	男		研究员	工程学院副院长	博士研究生	农业电气化与自动化	中心副主任作大田物无人化智慧农场首席科学家	华南农业大学工程学院	
2	李君	男		教授	工程学院院长	博士研究生	农业机械化工程	中心副主任无人化智慧果园首席专家	华南农业大学工程学院	
3	何杰	男		副教授	无	博士研究生	农业电气化与自动化	中心副主任智能装备共性技术首席专家	华南农业大学工程学院	
4	肖德琴	女		教授	无	博士研究生	农业电气化与自动化	智慧养殖场首席专家	华南农业大学数学与信息学院	
5	汪沛	女		副教授	无	博士研究生	农业电气化与自动化	无人农场管控平台	华南农业大学工程学院	
6	黄培奎	男		高级工程师	无	博士研究生	农业电气化与自动化	农业机械智能导航及自动作业	华南农业大学工程学院	
7	赵润茂	男		副教授	无	博士研究生	农业电气化与自动化	农田土壤信息智能感知及决策	华南农业大学工程学院	
8	臧英	女		教授	重点实验室常务副主任	博士研究生	农业机械化工程	农情信息感知及精准管控	华南农业大学工程学院	
9	张智刚	男		副教授	无	博士研究生	农业电气化与自动化	农业机械智能导航及自动作业	华南农业大学工程学院	

五、其他业绩

CERTIFICATE
获 奖 证 书

ROBOMASTER UNIVERSITY SERIES

ROBOMASTER
机甲大师高校联盟赛

华南农业大学 Taurus 战队

在**“第二十四届全国大学生机器人大赛 RoboMaster 2025 机甲大师高校联盟赛”3V3 对抗赛**的英雄机器人组中，荣获机器人竞技奖

一等奖

指导单位：
中国高等教育学会
中国工程院战略咨询中心

指导老师：赵润茂、黄培奎、何杰、汪沛、胡炼

参赛队员：林涵、陈永奇、张冠豪、谷源忠、吴泓佳

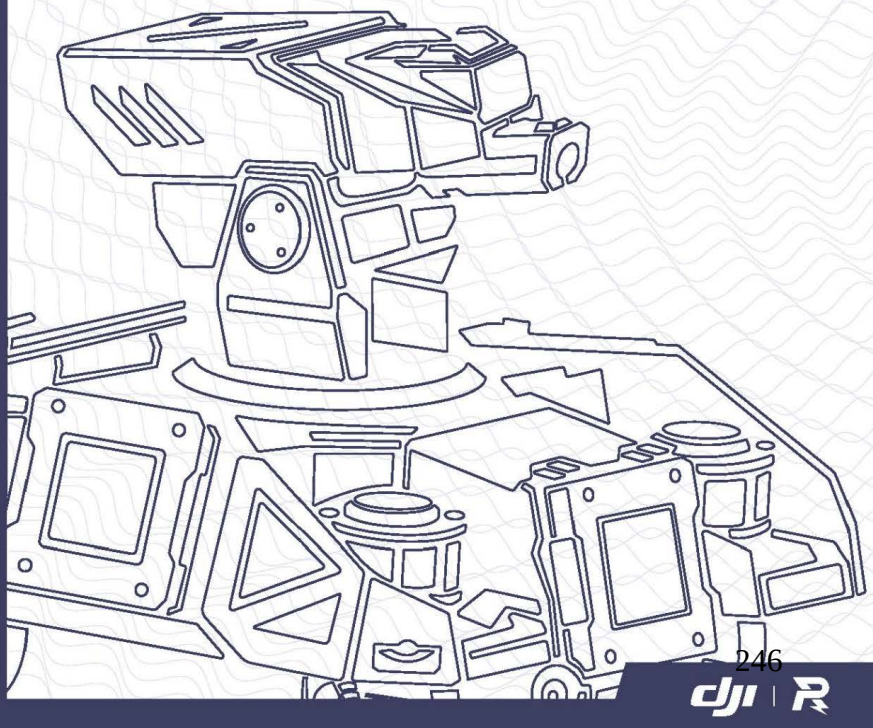

全国大学生机器人大赛组委会
2025 年 5 月

证书编号：RMUL2025YXAZDCW


荣誉证书
CERTIFICATE OF HONOR
在“天鹅杯”第十届国际大学生智能农业装备创新大赛中，经评审，荣获
一等奖
特发此证，以资鼓励！
单位名称：华南农业大学
作品名称：果树对靶变量施药机器人
获奖学生：张凯威,廖建贸,蔡昭锐,何浩文,张嘉威
指导教师：赵润茂,何杰
国际农业和生物系统工程委员会
证书编号：NZDS2025-B-006
二〇二五年五月

编号：23001233400

第十六届“高教杯”全国大学生
先进成图技术与产品信息建模创新大赛

获 奖 证 书

获奖项目：机械类 先进成图技术赛道 三等奖

获奖者姓名：姚聪

所在学校：浙江理工大学

指导教师：赵润茂、贺青川、马锃宏、杜小强

全国大学生先进成图技术与产品信息建模创新大赛组委会

2023.8.1

防伪查询

编号：23001120327

第十六届“高教杯”全国大学生先进成图技术与产品信息建模创新大赛

获 奖 证 书

获奖项目：机械类 优秀指导教师 三等奖

获奖学校：浙江理工大学

参 赛 者：姚聪、林伟信、谢妍、王麒程、邵柏恺、黄泽熙、马俊杰、徐大米、卢明

指导教师：赵润茂

全国大学生先进成图技术与产品信息建模创新大赛组委会

2023.8.1

防伪查询


荣誉证书
CERTIFICATE OF HONOR
授予：赵润茂
“天鹅杯”第九届国际大学生智能农业装备创新大赛
优秀指导教师
特发此证，以资鼓励！
国际农业和生物系统工程委员会
证书编号：NZDS2024-A-025
中国农业机械学会
中国农业工程学会
省部共建现代农业装备与技术协同创新中心
农业工程大学国际联盟
二〇二四年五月

生产实践锻炼证明

华南农业大学：

广州市汇奥机电有限公司是一家致力于现代农业机械装备推广、应用与技术研发的专业化企业。公司以拖拉机、联合收割机、插秧机等现代农业装备为核心，紧密围绕农业生产实际需求，提供涵盖农机装备应用、技术支持、性能测试及智能化升级改造的综合性整体解决方案，深度服务于智慧农业与农业机械化的高质量发展。

罗锡文院士团队与广州市汇奥机电有限公司在农机智能化改造与高效作业示范方面开展了深入合作。受委派，赵润茂老师自 2024 年 7 月至今，参与广州市汇奥机电有限公司在智能农机田间作业性能测试与技术优化方面的工作，已累计完成 100 余台/套高端农机装备的下地调试、技术指导与作业工作，两年间累计参与生产实践时间超 200 天。

特此证明！

广州市汇奥机电有限公司（公章）

证明人：周祖岳

2025 年 12 月 20 日

单　位：广州市汇奥机电有限公司

负责人：周祖岳　总经理

手机号：[redacted]